X-ray Study of the Plasma Heating and Particle Acceleration in Clusters of Galaxies

Naomi Kawano

Department of Physics, Faculty of Science, Hiroshima University
1-3-1 Kagamiyama, Higashi-Hiroshima, Hiroshima, 739-8526 Japan

August 21, 2006

Abstract

Clusters of galaxies are the largest gravitationally bound system in the universe. They are filled with the diffuse hot plasma called IntraCluster Medium (ICM), which radiates strong X-ray emission. Although the ICM is expected to cool down due to the energy loss by the radiative cooling (Cooling Flow hypothesis; CF), recent observations indicate that the ICM at the cluster center is heated up to some degree. This can not be explained by a simple CF picture. The plasma heating is considered to associate with the particle acceleration. The sign of the non-thermal emission by the particle acceleration has been detected in some clusters with the previous observations. However, their existence is under discussion due to the insufficient detection accuracy. Thus, the origin of the heating effect is not confirmed yet. Understanding plasma heating ans particle acceleration by investigating the thermal and non-thermal properties simultaneously brings a great benefit to treat cluster evolution and cosmology. We performed the systematic studies of the temperature structure and the amount of the cooled ICM for 22 clusters in order to examine the plasma heating, utilizing the spatially resolved data of the Chandra satellite. Meanwhile, for the study of the non-thermal emission, we utilized the HXD onboard Suzaku satellite, which have higher sensitivity than the previous ones.

The decline of the ICM temperature toward the center is recognized in all the clusters. The size of the observed cool region is consistent with that predicted by the radiative cooling, implying that the radiative cooling actually takes places. The central temperature scatters widely (0.64−5.2 keV) and is typically higher than 1 keV. Furthermore, the ratio of the central temperature to the cluster-wide one is found to be 0.3−0.6. These features are plainly inconsistent with the CF picture. The mass of the central cool plasma is much less by an order of magnitude than that predicted from the CF hypothesis. Such conflictions with the CF are also indicated from the absorption density profiles or the cooling flow rate. We compare these results with the expected properties by the proposed heating models. As a result, the hierarchical evolution with merger and radiative cooling is considered to be more preferable than the AGN jet at the cluster center or the thermal conduction.

For the non-thermal emission, which is fairly faint, we first develop the HXD PIN background estimation with good accuracy. Its systematic error results in as low as $\sim$3.5 %, and a sign of the non-thermal emission have found from Abell 3376 West-Relic (WR). The flux of $(5.1 \pm 1.8 \pm 6.1) \times 10^{-12}$erg s^{-1} cm^{-2} gives more restricted upper limit than that obtained with BeppoSAX. From the hard band spectra of XIS, we set an additional constraint on the hard X-rays from Abell 3376 Center, Abell 1060, Centaurus cluster offset region. The non-thermal luminosity from Abell 3376 WR is $<1.6\times10^{44}$ erg s^{-1}, which is $<$10 % of thermal one. Combining the HXD and XIS, the non-thermal emission from Abell 3376 WR seems to have a powerlaw spectra with the photon index around 2, and extends over $\sim$15−60$'$ area.

We also discuss the origin of the non-thermal emission and relativity with the plasma heating from the derived energetics.

Contents

List of Figures

List of Tables

Chapter 1

INTRODUCTION

Clusters of Galaxies are the largest self-gravitating system in the universe. A cluster contains thermal diffuse hot plasma

called IntraCluster Medium (ICM), as well as thousands of galaxies and dark matter. The dark matter carries a large fraction of the cluster mass, which provides the gravitational potential to confine the other two baryonic components of the ICM and galaxies. The thermal ICM is a few times as massive as the stellar component, and thus the most major observable component in clusters of galaxies. We can observe it only in X-ray wavelength. In the process of cluster evolution, the ICM has been virialized and heated up to high temperature ($kT = 10^{7-8}$ K). This is comparable to the depth of the gravitational potential, and then strong X-ray is emitted along with the potential. Recent X-ray observations revealed that clusters of galaxies are more energetic object than considered before; their temperature distribution and X-ray morphology exhibit complex appearance even in the relaxed clusters. Understanding these phenomena must deeply involve the dynamical process such as particle acceleration due to the shock wave or magneto hydrodynamic turbulence, as well as plasma heating.

The ICM temperature is observationally known to decline toward the cluster center. This is considered to be a result due to the radiative cooling since the time scale of the ICM cooling in the cluster center is shorter than the Hubble time. Once the ICM starts to cool, the pressure decreases in the cluster center. Then, a slow but massive inward plasma flow is produced, which is called Cooling Flow (Fabian 1994). This hypothesis can explain not only the temperature decline but also the steep rise of the X-ray surface brightness toward the cluster center, and it was widely believed. However, recent observations with ASCA, Chandra, and XMM-Newton found that there are many phenomenon which can not be explained by the simple Cooling Flow picture. The most remarkable properties conflicting with the Cooling Flow picture is the ICM temperature at the cluster center. It is not cooled down to <1 keV, which should be produced by Cooling Flow. Then, it has become a new consensus that some heating mechanism prevents the ICM from radiatively cooling in the central region of the galaxy clusters. This is called as "Cooling Flow Problem". It is essential to resolve this problem in order to know cluster evolution.

On the other hand, non-thermal hard X-ray generated via the particle acceler-

ation is also thought to have a great impact on astrophysical understanding. The acceleration in clusters of galaxies has a potential to be the origin of the "highest energy cosmic rays", which are extremely energetic particles with the energy of $\sim 10^{20}$ eV. This is because the particles can not escape from large cluster region and are confined in clusters of galaxies during being accelerated. Additionally, the relatively low density of the ICM can restrict the energy dissipation of the accelerated particles. The large scale radio emission over a few Mpc is observed in $\sim$10 % of galaxy clusters, and it gives us the evidence for the existence of high energy electrons. In the X-ray observations, the non-thermal emission from several clusters has been detected by BeppoSAX or RXTE satellites. It is observed as a excess hard X-rays above the thermal emission from the ICM, appearing in the energies above a few tens keV. However, the non-thermal emission is as faint as the sensitivity limit of those instruments and hence it was impossible to detect such a weak emission with good accuracy. In addition, there are no information on its distribution. Therefore, it has not been confirmed whether the detected hard X-rays are actually originated via particle acceleration in the clusters of galaxies.

In this way, plasma heating and the particle acceleration have not fully understood yet. We analyzed the detail distribution of the thermal parameters such as the ICM temperature, metal abundance, absorption column density, and mass of ICM or total gravitating matter in order to understand the thermal structure of plasma and the heating properties in the cluster center. Although such study for individual cluster is performed, general properties of thermal structure among cluster has not been investigated, and therefore we investigate it in this thesis. On the non-thermal emission by the particle acceleration, we studied it with Suzaku HXD, which has realized the lowest background and then the highest sensitivity in a few tens keV. This enables us to observe the non-thermal emission more accurately than that from the previous instruments. Moreover, we can obtain spatial distribution of the non-thermal emission by means of multi-pointing observations, thanks to the narrow field of view of the HXD. For this purpose, we also performed the background estimation of HXD PIN detector.

In Chapter 2, we review the physical statement and the past observational results of the thermal and non-thermal emission in clusters of galaxies. The instrumentation of the utilized four satellites (ASCA, Chandra, XMM-Newton, and Suzaku) is summarized in Chapter 3. The observations and data reduction are described in Chapter 4. In Chapter 5, we presents the thermal properties of the central cool plasma for the plasma heating, and the background estimation of HXD PIN and the study of the non-thermal emission for the particle acceleration. The obtained results are discussed in Chapter 6. Finally, we give a conclusion in Chapter7. Throughout this thesis, we adopt the Hubble constant of $H_0 = 50h_{50}$ km s^{-1} Mpc^{-1}. All the errors are given in the 90 % confidence level if there are no any cautionary statements.

Chapter 2

REVIEW

2.1 Clusters of Galaxies

2.1.1 Overview

Clusters of galaxies are the largest gravitationally bound systems in the universe. How have such a large object been formed ? In the large-scale structure of the universe, clusters of galaxies have found to be accounted for nodes of its web-like structure where 100−1000 galaxies concentrate (figure 2.1 left). The structure is formed due to gravitational instability after the radiation decoupling from the matter, which took place when the universe was only 0.38 million years old. The radiation and particles have been cooled enough in the decoupling process and then neutral hydrogen and helium atom were formed. The electric neutral matters have accumulated in the place where the dark matters gradually condensed (figure 2.1 right). Thus the galaxies was born and further clusters of galaxies was created by the gravitational interaction between galaxies. This is known as "bottom-up" scenario of universe.

Clusters of galaxies extends over a few Mpc in radius and have an optical luminosity of $10^{12-13} L_{\odot}$. Stars in the member galaxies are mightily responsible for important baryonic component in the clusters but their contribution is only ∼30% of all known baryons. The remaining mostly consists of diffuse hot plasmas (10^{7-8} K) called Intra-Cluster Medium (ICM) filling the vast volume of each cluster and emitting strong X-rays. Historically, the discovery of X-ray emission from clusters of galaxies such as Virgo, Coma, and Perseus clusters (Bryan et al. 1966; Frits er al. 1971; Grusky et al. 1971; Meekins et al. 1971), was unexpected and then exciting. There were two explanations for the diffuse emission at first; thermal bremsstrahlung from hot plasma, or inverse Compton of cosmic microwave background by high energy electrons. In 1976, He-like Fe-K line emission was detected from the Perseus cluster (Mitchell et al. 1976), which have revealed that the former is correct emission mechanism and the emitter should be the diffuse hot plasma, that is to say the ICM. Subsequent X-ray observations confirmed that the mass of the ICM reaches 2−5 times lager than that of member galaxies, and the luminosity is typically 10^{43-45} erg s^{-1} which is ∼10% of the bolometric luminosity of all stars

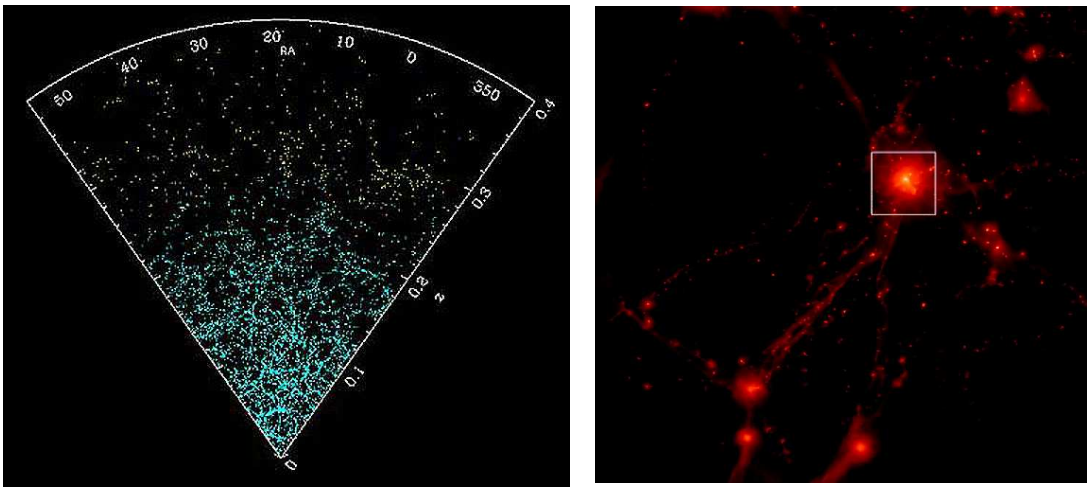

Figure 2.1: The large scale structure of the universe. left: Distribution of 11,339 galaxies in a slice of the Sloan Digital Sky Survey (SDSS). The galaxies organize into long, narrow walls with open spaces between them. right: An N-body simulation of cosmic structure formation assuming standard Λ Cold Dark Matter Model. The spatial scale is $\sim$36 Mpc. A galaxy cluster is created (white square) where the dark matter is condensed (Motl et al., 2004).

in it. X-ray observations also imply that the significant amount of dark matter exist in clusters of galaxies. Thus, the clusters of galaxies are extremely important objects for X-ray astronomy since the ICM is the most dominant component of cosmic baryons.

The origin of ICM is primarily thought to be primordial gas of hydrogen and helium which fell into the gravitational potential of dark matter, and was adiabatically compressed and heated. In the densest region of the heated gas, radiative cooling take place to form galaxies and the first-generation stars. However, the ICM contains heavy elements whose amount is $\sim$30 % of the cosmic abundance. Such a heavy element should be made by nucleosynthesis in the later universe after the formation of ICM. Therefore, it is natural to consider that they are generated in stars and transported to the intra-cluster space and mixed into the ICM. To be specific, after the heavy elements in stars are presumed to be strewed into the interstellar space of the galaxies via stellar mass loss and supernovae, they are transported into the ICM by the processes such as the ram pressure stripping or galaxy wind.

In addition to the thermal emission from the ICM, non-thermal emission related to the particle acceleration is possible term in the clusters of galaxies for a long time. Theoretically, there is two fundamental mechanism of particle acceleration in clusters of galaxies; the first order Fermi acceleration by shock wave generated from the merging among clusters or the motion of member galaxies, and the second order Fermi acceleration by turbulent releasing energy via magnetic reconnection which occur when the member galaxies confuse the magnetized ICM. The high energy electrons accelerated thorough such processes are considered to boost microwave background by accelerated electrons by inverse Compton scattering. This behavior might appear as non-thermal emission in clusters of galaxies. Cluster-wide radio

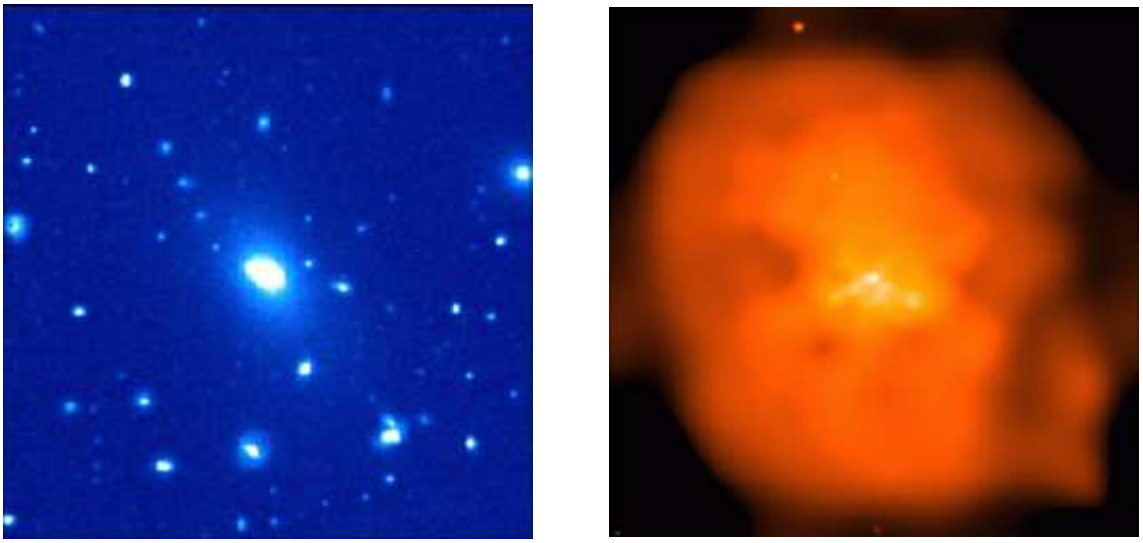

Figure 2.2: The optical and X-ray image of Abell 2199, in ∼300× 300 kpc. The ICM emission satisfies between the stellar component of galaxies.

halos detected from radio observation (e.g. Coma cluster; Deiss et al. 1997; Thierback et al. 2003), and its spectra with a steep index suggest that it should be the synchrotron emission caused by the accelerated electrons of $\gamma \sim 10^{3-4}$ in clusters of galaxies.

The emissivity of non-thermal emission is in proportion with the density while that of thermal emission of ICM correlates to the square of density. Therefore, non-thermal emission is considered to have much weaker X-ray flux than that of ICM emission, and it is necessary to be observed in higher energy of several dozen keV where the thermal emission disappears. With BeppoSAX satellite, the non-thermal emission have been detected from 7 clusters of galaxies at 2 σ level. However, it is suspicious whether the non-thermal emission is really detected because there are large uncertainty on background level due to technical difficulty of observation and the distribution of non-thermal emission is not known at all.

2.1.2 Optical Observation

Clusters of galaxies are identified in optical observations and the number of catalogued clusters reaches to several thousand at least. The famous catalog complied by Abell (1985) contains 2712 clusters. This accounts for northern rich clusters while southern rich clusters are added by Abell, Corwin, and Olowin (ACO catalogue, 1989). Zwicky Catalog (Zwicky et al. 1961-1968) is also popular. As a catalog for poor clusters, which have less member galaxies than rich clusters, MKW (Morgan, Kayser, and White 1975) and AMW (Albert, White, and Morgan 1977) are well known. Groups of galaxies, which are small system with 10-100 galaxies and essentially same as clusters (in other words, mini-sized clusters), are extensively investigated by Hickson er al. (1989) to be catalogued (HCG Catalogue).

Several schemes have been used to classify clusters of galaxies according to the optical morphology. The most applied classifications are Bautz-Morgan Type (Bautz

& Morgan 1970) and Rood-Sastry Type (Rood &Sastry 1971). In the Bautz-Morgan classification, clusters of galaxies are categorized three types, Bautz-Morgan Type I, II, and III, by the degree of bright galaxies which dominate a cluster. The representative images of each type are shown in figure 2.4 On the other hand, Rood-Sastry system classifies clusters to six categories on the basis of the distribution of the brightest ten galaxies. These two schemes are associated each other as shown in figure 2.3. Rich clusters tend to have dominant galaxies in the center, and hence are classified as Bautz-Morgan Type I and Rood-Sastry Type cD to C while poor clusters distribute over various types. Rood-Sastry proposed a possible evolutionary sequence from irregular (I) to regular (cD), that is to say, from a dynamically less-relaxed irregular system to a well-relaxed regular one (Rood & Sastry 1982). This scenario is supported with many simulations (e.g. White 1976; Carnevali et al. 1981).

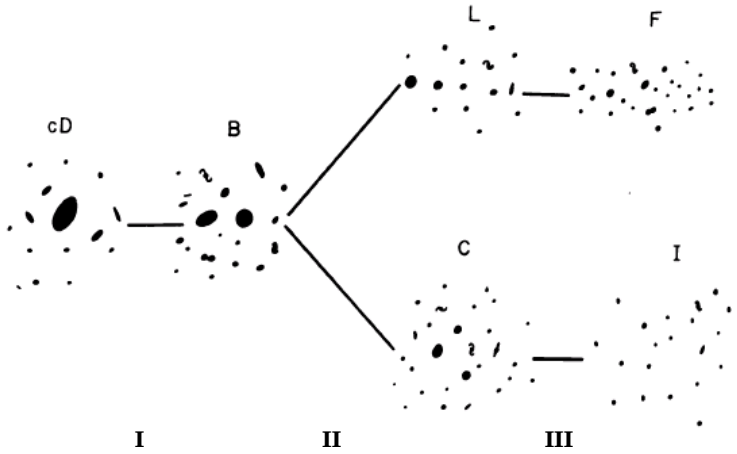

Figure 2.3: The classification of clusters of galaxies. The I, II, and III represent the Bautz-Morgan classifications, and cD, B, C, ... represent the Rood-Sastry classification.

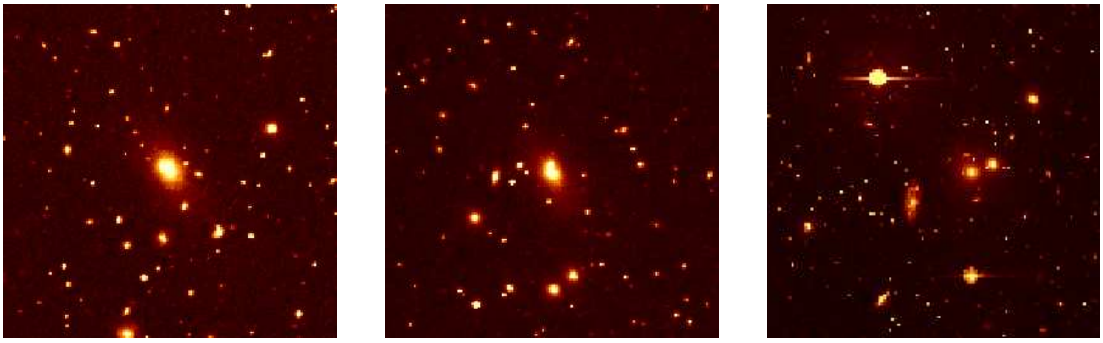

Figure 2.4: The optical image of a Bautz-Morgan type I cluster (left; Abell 2199), a type II cluster (middle; Abell 2634), and a type III cluster (right; Abell 1060). The physical scale roughly corresponds to 500 kpc.

The spatial distribution of galaxies in a cluster empirically follows King profile (King 1962);

$$N(R) = N_0 \left[1 + \left(\frac{R}{R_c}^2\right)\right]^{-\frac{2}{3}}. \quad (2.1)$$

Here, R_c is the core radius, giving a typical extent of the cluster and become around 250 kpc in general. N_0 is the number density of central galaxies. The King model is analytic approximation to the equation describing particle distribution in a self-gravitational hydrostatic isothermal system and reproduces the isothermal profile well in the range of R <2.5 R_c.

The line-of-sight velocity dispersion σ_v of galaxies is derived by measuring their redshifts. It reflects the depth of the gravitational potential of the system and ranges from 500 km s^{-1} to 1300 km s^{-1} for rich clusters. Introducing the system size V, the total gravitational mass of cluster $M_{tot}$is estimated as

$$M_{tot} \sim 3\sigma_v^2 \frac{V}{G}. \quad (2.2)$$

Here G is the gravitational constant. If a cluster has a velocity dispersion of 1000 km s^{-1}, $M_{tot} \sim 10^{15} M_\odot$ within 1 Mpc. $M_\odot$ is the solar mass (2×10^{33} g). This value is larger by an order of magnitude than that of the visible mass,i.e., the mass of stellar component in galaxies. This is known as "missing mass" problem, representing the existence of dark matter as a major portion of M_{tot}. The total kinetic energy of cluster become $\frac{3}{2} M_{tot} \times \sigma_v^2 \sim 10^{64}$ erg. Thus the cluster is the most energetic objects in the universe.

2.2 X-ray Properties of the Intracluster Medium

In this section, we give an outline about the fundamental physics of ICM to describe the X-ray emission mechanism, mass determination, and other intimately related matters along with the observational results in some cases.

2.2.1 Emission Mechanism

All the emission processes in clusters of galaxies are raised up along with the two-body interaction between electrons and ions. Therefore, the emissivity (erg s^{-1} cm^{-3}) of the ICM is written as

$$\epsilon = n_e n_i \Lambda(T, Z), \quad (2.3)$$

where n_e and n_i are the density of electrons and ions, respectively. Except for the dependency of ϵ on the particle density, there remains the dependency of the temperature T and metal abundance Z described by cooling function $\Lambda(T, Z)$. Figure 2.5 shows the cooling function of optically thin plasmas as a function of ICM temperature, with fixed metal abundance to one solar (Gehrels &Williams 1993). In the range of ICM temperature (10^{7-8} K), it is perceived that the radiation from ICM is dominated by thermal bremsstrahlung (free-free) and atomic line (bound-bound) emission.

Thermal bremsstrahlung is responsible for the continuum component of X-ray spectrum emission which become dominant when the ICM have higher temperature (> 5 keV). Its emissivity (erg s^{-1} cm^{-3} Hz^{-1}) is given as

$$\epsilon_\nu^{ff} = 6.8 \times 10^{-38} \Sigma_{\rm i} Z_{\rm i}^2 n_{\rm e} n_{\rm i} T^{-\frac{1}{2}} \bar{g}_{ff} \exp\left(-\frac{h\nu}{kT}\right), \tag{2.4}$$

where $Z_{\rm i}$ and $n_{\rm i}$ is the charge and number density of the ion i, $n_{\rm e}$ is number density of electron in the cgs unit, and $\bar{g}_{ff}$ is Gaunt factor. The Gaunt factor takes values about unity, and weak dependence on T and the radiation frequency ν (Rybicki & Lightman 1979). As seen in this equation and figure 2.6, the spectrum of thermal bremsstrahlung go into a nosedive around the ICM temperature. The total emissivity integrated over the frequency (erg s^{-1} cm^{-3}) becomes

$$\epsilon^{ff} = 1.4 \times 10^{-27} T^{-\frac{1}{2}} n_{\rm e} n_{\rm i} \Sigma_{\rm i} Z_{\rm i}^2 \bar{g}_B, \tag{2.5}$$

where $\bar{g}_{\rm B}$ is averaged Gaunt factor which ranges 1.1$-$1.5.

Meanwhile, the line emission is another important spectral component of ICM radiation. In the ICM, the elements exist in the form of H/He like or completely ionized, because of proximity the ICM temperature to the K-shell ionization potential of the heavy elements such as O, Ne, Mg, Si, S, and Fe. Then, ions emit the resonance K-shell lines when ions collisionally excited by free electrons return into ground state or lower states. Figure 2.6 shows the model spectra of thin thermal plasmas. In the lower temperature of < 2 keV, resonance L-shell lines become to dominate the spectra of ICM in behalf of K-shell lines as its degree of ionization declines. These lines carry as high luminosity as the thermal bremsstrahlung continuum (figure 2.5). The emission line spectra from thin hot plasma in an ionization equilibrium is calculated by various authors (e.g. Raymond and Smith 1977; Masai 1984, Kaastra and Mewe 1993). The predictions for K-shell lines are consistent between each method while the results differ for L-shell lines due to the difficulties in calculating the ionization and recombination rate of L-shell electrons (e.g. Masai 1997).

Taking account into bremsstrahlung continuum and atomic line, the total X-ray luminosity of galaxy clusters is represented as

$$L_{\rm X} = \int dV \int n_{\rm e}^2 (\epsilon_\nu^{ff} + \epsilon_\nu^{lines}) d\nu = \int n_{\rm e}^2(R)\ \Lambda(T(R), Z(R))\ dV, \tag{2.6}$$

where $\int n_{\rm e}^2 dV$ is called emission measure, which determines the luminosity of the ICM at given T and Z.

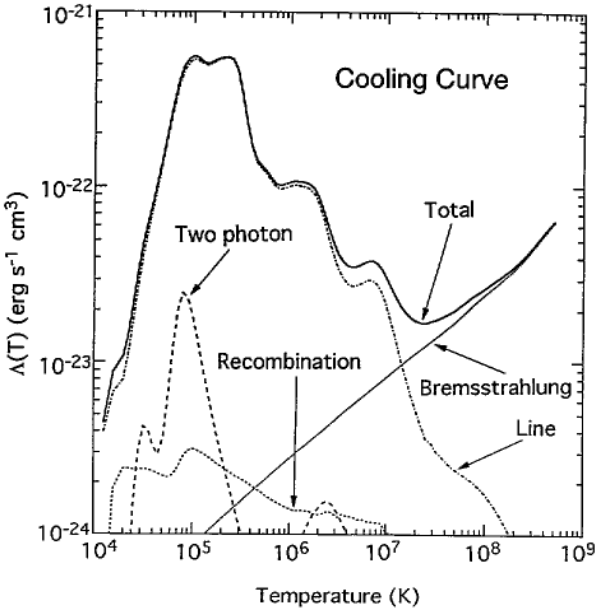

Figure 2.5: Cooling function of optically thin thermal plasmas with one solar abundances. The emission contribution of each component changes in proportion to the metal abundances.

The ICM can be construed as collisional plasma as a whole (§2.2.2). In such system, thermodynamical equilibrium is lead by the binary Coulomb collisions. The time scales of energy transfer by Coulomb collision between electron-electron, proton-proton, and electron-proton are given as

$$t_{\rm eq}(e,e) \sim 3.1\times10^5 \left(\frac{\ln\Lambda}{40}\right)^{-1} \left(\frac{T_{\rm e}}{10^8{\rm K}}\right)^{\frac{3}{2}} \left(\frac{n_{\rm e}}{10^{-3}{\rm cm}^{-3}}\right)^{-1} \ {\rm yr}, \tag{2.7}$$

$$t_{\rm eq}(p,p) \sim 1.3\times10^7 \left(\frac{\ln\Lambda}{40}\right)^{-1} \left(\frac{T_{\rm e}}{10^8{\rm K}}\right)^{\frac{3}{2}} \left(\frac{n_{\rm e}}{10^{-3}{\rm cm}^{-3}}\right)^{-1} \ {\rm yr}, \tag{2.8}$$

$$t_{\rm eq}(e,p) \sim 5.7\times10^8 \left(\frac{\ln\Lambda}{40}\right)^{-1} \left(\frac{T_{\rm e}}{10^8{\rm K}}\right)^{\frac{3}{2}} \left(\frac{n_{\rm e}}{10^{-3}{\rm cm}^{-3}}\right)^{-1} \ {\rm yr}, \tag{2.9}$$

where Λ is the Coulomb logarithm. These time scale are all shorter than the Hubble time, indicating that the ICM is under the thermal equilibrium unless clusters have undergone any significant heating or cooling event.

Once an isothermal system is built, the ICM loss its energy by radiation. Considering the energy per unit volume $3n_{\rm e}kT$ and the emissivity $n_{\rm e}n_{\rm i}\Lambda(T,Z)$, the radiative cooling time of the ICM is represented as

$$t_{\rm cool} = \frac{3n_{\rm e}kT}{n_{\rm e}n_{\rm i}\Lambda(T,Z)} \sim 8.5\times10^{10} \left(\frac{n_{\rm e}}{10^{-3}{\rm cm}^{-3}}\right)^{-1} \left(\frac{T}{10^8{\rm K}}\right)^{\frac{1}{2}} \ {\rm yr}. \tag{2.10}$$

The cooling time is longer than the Hubble time in the ordinary cases, so that the radiative cooling in clusters of galaxies is thought not to be significant.

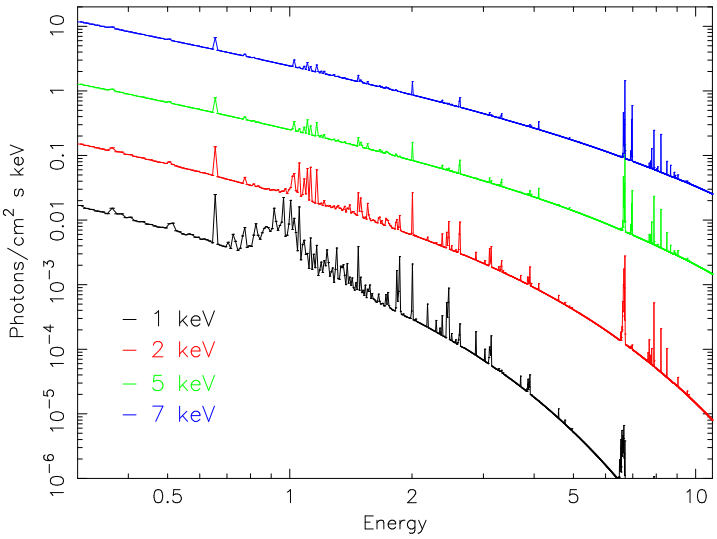

Figure 2.6: Model spectra of optically thin thermal plasmas with temperature of 1, 2, 5, 7 keV, calculated with the MEKAL code (Mewe et al. 1995; Kaastra et al. 1996). The metal abundances are fixed to 0.3 solar, and normalizations are arbitrary.

2.2.2 Spatial Distribution and Mass Profile

Being very hot (10^{7-8} K) and thin (10^{-3} cm^{-3}), the ICM can be regarded as an ideal highly-ionized plasma. The optical depth of the ICM for Thomson scattering is given as

$$\tau \sim 10^{-2} \left(\frac{n_{\rm e}}{10^{-3}{\rm cm}^{-3}} \right) \left(\frac{L}{1{\rm Mpc}} \right), \tag{2.11}$$

where L is typical scale of a cluster. Thus the ICM is optically thin and virtually transparent in all frequencies.

Since the ICM is confirmed in the gravitational potential of dark matter, the ion sound velosity is

$$c_s = \sqrt{\gamma kT/\mu m_{\rm p}} = 1.5 \times 10^8 \left(\frac{T}{10^8{\rm K}} \right)^{\frac{1}{2}} \ {\rm cm\ s}^{-2}, \tag{2.12}$$

where $\mu \sim 0.6$ is averaged molecular weight, $\gamma \sim 1.7$ is the specific heat ratio. Then the sound crossing time becomes

$$t_s \sim 6.6 \times 10^8 \left(-\frac{T}{10^8{\rm K}} \right)^{\frac{1}{2}} \left(\frac{L}{1{\rm Mpc}} \right) \ {\rm yr}. \tag{2.13}$$

This is much shorter than the Hubble time, i.e., the age of clusters.

In contrast, the mean free path of Coulomb collisions between ions and electrons is calculated to be

$$\lambda \sim 10^{23} \left(\frac{T}{10^8 K} \right)^2 \left(\frac{n_{\rm e}}{10^{-3}{\rm cm}^{-3}} \right)^{-1} \ {\rm cm}. \tag{2.14}$$

Let us introduce two characteristic length of the ICM, the Debye length and Larmor radius. The former is given as

$$r_{\rm D} = \sqrt{\frac{kT}{4\pi n_{\rm e} e^2}} = 2.2 \times 10^6 \left(\frac{T}{10^8 {\rm K}}\right)^{\frac{1}{2}} \left(\frac{n_{\rm e}}{10^{-3} {\rm cm}^{-3}}\right) \ {\rm cm}, \tag{2.15}$$

and the latter is given as

$$r_{\rm L} = \frac{m_{\rm i} c v_\perp}{Z_{\rm e} B} = 3.5 \times 10^9 \left(\frac{v_\perp}{1000 \ {\rm km/s}}\right) \left(\frac{B}{1 \mu {\rm G}}\right)^{-1} Z^{-1} \ {\rm cm}. \tag{2.16}$$

Here, B is magnetic field in the ICM, $v_\perp$ is velocity of ion perpendicular to the magnetic field, and Z is atomic number of ion. Comparing these with the mean free path above, we get $\lambda \gg r_{\rm D}$ and $\lambda \gg r_{\rm L}$, indicating that the ICM is completely collisionless classical plasma in the local scale. However, the mean free path is much shorter when compared with the cluster extent and then the ICM is regarded as collisional plasma if viewed in overall spatial and time scale. Therefore we can assume that the ICM is under the hydrostatic equilibrium.

Under the hydrostatic equilibrium, the pressure gradient in the ICM is balanced with the gravitational force;

$$\frac{1}{\rho_{\rm gas}} \frac{dP_{\rm gas}}{dr} = -\frac{d\phi}{dr}, \tag{2.17}$$

where $P_{\rm gas}$ is ICM pressure, ϕ is the gravitational potential, and $\rho_{\rm gas}$ is weight density described as $\rho_{\rm gas} = \mu m_{\rm p} n_{\rm e}$ with mass of proton $m_{\rm p}$. Since the ICM density is low enough, the equation of state of ideal gas is written as

$$P_{\rm gas} = \rho_{\rm gas} kT. \tag{2.18}$$

Here k is the Boltzman constant. When the a spherical symmetry is assumed, the equation 2.17 is revised to

$$\frac{dP_{\rm gas}}{dR} = -\mu m_{\rm p} n_{\rm gas} \frac{G M_{\rm total}(R)}{R^2}, \tag{2.19}$$

where G is gravitational constant, and $M_{\rm total}$ is the total gravitational mass within the radius R. By means of this relation, we can determine the distribution of the total gravitational mass $M_{\rm total}(R)$ as

$$M_{\rm total} = -\frac{kT}{\mu m_{\rm p} G} \ R \ \left(\frac{d \log T}{d \log R} + \frac{d \log n_{\rm gas}}{d \log R}\right). \tag{2.20}$$

Since the ICM temperature T and density $n_{\rm gas}$ are measurable from the X-ray observations, we can obtain the total gravitational mass as well as the ICM mass (equation 2.26). The mass of the remaining major component of cluster, member galaxies, are estimated from the optical observations. Then, it is possible to understand the whole mass profiles of clusters. Figure 2.7 shows an example for the mass profile of Fornax cluster obtained with ASCA, which gives us general properties

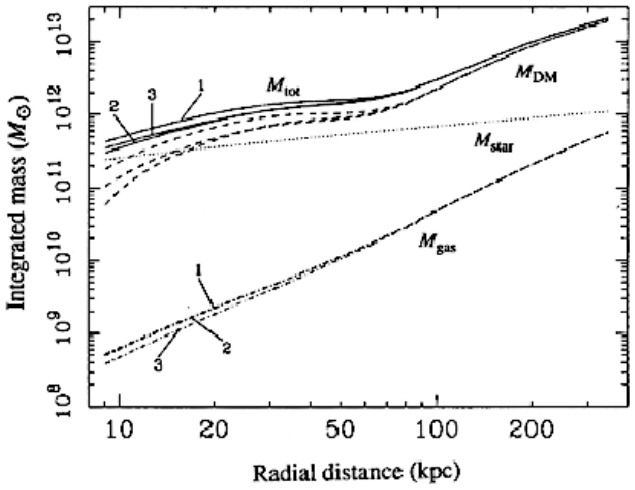

Figure 2.7: Integrated mass distribution of Fornax cluster (Ikebe et al. 1996). The total gravitating mass ($M_{\rm tot}$), dark matter mass($M_{\rm DM}$), ICM mass($M_{\rm gas}$), and stellar mass ($M_{\rm star}$) are individually plotted, and three curves for each quantity correspond to different plasma models.

among the three mass component. The stellar component is more concentrated in the cluster center, while the ICM is more extended than the dark matter distribution. The mass ratio of $M_{\rm gas}/M_{\rm star}$ ranges $\sim 2-5$ in overall cluster (a few Mpc). The baryon fraction of $(M_{\rm gas}+M_{\rm star})/M_{\rm tot}$ is typically $\sim$0.15, being consistent with the most up-to-date cosmological value of $\Omega_{\rm b}/\Omega_{\rm m}=0.18$ (Spergel et al. 2003).

The equation 2.17 for the pressure balance of ICM equilibrium can be rewritten as

$$\frac{kT(R)}{\mu m_{\rm p}}\frac{d\ \log\ n_{\rm gas}(R)}{dR}=-\frac{d\phi(R)}{dR}. \tag{2.21}$$

In the same way, the hydrostatic equilibrium equation of gravitating matter becomes

$$\sigma^2(R)\frac{d\ \log\ \rho_{\rm gas}(R)}{dR}=-\frac{d\phi(R)}{dR}, \tag{2.22}$$

where $\sigma^2(R)$ is velocity dispersion of the gravitating matter. In Combining the equation 2.21 with equation 2.22, we get the relation of $n_{\rm gas}\propto\rho_{\rm gas}^{\beta}$, and here

$$\beta\equiv\frac{\mu m_{\rm p}\sigma^2}{kT}=0.726\left(\frac{\sigma}{10^3{\rm km/s}}\right)^2\left(\frac{T}{10^8{\rm K}}\right)^{-1}, \tag{2.23}$$

Assuming that clusters of galaxies is under self-gravitating isothermal system, which obeys King profile, we can solve the equation 2.17 analytically,

$$\rho(R)=\rho_0\left[1+\left(\frac{R}{R_{\rm c}}\right)^2\right]^{-\frac{3}{2}}. \tag{2.24}$$

Then, we obtain the ICM density,

$$n_{\rm gas}=n_0\left[1+\left(\frac{R}{R_{\rm c}}\right)^2\right]^{-\frac{3}{2}\beta}. \tag{2.25}$$

This is so-called beta-profile (Cavaliere and Fusco-Famiano 1976). The parameter β shows the ratio of specific energy per unit mass between the gravitating matter and the ICM, and emerges as the steepness in the ICM radial distribution. When we integrate it over the cluster volume, the total mass distribution of the ICM within the radius R is given as

$$M_{\rm gas}(R) = \int_0^R 4\pi R'^2 \mu m_{\rm p} n_{\rm gas}(R')\ dR'. \tag{2.26}$$

The emissivity of the ICM is in proportion to $n_{\rm e}n_{\rm i} \sim n_{\rm e}^2$ as shown in the equation 2.3. By integrating the emissivity along the line-of-sight, X-ray surface brightness can be solved as

$$S_{\rm b}(r) = 2\int_0^\infty n_{\rm gas}^2 \Lambda(T,A) dl = S_0 \left[1 + \left(\frac{r}{R_{\rm c}}\right)^2\right]^{-3\beta+\frac{1}{2}} \tag{2.27}$$

where r is two-dimensional radius, and S_0 is normalization represented as

$$S_0 = n_{\rm e}^2 \Lambda(T,Z) \frac{\sqrt{\pi} r_{\rm c}}{4\pi D_{\rm L}^2} \frac{\Gamma(3\beta - 1/2)}{\Gamma(3\beta)} \ \ {\rm erg\ s^{-1} cm^{-4}}. \tag{2.28}$$

This formula is known to well represent the observed X-ray surface brightness (Jones & Forman 1984) although the integration to the infinite radius is not realistic.

2.2.3 Correlation Between the Observed Parameters

The X-ray luminosity of cluster was known to correlate with the cluster richness, in other words, temperature, as shown in figure 2.8. When the ICM temperature become to be measured with higher accuracy through the X-ray spectroscopy, a clear correlation of $L_{\rm X} = (kT)^\alpha$ with $\sigma \sim 2.5-3$ (e.g. Mushotzky 1984; David et al. 1993; Markevitch 1998; Fukazawa 1997) have been found. However, the luminosities scatters with large factor of ~ 10 even for the same temperature. Since the scatter is suppressed by eliminating the contribution of central emission (Markevitch 1998), it is considered that the $L_{\rm X} - T$ relation is affected by the central excess emission (§2.2.7). When the central density derived after excluding the central excess component ρ_0 is introduced, the clusters of galaxies populate a planar distribution in the global parameter space of logρ_0, log$R_{\rm c}$, and log$T$ (Fujita & Takahara 1999). This is called "fundamental plane" of clusters. They indicated that the $L_{\rm X} - T$ plane have slight offset from the plane, causing rather large scatter.

The correlation between ICM temperature and velocity dispersion is also found. The velocity dispersion of the member galaxies should be the same as that of dark matter since the galaxies are regarded as the collisionless particles. In fact, the equation 2.23 leads a strong correlation between the velocity dispersion of galaxies and the ICM temperature of $T \propto \sigma^2$, which predicts that the ICM and galaxies are heated by only gravity. However, observational results have revealed flatter profile with the index of $\sim$1.5$-$1.6 (e.g. Lubin & Bahcall 1993; Bird et al. 1995; Girardi et al. 1996; Xue &Wu 2000), as shown in Figure 2.9 which is an example of $kT - \sigma$

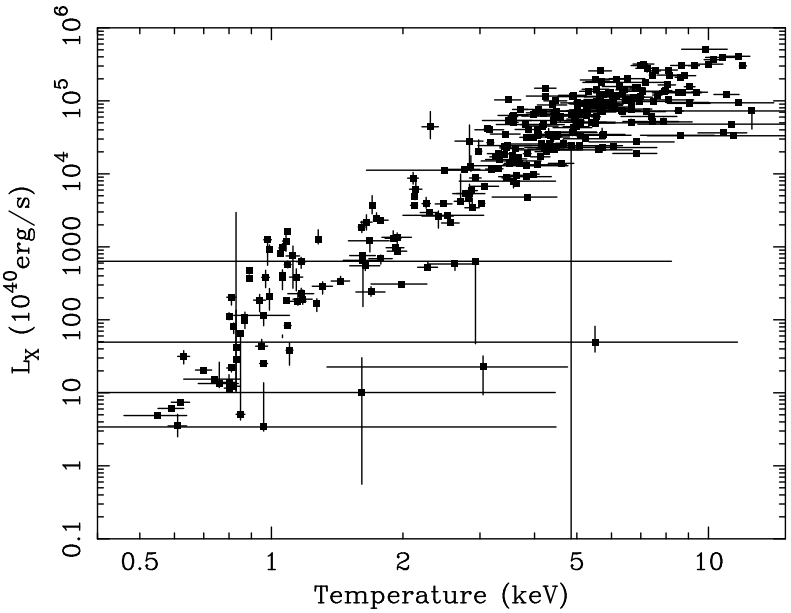

Figure 2.8: X-ray bolometric luminosity against the temperature of ICM observed with ASCA.

relation reported by Xue and Wu (2000). Therefore, some authors propose that the non-gravitational heating mechanism such as supernovae causes smaller index, especially in poor clusters (e.g. Bird et al. 1995; Ponman, Cannon, & Navarro 1999; Wu, Fabian, & Nulsen 1999; Lowenstein 2000).

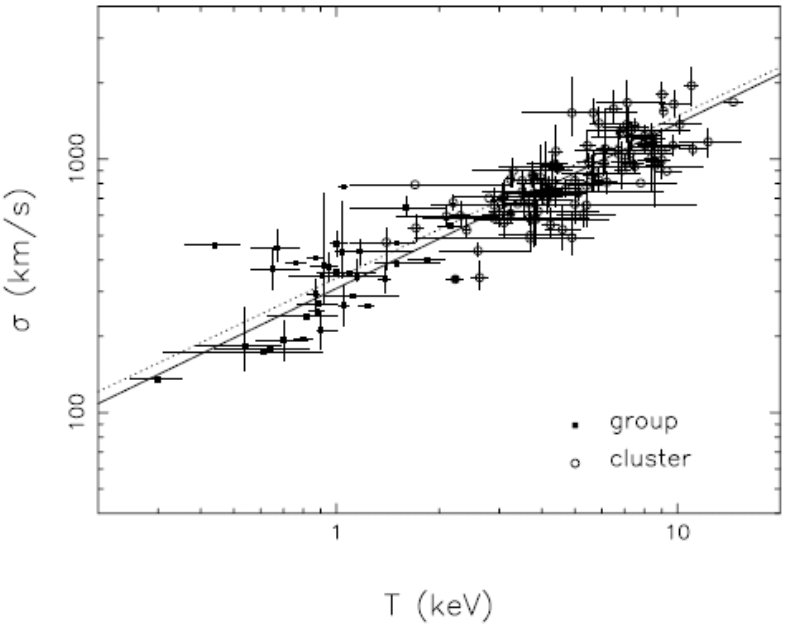

Figure 2.9: The $kT - \sigma$ relation of clusters and groups. Data consists of 274 clusters (open circle) and 66 groups (filled square). The solid line indicates the relation, $\mu m_{\rm e}\sigma^2 = kT$.

2.2.4 X-ray Emission from Discrete Sources

In clusters of galaxies, the discrete sources occasionally emit strong X-rays as well as the non-thermal emission while it is negligible for the thermal emission. There are mainly two kinds of point sources; one is active galactic nuclei (AGNs) in individual member galaxies of clusters, and the other is compact stellar-mass discrete sources to which mass accrete from their companion stars. Among latter, the most abund and luminous population is low mass X-ray binaries (LMXB) which consist of low mass stars and weakly magnetized neutron stars.

An AGN is a huge black hole with a mass of $\sim 10^{6-8} M_{\odot}$. When matter accrete to the black hole releasing vast gravitational energy, the emission over the wide wavelength of radio to γ-rays is observed as shown in figure 2.10. Their spectra are represented by a single powerlaw model with $\Gamma = 1 \sim 2$. The most bright sources among them have the luminosity up to $\sim 10^{45}\mathrm{ergs}^{-1}$. Since AGNs are often sitting in the center of galaxies, the most of the X-ray bright AGNs are identifiable as point like X-ray sources which coincident in the same position as galaxies in the optical image. AGNs are also identified and catalogued by radio and optical observations.

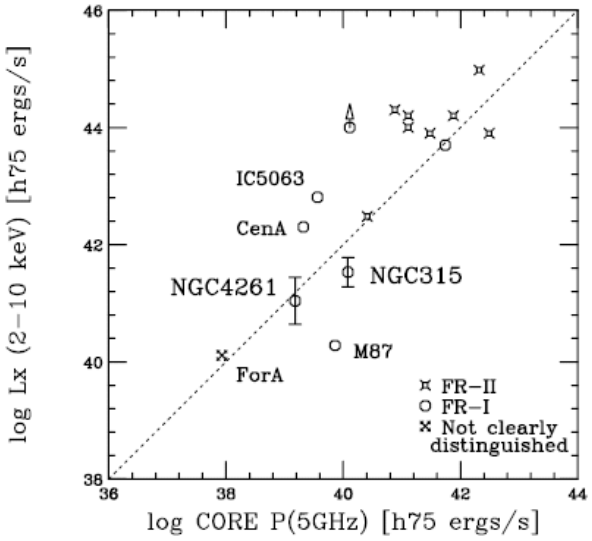

Figure 2.10: The X-ray luminosity of several AGNs as compared with the radio luminosity of core region (Matsumoto et al. 2001).

The spectra of the LMXB is known to be approximated by a ∼10 keV bremsstrahlung model (e.g. Makishima et al. 1989; Matsushita et al. 1994; Matsumoto et al. 1997). Their integrated luminosity within a galaxies reached up to $\sim 10^{40}\mathrm{ergs}^{-1}$ which is not negligible despite of fairly low X-ray luminosity of each LMXB ($\sim 10^{36-37}\mathrm{ergs}^{-1}$). The X-ray luminosity of LMXBs and their optical B-band luminosity is founded to have a linear correlation of $L_{\mathrm{X}} \sim 10^{-3.81} L_{\mathrm{B}}$. Figure 2.11 is an example obtained with ASCA (Matsushita 1998). Such results give evidence to the sight that the number of X-ray binaries in galaxy should be roughly proportional to its total stellar content and then the luminosity also be.

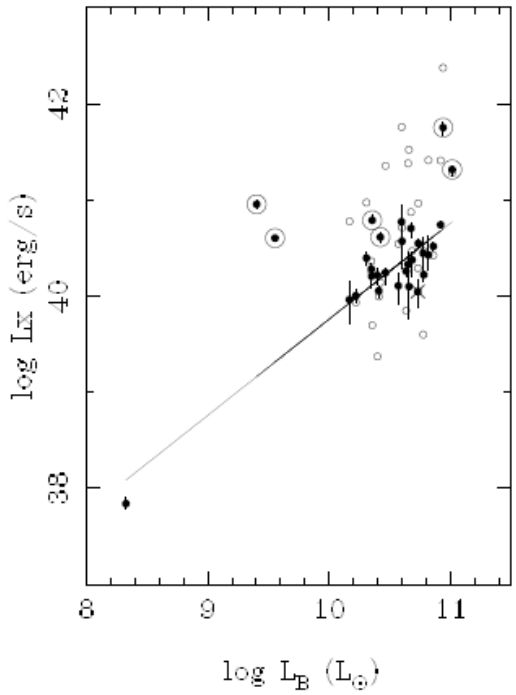

Figure 2.11: X-ray luminosity of the galaxy observed with ASCA as compared with the optical B-band luminosity in the 0.5−10 keV band. The filled circles are the luminosity of the hard component in the X-ray spectra of elliptical galaxies, the open circles are those of the ICM component, and the double circles are the galaxies possibly hosting an AGN.

2.2.5 Magnetic Field

Magnetic fields of a few μG are ubiquitous in the universe. Then it is also expected to exist in clusters of galaxies since the ICM is ideal collisional plasma. Actually, the ICM have magnetic field although the original mechanism to generate it has not been determined. Magnetic field in the ICM is measured to be a few μG as above by using the radio observation of "Faraday Rotation". In magnetized ICM, the refraction index for electromagnetic waves propagating along the field line depends on the sense of circular polarization as well as on the wave frequency. Therefore, linearly polarized wave, which is a superposition of the left and right circularly polarized wave, exhibits a rotation of the polarization plane when it propagates through the plasma. This rotation effect is called Faraday Rotation, and quantified as

$$\Delta\chi = RM\lambda^2 \text{ radian}, \tag{2.29}$$

$$RM = \frac{e^3}{2\pi m_{\rm e}^2 c^4}\int n_{\rm e}\vec{B}\cdot d\vec{l} \tag{2.30}$$

$$= 812\int\left(\frac{n_{\rm e}}{cm^{-3}}\right)\left(\frac{\vec{B}}{\mu{\rm G}}\right)\cdot\left(\frac{d\vec{l}}{kpc}\right) \text{ radian m}^{-2}. \tag{2.31}$$

Here, $\Delta\chi$ is the charge in position angle of polarization, RM is a quantity called rotation measure, λ is the wavelength of the electromagnetic wave, $d\vec{l}$ is the line-of-

sight length of the field, and $\vec{B}$ is the magnetic field. Thus, the RM measurements provide us the strength of B, combining the $n_{\rm e}$ from X-ray observation.

The magnetic energy $B^2/8\pi$ is $1-2$ orders smaller than the specific energy of the ICM $3n_{\rm e}kT$. However, its energy become comparable to the specific energy of the ICM if the magnetic field are inhomogeneous and enhanced locally through the motion of member galaxies which have their own magnetic field, turbulence of the ICM, and so on. Taylor and Perley (1993) have reported that locally tangled and enhanced magnetic field $\sim$30 μG against the spatially-averaged $\sim$6 μG was founded in the Hydra A cluster. Thus, the magnetic field may affect on the baryonic components in clusters of galaxies. Therefore, the magnetic field is important quantity to understand the particle acceleration and the resulting plasma heating in the clusters of galaxies.

2.2.6 Magnetohydrodynamic Turbulence

As described in the previous section, the ICM is magnetized on some level. Since a cD galaxy is in the bottom of potential well and is thought to be free from ram pressure by the mignetized ICM, it is expected that relatively ordered magnetic field around it. The fields in the cluster center can be categolized into "open" and "'closed' ones. The former is connecting to the outer region while the latter is tied to be cD galaxy at both ends. The open-field regions are suspected to have the same temperature as the peripheral regions, due to the efficient thermal conduction along the field lines. In contrast, the closed-field regions would be thermally insulated from outer regions of the magnetic field. Therefore, it is natural to consider that the cool plasma stay in the closed-field regions while the hot plasma are in the open-field regions. This is called cD corona model (Makishima et al. 2000) after the solar corona. When the non-cD galaxies, which also have their own magnetosphere, are moving through the magnetized ICM under the environment, they are expected to strongly interact with magnetic field. As a result, the galaxies drag the intracluster field lines, and then the field lines are pushing and stretching them, causing a magnetohydrodynamics (MHD) turbulence in the ICM. The stretched filed will finally experience the magnetic reconnection and release the magnetic energy of $B^2/8\pi$. Thus, the ICM is heated up.

The energy loss rate of a single galaxy by the drag force is represented as

$$\left|\frac{dE}{dt}\right| = \pi\rho_{\rm gas}v^3R_{\rm D}^2 \tag{2.32}$$

$$= 5\times10^{41}\frac{n_{\rm gas}}{10^{-3}{\rm cm}^{-3}}\frac{v}{500{\rm kms}^{-1}}^3\frac{R_{\rm D}}{10{\rm kpc}}^2 \quad [{\rm erg\ s}^{-1}]. \tag{2.33}$$

Here, v is the velocity of the galaxy motion, and $R_{\rm D}$ is the effective radius of the galaxy-ICM interaction (Sarazin 1988). If there are 100 member galaxies with the effective radius of 10 kpc, the heating luminosity of $\sim10^{43}$ erg s^{-1} is produced, implying that the kinetic energy of $\sim10^{62}$ erg is released into the ICM over the Hubble time.

The MHD turbulence is also generated when the galaxy clusters experience the merger in their evolution. From the numerical MHD simulations, such turbulence actually appears as shown in figure 2.12 (Roettiger et al. 1999). Since cluster mergers are capable of supplying large amount of kinetic energy which is comparable to the thermal energy over Mpc scale, this may be able to produce the cluster-wide radio emission called radio halo or relic (see §2.1). Thus, the MHD turbulence is considered to plays an important role for the particle acceleration as well as the plasma heating.

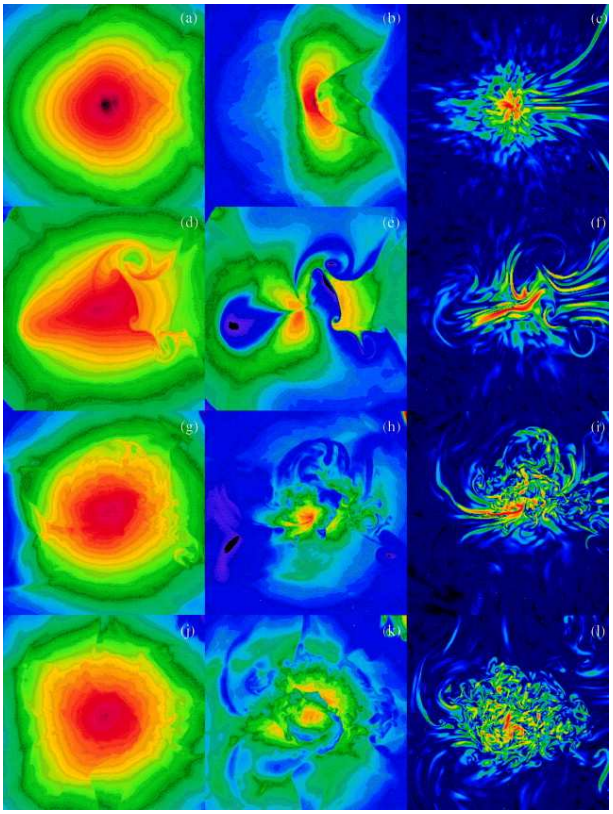

Figure 2.12: The evolution of the gas density (left column), the ICM temperature (middle column), and magnetic pressure (right column) presented as cross sections through the cluster center in the plane of the merger. The top panels are at t = 0, time of core coincidence, and the others are at t = 1.3, 3.4, 5.0 Gyr, from above. Each panel is 3.75×3.75 Mpc.

2.2.7 Radiative Cooling

The ICM have longer cooling time than the Hubble time in usual cases and then do not radiatively cooling. However, the situation fairly changes in the central region of clusters. The density of central ICM reaches $\sim 10^{-2}\mathrm{cm}^{-3}$, and then the cooling time is diminished to $\sim 10^{8-9}$ yr, by substituting the temperature of 10^{7-8} keV into equation 2.10. Thus, it is expected that the ICM at the center have cooled down due to the energy loss through the radiation. Actually, X-ray observations of clusters provide us the symptom of radiative cooling such as the central excess emission

over the β model (e.g. Jones & Forman 1984) and lower temperature component than the peripheral ICM (e.g. Fabian et al. 1994). Once radiative cooling take place at the cluster center, the pressure decrease and then the surrounding plasma inflows toward the center to balance the pressure provided by increasing density. Despite this, the balance is never achieved due to the enhancement of the radiation by the density increase as $\epsilon \propto n_{\rm e}^2$. The ICM then cools more and more. This positive feedback mechanism is called "cooling flow" (Fabian & Nulsen 1977) and can explain the observational facts as above.

When it is assumed that the brightness of the central excess emission is formed by the gravitational energy release of infalling plasma, the mass flow rate of the ICM toward the center can be estimated as

$$\Delta L = \frac{5}{2}\frac{\dot{M}}{\mu m}kT, \tag{2.34}$$

where ΔL is brightness of the central cool plasma, and $\dot{M}$ is mass flow rate called cooling rate (Fabian 1994). In general, the cooling rate ranges $50-100\ M_\odot$/yr although some clusters (e.g. Abell 478, Abell 1795, Abell 2029, Hydra A cluster) have significantly large rate of $> 500\ M_\odot$/yr. This implies that the mass of cool plasma becomes as huge as $10^{11-13} M_\odot$.

However, ASCA have revealed mightily different results from the previous ones, thanks to ASCA's spatial spectroscopy over the wider-energy band up to 10 keV. The cooling rate observed with ASCA is smaller by an orders of magnitude than that observed before in many clusters, as shown in figure 2.13 (Makishima et al. 2001). In the strong cooling flow cluster, Abell 1795, the central excess emission exists even in higher energy band of 3−10 keV (Xu et al. 1998), which implies the excess is not caused by only cooled plasmas. Furthermore, the spectra of Centaurus cluster, which is another cooling flow cluster, have never been represented by a single temperature plasma model but by two temperature within the central ∼30 kpc (Ikebe et al. 1999). Such observational facts are confirmed with XMM-Newton (Takahasi 2004), and apparently conflicts with the picture predicted from the cooling flow model. Thus, the cooling flow model folds many problems which is so-called "cooling flow problem". Anyway, it is clear that some heating effect which heats the ICM at the very center is necessary to explain lesser mass of the central cool plasma. Although various candidates, such as heating by AGNs, thermal conduction, heating via galaxy motions, magnetic reconnection, and heating by waves raised in the ICM etc., have been proposed, there is no heating mechanism which has significant advantages against other one.

2.3 High Energy Electrons in Diffuse Plasma

2.3.1 Powerlaw Population of High Energy Electrons

The non-thermal emission have been observed in some kinds of diffuse plasmas, such as supernova (SN) and AGN. These emissions are generated and radiated via the process of synchrotron, inverse Compton scattering, and non-thermal bremsstrahlung,

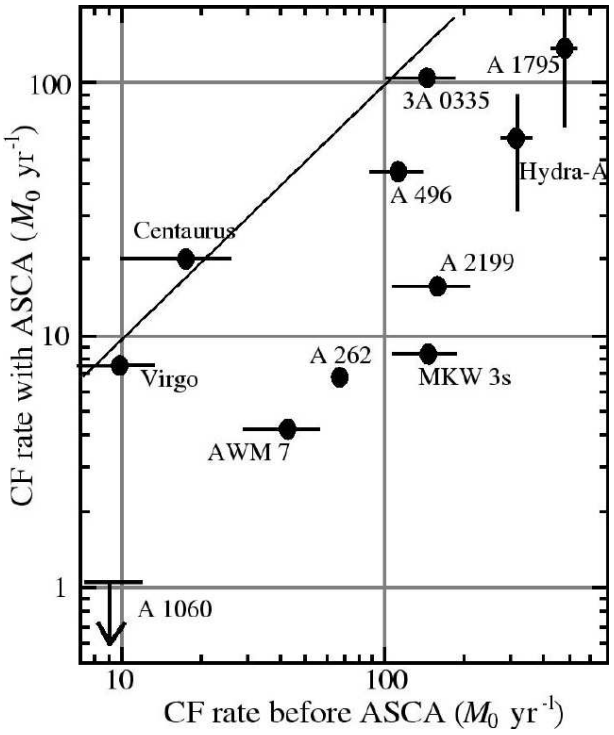

Figure 2.13: Comparison between the cooling flow rate measured with ASCA and those reported previously (Edge et al. 1992). The ASCA values of cooling flow rate were taken from Ikebe et al. (1997) for Hydra A cluster, Ikebe et al. (1999) for Centaurus cluster, and Xu et al. (1998) for Abell 1795, and for the other values were calculated by using the luminosity of cool components (Fukazawa 1997; Fukazawa et al. 2000).

and provides the strong evidences for the existence of high energy electrons. High energy particles are thought to be generated through the shock acceleration. One possible scenario is the first order Fermi acceleration in various shocks. Another is the second order Fermi acceleration by randomly moving scatterers, such as magneto-hydro-dynamical turbulence. In the clusters of galaxies, these accelerating processes are caused by the shock wave, galaxy motion through the plasma, and merging events between galaxies, groups, or clusters. In this section, we provide brief theoretical review of these emission and life times of high energy particles, especially electrons.

Relativistic particles exhibit a powerlaw like energy distribution, in the form of

$$N_{\rm e}(\gamma) = N_0 \gamma^{-\mu}. \tag{2.35}$$

Here, γ is the Lorentz factor of the electrons giving their energy of $\gamma m_{\rm e} c^2$, $N_{\rm e}(\gamma)$ is the number density of electrons within the energy range of $\gamma \sim \gamma + d\gamma$, and μ is the powerlaw index. In fact, the cosmic rays reaching on the earth have a powerlaw spectrum as shown in figure 2.14.

The cosmic rays below 10^{18} eV is considered to be products of Galactic sources. On the other hand, clusters of galaxies, which is one of the extragalactic sources, are suspected as a candidate yielding the cosmic rays above 10^{18} eV because of their largeness and then the possibility such that the particles experience acceleration

again and again. However, the evidence for it have not been revealed yet.

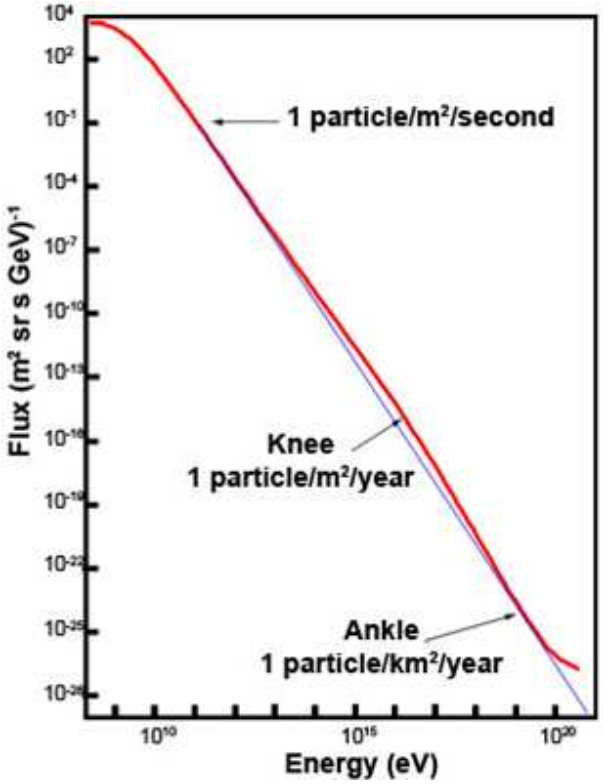

Figure 2.14: The spectra of cosmic rays reaching on the earth. The puffery around 10^{16} eV and dip around 10^{19} eV are called "knee" and "ankle" in connection with its spectral shape, respectively.

2.3.2 Synchrotron Emission

When the relativistic electrons interact with magnetic field, synchrotron emission is produced. The frequency of synchrotron emission for an electron with energy $\gamma m_{\rm e}c^2$ moving across a magnetic field B is given as

$$\nu_{\rm sync} = 4.2 \left(\frac{B}{\mu G}\right) \gamma^2. \tag{2.36}$$

Then the energy loss function due to synchrotron emission is

$$b_{\rm sync} = \frac{4}{3}\frac{\sigma_{\rm T}}{m_{\rm e}c}\gamma^2 U_{\rm B}. \tag{2.37}$$

Here, $\sigma_{\rm T} = 6.65 \times 10^{-25}{\rm cm}^{-2}$ is the Thomson cross section, $m_{\rm e} = 9.1 \times 10^{-28}$g is the electron mass, $c = 3.8 \times 10^{10}$cm s^{-1} is the light speed, and $U_{\rm B} = \frac{1}{8\pi}B^2$erg cm^{-2} is the energy density of the magnetic field (Sarazin 1999).

Assuming that the powerlaw distribution of electrons (i.e. the equation 2.35), the spectrum of the synchrotron emission also becomes powerlaw form represented as

$$\frac{dL_{\rm sync}}{d\nu} = \frac{\sqrt{3}e^3 B N_0}{m_{\rm e}c^2}\frac{\Gamma(\frac{3\mu+19}{12})\Gamma(\frac{3\mu+1}{12})}{(\mu+1)}\left(\frac{3eB}{2\pi m_{\rm e}c\nu_{\rm sync}}\right)^{\alpha}, \tag{2.38}$$

where $e = 4.8 \times 10^{-10}$ is the electron charge in cgs unit, Γ is the gamma function (Rybicki & Lightman 1979), and $\alpha = (\mu - 1)/2$ is the energy index.

2.3.3 Inverse Compton Emission

The relativistic electrons also scatter off lower energy photons via inverse Compton (IC) scattering. The formulary description of the IC emission resemble those of synchrotron since the fundamental emission mechanism is similar to the synchrotron process. When an electron with energy $\gamma m_{\rm e} c^2$ scatters off a photon with its energy $h\nu_{\rm seed}$ and the energy relation of $h\nu \ll \gamma m_{\rm e} c^2$ is approved (here h is the Plank constant), the frequency of the IC photon is represented as

$$\nu_{\rm IC} = \frac{4}{3}\gamma^2 \nu_{\rm seed}. \tag{2.39}$$

The energy loss function is then given as

$$b_{\rm IC} = \frac{4}{3}\frac{\sigma_{\rm T}}{m_{\rm e} c}\gamma^2 U_{\rm seed}, \tag{2.40}$$

where $U_{\rm seed}$ is the energy density of the seed photons.

The most natural origin which can provide the seed photons in the universe is the cosmic microwave background radiation (CMB). The CMB photons present everywhere and emit black body radiation with $T_{\rm CMB} = 2.73K$. Taking it as the seed photons, the spectrum of the IC emission again becomes a powerlaw shape which is given as

$$\frac{dL_{\rm IC}}{d\nu} = \frac{3\pi\sigma_{\rm T}}{h^2 c^2} b(\mu) N_0 (kT_{\rm CMB})^3 \left(\frac{kT_{\rm CMB}}{h\nu_{\rm IC}}\right)^{\alpha}, \tag{2.41}$$

$$b(\mu) = \frac{2^{\mu+3}(\mu^2 + 4\mu + 11)\ \Gamma\left(\frac{\mu+5}{1}\right)\ \zeta\left(\frac{\mu+5}{1}\right)}{(\mu+3)^2(\mu+1)(\mu+5)}. \tag{2.42}$$

$$\tag{2.43}$$

Here, ζ is the Reimann zeta function (Sarazin 1999).

From above equations, the luminosity ratio of the synchrotron and IC emission is simply given as

$$\frac{L_{\rm IC}}{L_{\rm sync}} = \frac{U_{\rm CMB}}{U_{\rm B}}. \tag{2.44}$$

Here, $U_{\rm CMB}$ is the energy density of the CMB, and have been known by the observations. Since $L_{\rm IC}$ and $L_{\rm sync}$ are obserbable quantity, the rest parameter $U_{\rm B}$ can be obtained. This is precious way to measure the cluster averaged magnetic field.

2.3.4 Non-thermal Bremsstrahlung Emission

The non-thermal bremsstrahlung is caused by the superthermal electrons with energies of $\sim$10$-$200 keV, in different from relativistic electrons yielding the synchrotron and IC radiation. Such electrons collide with low energy thermal plasma to emit

non-thermal bremsstrahlung radiation (e.g. Ensslin et al. 1998; Sarazin & Kempner 2000). Sarazin and Kempner (2000) treat two kinds of the candidates as the superthermal electrons; the low energy end of a population of electrons being accelerated to high energies by shocks or turbulence, or the remnant of an older non-thermal population that is losing energy and rejoining the thermal distribution as a result of Coulomb interactions. Hence, they can be called as the "trans-relativistic" superthermal electrons.

Following them, we introduce a powerlaw momentum distribution for these electrons. The number distribution of electrons with momenta in the range of $P \sim P + dP$ is defined as

$$N_{\rm e} = N_0 p^{\mu}, \tag{2.45}$$

where $p \equiv P/m_{\rm e}c$ is the normalized momentum and μ is the powerlaw index which become the same as that in equation 2.35 at the relativistic limit.

At the non-relativistic limit, the Bethe-Heitler bremsstrahlung cross section (Heitler 1954) is

$$\frac{d\sigma(p,\epsilon,Z)}{d\epsilon} = \frac{32\pi}{3}\frac{e^6}{m_{\rm e}^2 c^4 h}\frac{Z^2}{p_{\rm i}^2 \epsilon}\ln\left(\frac{p_{\rm i}+p_{\rm f}}{p_{\rm i}-p_{\rm f}}\right), \tag{2.46}$$

where $p_{\rm i}$ and $p_{\rm f}$ are the initial and final values of the normalized electron momentum, Z is the atomic number of ions, and ϵ is the produced photon energy in the unit of erg.

From the equation, spectrum of the non-thermal bremsstrahlung emission caused by the electrons with a powerlaw momentum distribution is calculated as

$$\frac{dL_\epsilon}{d\epsilon} = \frac{32\pi^{\frac{3}{2}}}{3}\frac{e^6}{m_{\rm e}c^4 h}\left[\frac{\Gamma(\frac{\mu}{2})}{\mu\Gamma\left(\frac{\mu+1}{2}\right)}\right] \times (\Sigma n_{\rm Z} Z^2) N_0 \left(\frac{m_{\rm e}c}{2\epsilon}\right)^{\frac{\mu}{2}} \tag{2.47}$$

This spectrum for nonrelativistic electrons agrees quit well with that calculated by fully including the trans-relativistic or relativistic effects when $\mu \sim 4$ (Sarazin et al. 2000). Thus, the equation 2.47 provides us a good approximation for the non-thermal bremsstrahlung emission.

In the relativistic frame, the energy loss function for electrons with energy of $\gamma m_{\rm e}c^2$ is given as

$$b_{\rm bremss}(\gamma) \sim 1.51 \times 10^{-16} n_{\rm e}\gamma[\ln(\gamma) + 0.36], \tag{2.48}$$

which includes the electron-ion and electron-electron bremsstrahlung (Sarazin 1999).

2.3.5 Cooling Time

High energy electrons loss their energies by Coulomb losses as well as by the radiation via three process explained above. Coulomb loss due to collisions with thermal electrons is represented as (e.g. Rephaeli 1979),

$$b_{\rm Coulomb} \sim 1.2 \times 10^{-12} n_{\rm e}\left[1.0 + \frac{\ln(\gamma/n_{\rm e})}{75}\right]. \tag{2.49}$$

Then, the cumulative energy loss of high energy electrons becomes as

$$b(\gamma) = b_{\rm sync} + b_{\rm IC} + b_{\rm bremss} + b_{\rm Coulomb}. \tag{2.50}$$

Figure 2.15 shows the individual components of the equation 2.50 (Nakazawa 2000). The cooling time, i.e. $\tau_{\rm cool} = \gamma/b(\gamma)$, is also overlaid with them. The high energy electrons can live at most for 10^9 when $\gamma = 100 - 300$, which is shorter than the Hubble time. This implies that the observed high energy electrons are considered to be accelerated at the moment and at the very location.

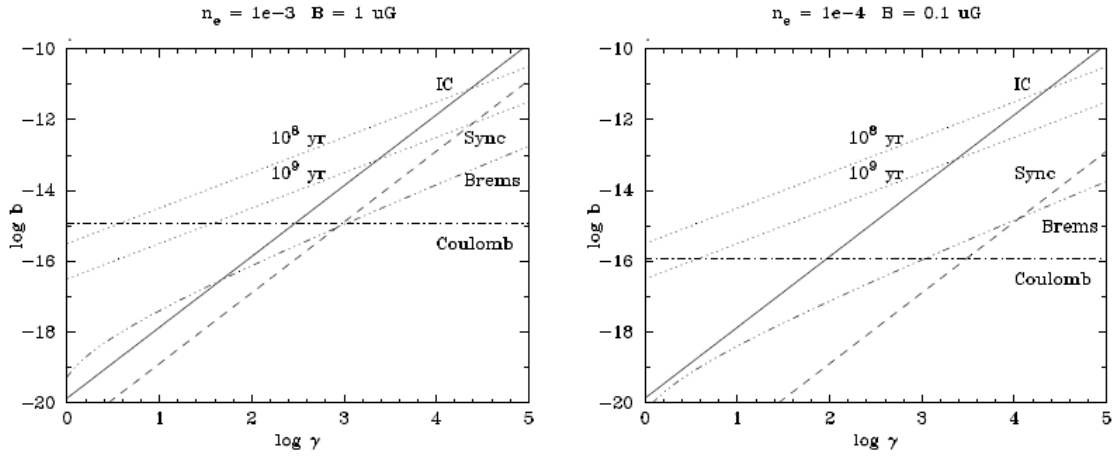

Figure 2.15: The energy loss function under the condition of $n_{\rm e} = 1 \times 10^{-3}{\rm cm}^{-3}$ and $B = 1\mu$G (left), and $n_{\rm e} = 0.1 \times 10^{-3}{\rm cm}^{-3}$ and $B = 0.1\mu$G (right). The dotted lines indicate the cooling time of 10^8 yr and 10^9 yr, respectively.

2.4 Non-thermal Emission in Clusters of Galaxies

2.4.1 Cluster Radio Halos

There are two kinds of radio sources in the clusters of galaxies. One is the radio galaxy associated with the individual galaxies. Many of them host a compact radio source associated with the AGN, and in some cases, have the extended radio emission called "lobes" which lie on either side of galaxy. The lobes are provided by the jet from AGN. An example of this kind radio sources is shown in figure 2.16.

The other source is more diffuse radio emission associated with the ICM in the clusters. This divided three classes: cluster-wide halos, relics, and mini-halos (Feretti &Giovannini 1996). The emission mechanism of each class is considered to be synchrotron radiation due to the interaction of non-thermal relativistic electrons with magnetic field of the ICM ($\sim \mu$G). Figure 2.17 and 2.18 show the radio image of each class, and radio spectra from the cluster-wide halos of Coma cluster, respectively.

Both cluster-wide halos and relics exhibit low surface brightness, large size ($\sim$1 Mpc), and steep radio spectrum ($\alpha \sim$1). The former are located at the cluster centers and have low or negligible polarized emission, while the latter are located at

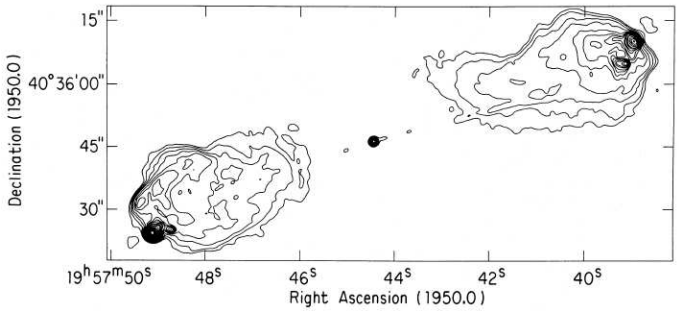

Figure 2.16: The radio image of radio galaxy Cygnus A at 5 GHz (Dreher et al. 1987). $1'$ corresponds to $66h_{75}^{-1}$ kpc.

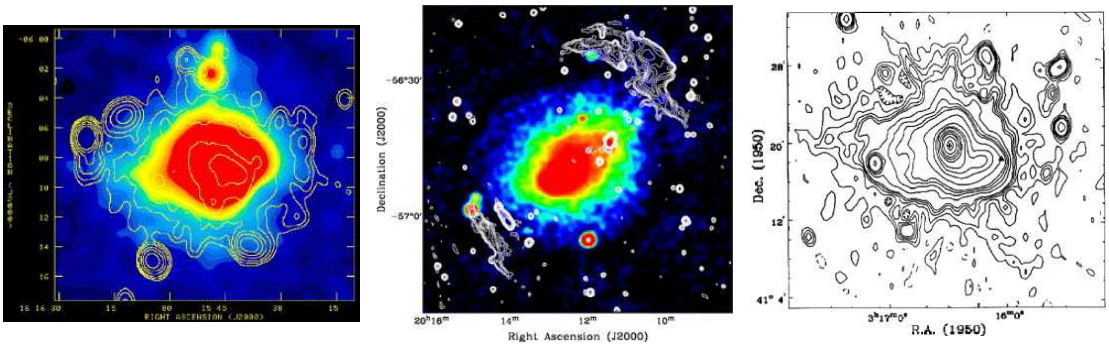

Figure 2.17: The images of diffuse radio emission in clusters of galaxies; cluster-wide halo of Abell 2163 (left), relics of Abell 3776 (middle), and mini-halo of Perseus cluster(right).

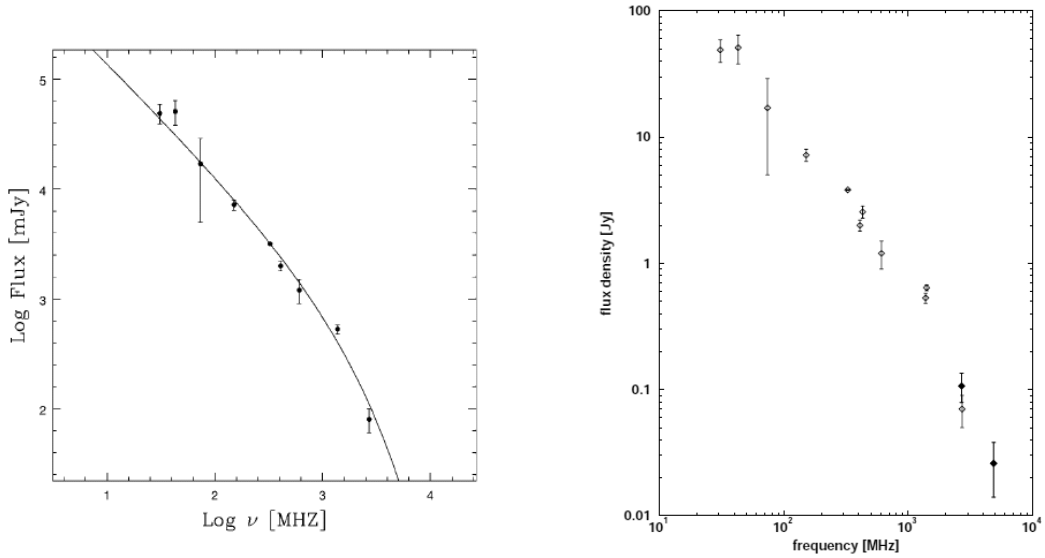

Figure 2.18: The surface brightness profile (left) and spectrum (right) from Coma cluster in the radio band.

peripheral regions and are highly polarized (∼20 %). Radio halos and relics have been thought to be a rare phenomenon. The clusters showing these diffuse radio emissions is only ∼10 % (Giovannini & Feretti 2002) although the detection rate is

increase up to ∼35 % if clusters with high X-ray luminosity ($L_{\rm X} > 10^{45}{\rm ergs}^{-1}$) is considered. The basic properties are listed in table 2.1 and 2.2.

Table 2.1: Observed parameters of cluster radio halos (Feretti & Giovannini 1996)

cluster	size (kpc)	$P^a_{1.4}$ (erg Hz^{-1})	$P^b_{\rm tot}$ (erg Hz^{-1})	α^c
Coma cluster	550	3.2×10^{30}	6.1×10^{40}	1.34
Abell 2163	–	1.8×10^{32}	3×10^{41}	–
Abell 2218	250	7.9×10^{29}	9.0×10^{39}	1.1
Abell 2255	725	2.5×10^{30}	1.6×10^{41}	>1.5
Abell 2256	700	1.2×10^{30}	1.6×10^{41}	1.9
Abell 2319	660	5.1×10^{30}	9.2×10^{40}	1.3

a: Radio flux at 1.4 GHz,
b: Radio luminosity in the range of 10 MHz−10 GHz,
c: Energy index of radio spectra.

Table 2.2: Observed parameters of cluster radio relics (Feretti & Giovannini 1996)

name	cluster	size (kpc)	$P^a_{1.4}$ (erg Hz^{-1})	$P^b_{\rm tot}$ (erg Hz^{-1})	α^c
0038-096	Abell 85	200	5.1×10^{30}	1.6×10^{41}	>1.5
0917+75	Abell 786	780	2.0×10^{31}	1.7×10^{41}	1.34
1253+275	Coma cluster	580	1.7×10^{30}	2.0×10^{40}	1.1
Coma Bridge	Coma cluster	970	4.9×10^{29}	1.6×10^{40}	1.5
1401-33	AS 753	220	1.0×10^{30}	2.5×10^{40}	1.4
2006-56	Abell 3667	870	2.6×10^{31}	3.7×10^{41}	1.2

a: radio flux at 1.4 GHz,
b: Radio luminosity in the range of 10 MHz−10 GHz,
c: Energy index of radio spectra.

Radio halos and relics are found in the on-going merging clusters in the most cases. Govoni et al. (2004) have reported for some clusters that the radio emission is associated with the high temperature region, where the effect of merger heating is expected to emerge. Furthermore, in such high-temperature merging regions, the spectrum of radio emission hardens (Feretti et al. 2004). These results imply the contribution of high energy electrons accelerated by the merger shock. On the other hand, there are clusters which show no such correlation, in which another acceleration mechanism such as turbulent may works. For the large-scale halos and relics of > 1 Mpc, the correlation between the radio power of halos and their X-ray luminosity also have been known ($P_{\rm 1.4GHz} \propto L_{\rm X}^{1.68\pm0.15}$). Recently, the presence of a cutoff in this correlation is suggested when smaller size radio halos are considered, as shown in figure 2.19 (Bacchi er al. 2003). Thus, low luminosity radio halos could be absent in clusters as the observation do.

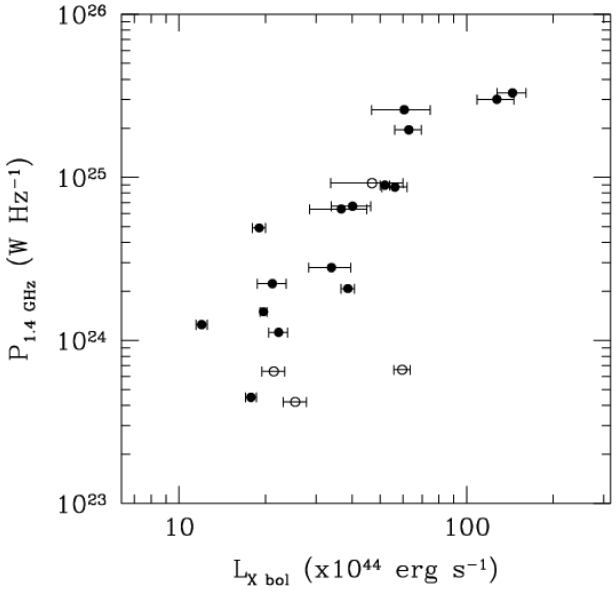

Figure 2.19: The correlation between the monochromatic power of radio halos at 1.4 GHz and cluster bolometric X-ray luminosity (Bacchi et al. 2003) for halo sizes >1 Mpc (closed circle) and <1 Mpc (open circle).

Mini-halos found in the resent observations, are also diffuse radio sources, extended on smaller scale (< 500 kpc) than the radio halos or relics. They are observed only with a cooling flow clusters and are not associated with on-going cluster merger activity. Gitti, Brunetti, and Setti (2002) suggested that the synchrotron emission from the mini-halo is due to a remnant of population of relativistic electrons re-accelerated by hydro-magneto-dynamic turbulence in the cooling flow via second order Fermi acceleration. The correlation of the integrated radio power with the cooling flow power ($\dot{M}kT/\mu m_{\rm p}$) shown in figure 2.20 (Gitti et al. 2004) implies that the radio power emitted by mini-halos could be supplied by that of the cooling flow. Very recently, the alternative possibility of hadronic origin for radio mini-halo has also been proposed although further study and observations are necessary for more specific discussion.

2.4.2 Hard X-ray Emission

The diffuse radio emissions referred in the previous section surely exhibit the existence of high energy electrons in the clusters of galaxies. Such electrons are expected to scatter off the CMB photons via IC process and produce the non-thermal emission represented with a powerlaw spectra. The non-thermal emission would be observed as an excess hard emission in X-ray spectra because the thermal emission of the ICM rapidly drops above its temperature. HEAO-A1 (Rephaeli et al. 1987) or OSSE (Rephaeli et al. 1994) have searched for the excess emission in very hard band although all observations could determine only the upper limit.

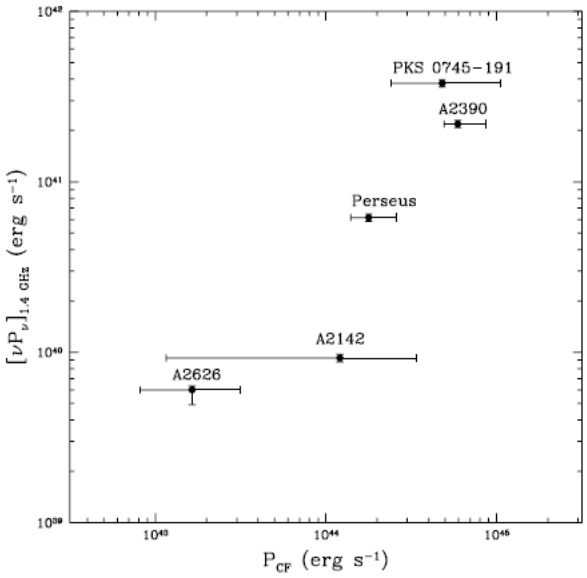

Figure 2.20: The correlation between the radio power at 1.4 GHz (νP_ν) and the cooling flow power ($P_{\rm CF} = \dot{M}kT/\mu m_{\rm p}$) for the mini-halo clusters.

Recently, BeppoSAX (Boella et al. 1997) and RXTE (Bradt et al. 1993) have detected excess hard emissions from the Coma cluster (Fusco-Famiano et al. 1999; Rephaeli et al. 1999), Abell 2256 (Fusco-Famiano et al. 2000), Abell 2199 (Kaastra et al. 1999), and Abell 3667 (Fusco-Famiano et al. 2001) although Abell 2199 shows only marginal evidence in the external region of clusters. Figure 2.21 shows the X-ray spectra of them.

Furthermore, Nevalainen et al. (2004) have re-analyzed 27 clusters of galaxies with BeppoSAX. The sign of excess hard emission have found at 2 σ level in seven clusters such as, Abell 2142, Abell 2199, Abell 2256, Abell 3376, Coma cluster, Ophiuchus cluster, and Virgo cluster. The observed parameters of the excess hard emission for seven clusters is listed in the table 2.3. The luminosity of excess emission occupies only 1−20 % of the thermal luminosity in general. In addition, such excess have found in the group of galaxies HCG 62 (Nakazawa 2000; Fukazawa et al. 2001), due to excellently low and stable background of ASCA and its lower temperature. All these clusters except for Abell 2199 exhibit some degree of merger signatures, implying the relevancy between the merger and the high energy electrons. However, the background of BeppoSAX have higher count rate than the cluster source, and high systematic uncertainty which is comparable to statistical one. The spatial distribution of the excess hard emission is not known besides that. Thus, there is no evidence whether the observed hard emission is caused by the high energy electrons. If the excess hard emission could be detected in the relaxed cooling flow clusters as well as merging clusters, it is regarded as more universal emission among clusters of galaxies since they also show the diffuse radio emission (i.e. mini-halo).

Hereafter, we mention the observed spectral properties of excess hard emission and estimated magnetic field focusing mainly on Coma, Abell 2256, Abell 3776, Abell 2199, and HCG 62. The spectra of Coma cluster is fitted well by a $8.5^{+0.6}_{-0.5}$ keV thermal component and a powerlaw with a photon index of $\Gamma = 1.57^{+0.36}_{-0.39}$ (Fusco-Famiano et al. 1999), which is consistent later results combined with second observation with BeppoSAX (Fusco-Famiano et al. 2004). If only the thermal component is considered, the resulting temperature become unrealistic value above 40 keV. The flux of the hard emission $\sim 2.2 \times 10^{-11}$ergcm^{-2}s^{-1} occupies $\sim$2$-$10 % of the ICM thermal flux in the energy range of 2$-$10 keV. In the same way, the spectra of Abell 2256, Abell 2199, Abell 3776, and HCG 62 are fitted with the photon index of 1.3$-$2.7. The fluxes of excess hard emission for Abell 2256, Abell 2199, Abell 3776, and HCG 62 are a factor of $\sim$0.5, $\sim$0.5, $\sim$0.3, $\sim$0.05 of Coma cluster, respectively. Magnetic field can be estimated by assuming IC scattering and combining with the radio luminosity as conducted in equation 2.44. With this derivation method, each cluster have smaller magnetic field than that measured by the Faraday Rotation of a few μG. Coma cluster shows the magnetic field of 0.14μG as against $\sim 6\mu$G from the Faraday Rotation (Feretti et al. 1995). However, Feretti et al. (1995) also have found that there are weaker and larger scale magnetic field component in the range of 0.1$-$0.2 μG, and therefore the $\sim$6 μG field could be local phenomenon around radio galaxy NGC 4869. We summarized these parameters in table 2.4.

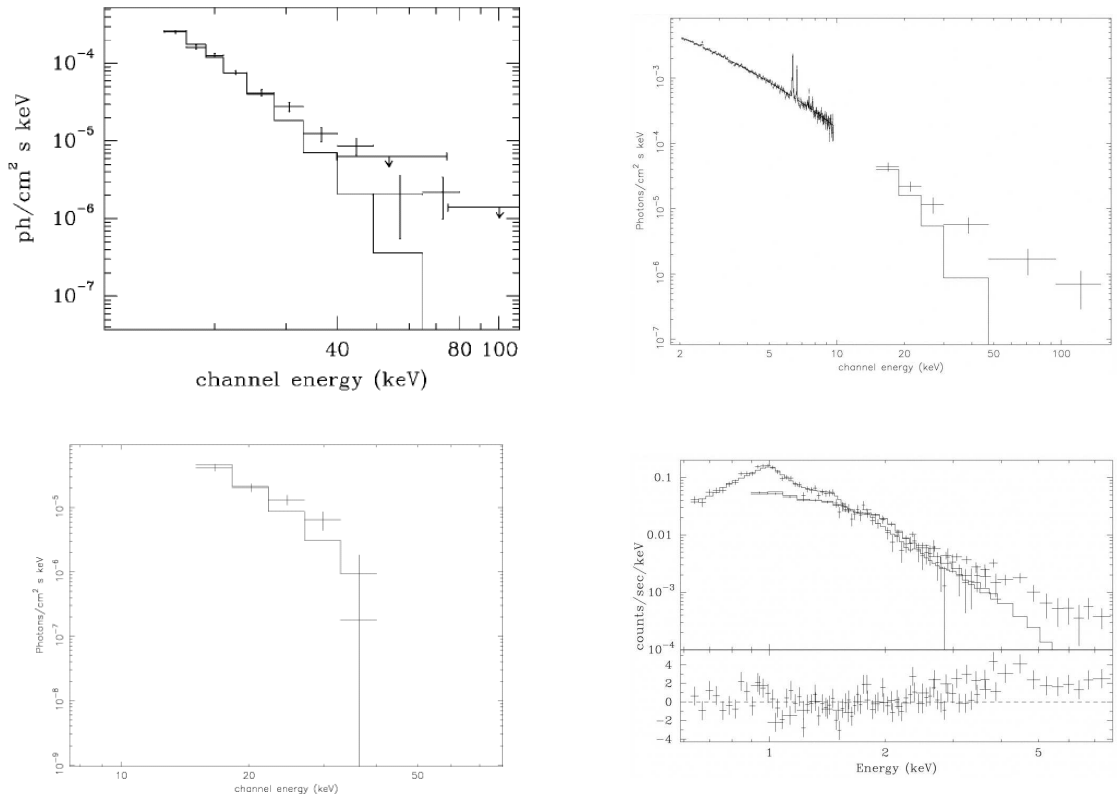

Figure 2.21: The spectra of Coma cluster (top left), Abell 2256 (top right), Abell 3776 (bottom left), and HCG 62 (bottom right) obtained with BeppoSAX.

Table 2.3: Observed parameters of excess hard emission

name	$\sigma^a_{\rm HXR}$	$R^b_{\rm thermal}$ (count s^{-2})	$R^c_{\rm HXR}$ (count s^{-2})	$L^d_{\rm thermal}$ (10^{43} erg s^{-1})	$L^e_{\rm HXR}$ (10^{43} erg s^{-1})
Virgo cluster	4.1	0.3±0.2	22.8±5.6	$23.5^{+0.6}_{-0.6}$	0.17±0.04
Abell 3376	2.7	0.4±0.2	8.2±3.0	$39.9^{+1.3}_{-1.3}$	9.2±3.4
Abell 2256	2.5	4.1±0.5	7.5±2.9	$69.7^{+1.2}_{-1.2}$	13.6±5.3
Coma cluster	2.4	30.9±0.8	8.4±3.5	$82.1^{+1.6}_{-1.6}$	2.6±1.1
Abell 2142	2.1	$11.9^{+1.6}_{-1.8}$	10.1±4.8	97^{+15}_{-11}	42.0±19.7
Abell 2199	2.1	1.6±0.4	7.1±3.4	48^{+2}_{-2}	3.4±1.6
Ophiuchus cluster	2.0	$66.2^{+2.0}_{-1.2}$	$8.8^{+4.1}_{-4.3}$	91^{+6}_{-5}	3.7±1.8

a: the non-thermal confidence level (AGN contribution is subtracted),
b: the thermal count rate predicted in 20−80 keV,
c: the non-thermal count rate in 20−80 keV (AGN contribution is subtracted),
d: the luminosity of non-thermal component in 20−80 keV (AGN contribution is subtracted),
e: the luminosity of thermal component in 0.1−2.4 keV.

Table 2.4: spectral parameters of excess hard emission

name	kT (keV)	α	$F^a_{\rm HXR}$ (erg s^{-1} cm^{-2})	$B^b_{\rm HXR}$ (μG)	$B^c_{\rm FR}$ (μG)
Coma cluster	$8.5^{+0.6}_{-0.5}$	$1.57^{+0.5}_{-0.4}$	(2.2±0.2)×10^{-11}	0.14	6/0.1−0.2
Abell 2256	$6.95^{+0.45}_{-0.35}$	1.3−2.7	(1.2±0.2)×10^{-11}	0.05	–
Abell 2199	4.71± 0.13	1.81±0.25	(1.0±0.25)×10^{-11}	–	–
Abell 3776	7.0±0.6	2.1	(6.4±1.3)×10^{-12}	0.41	–
HCG 62 group	$0.96^{+0.3}_{-0.6}$	$1.5^{+1.2}_{-0.7}$	5.5−8.4×10^{-13}	< 0.12	–

a: Flux of excess hard emission in 20−80 keV. For A2256, the error of 15% is derived from the PDS count rate error (1σ) presented in Fusco-Famiano et al. (2000). For Coma cluster and Abell 3376, we assumed ∼10% and ∼20% error in flux by scaling the error of Abell 2256 with their flux ratio. For Abell 2199 the original paper presents the flux in 0.1−100 keV range. This is converted to 20−80 keV band by assuming $\alpha = 1.8$.
b: Magnetic field calculated from excess hard emission when the IC scattering is assumed.
c: Magnetic field estimated from Rotation Measure.

Since the non-thermal excess emission have a powerlaw like spectrum, its flux becomes larger in the lower energy. On the other hand, the thermal component get fainter below $\sim$1 keV due to the Galactic absorption. This implies that the non-thermal emission would exhibit an excess from the thermal one in the low energy band as well as the hard excess in the higher energy. Such "soft excess" have been observed with EUVE (Extreme Ultravaiolet Explorer) from Coma cluster (Lieu et al. 1996a), Virgo cluster (Lieu et al. 1996b), Abell 1795 (Mittaz et al. 1998), and Abell 2199 (Lieu & Mittaz 1998). X-ray soft excess is considered to be unrelated to the cooling flow because it is observed in Coma cluster which does not contain cooled plasma. The obtained energetics can be explained well when the inverse Compton scattering is assumed for its emission mechanism. Moreover, its relative strength to the thermal emission increase at the cluster periphery in some clusters, indicating that soft excess has a extent wider than that of the thermal component. This supports the IC interpretation because the seed photons of the CMB distributes uniformly in the universe. On the other hand, this soft excess is also interpreted as the thermal plasma with the temperature of 10^{5-7} K, which called "Warm-Hot Intergalactic Medium (WHIM)". About half amount of the baryonic matter predicted cosmologically have not been confirmed observationally. Then, WHIM is expected to account for the missing baryon. However, it is under discussion whether which origin is valid for X-ray soft excess since WHIM is not directly detected yet.

Chapter 3

INSTRUMENTATION

For the thermal emission, it is necessary to study the detail structure of ICM temperature, surface brightness, and so on. Then we use Chandra which has the highest spatial resolution among the X-ray satellites. In order to efficiently examine the existence of the non-thermal emission from clusters of galaxies, four satellites are utilized in this thesis. These are ASCA, Chandra, XMM-Newton and Suzaku. We here briefly summarize the design and performance of each satellites.

3.1 Spacecraft

3.1.1 ASCA

ASCA (Advanced Satellite for Cosmology and Astrophysics; Tanaka et al. 1994) is the forth Japanese X-ray astronomy observatory. The satellite was launched on February 1993 from Kagoshima Space Center (KSC) of ISAS with M-3S-II-7 three stage rocket. ASCA has achieved a near-circular orbit with a perigee of 520 km, apogee of 620 km, and an inclination of 31°. About eight years after launch, ASCA re-entered the atmosphere on March 2, 2001.

In figure 3.1, we show the in-orbit configuration of ASCA. The satellite is equipped with four identical X-ray telescope (XRT). At the four foci, two gas scintillation imaging proportional counters (GIS) and two X-ray CCD camera (SIS) are located. ASCA is the first satellite that simultaneously performs imaging and spectroscopy in the wide energy band of 0.5−10.0 keV. The lowest background of the GIS at higher energy is valuable even today for searching the non-thermal emission of clusters.

3.1.2 Chandra

Chandra X-ray Observatory (Weisskopf et al. 2000), named in honor of Dr. Subrahmanyan Chandrasekhar, is the X-ray component of NASA's four Great Observatories. Chandra was launched by NASA's Space Shuttle *Columbia* on July 23, 1999. The satellite has an elliptical orbit with a perigee of ∼10,100 km, a apogee of ∼138,000 km. It allows uninterrupted observing intervals of more than 170 ks due to its orbital period of 63.5 hours. Chandra's extremely high spatial resolution

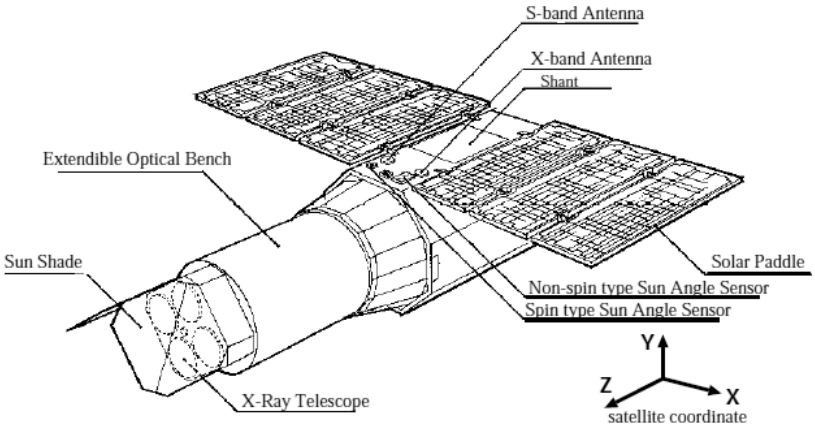

Figure 3.1: The schematic view of ASCA satellite.

of 0.5″, which is ∼50 times higher than that of the previous satellites, has greatly developed the structural study of various targets.

An outline drawing of chandra is shown in figure 3.2. Chandra has an X-ray telescope denoted as the High Resolution Mirror Assembly (HRMA). Two objective transmission gratings (OTG), the High Energy Transmission Grating (HETG), and the Low Energy Transmission Grating (LETG), are located at the aft of HRMA. On the focal plane, there are two sets of detectors. One is the imaging spectroscopic CCD arrays (Advanced CCD Imaging Spectroscopy;ACIS), and another is the imaging micro-channel plate (High Resolution Camera; HRC).

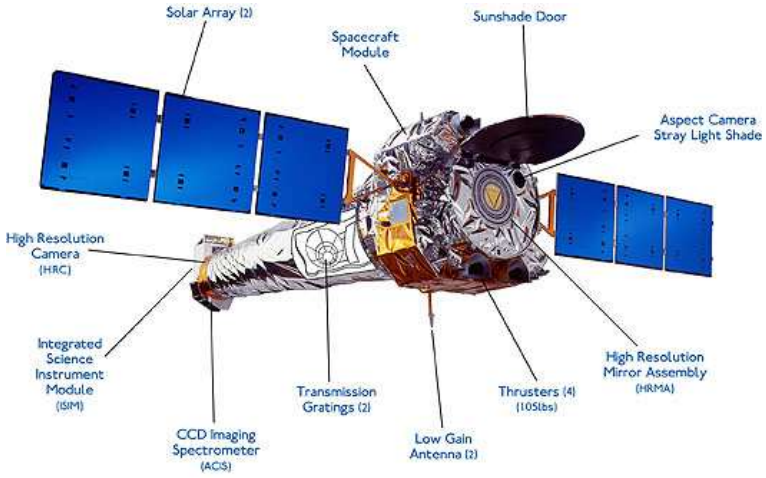

Figure 3.2: The schematic view of Chandra satellite.

3.1.3 XMM-Newton

XMM-Newton (X-ray Multi-Mirror Mission) is the second cornerstone of the Horizon 2000 program of the European Space Agency (ESA). The satellite was launched on December 10, 1999, into a highly eccentric orbit with an apogee of ∼115.000 km, a perigee of ∼6,000 km and an orbital inclination of 33°. XMM-Newton is also able

to acquire the long exposure data of $\sim$ 140 ks like Chandra satellite. The most important characteristic is high X-ray collecting capability due to its large effective area.

The schematic view of XMM-Newton is shown in Fig 3.3. The satellite has three X-ray mirror assembly as represented by the name of X-ray Multi-Mirror Mission. The telescope is coupled to the X-ray CCD arrays (European Photon Imaging Camera; EPIC) and the reflection grating spectrometer (RGS). The EPIC detector consists of two front-illuminated CCD, EPIC-MOS1, MOS2 (Metal-Oxide-Semiconductor type), and a back-illuminated CCD EPIC-PN (p-n junction type). Furthermore, optical/UV telescope called Optical Monitor (OM) is also equipped. All these instruments can be operated simultaneously and independently.

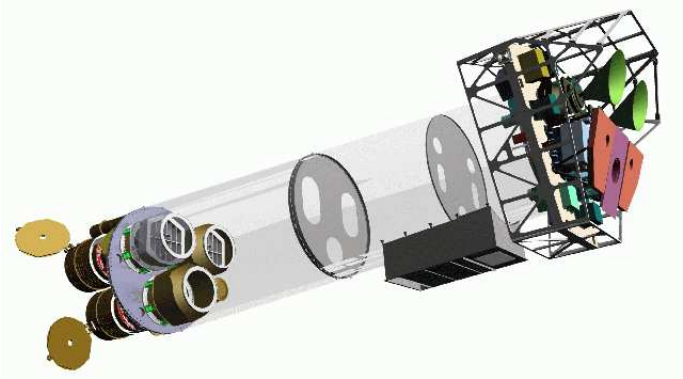

Figure 3.3: The schematic illustration of XMM-Newton satellite.

3.1.4 Suzaku

Suzaku (Astro-E2) is the newest X-ray observatory and the fifth Japanese X-ray mission after ASCA. This satellite was successfully launched from Uchinoura Space Center (USC), which is same site as KSC, by a M-V (mu-five) launcher on July 10, 2005. It is the recovery mission to Astro-E, which was lost on February 10, 2000 due to malfunctioning in the first stage of the launch vehicle. Suzaku was launched into an near-Earth circular orbit with the altitude of $\sim$550 km and the inclination of 31°. The most remarkable advantage is data accession over the broad-band energy range from 0.3$-$600 keV.

Fig 3.4 shows a schematic drawing of Suzaku. Suzaku has five X-ray Telescope (XRT) and two kinds of detectors on the focal plane, which are the X-ray Spectrometer (XRS) and the X-ray Imaging Spectrometer (XIS). XRS is placed on the focal plane of one of the XRTs, namely XRT-S. XISs consist of one back-illuminated and three front-illuminated X-ray sensitive CCD, and are coupled to the remaining four telescopes (XRT-I). These cover energy range below $\sim$10 keV. The Hard X-ray Detector (HXD) is also employed with Suzaku which is responsible for observation in higher energy of 10$-$600 keV. On August 8 2005, to our deep regret, XRS was left irreparable condition because of the liquid helium coolant venting to space. However, Suzaku's broad-band observation, low background and high CCD energy resolution by the combination of the XIS and HXD provide us novel data series.

The performance between four satellites is compared in table 3.1.

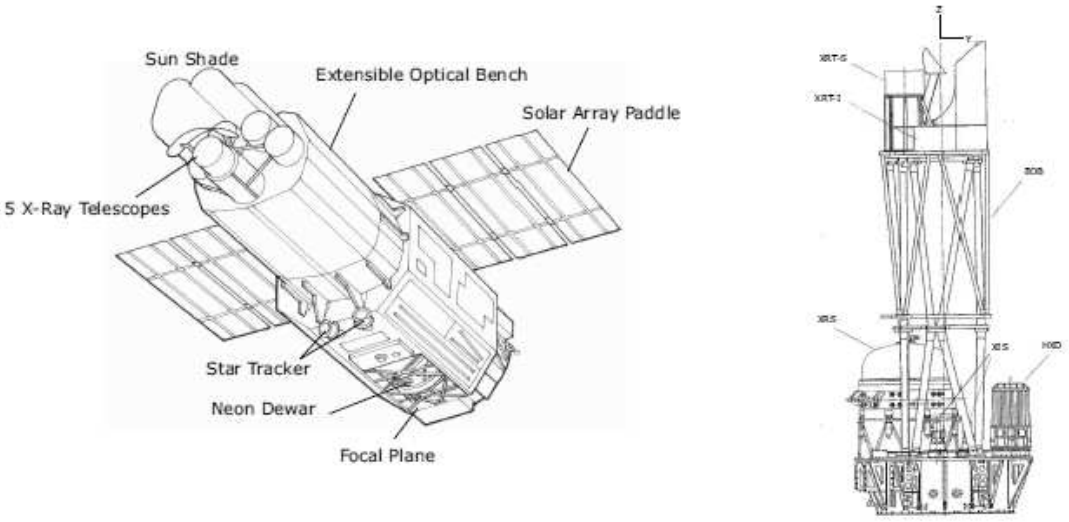

Figure 3.4: The schematic drawing of Suzaku satellite (left) and the side-view (right).

Table 3.1: Basic performance of X-ray satellites

	effective area	$\Delta E/E^a$ (%)	$\Delta\theta^b$ (arcsec)	energy band (keV)	FOV (arcmin)
ASCA	1300	3	180	0.4−15	50
Chandra	600	2	0.5	0.3−10	10
XMM-Newton	3000	2	10	0.3−15	30
Suzaku (XIS/HXD)	1450 / 160-330	2/ –	100/–	0.2−600	$10/0.56^{\circ}$ [c]

a; measured at 6.7keV (Fe-K) b; angular resolution c; measured at 20 keV

3.2 The X-ray Telescope

The X-ray telescope is different from well-known optical telescope. X-rays are totally reflected off when their incident angle from the surface is shallower than a certain critical value. In achieving total reflect of X-rays, the critical angle should be limited to less than $\sim 1^{\circ}$ because the refraction index of metal become slightly less than 1 for the wave length of X-rays.

All satellites introducing here embrace the multilayer concentric thin-walled, grazing-incident mirrors, what we call the Wolter Type-I mirrors (figure 3.5). These mirror consist of two section; the front section of a paraboloid mirror and the rear section of a hyperboloid mirror. Then the incident X-rays are collected on focal point after twice reflection. The telescopes onboard ASCA and Suzaku is somewhat different from the others in point of employing conical approximation to the exact paraboloid or hyperboloid surface. We present the structure and feature of each mirror below, and their design parameters and performance in the table 3.2−3.5.

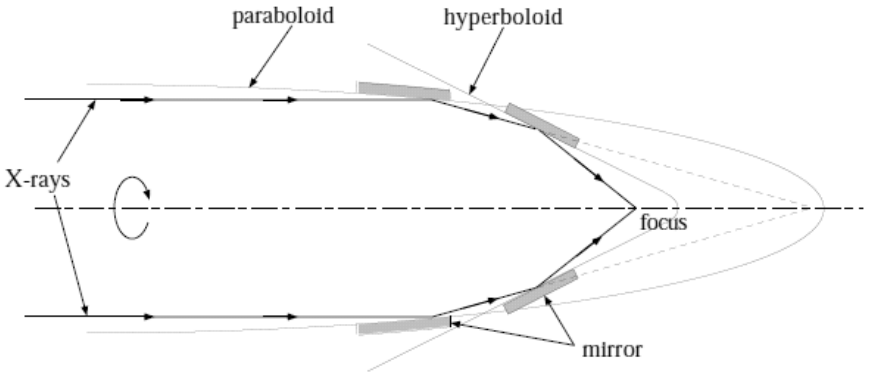

Figure 3.5: The schematic view of Wolter Type-I mirrors.

ASCA XRT

ASCA XRT are made up of 120 thin aluminium foils. The bent foils are $\sim$10μm lacquer-coated to improve the surface smoothness, and $\sim$50 nm gold-evaporated to increase the reflectivity. The 120 shells are closely packed in onion-ring configuration with a typical space of 1 mm. The diameter of the innermost and the outermost are 120 mm and 345 mm, respectively. In practice, the foils are produced and packed in four quadrants, and aligned by 13 alignment bars into 14 sectors as shown in figure 3.6. The basic parameters are listed in table 3.2.

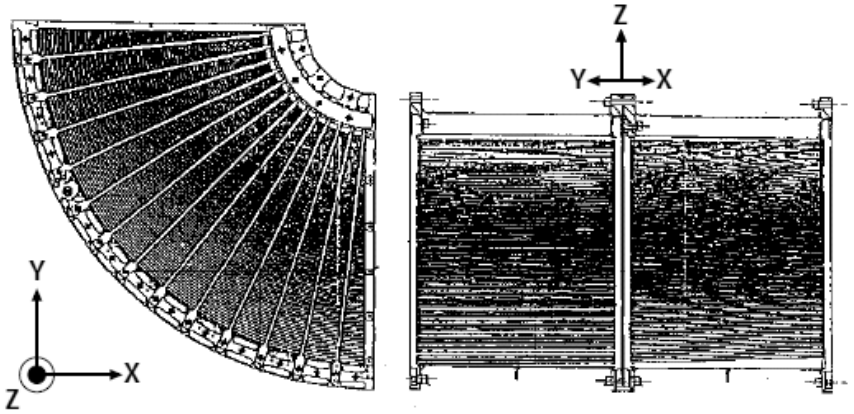

Figure 3.6: The schematic view of ASCA XRT.

Table 3.2: Design parameters and performance of ASCA XRT

Substrate (thickness)	Aluminium (127 μm)
Mirror coating (thickness)	Acrylic lacquer (10 μm) & Gold (50 nm)
Total height	100 mm
Weight (four XRTs)	40 kg
Number of nested shells	120
Mirror diameter (inner / outer)	12.0 / 34.5 cm
Focal length	3.5 m
Geometrical area	558 cm^2
Effective area (@ 1, 7 keV)	1300, 600 cm^2
Field of view (@ 1.5, 8 keV)	24, 16 arcmin
Angular resolution (HPD)	3 arcmin

Chandra HRMA

HRMA consist of four pair of Wolter Type-I mirrors as shown in figure 3.7. The substrate is Zerodur glass, which is polished and coated with iridium on a binding layer of chromium. Then the HRMA is much heavier than that of ASCA XRT. The four mirrors are identified to 1, 3, 4, 6 toward the outer and the diameter of mirror pair ranges from 65 to 123 cm. HRMA has achieved the highest spatial resolution of 0.5″ by polishing technique with high precision. The basic characteristics are summarized in table 3.3.

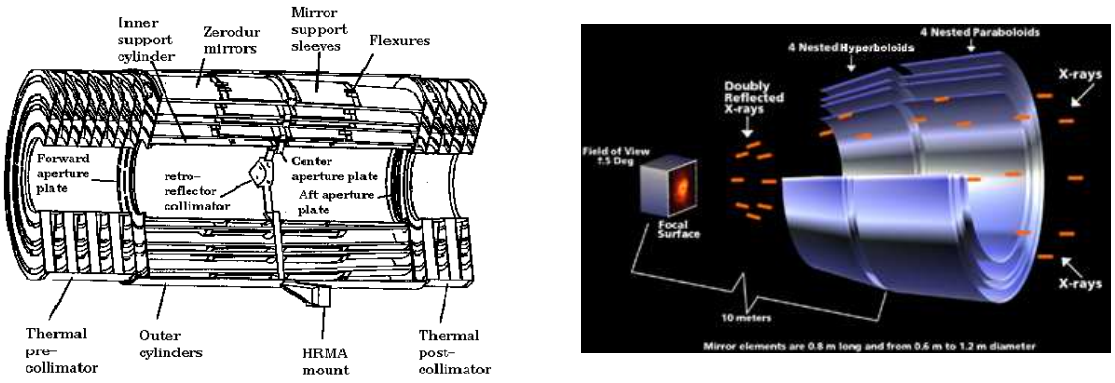

Figure 3.7: The four nested HRMA mirror pair (left) and illustration of X-ray grazing path (right).

Table 3.3: Design parameters and performance of Chandra HRMA

Optics	Wolter Type-I
Mirror coatings (thickness)	Iridium (330A)
Mirror lengths (paraboloid or hyperboloid)	84 cm
Mirror outer diameters (1,3,4,6)	1.23,0.99,0.87,0.65 m
Total length (pre-collimator to post-collimator)	276 cm
Unobscured clear aperture	1145 cm^2
HRMA mass	1484 kg
Focal length	10.066±0.002 m
PSF FWHM (with detector)	0.5 arcsec
Effective area (@ 0.25, 5.0, 80. keV)	800, 400, 100 cm^2
Ghost-free field of view	30 arcmin dia

XMM-Newton Telescope

Each telescope onboard XMM-Newton consists of 58 thin shells nested in a coaxial and co-focal configuration (figure 3.8). They are made from thin monolethic gold-coated nickel. The mirror diameter is 30.6 cm at the innermost and 70.0 cm at the outermost. A large number of mirrors have increased the effective area up to higher energy range (see the next section). As shown in figure 3.9 right, two of three telescopes for MOS1 and MOS2 are equipped with grating stacks on the optical path. The grating diffract half of the incident X-rays into the RGS detectors to produce dispersed image of point source, while the remaining non-diffracted X-rays from zero-order images on the MOS detectors. The basic parameters are shown in table 3.4.

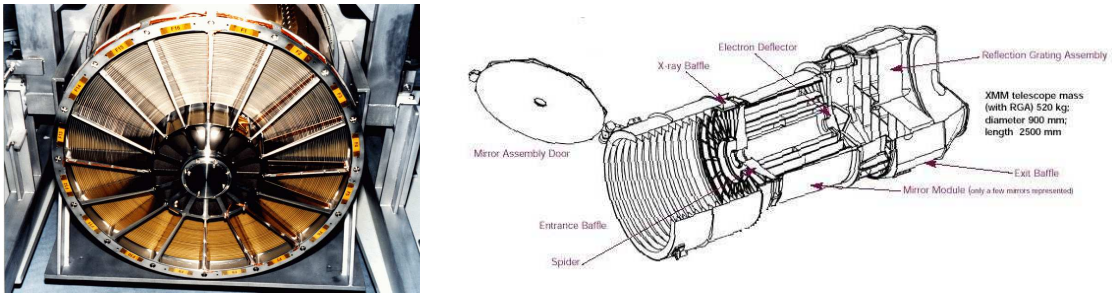

Figure 3.8: The photograph and schematic view of XMM-Newton telescope.

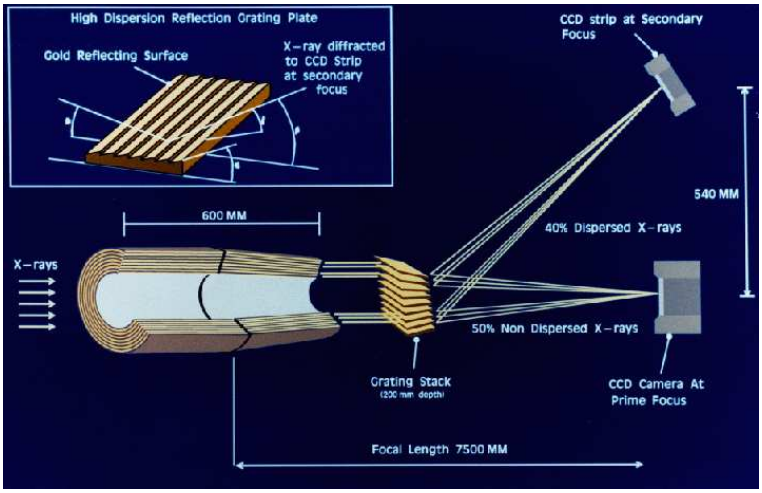

Figure 3.9: The illustration of XMM-Newton telescope, together with the EPIC MOS camera and the RGS instrument.

Table 3.4: Design parameters and performance of XMM-Newton Telescope

Optics	Wolter Type-I
Mirror substrate	Nickel
Mirror coating (thickness)	Gold (250 nm)
Mirror lengths (paraboloid or hyperboloid)	60 cm
Mirror diameter (inner / outer)	30.6 / 70.0
Mirror thickness (inner / outer)	0.47 / 1.07
Focal length	7.500 m
Mirror module mass	420 kg
Effective area (@ 1.5, 8.0, 12 keV)	1475, 580, 130 cm^2
Field of View	30 arcmin dia

Suzaku XRT

Suzaku XRT employs 175 tightly nested mirror shells which are made up of thin aluminium foils (figure 3.10). The mirror size ranges from ∼12 to ∼40 cm in diameter. The replicated method is utilized to make the foil surface smooth, being different from the method of polishing mirror directly like Chandra and XMM-Newton. In this technique, the foils are generated from the mandrel whose surface have sub-nanometer smoothness over a wide spatial frequency. Then a high aperture efficiency can be achieved, providing a light-weight telescope with a large effective area. Although the thin foils with conical approximation makes the angular resolution significantly worse than those of Chandra and XMM-Newton, it is considerably better than those of ASCA XRT which employs thin foil but no replication process. The basic parameters are shown in table 3.5.

Figure 3.10: The photograph of Suzaku XRT.

Table 3.5: Design parameters and performance of Suzaku XRT (XRT-I)

Substrate (thickness)	Aluminium (155 μm)
Mirror coating	Gold
Total height	279 mm
Weight	19.5 kg
Number of nested shells	175
Mirror diameter (inner / outer)	11.8 / 39.9 cm
Focal length	4.75 m
Plate scale	0.724 mm arcmin^{-1}
Geometrical area	873 cm^2
Effective area (@ 1.5, 8 keV)	440, 250 cm^2
Field of view (@ 1.5, 8 keV)	17, 13 arcmin
Angular resolution (HPD)	2 arcmin

3.2.1 Effective Area

The reflectivity of X-rays depends on not only its incident angle but also its energy. Then the effective area of telescope varies depending on these two quantities. Figure 3.11 shows the comparison of the effective area between four satellite telescopes as a function of energy. Only the telescope characteristics are included here. The sharp drop around 2 keV is due to M-edge of evaporated material; gold on ASCA XRT, XMM-newton' mirror, and Suzaku XRT, and iridium on Chandra HRMA. Mirrors become no longer reflective above $\sim$10 keV. The effective area of XMM-Newton mirror is the largest over the energy range of 0.1$-$10 keV. The back-illuminated CCD chip onboard Chandra, XMM-Newton, Suzaku have a larger effective area than those of the front-illuminated in the lower energy and then are more sensitive to low energy X-rays. The vignetting effect due to the incident angle of X-rays is shown in figure 3.12. XMM-Newton telescope is less affected by vignetting than

other satellites because of tightly nested mirror providing high reflectivity even in its outer part and then high vignetting factor.

Recently, anxious degradation of XIS efficiency have been found. Although it is likely to occur because CCD and surrounding structure is contaminated by out gas from the satellite, the rate of degradation is unexpectedly high. This indicates that some kinds of additional absorbing material is appendant onto the Optical Blocking Filter (OBF) in front of XIS. The rate is different from sensor to sensor, and also position to position on OBF. Then it is given as a function of the observation date after XIS door open, and detector coordinate. From the overall spectral feature of absorption, the chemical composition of absorber is suspected to be Carbon and Oxygen with the number ratio C/O = 6. Now, we can incorporate such effects of contamination into the arf file which is created with arf generator xissimarfgen.

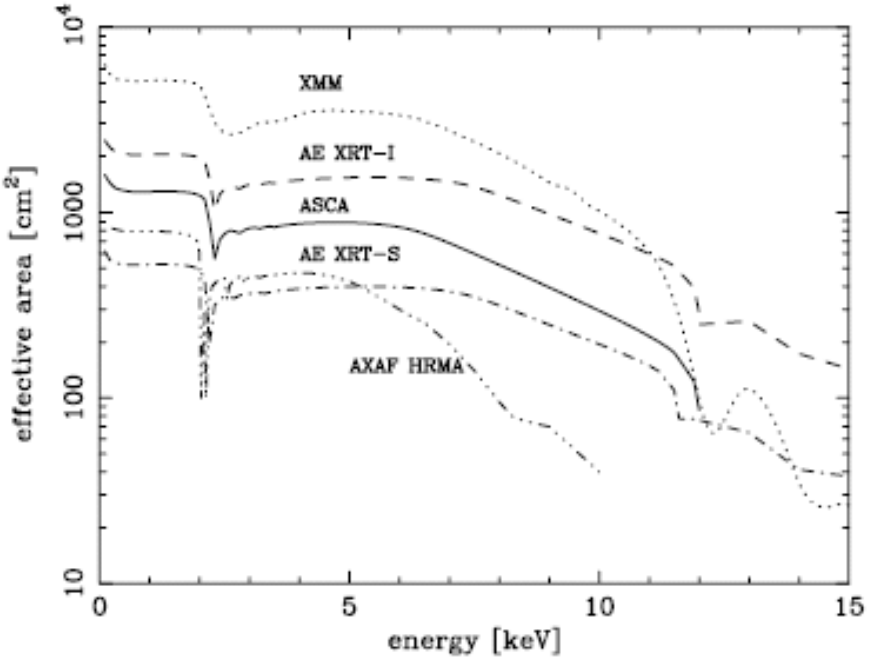

Figure 3.11: The effective area of ASCA, Chandra, XMM-Newton, and Suzaku. Only the telescope response are included.

3.2.2 Point Spread Function

Even if incident X-rays come from the point source, X-ray image broadens at some degree due to the precision of alignment between the telescope and detectors or polish of mirror surface as shown in the top panels of figure 3.13 (an example of XMM-Newton mirror). Point Spread Function (PSF) is the function to describe this broadening. PSF is defined as the two-dimensional brightness distribution created on the focal plane by a monoenergetic point source at a certain location in the field of view. The bottom panel of figure 3.13 shows the PSF of the XMM-Newton telescope as an example.

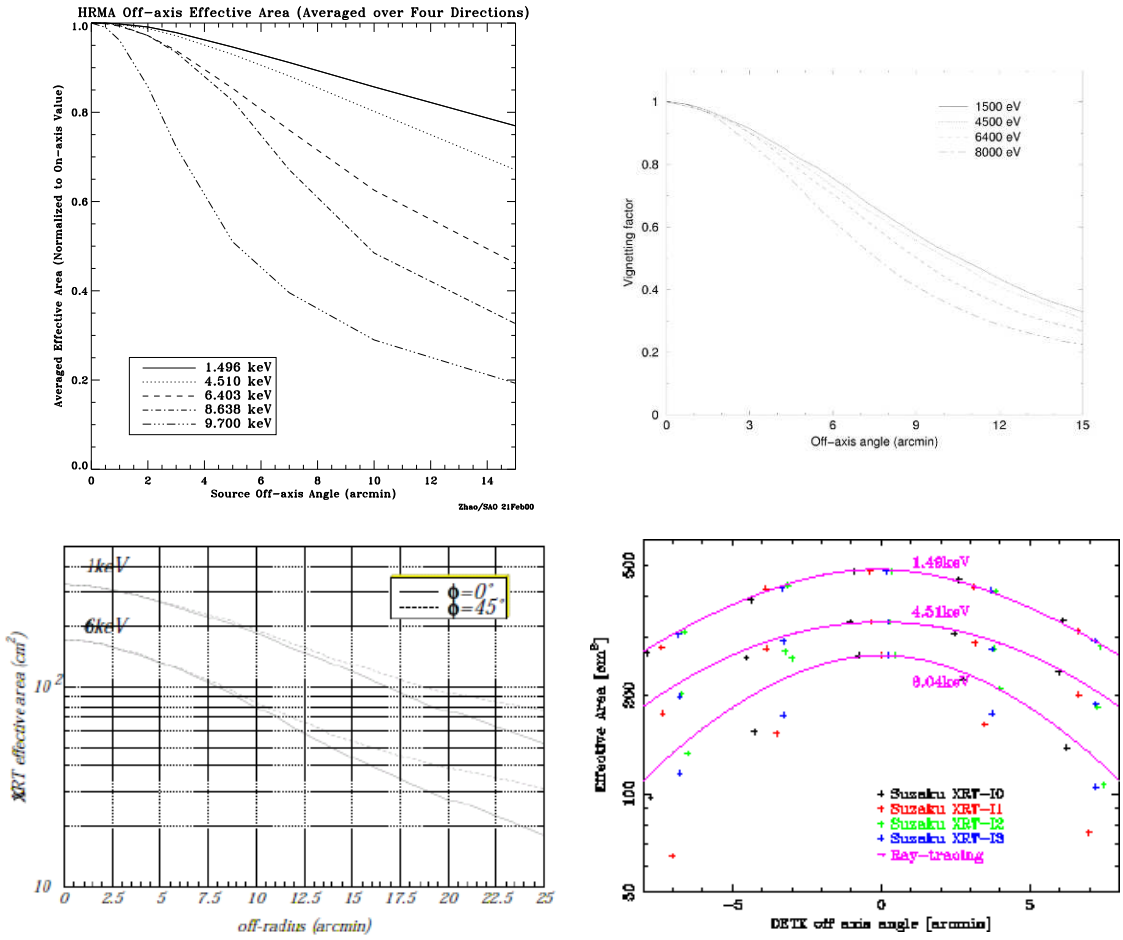

Figure 3.12: The effective area transition according to the incident angle of ASCA (top left), Chandra (top right), XMM-Newton (bottom left), and Suzaku(bottom bottom).

A useful parameter characterizing PSF is encircled energy fraction, which is two-dimensional integral of the PSF calculated as a function of radius from the image center. The PSF and then encircled energy again depend on X-ray energy and incident angle. Therefore, the PSF spreads and encircled energy fraction decreases when the off-axis angle increase due to mirror aberration enlargement, and also when the X-ray energy increases due to enhancement of X-ray scattering.

The encircled energy functions are shown in figure 3.14. Chandra HRMA shows narrow profile when compared with other telescopes, indicating HRMA's good angular resolution. X-ray image broadening of Chandra HRMA exhibits strong dependence for energy (more broad in higher energy) while on Suzaku XRTs there is little energy dependence. XMM-Newton's mirror has small energy dependency and PSF becomes sharp in higher energy unlike Chandra HRMA.

Figure 3.15 shows the dependency of encircled energy against X-ray incident angle. Here the encircled energy is represented as the radius which contains 50% or 90% photons from point source. PSF become broad according to enhancement of the incident angle in both Chandra and XMM-Newton. Furthermore, the energy dependency of XMM-Newton PSF reverses from the relation mentioned above in

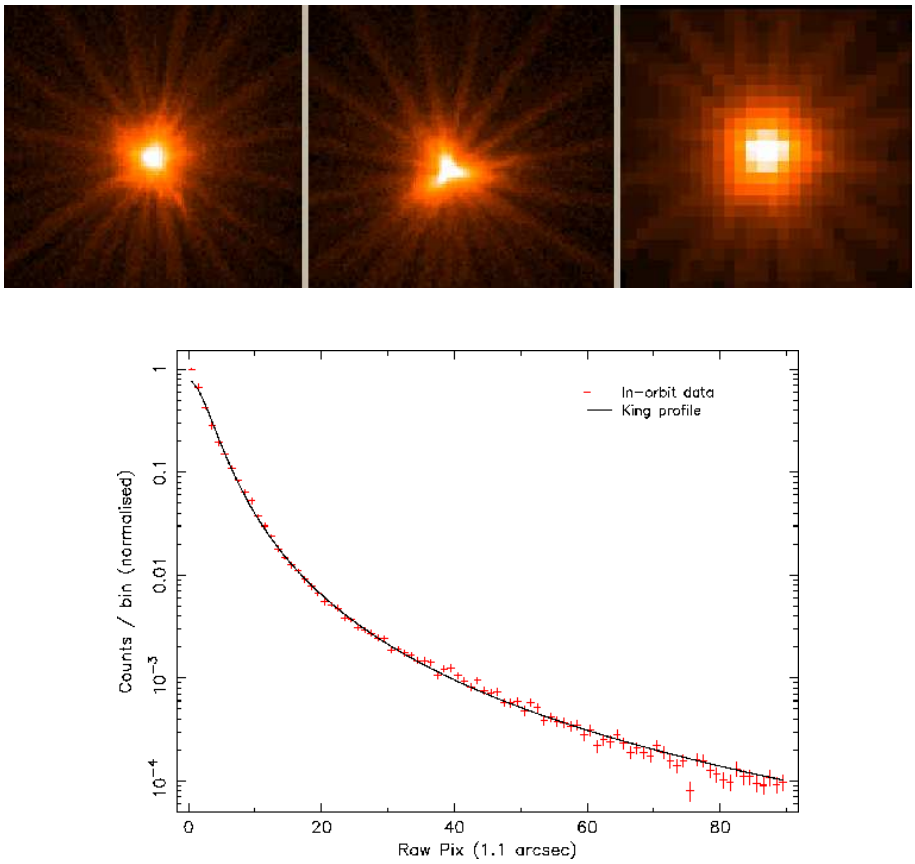

Figure 3.13: The image of point source obtained with MOS1 (top left), MOS2 (top middle), pn (top right), and PSF (bottom) of Newton telescope.

proportion to the off-axis angle.

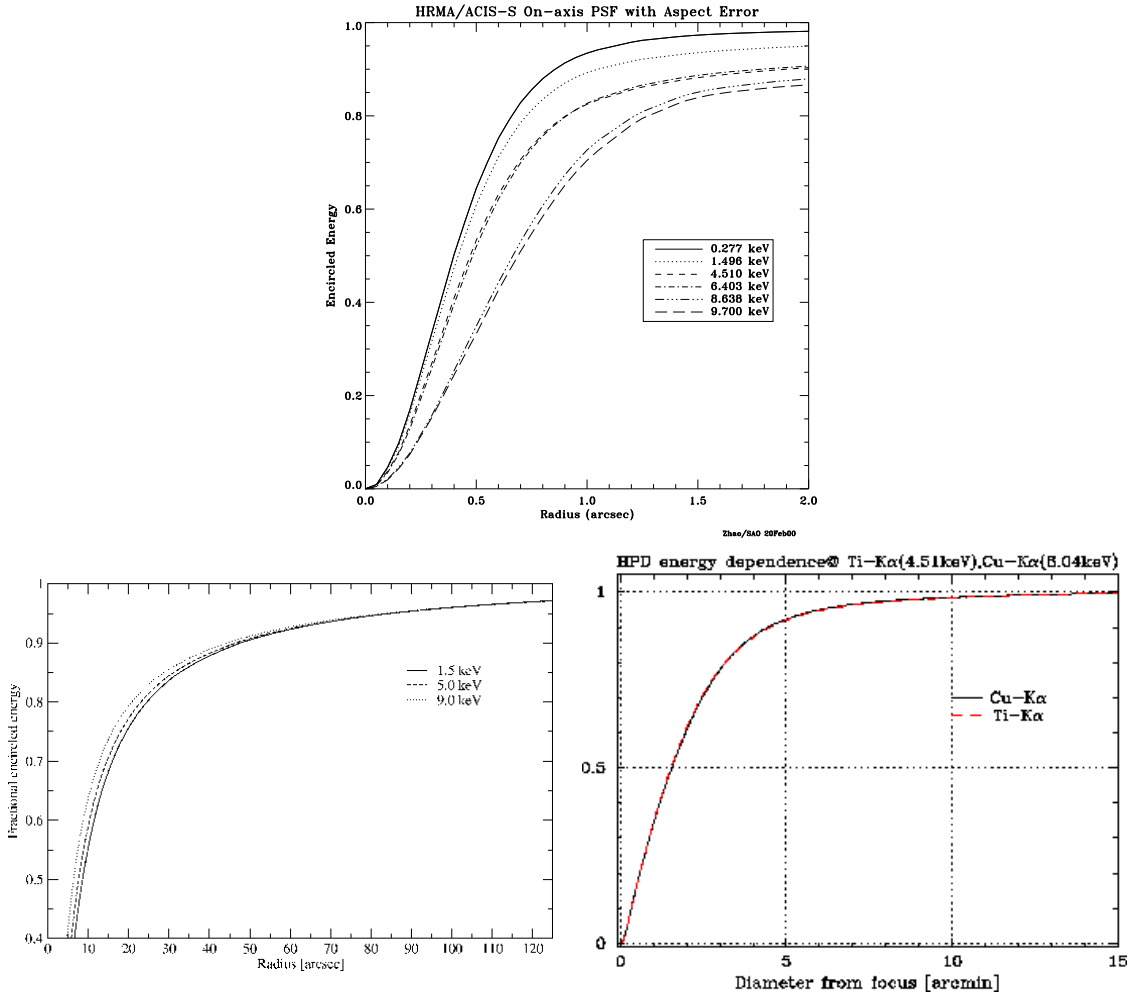

Figure 3.14: The fractional encircled energy of Chandra (top panel), XMM-Newton (bottom left), Suzaku (bottom right).

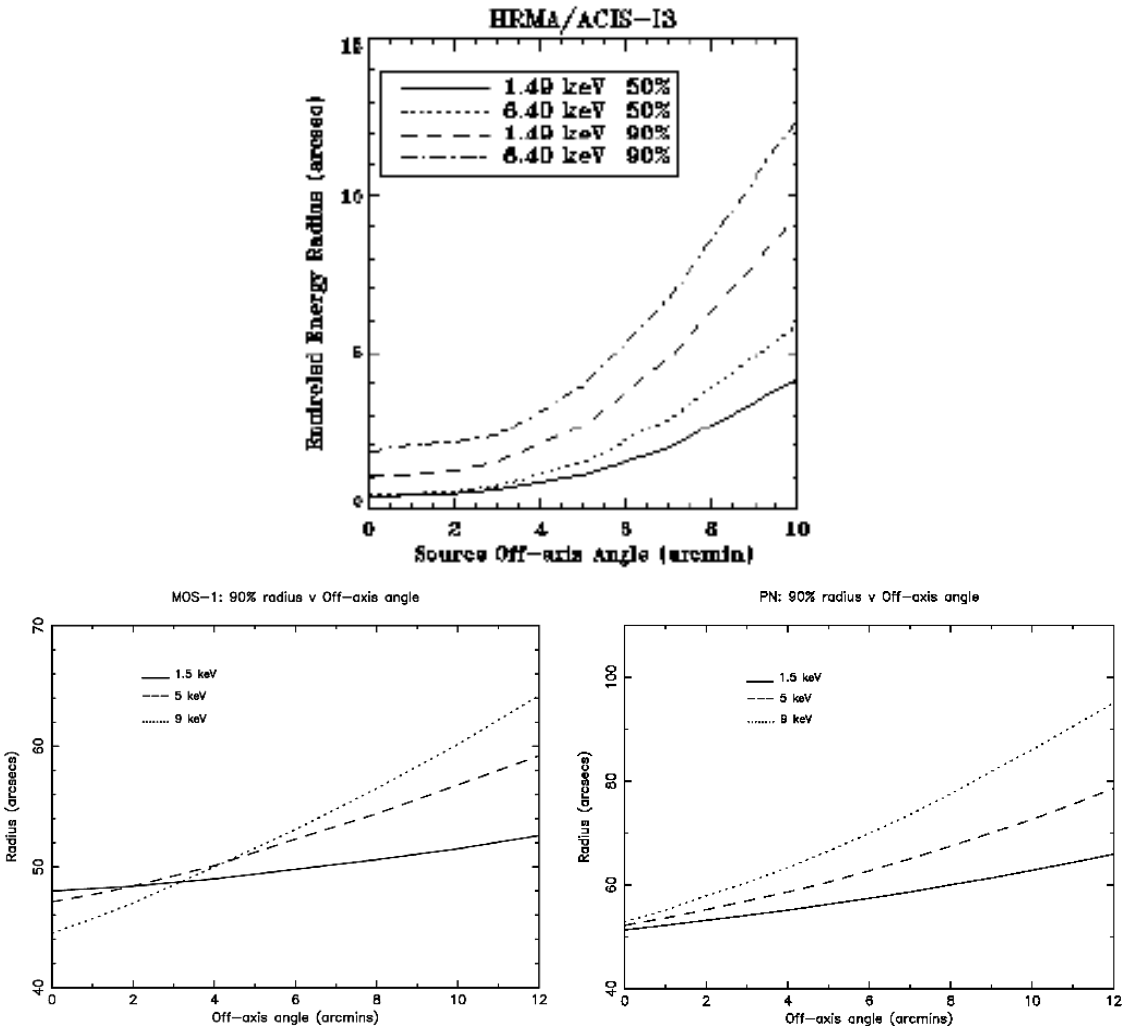

Figure 3.15: The angular dependency of fractional encircled energy. Chandra (top panel) and XMM-Newton (bottom panels, left: MOS, right: pn).

3.3 X-ray sensitive CCD Camera

The ASCA satellite for the first time has carried on-board X-ray sensitive CCD camera operated in single-photon mode. Thereafter, CCDs are utilized as the most standard focal plane imaging detector. In combination with X-ray telescopes, CCDs enable us to measure the position and energy of each detected X-ray photon, meaning that we can obtain image and spectra at once in a typical energy range of $\sim$0.5$-$10 keV. The basic configuration or properties of the CCDs onboard each satellite are explained below.

ASCA SIS

The ASCA SIS is the first X-ray CCDs in orbit. Figure 3.16 shows a cross sectional view of SIS. The SIS system consists of SIS0 and SIS1, and each detector is made up of four CCD chips of 11 mm square (figure 3.17). The four CCD chips are aligned in square with narrow separation to cover $\sim 20' \times 20'$ square region on the sky. Each chip has 4096$\times$4096 pixel, and the size of one pixel corresponds to 27μm. Basic parameters and performance of the SIS are listed in table 3.6.

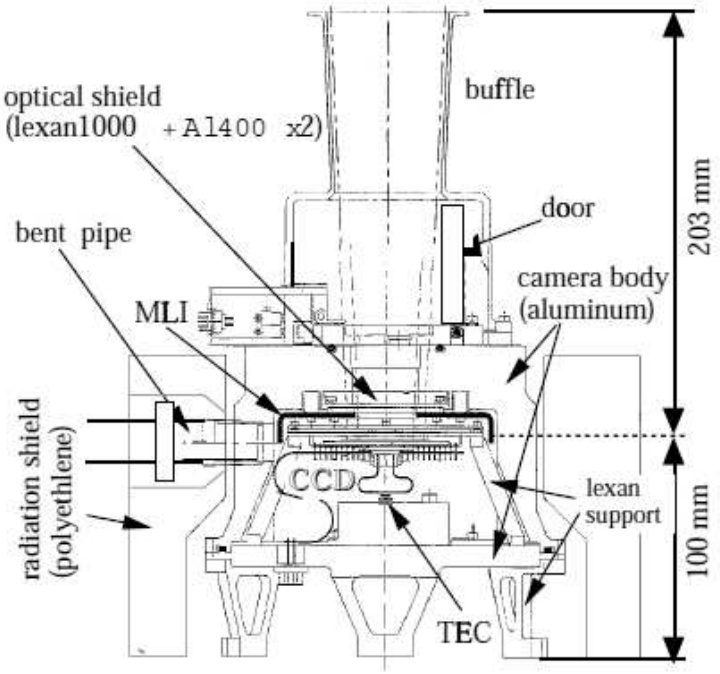

Figure 3.16: The cross sectional view of ASCA SIS.

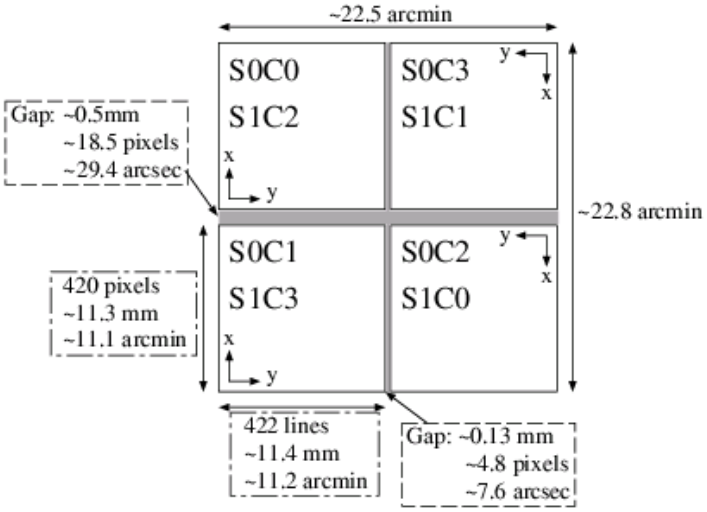

Figure 3.17: The focal-plane layout of ASCA SIS.

Table 3.6: Basic features of ASCA SIS

Illuminated method	Front illuminated
CCD format	420 pixels ×422 lines
Pixel size	27μm
Array size	11×11 mm
Covered sky area	11×11 arcmin
Depletion layer	40μm
Quantum efficiency	80 % (@ 5.9 keV)
Detector operating temperature	-62°C
Energy band	0.4−12 keV
Energy resolution	2 % (@ 5.9 keV)

Chandra ACIS

The Chandra ACIS has two types of chips with different irradiation method; front-illuminated (FI) and back-illuminated (BI). There are two BI chips and eight FI chips in Chandra ACIS as shown in figure 3.18 and 3.19. Each CCD chip consists of 1024×1024 pixels whose one pixel size is 24μm. Their design and basic properties are shown in table 3.7. As mentioned above (figure 3.11), the detection efficiency of BI devices for lower energy X-ray photons is better than that of FI devices due to less absorption of soft X-ray photons by electrodes. The ACIS can be physically moved on the focal plane, so that the HRMA's optical axis fall on the desired CCD chip.

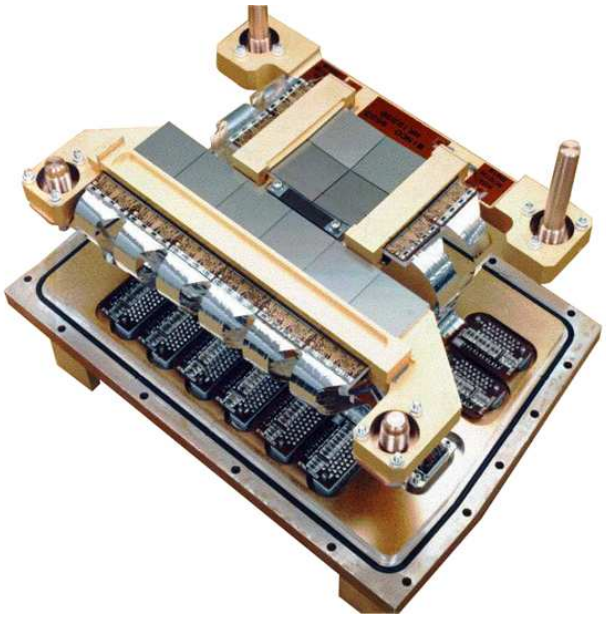

Figure 3.18: The photograph of Chandra ACIS.

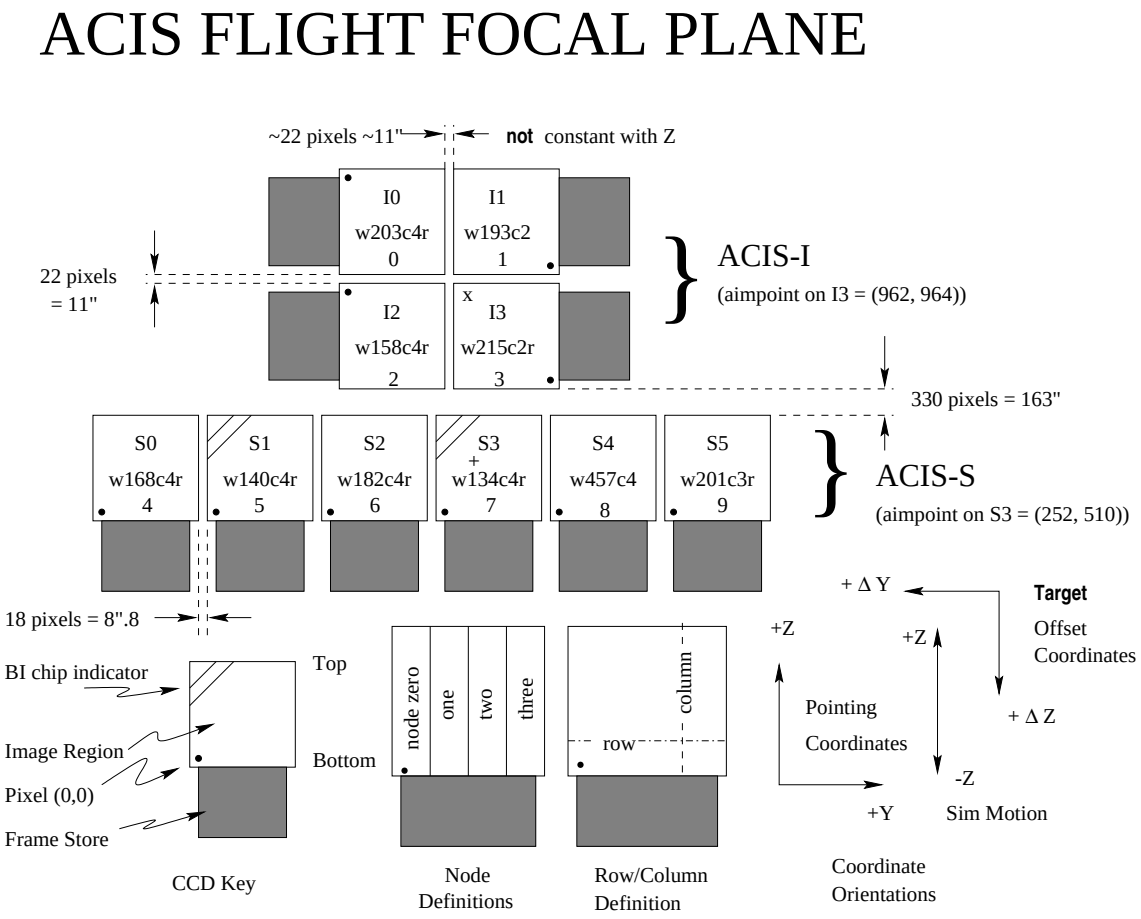

Figure 3.19: The focal-plane layout of ACIS CCD chips.

XMM-Newton EPIC

XMM-Newton has three CCD cameras called EPIC. Two of them are MOS CCD arrays and the another is pn CCD array. Their photograph is shown in figure 3.20.

Table 3.7: Basic features of Chandra ACIS

CCD format	1024×1024 pixels
Pixel size	24.0 μmicrons (0.492±0.0001 arcsec)
Array size	16.9×16.9 arcmin; ACIS-I
	8.3×50.6 arcmin; ACIS-S
Effective area (FI)	110, 600, 40 cm^2 @ 0.5, 1.5, 8.0 keV
Quantum efficiency (FI)	$>$ 80%, $>$ 30% (@ 3.0-5.0, 0.8-8.0 keV)
Quantum efficiency (BI)	$>$ 80%, $>$ 30% (@ 0.8-6.5, 0.3-3.0 keV)
Minimum row readout time	2.8 ms
Frame transfer time	41 μsec (per row)
Point-source sensitivity	4×10^{-15}ergscm^{-2}s^{-1}
	(in 10^4sec, 0.4–6.0 keV)
Detector operating temperature	-90∼-120°C

The MOS contains seven chips as illustrated in figure 3.21. The size of each chip is 2.4 cm square and each chip has 600×600 pixel of 40μm. Since they are installed behind mirror assemblies which are equipped with the reflection gratings, about a half of the incoming X-ray photons reaches. The seven chips are arranged to have the slightly different height for the purpose of suppressing the inter-chip gaps and tracing the slightly curving focal plane better. On the other hand, the pn camera utilizes 12 chips of 3×1 cm size on a common plane. There are 199×64 pixels of 150μm. The MOS camera has a better angular resolution due to the its smaller pixel size, while the pn possesses higher efficiency in the lower energy range because of adopting the back-illuminated method as Chandra ACIS. Basic parameters are listed in table 3.8.

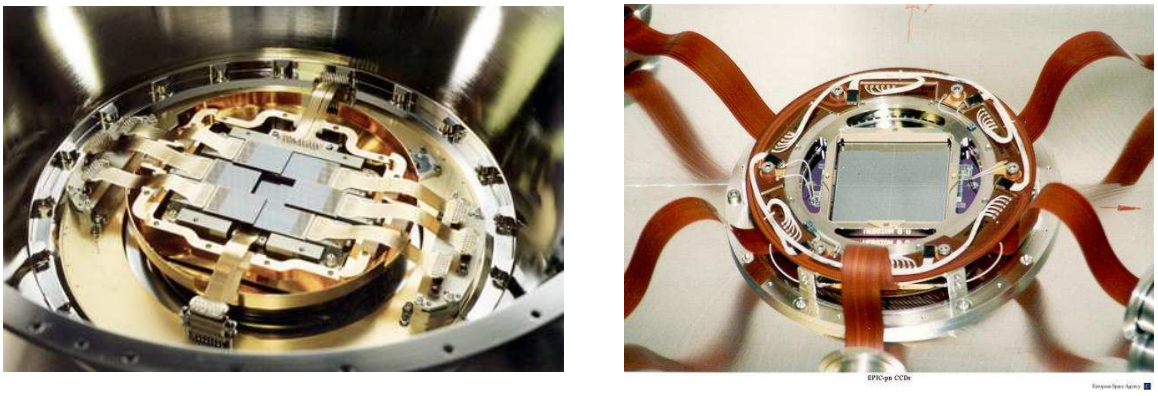

Figure 3.20: The photograph of XMM-Newton EPIC MOS (left) and pn (right).

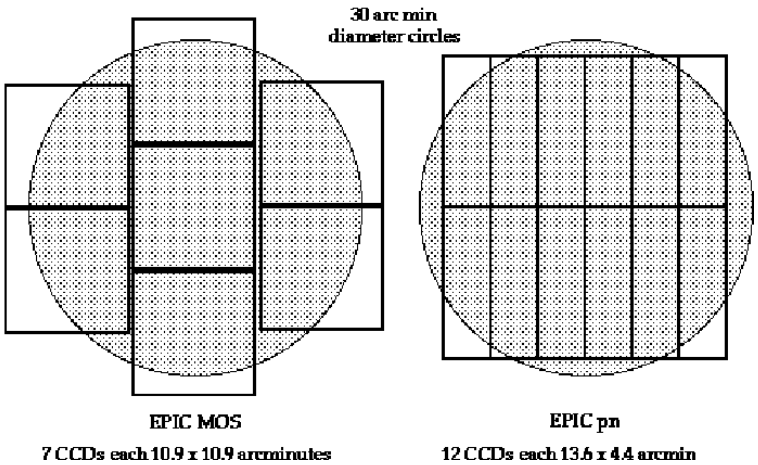

Figure 3.21: The focal-plane layout of EPIC MOS (left) and pn chips (right).

Table 3.8: Basic features of XMM-Newton EPIC

	MOS	pn
Illumination method	Front illuminated	Back illuminated
CCD format	600×600 pixels	199×64 pixels
Pixel size	24.0 μm (1.1 arcsec)	150.0 μm (4.1 arcsec)
Chip size	2.4×2.4 cm^2	3×1 cm^2
Coverd sky area	10.9×10.9 arcmin	13.6×4.4 arcmin
Time resolution	2.6 s	73.4 ms
Depletion layer	30-40μm	300μm
Detector operating temperature	-100, -120°C	-90°C
Energy band	0.15−12 keV	0.15−15 keV
Energy resolution	70eV	80eV

Suzaku XIS

Suzaku XIS has four CCD devices (XIS-0, XIS-1, XIS-2 and XIS-3). Each device is fixed on the focal plane of the corresponding XRT-I and consists of a single CCD chip as shown in figure 3.22. The exposure area of 1024×1024 pixels is divided into four segments. XIS also employs two kinds of chips as well as Chandra ACIS and XMM-newton EPIC pn; XIS-1 is a back-illuminated and the others are front-illuminated devices. Design parameters and performances are summarized in table 3.9. The most remarkable feature of Suzaku XIS is the simultaneous achievement of good energy resolution and the large effective area in lower energy range.

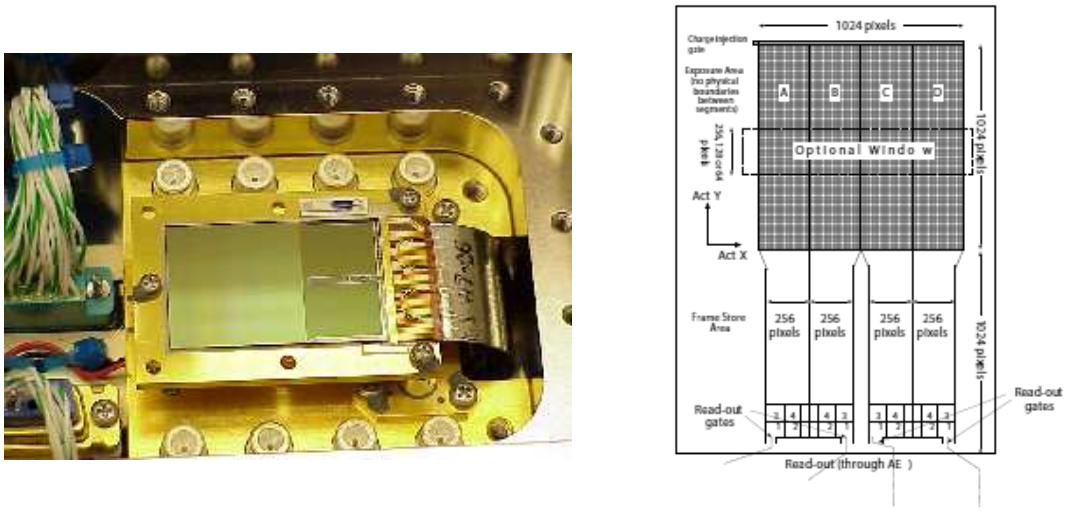

Figure 3.22: The picture (left) and schematic view (right) of Suzaku XIS chip.

Table 3.9: Basic features of Suzaku XIS

CCD format	1024×1024 pixels
Pixel size	24.0 μm (0.492±0.0001 arcsec)
Coverd sky area	17.8×17.8 arcmin
Effective area (FI)	344 cm^2, 147 cm^2 (@ 1.5 keV)
Effective area (BI)	393 cm^2, 103 cm^2 (@ 1.5 keV)
Systematic noise	$<$ 2 electrons per pixel
Time resolution (Normal / P-sum mode)	8s / 7.8 ms
Depletion layer	50-70μm
Dark current	¡ 0.1 electrons s^{-2} pixel^{-1}
Readout noise	¡ 3-4 electrons rms, typical

3.3.1 Energy Resolution

The number of electron-hole pair generated in CCDs via photoelectric absorption is in proportion to the energy of incident X-ray photons. This relation is applied to measure the energy of detected X-rays on CCDs. Thus the energy resolution of CCDs rely on the statistical fluctuation of the number of electron-hole pairs. Although electric noise of pre-amplifier read-out circuit also affect the energy resolution, the effect is generally much smaller than that of statistical fluctuation of electron-hole pairs. Thermal noise is also negligible because CCDs are kept to be sufficiently low temperature. Then, the energy resolution can be as following,

$$\Delta E(FWHM) = 2.35 \times \sqrt{F \times \frac{E}{W}} \quad [eV] \tag{3.1}$$

Here, F is Fano factor, which is 0.315 for crystalline silicon, E is the energy of the incident X-ray photon, and W is the mean ionization energy of silicon. Figure

3.23−3.26 shows the energy resolution of each CCD camera of four satellites. As seen in figure 3.25a, the energy resolution of XMM-Newton EPIC MOS is getting worse by ∼13 % since its launch because the CTI (Charge Transfer Inefficiency) increases due to the radiation damage. This is inevitable issue for CCD detectors, and then it is suspected for Suzaku XIS to follow the same path as EPIC MOS.

The BI chip of Chandra ACIS exhibits poorer resolution than those of FI chip in pre-launch phase. The FI chips have strongly suffered the radiation damage, leaving the ACIS detectors on the optical axis of the HRMA during a month after the launch. As a result, the energy resolution of FI chips gets worse and becomes a function of the raw number; near pre-launch values is close to that of the frame store region and it is substantially degraded in the farthest row. This is shown in figure 3.27. Meanwhile, the BI CCDs are not impacted for that the electrodes are somewhat apart from the focal plane of HRMA.

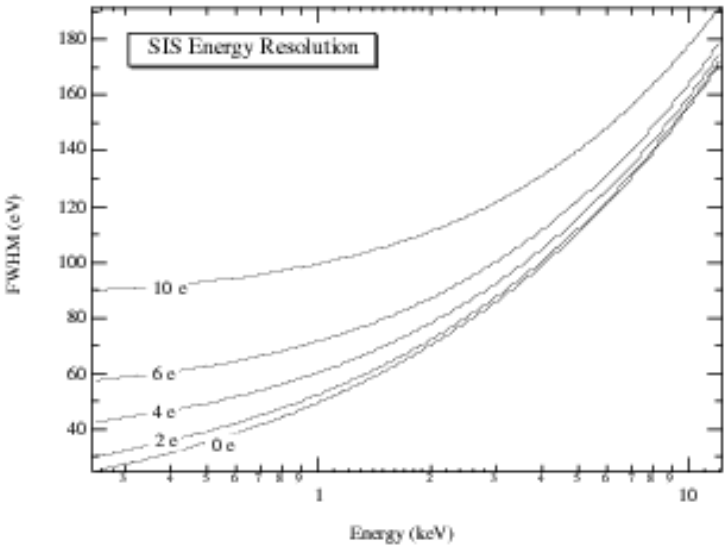

Figure 3.23: The energy resolution of ASCA SIS as a function of incident energy, plotted for different read-out noise noted by the equivalent number of electrons.

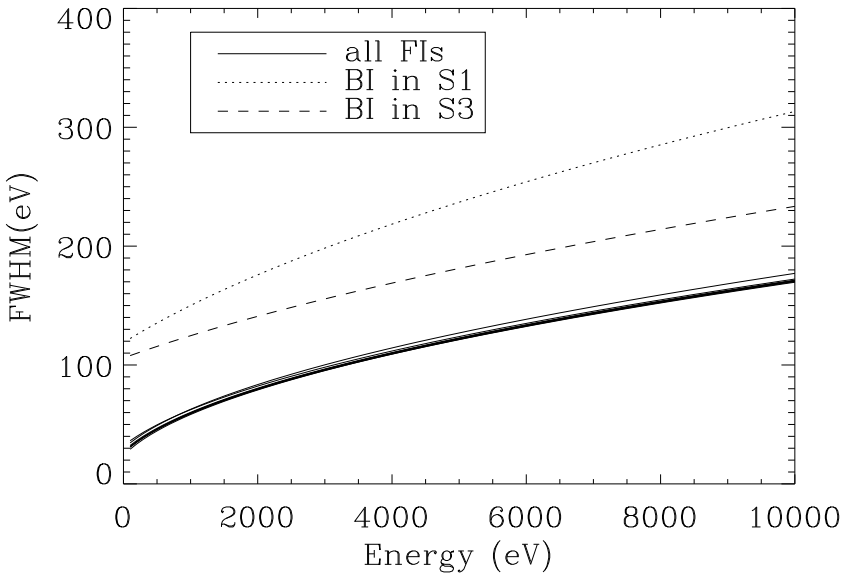

Figure 3.24: The energy resolution of Chandra ACIS as a function of incident energy.

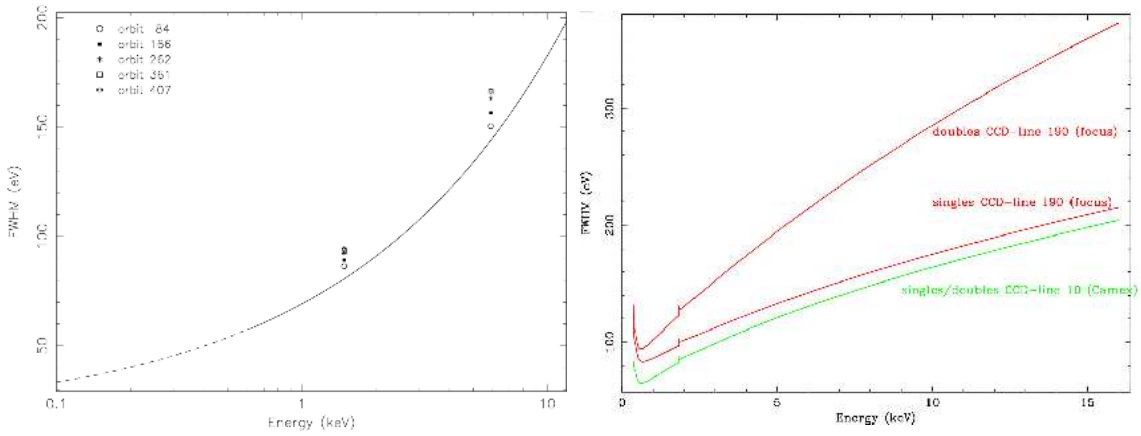

Figure 3.25: The energy resolution of XMM-Newton EPIC MOS (left) and pn (light). The dots in MOS energy resolution are measured in orbit.

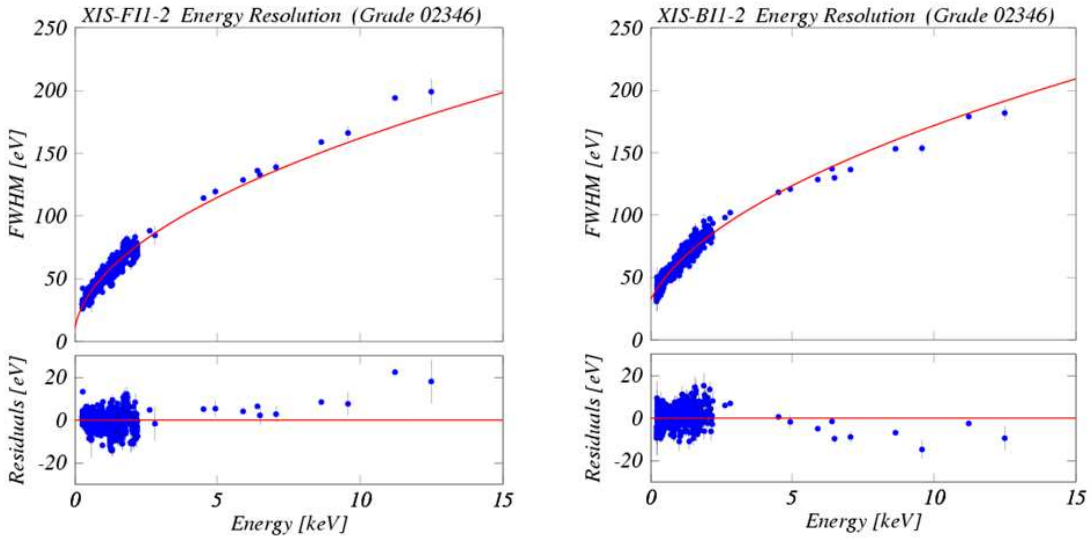

Figure 3.26: The energy resolution of Suzaku XIS FI chip (left) and BI chip (right) as a function of incident energy. The dots are measured in orbit.

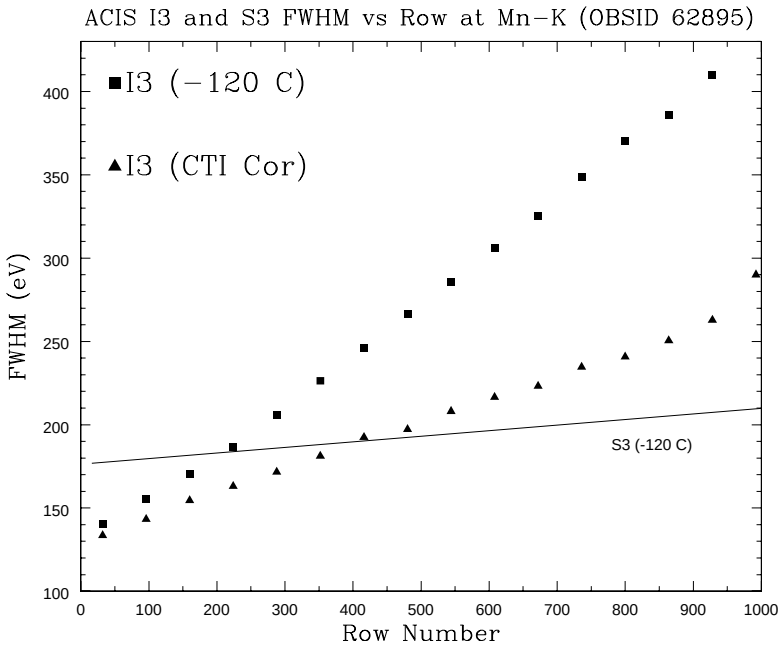

Figure 3.27: The correlation between the energy resolution at Mn-K line and row number for ACIS-I3 (FI) chip.

In addition to the energy profile, we mention the emission line profile, especially tail structure in lower energy of the lines. The low energy X-ray photons are photoelectrically absorbed near the surface of the depletion layer and electron clouds is generated. Such electron clouds cause the tail structure of detected emission lines. In the FI chips, electron clouds are absorbed in the boundary between depletion layer and electrodes and can not be detected, while in the BI chips, the attainability of electrons to the electrodes become lower due to farness from it.

Figure 3.28 shows the oxygen line profile (0.7 keV) of XMM-Newton EPIC MOS/pn, and Suzaku XIS-023/XIS-1. XMM-Newton EPIC has large tails and these are known also in Chandra ACIS. The tail consists of two component; the bellied portion just below the line which depends on the electron collecting efficiency, and constant portion caused by electron absorption in the boundary between non-sensitive layer and depletion layer. Compared with them, the contribution of the tail in Suzaku XIS is much smaller, indicating that Suzaku XIS is available to the analysis using emission line such as metal abundances.

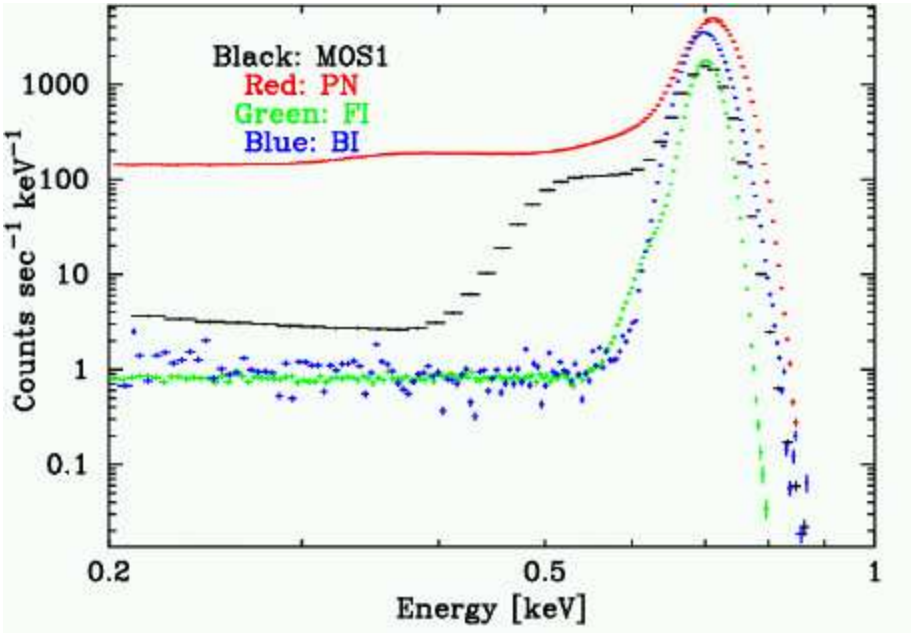

Figure 3.28: The spectral line of Oxygen at 0.7 keV. XMM-Newton EPIC MOS (black) / pn (red) and Suzaku XIS FI (green) / BI (blue).

3.3.2 Event Grades

An X-ray photon can create signals in multiple pixels on a CCD chip due to charge splitting while cosmic rays and pileup events also emerge as multiple-pixel events. Therefore, the proper pixel patterns should be selected to collect the true X-ray events. To do this, hit pattern of each detected event is divided into plural grades in according to the event quality. Adequate grade selection is really meaningful in the sense that it enables us to reduce the background events and improve the signal-to-background ratio.

ASCA and Suzaku utilize the same event grade technique in which X-ray events are assigned in eight grades judged from 3×3 pixels (a pixel showing the highest pulse-height and surrounding 8 pixels). Chandra's grade also use 3×3 pixels but possesses 256 grades. The event corresponding to grades 0, 2, 3, 4, 6 of ASCA's grade is treated as true X-ray event in all of these instruments. The relationship of Chandra event grade to those of ASCA/Suzaku is listed in table 3.10.

On the other hand, XMM-Newton EPIC MOS determine the event grades by means of 5×5 pixels and it is divided into 31 patterns (figure 3.29). Most events with grade 0-25 (more conservatively grade 0-12) are considered to come from real X-rays for MOS. Grade 26-31 are not expected from genuine X-rays, but from Si-fluorescence, pileups (especially for 26-29), or cosmic rays (especially for 30 and 31). Figure 3.30 shows 13 valid patterns for the pn camera without the event pattern created by single X-ray.

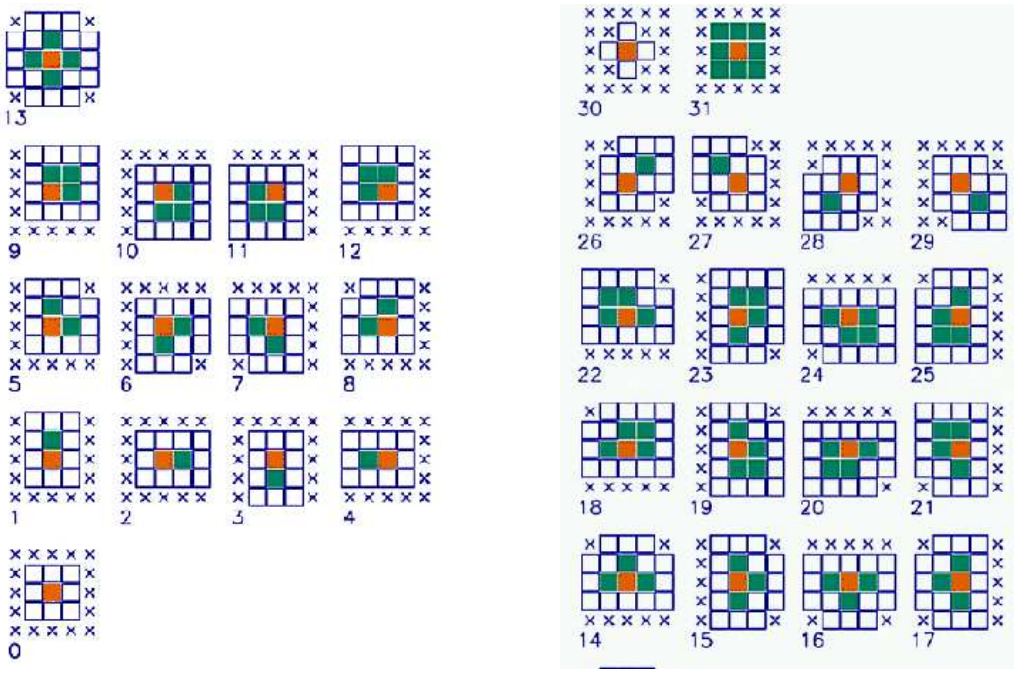

Figure 3.29: The event grade patterns of XMM-Newton EPIC MOS.

Table 3.10: The relationship of ACIS grade to ASCA/Suzaku grade

ACIS Grades	ASCA/Suzaku Grades	Description
0	0	single pixel events
64 65 68 69	2	vertical split up
2 34 130 162	2	vertical split down
16 17 48 49	4/3	horizontal split right
8 12 136 140	3/4	horizontal split left
72 76 104 108	6	"L" & quad, upper left
10 11 138 139	6	"L" & quad, down left
18 22 50 54	6	"L" & quad, down right
80 81 208 209	6	"L" & quad, up right
1 4 5 32 128	1	diagonal split
33 36 37 129		
132 133 160 161		
164 165		
3 6 9 20 40		"L" -shaped split with corners
96 144 192 13 21		
35 38 44 52 53		
97 100 101 131		
134 137 141 145		
163 166 168 172		
176 177 193 196		
197		
24	7	3-pixel horizontal split
66		3-pixel vertical split
255		all pixels
all others		

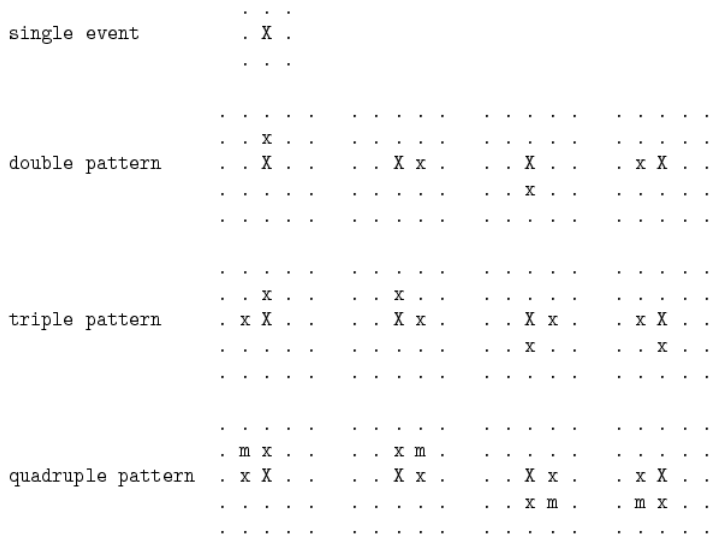

Figure 3.30: The event grade patterns of XMM-Newton EPIC pn.

3.3.3 Background

The background of X-ray observation is categorized into cosmic X-ray background (CXB) and instrumental non X-ray background (NXB) in general. The CXB consists of extra-Galactic X-ray background seen uniformly over the whole sky and local diffuse X-ray background. The former have been found to be a superposition of unresolved faint X-ray source (e.g. distant AGN). The latter is mainly thermal emission from hot plasma with temperature of 0.15−1 keV associated with our Galaxy or localized around the solar system. The CXB is rather uniform with directional variations up to ∼30 % below ∼2 keV and up to ∼5 % above that.

The NXB consists of instrumental detector noise, which is dominant in low energies below ∼200 eV, and particle background. When high energy particles such as $>$ 100 MeV interact with the detectors and surrounding structure, background with a flat continuum and fluorescence lines are created. The effect is more serious and unpredictable to the observatory having highly eccentric orbit and consequently spending most of time outside the Earth's magnetosphere like Chandra and XMM-Newton. In fact, the periods called "flaring" is observed with their instruments, where the background level is sporadically enhanced by an order of magnitude (figure 3.31). Now it is thought to be due to soft protons below 1 MeV and such soft protons cannot penetrate the Earth's magnetosphere. ASCA and Suzaku have a near-Earth orbit inside the magnetosphere and then did not experience flaring effect.

Figure 3.32 shows the NXB spectra, in which the data during flare is excluded for Chandra and XMM-Newton. The NXB is measured from observation with closed filter for Chandra and XMM-Newton and night Earth observation for ASCA and Suzaku. Each spectrum has the instrumental line from several elements (O, Si, Al, Ni, Au, etc.) and the background level reflect the effects of particles as mentioned above. The unfolded spectra of total background obtained from the blank sky is shown in figure 3.33. The CXB (green line) is significant below 2 keV and the NXB

is dominant above that in the instruments without ASCA SIS and Suzaku FI chip. Thus, ASCA SIS and Suzaku FI cameras have achieved low background and high signal-to-background ratio even above 5 keV.

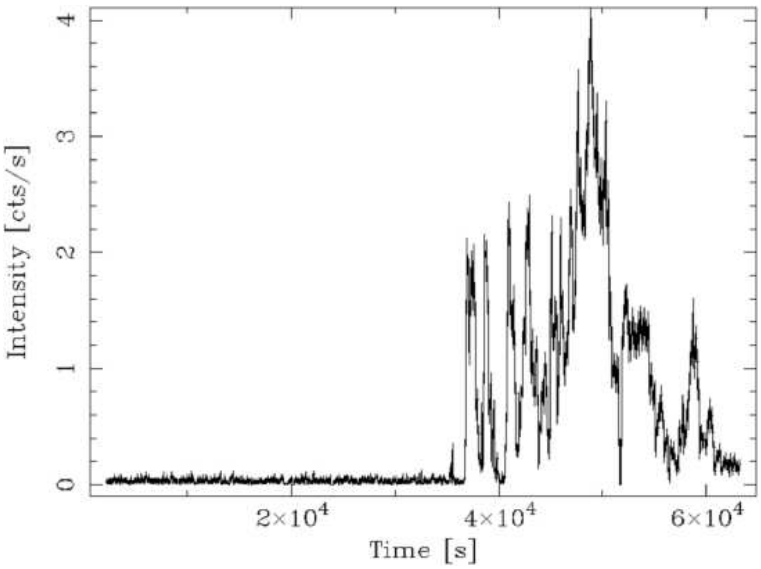

Figure 3.31: The sporadic increase of the EPIC background count rate affected by soft protons called ″background flares″.

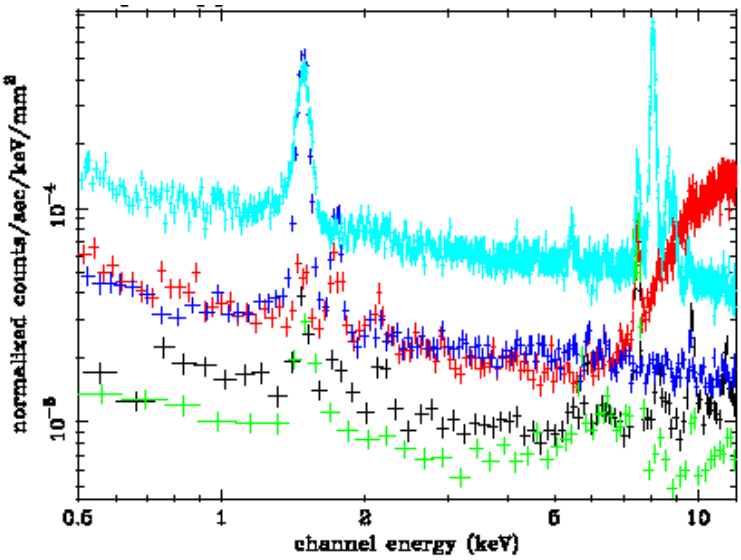

Figure 3.32: The NXB spectra of ASCA SIS (green), Newton MOS (blue), Newton pn (light blue), and Suzaku XIS (FI:black, BI:red).

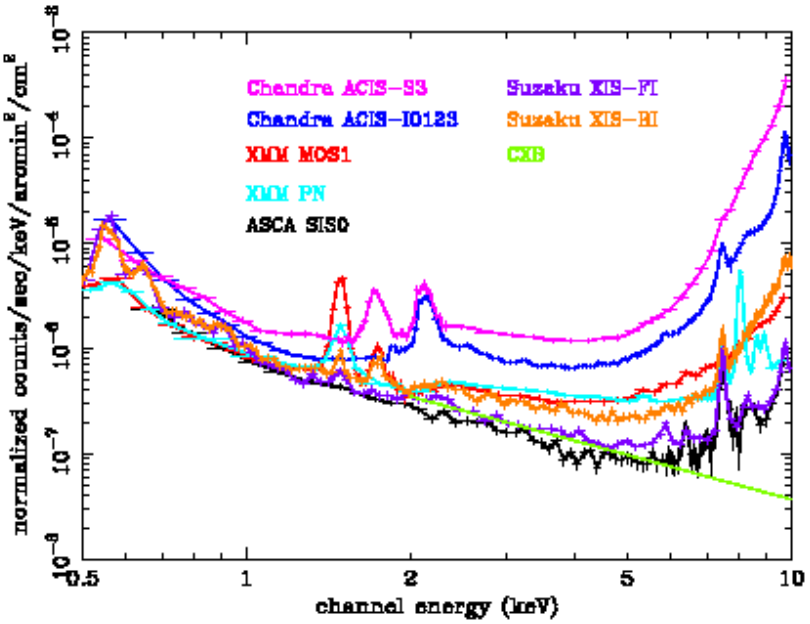

Figure 3.33: The total background of ASCA SIS (black), Chandra ACIS S3(magenda)/I0123(blue), XMM-Newton EPIC MOS(red)/pn(light blue), and Suzaku XIS FI(purple)/BI(orange).

3.4 ASCA GIS

3.4.1 Overview

The GIS is the imaging gas scintillation proportional counter (Makishima et al. 1996; Ohashi et al. 1996). The application of the gas scintillation technique to the Japanese X-ray satellite is the second attempt after the successful operation of the SPC on board Temma (Tanaka et al. 1984; Koyama et al. 1984). The GIS consists of two detector assemblies, namely GIS2 and GIS3. They are coupled to two of four XRTs, and measure the pulse-height and positions of incoming X-rays. The feature of GIS is large field of view, finer timing resolution, and high quantum efficiency (QE) in higher energy band. Therefore, the GIS plays a complementary role to SIS.

A schematic view of the GIS is shown in figure 3.34. X-ray entering through the GIS window, whose electric potential is held at -6000 V, are absorbed in the drift region. Via photo-ionization, primary electrons are generated and slowly drifts to the intermediate mesh of -5300 V. Then the cloud is accelerated due to the strong field toward the ground mesh which is placed in front of the quartz window. In this process, the electrons excite Xe producing a large number of UV photons of $\sim$170 nm wavelength. The distribution and the intensity of these UV flux are measured by the imaging photo-multiplier tube after the passage of quarts window. The UV flux is proportional to the X-ray energy with accuracy of several %, and then we can determine the energy of incident X-ray photons. This is the detection principle of the GIS. Basic parameters and performance are summarized on table 3.11 and §3.4.2.

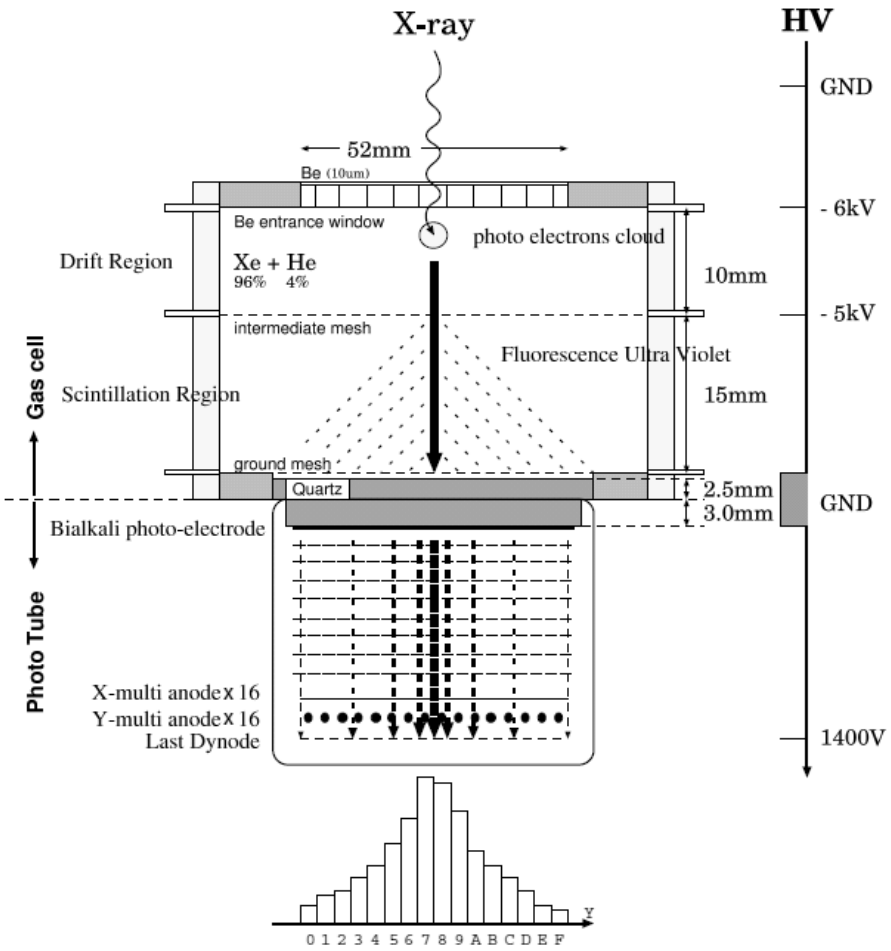

Figure 3.34: The schematic view of ASCA GIS sensor system.

Table 3.11: Basic features of GIS

Entrance Window (thickness)	Beryllium (10μm)
Absorption Material	Xe (96%) + He (4%), 10 mm depth, 1.2 atm at 0°C
Positional Resolution	100 nm
Effective area	50 mm diameter
Positional resolution	0.5 mm
Energy band	0.7−15 keV
Energy resolution	8 % (@ 5.9 keV)

3.4.2 Performances

Here, we introduce some fundamental performance of GIS. Figure 3.35 and 3.36 show the effective area and energy resolution of GIS. The GIS has larger effective area above ∼5 keV, while that of SIS is surpassing below ∼2 keV. The energy resolution is ∼8 % at 5.9 keV and is worse by a few factor than that of SIS on the whole

(figure 3.23). This is because the higher energy of ∼30 eV is necessary to ionize the absorption gas filled in gas cell compared to 3.65 eV of SIS's silicon.

The instrumental background and total background which contains CXB are shown in figure 3.37. Intrinsic Cu-K (8.0 keV), Sn-L (3.4 keV), Xe-L (4.1 keV), Mg-K (1.25 keV), and Al-K (1.49 keV) are seen. When compared with SIS (figure 3.33), GIS shows quite low background equally to that of SIS. What is more, the background of GIS is estimated very well, up to an accuracy of ∼2 % against ∼10 % of SIS.

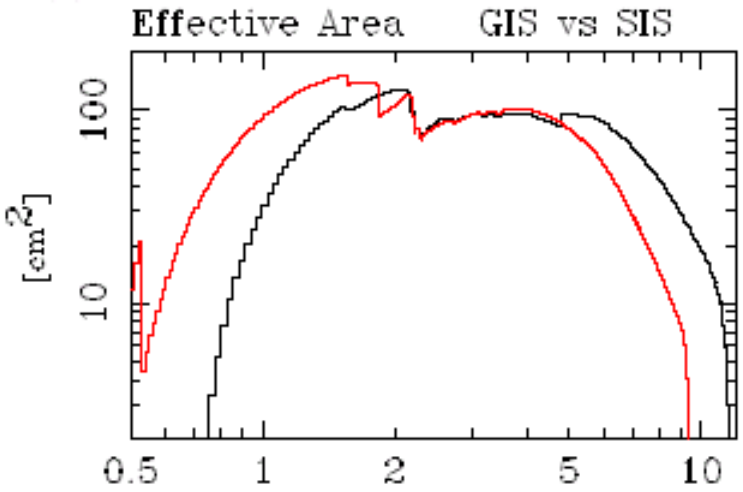

Figure 3.35: The effective area of ASCA GIS (black) and SIS (ref).

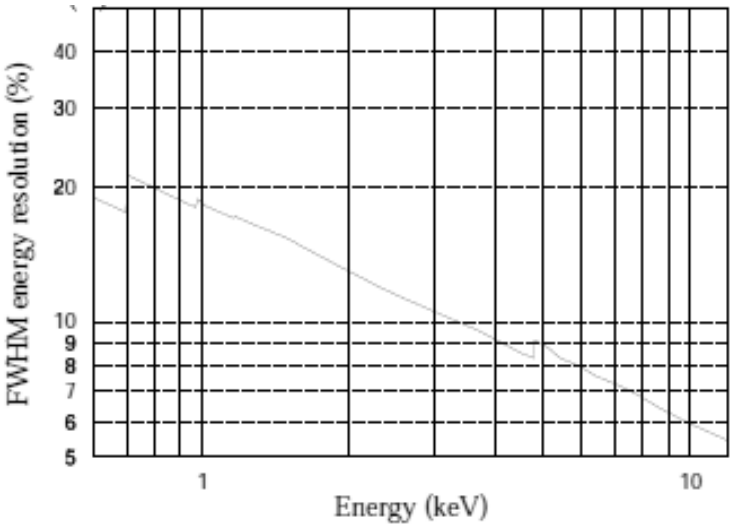

Figure 3.36: The energy resolution of ASCA GIS as a function of energy.

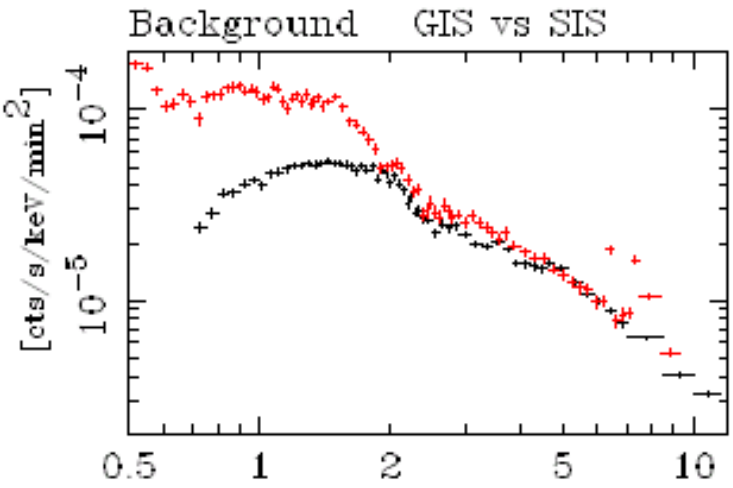

Figure 3.37: The background spectra of ASCA GIS (black) and SIS (gray).

3.5 Suzaku HXD

3.5.1 Overview

The Hard X-ray Detector (HXD) is a non-imaging, collimated hard X-ray instrument sensitive in wide energies of 10−600 keV. As shown in figure 3.38, the HXD consists 16 main detectors called "Well" unit arranged in a 4×4 array, surrounded by 20 thick crystal scintillators for active shield. Each main detector (the bottom panel of figure 3.38) has two types of detector which are four 2 mm-thick silicon PIN diodes inside BGO shield and GSO (Gd_2SiO_5 : Ce 0.5 %) / BGO ($Bi_4Ge_3O_{12}$) phoswitch scintillation counter. The PIN diodes are mainly account for softer X-ray photons below ∼40 keV, while the GSOs are account for harder photons penetrating the diodes.

The most remarkable feature of HXD is its low background. Accomplishing this, the HXD fully employs ingenious techniques to reduce background, as follows. First, the charged particles, cosmic diffuse γ-rays, and X-rays outside the field of view is rejected by active shield of 20 thick BGO counters which surrounds Well units and have high stopping power for γ-rays. Secondly, the the GSO have a faster scintillation time constant than that of BGO. This enables the background to be suppressed again by using the technique of pulse-shape discrimination and anti-coincidence. Anti-coincidence among units arranged in the form of 6×6 matrix is also important facility. Furthermore, a tight collimation by Well-shaped active BGO shield and fine collimator (FC) which is made up of phosphorous bronze, limits the field of view to 4.5×4.5° for GSO and $34' \times 34'$ for PIN in order to diminish the contamination of X-rays having a large incident angle. Detector materials is, of course, selected by emphasis on low radioactive contamination and expected low activation background. Flexible event selection both onboard and at ground is also vital.

Figure 3.39 shows the sensitivity of various instruments in hard X-ray and soft γ-ray band. Due to the low background by novel contrivances above, the HXD

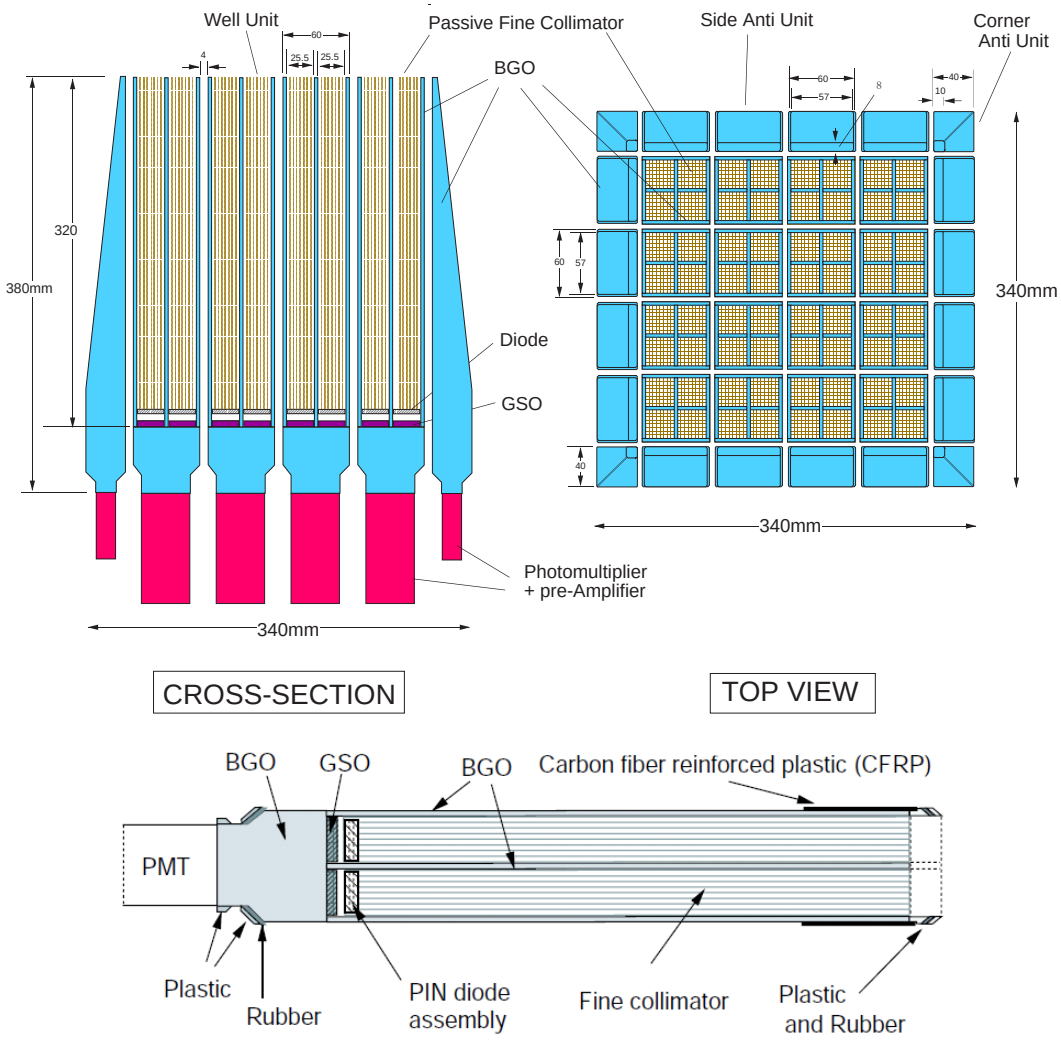

Figure 3.38: The schematic view of Suzaku HXD. Top panel shows side view (left) and top view (right). Bottom panel shows a cross sectional view of single Well unit.

have achieved the highest sensitivity, especially in ∼20−50 keV range. This is great advantage to detect the weak emission such as non-thermal emission from clusters of galaxies. Then, only the data of PIN diodes are analyzed in this study. The details of the PIN detector are described in the next section.

Table 3.12: Basic features of HXD

	PIN	GSO
Field of view	34×34 arcmin	4.5×4.5 degree
Energy band	10−60 keV	30−600 keV
Energy resolution	3 keV	$7.6/\sqrt{E_{MeV}}$ %
Effective area	160 cm^2 (@ 20 keV)	260 cm^2 (@ 100 keV)
Time resolution	61μm	61μm

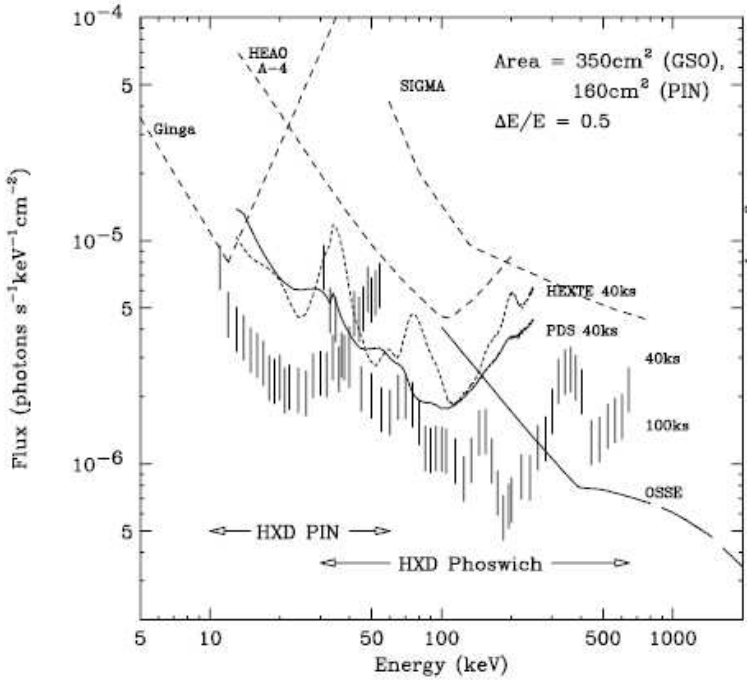

Figure 3.39: The sensitivity of Suzaku HXD compared with other instruments.

3.5.2 PIN Silicon Solid-State Detector

Figure 3.40 shows the schematic view and picture of PIN detector. Each PIN sensor is made up of 2 mm-thick silicon diode, whose thickness enables to detect hard X-ray photons of 10-50 keV, and arranged in the ceramic package of tetron-epoxy. The size of the exposure area is ∼15.5 mm square. The 8×8 matrix configuration of PIN secures larger effective area as shown in figure 3.41. The energy resolution of ∼3 keV at 40 keV have been achieved in orbit. As described above, the FC in front of each PIN sensor has important role of reducing the confusion of background. Figure 3.42 shows the pre-launch background of PIN. The background of PIN is effectively suppressed by the technique of anti-coincident or valid event selection and roughly same level as that in orbit.

The alignment of FC-PIN is also important in order not to loss the effective area. To measure the optical axis of each FC-PIN, we performed 17 pointing observation of Crab nebula. As shown in figure 3.43, the average alignment angle has rather large offset of ∼4′ from that of XIS in the X-axis although the dispersion of optical axes between 64 FC-PIN falls within ∼7% in peak-to-peak and ∼3.1% in RMS (root mean square). Therefore, Suzaku sets up two kinds of optical axes; (0,0) for XIS namely XIS nominal and (+3.5,0) for HXD namely HXD nominal. The observer can select the pointing mode suitable for the desired target. The loss of detection efficiency is suppressed to only a few % even when observed on XIS nominal.

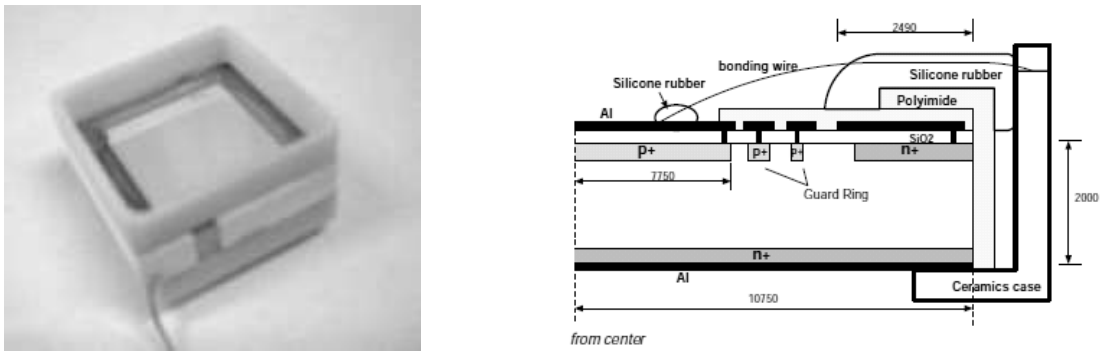

Figure 3.40: The photograph (right) and schematic view (right) of HXD PIN detector.

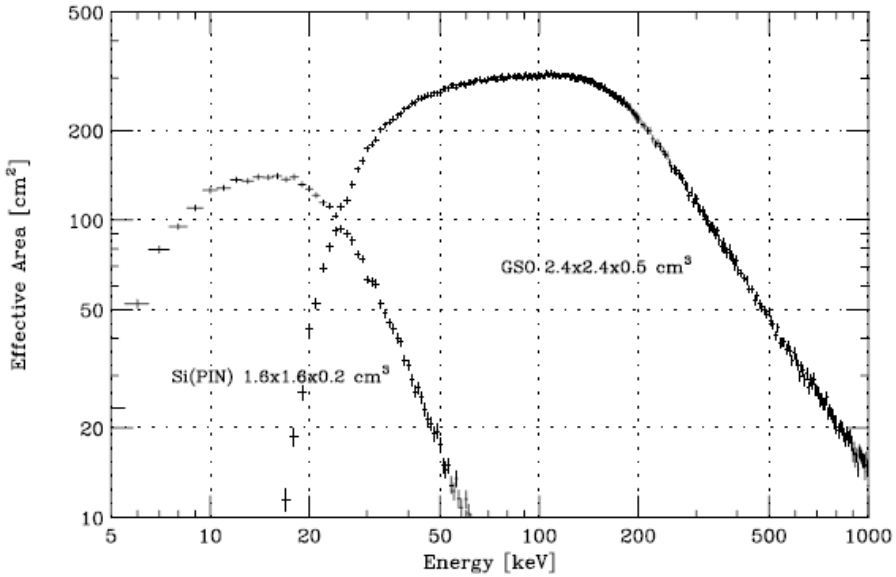

Figure 3.41: The effective area of HXD PIN/GSO.

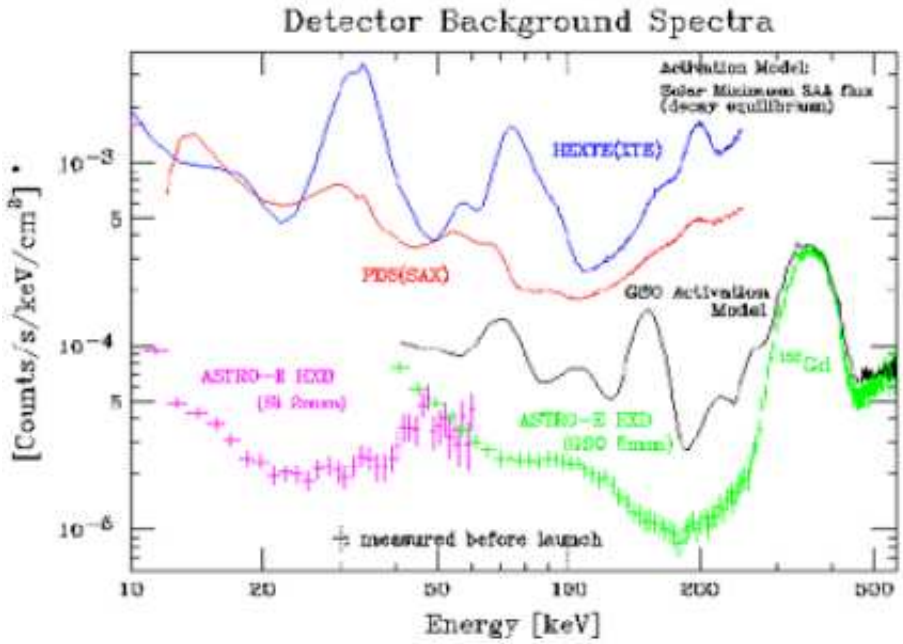

Figure 3.42: The pre-launch background of HXD PIN.

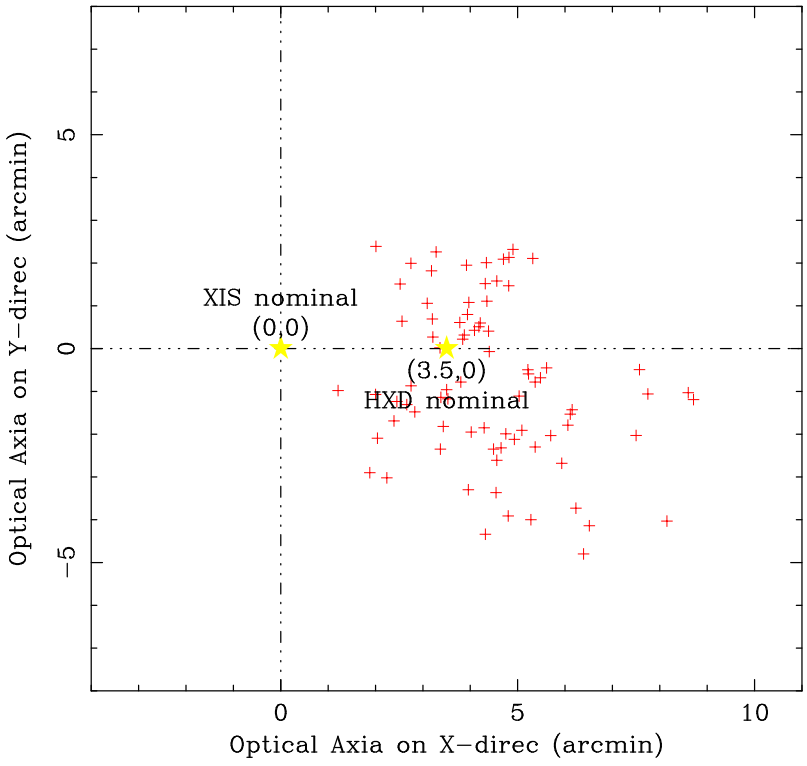

Figure 3.43: The optical axis distribution of each PIN.

Chapter 4

OBSERVATIONS AND DATA REDUCTIONS

4.1 Target Selection

4.1.1 Selection Criteria

In this thesis, there are two subjects to discuss the heating and particle acceleration in clusters of galaxies. One is the heating mechanism of the thermal plasma in the central region of the cooling flow clusters (§2.2.7). The other is the search for the non-thermal hard excess emission from clusters of galaxies. Then, the targets are individually selected according to each purpose.

The targets for the plasma heating are selected from the archival data of Chandra because it is possible to investigate the thermal structure of plasma in detail thanks to Chandra's high spatial resolution. The selection criteria is as follows.

- The clusters which are recognized as the cooling flow cluster in the previous observations.
- The redshift should be $z \sim 0.01 - 0.1$, in order to cover the central cool region ($\sim$ 100 kpc), and resolve the spatial scales of $\sim$5 kpc.
- The X-ray brightness is higher than 1.0×10^{42}erg s^{-1} and the exposure time is longer than 20 ks in order to spatially resolved spectroscopy with sufficient photon statistics.
- The clusters which have various ICM temperatures (1$-$10 keV) because of the understanding the temperature dependency of the thermal properties.
- The clusters which is observed with BI (ACIS-S3) chip due to high efficiency for the cooler plasma.

By applying these criteria, we finally selected 18 clusters and 4 groups of galaxies. We include Abell 1835 and NGC 5044 in our analysis although their redshifts are out of range against the above limitation. Abell 1835 shows strong cooling flow

features and has a high ICM temperature which is precious because the higher temperature clusters are lacking in our targets. NGC 5044 is one of the brightest galaxy groups which is studied well in the previous observations and shows cooling flow sign although it is rather weak. The basic properties of these sample clusters are summarized in table 4.1.

For the non-thermal study, Suzaku data is necessary. In order to effectively detect the non-thermal emission, it is desired that the ICM have a moderate temperature. Then, we investigate how contributes the flux of the various ICM temperature to the non-thermal one. Figure 4.1 shows simulated spectra of the thermal and non-thermal emission when observed with the HXD PIN detector. The thermal component is represented by the MEKAL model with abundance 0.3 solar and the typical cluster flux of 1.0×10^{-10}erg s^{-1} cm^{-2} in the 2−10 keV band. The non-thermal emission is assumed to have a powerlaw spectrum with photon index of $\Gamma = 2$, and have a flux of 10% and 20% of the thermal one (i.e. 1.0×10^{-11}erg s^{-1} cm^{-2} and 2.0×10^{-11}erg s^{-1} cm^{-2}). When the non-thermal flux is 10% of the thermal flux, we enable to observe the non-thermal emission above ∼15 keV for the 3 keV plasma emission while this lower limit is increased up to ∼30 keV for the 7 keV plasma. As the ICM temperature becomes higher and higher, it is more difficult to distinguish the non-thermal emission from the thermal one of the ICM. Thus, the detection of the non-thermal emission is largely depending on the ICM temperature.

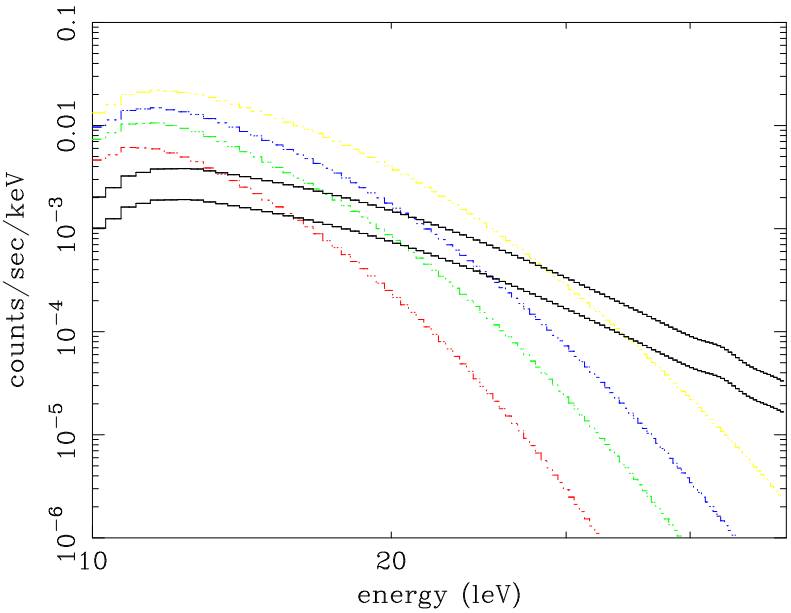

Figure 4.1: The simulated spectra of the thermal and non-thermal emission with HXD PIN. The thermal components are assumed to have the ICM temperature of 3 (red), 4 (green), 5 (blue), and 7 (yellow) keV. The fluxes are fixed to 1.0×10^{-10}erg s^{-1} cm^{-2}. The non-thermal fluxes are 10% and 20% of the thermal component (black).

Up to now, Suzaku has observed 12 clusters of galaxies. Of these clusters, we select the targets which satisfy the limitation of the ICM temperature explained above and other conditions as follows.

- The ICM properties, such as the ICM temperature, metal abundance, and X-ray flux, are relatively well known from the previous observations.
- The ICM temperature is lower than 4 keV in order to observe the non-thermal emission in 10−30 keV band where the PIN has a maximum sensitivity.
- The AGN or X-ray bright point sources are not contained.

As a result, we selected three galaxy clusters. The basic properties are shown in the table 4.2. Of all them, Abell 3376 is only the target which shows on-going merging and the sign of excess hard emission with BeppoSAX. All clusters were observed with multi-pointings centered on the cluster center and offset region. This gives us the information about the spatial distribution of the non-thermal emission.

Table 4.1: Basic properties of the targets for thermal emission study.

name	redshift	kT^a (keV)	$L_{\rm X}^b$ (erg s^{-1})	$\dot{M}$ ($M_\odot$ yr^{-1})	references
Ophiuchus	0.0280	11.99±0.34	6.0×10^{45}	159	1,2
Able 478	0.0777	7.56±0.32	4.2×10^{45}	990	1,2
Abell 2029	0.0881	7.45±0.19	3.5×10^{45}	499	1,2
Abell 1835	0.2532	7.11±0.59	6.8×10^{45}	1106	1,5
Perseus	0.0179	6.36±0.11	3.6×10^{45}	208	1,2
Abell 1795	0.0631	5.76±0.25	6.8×10^{45}	523	1,2
Abell 3558	0.0480	5.26±0.16	1.2×10^{45}	25	1,6
Abell 3112	0.0750	4.45±0.15	1.0×10^{45}	565	1,2
Abell 496	0.0329	4.09±0.07	5.4×10^{44}	136	1,2
Abell 2199	0.0302	4.07±0.07	6.1×10^{44}	208	1,2
Abell 4059	0.0475	3.96±0.12	4.6×10^{44}	173	1,2
Centaurus	0.0114	3.64±0.06	2.8×10^{44}	25	1,2
Hydra A	0.0538	3.58±0.14	7.6×10^{44}	489	1,2
2A0335+096	0.0349	3.12±0.07	6.2×10^{44}	181	1,2
Abell 2052	0.0350	2.98±0.07	3.1×10^{44}	114	1,2
Sérsic159-03	0.0580	∼2.69	3.2×10^{43}	230	8,9
Abell 262	0.0163	2.13±0.05	8.5×10^{43}	62	1,2
MKW 4	0.0200	1.61±0.04	3.1×10^{43}	20	1,3
NGC 533	0.0174	1.33±0.10	6.3×10^{42}	–	1
NGC 507	0.0190	1.21±0.03	2.6×10^{43}	40	1,4
HCG 62	0.0137	1.07±0.03	6.4×10^{42}	–	1,7
NGC 5044	0.0082	1.01±0.01	1.6×10^{43}	25	1,7

a: the ICM temperature, b: X-ray brightness in the 0.5−10 keV band,
c: cooling flow rate.
1: Fukazawa et al. (2004); 2: Edge et al. (1992); 3: Canizares et al. 1983 (Einstein); 4: Kim and Fabbiano 1995 (ROSAT); 5: Allen et al. (1996); 6: Bardelli et al. 1996 (ROSAT); 7: Mulchaey et al. 1996 (ROSAT); 8: Allen & Fabian 1997 (ROSAT); 9: Kaastra et al. (2001).

Table 4.2: Basic properties of the targets for non-thermal emission study.

name	redshift	$N_{\rm H}^{a}$ (10^{-20}cm^{-2})	kT^{b} (keV)	$A_{\rm Fe}^{c}$ (solar)	$F_{\rm X}^{d}$ (erg s^{-1} cm^{-2})
Abell 3376	0.0460	4.74	3.98±0.19	0.24±0.08	2.5×10^{-11}
Abell 1060	0.0114	4.98	3.03±0.07	0.40±0.06	7.6×10^{-11}
Centaurus	0.0114	8.12	3.64±0.06	0.44±0.05	1.6×10^{-10}

a: the column density, b: the ICM temperature,
c: metal abundance, d: X-ray flux in the 0.5−10 keV band.
All the parameters are observed with ASCA (Fukazawa et al. 2004).

4.1.2 Observations

We obtained the archival data for the cooling flow targets from the Chandra X-ray Center (CXC, http://chandra.harvard.edu/), and the data of the performance verification observations for the non-thermal emission targets from the Science Working Group of Suzaku. The observation logs are summarized in the table 4.3 and table 4.4. For more precise discussion and consistency verification on the spatial distribution of the non-thermal emission, we utilized the data obtained with other instruments. Then, the logs of these observations are also shown in the table 4.4.

We also give an introduction for the observations of three clusters which observed with Suzaku because they have offset pointing. Figure 4.2 shows the X-ray image obtained with XMM-Newton for Abell 3376, and with GIS for Centaurus cluster and Abell 1060. The HXD's field of view and the spectral integrated area with XIS are superposed together. Centaurus cluster have observed three times at the center, $8'$ offset region in the direction of north, and south. Abell 1060 was observed in two pointing of its center and $10'$ east area from the center. For Abell 3376, two pointing observation have performed since it have two radio relics at the east and west end of the thermal X-ray emission. One contain the cluster central region and east relic while the other observed the west relic region.

Table 4.3: Observation logs of the targets for thermal emission study (Chandra).

target	ID	position (α, δ J2000)	date (yy/mm/dd)	exposure time (sec)
2A0335+096	919	03:38:40.5,+09:58:11.6	2000/09/06	19728
Abell 2199	498	16:28:38.5,+39:33:03.0	1999/12/11	18922
Abell 1795	494	13:48:52.7,+26:35:27.0	1999/12/20	19522
Abell 2052	890	15:16:44.4,+07:01:20.0	2000/09/03	36754
Abell 262	2215	01:52:46.5,+36:09:07.9	2001/08/03	28744
Abell 2029	891	15:10:56.1,+05:44:38.0	2000/04/12	19813
Abel 478	1669	04:13:25.4,+10:27:57.1	2001/01/27	42397
Hydra A	576	09:18:05.7,-12:05:45.0	2000/06/06	19526
Centaurus	504	12:48:48.7,-41:18:44.0	2000/05/22	31715
HCG 62	921	12:53:05.7,-09:12:20.0	2000/01/25	48530
NGC 507	317	01:23:39.0,+33:15:24.0	2000/10/11	18422
Abell 1835	495	14:01:02.0,+02:52:40.0	1999/12/11	19522
Ophiuchus	3200	17:12:27.8,-23:22:11.5	2002/10/21	50532
Perseus	1513	03:19:48.5,+41:30:27.0	2000/01/29	24738
Abell 3112	2516	03:17:57.7,-44:14:17.5	2001/09/15	16919
Abell 3558	1646	13:27:56.9,-31:29:43.9	2001/04/14	14419
Abell 496	931	04:33:37.8,-13:15:43.0	2001/08/07	18918
Abell 4059	897	23:57:00.0,-34:45:30.0	2000/09/24	22302
Sérsic159-03	1668	23:13:58.3,-42:43:35.0	2001/08/13	9949
MKW 4	3234	12:04:26.7,+01:53:43.3	2002/11/24	29961
NGC 5044	798	13:15:24.1,-16:23:06.0	2000/03/19	20463
NGC 533	2880	01 25 31.4,+01 45 32.8	2002/07/28	37604

Table 4.4: Observation logs of the targets for non-thermal emission study.

target	instrument	position (α, δ J2000)	date (yy/mm/dd)	exposure time[a] (sec)
Abell 3376	Center/East-Relic			
	Suzaku	06:02:15.000,-39:57:00.00	2005/10/06	120448/89983
	Chandra	06:02:18.056,-39:59:30.75	2002/03/16	44267
	ASCA	06:01:35.040,-39:56:09.60	1996/02/04	12224
Abell 3376	West-Relic			
	Suzaku	06:00:00.000,-40:01:58.80	2005/11/07	127240/102734
Abell 1060	Center			
	Suzaku	10:36:42.816,-27:31:41.88	2005/11/20	40466/41589
	Chandra	10:36:17.510,-27:34:09.56	2001/06/04	31898
	Newton	10:36:51.300,-27:34:09.56	2004/06/29	37598
	ASCA	10:36:26.400,-27:28:58.80	1993/06/29	17926
Abell 1060	Offset			
	Suzaku	10:38:03.840,-27:31:41.88	2005/11/22	55510/30319
Centaurus	Center			
	Suzaku	12:48:49.296,-41:18:39.96	2005/12/27	37836/27868
	Chandra	12:48:49.559,-41:20:01.42	2001/06/04	31898
	Newton	12:48:49.280,-41:18:40.00	2002/01/03	47122
	ASCA	12:48:21.600,-41:19:44.40	1995/07/19	53595
Centaurus	Offset1			
	Suzaku	12:48:49.296,-41:18:39.96	2005/12/28	45336/32162
Centaurus	Offset2			
	Suzaku	12:48:49.296,-41:10:40.80	2005/12/29	44051/30206

a: the exposure time of Suzaku is denoted as XIS/HXD in order.

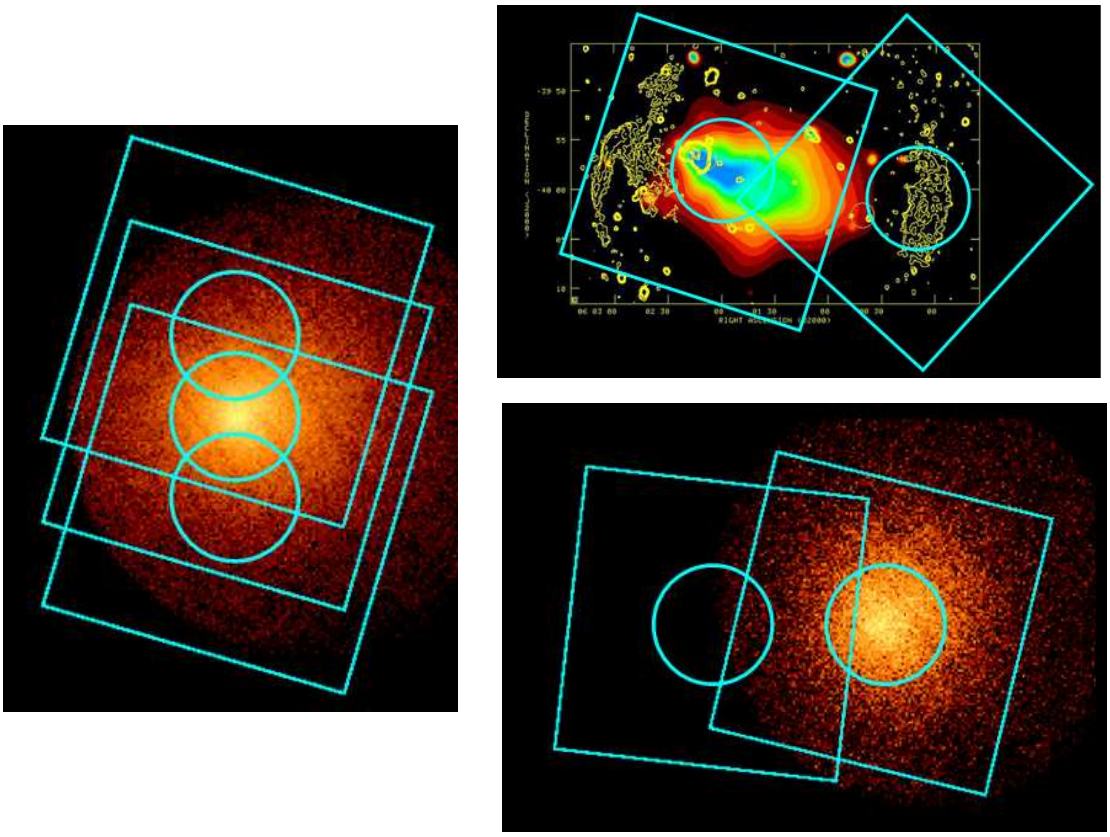

Figure 4.2: The HXD (square) and XIS (circle) field of view in the observation of Centaurus cluster (left), Abell 3376 (top right), and Abell 1060 (bottom right). Here, XIS FOV is limited to central 7' circle which corresponds to the spectral integrated area in spectral analysis. X-ray image are obtained with XMM-Newton for Abell 3376 and ASCA GIS for the others. Radio contour is also superposed on the image of Abell 3376.

4.2 Data Reduction

Before extracting the images and spectra, we have to screen the events in each of observational data which are usually available in the FITS format. For the Chandra data, we retrieved archival "Level 1" event (almost law data) files from the CXC. Then, we created "Level 2" event files, by filtering the events with "good time interval (GTI)", excluding the hot pixels and cosmic ray afterglows, applying the newest gain maps, and correcting the pulse heights for CTI (§3.3.1). The processing is performed with the software package Chandra Interactive Analysis of Observations (CIAO) version 2.3 and the calibration data base CALDB 2.21.

In the case of XMM-Newton, we retrieved publicly available Observation Data Files in the FITS format from the SOC, in which some quantities are not to be calibrated yet. Applying the newest calibration files by means of the Science Analysis Software package of version 5.3.3, the screened event files are created in a similar way to Chandra.

Occasionally, the observational data with Chandra and XMM-Newton contains the background flaring caused by the soft protons (§3.3.3). These time periods are not excluded even in the screened event files. Therefore, we extract the light curve from the screened event files, and discard the period when the count rate deviate by more than 3 σ from the average rate during no flare period.

The ASCA archival data are published by the center for PLAnning and INformation system at ISAS/JAXA on the web (http://www.darts.isas.ac.jp/). These files are already cleaned against the earth occultations, the high background orbital periods, and the passages through the South Atlantic Anormaly (SAA). Then, we discarded the periods the high count rate as described above.

In the case of Suzaku XIS, we retrieved the screened event files which are published only for the member of the Suzaku Science Working Group. The events are already screened in the same way as ASCA and the remaining bad events are again rejected by checking the light curve. For HXD data, the screened event files are available in a similar way as the XIS. However, we uniquely created the screened spectra and light curves for convenience from the second fits files (SFF), which are processed through the official event selections but have the energy channels and time regions corresponding to the background data we estimated (§5.5).

As well as the flaring in the Chandra or XMM-Newton, we must take care the removal of point sources. The thermal component exhibits the strong emission in the central region of galaxy clusters and is not suffered even if some point sources exist there. However, the situation may become different in the outer region where the thermal flux is diminished. Then, we estimate the flux of the point sources in each concentric annulus which we defined later (in §4.4.1) by means of the script *wavedetect* which is contained in the CIAO package. The total flux of the detected point sources have found to occupy only a few % of the thermal one at most although the contamination is rather higher by a factor of $\sim$2 for HCG 62. In this way, the effect of the point sources is found to be negligible, and hence we did nothing on the rejection of the point sources for the cooling flow clusters. On the other hand, the non-thermal emission is much weaker than the thermal emission. Utilizing

ROSAT PSPC point source catalog (2RXP catalog), and the X-ray images observed with XMM-Newton or Chandra, we model the spectra of the point sources for non-thermal target. The details on the point source such the flux or count rate is shown in §5.6.1.

4.3 Background

In order to estimate the background level and to subtract it from the on-source spectra or images, we applied the blank-sky data in data analysis with Chandra and XMM-Newton. For the extended targets, it is mightily recommended to use the blank-sky data rather than off-source region of the same field of view because it contains the positional dependency of the background. A set of the blank-sky data are complied by Markevitch (2001) for the Chandra data, and we can select an appropriate background file in each observation with the script *acis_bkgrnd_lookup* provided by CXC. Also in the XMM-Newton, the background templates are publicly released by the University of Birmingham group (Ponman 2003).

In the case of XIS, the background generator *xisntebgdgen* is available for the SWG members. The background of the XIS varies in the short time scale, mainly depending on the cutoff rigidity (COR) which indicates the shielding power against the incoming proton by the earth's magnetic field and defined as the electron momentum (in the unit of GeV/c), which can penetrate magnetic field on each position of the earth. In the framework of *xisntebgdgen*, the background files sorted by each cutoff rigidity are firstly generated from the night earth data base. Then, the background data are summed overall cutoff rigidity according to the frequency distribution of the cutoff rigidity calculated from the house keeping information of each on-source event file. By comparing the generated background with real night earth data, the accuracy of the XIS background generated in this way is reported to become $\sim$3$-$4% by the Suzaku XIS team. In order to confirm the background accuracy, we tried to compare the line intensity of Ni ($\sim$ 7.5 keV) and Au ($\sim$ 9.7 keV) between the background data and night earth data in the NEP observation because the continuum levels of NEP are unknown due to the CXB contribution. Although the level of generated background tends to be lower than that of the night earth data, the line intensity are consistent within 5% and this would be the systematic error of XIS background.

The background data of HXD are already created by the two method on the basis of the light curves during earth occultations, and are published only for the SWG members. Apart from these data, we estimated the background in our own way because it is most important to understood its properties well in the study of the non-thermal emission. The details about the HXD background estimation are described in §5.5.

4.4 Spectral Analysis

4.4.1 Derivation of Spectra

As the basic method to obtain the thermal properties of the ICM, the spectral parameters such as the ICM temperature or metal abundances are evaluated as a function of the radius from the cluster center. Then, we divided each cluster into 11 concentric annular region, centered on the X-ray emission peak which coincides with the position of the cD galaxy within a few arcsec. The annular regions are chosen as $0-10''$, $10-20''$, $30-40''$, $40-50''$, $50-60''$, $60-90''$, $90-120''$, $120-150''$, $150-180''$, and $180-240''$, so that each region has good photon statistics (more than 3000 photons) after the background subtraction. In the deprojection analysis (§4.4), we utilized the wider annuli of $0-15''$, $15-30''$, $30-45''$, $45-60''$, $60-90''$, $90-120''$, $120-150''$, $150-180''$, and $180-240''$ in order to avoid the enhancement of the data error. Figure 4.3 shows an example of the concentric annular region for projected and deprojected spectra analysis.

For the non-thermal analysis, other instruments are utilized in addition to Suzaku HXD. We can obtain the information about the spatial distribution of the non-thermal emission, taking advantage of the FOV size difference of each instrument. In practice, we extract the spectra with different accumulating region of 3, 7, 10, and 15 arcmin circles for Chandra ACIS-S, Suzaku XIS, XMM-Newton MOS1, and ASCA GIS, respectively.

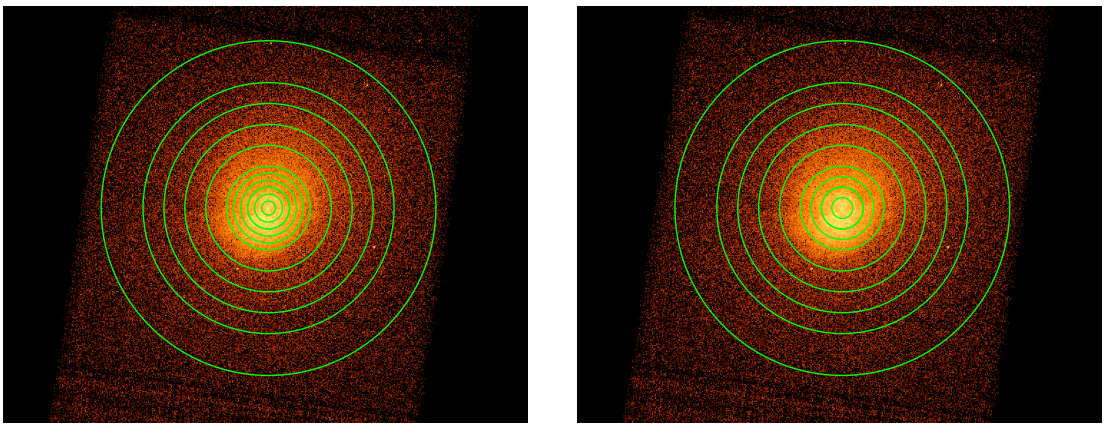

Figure 4.3: The integration region of the annular spectra for projected (left) and deprojected (right) analysis supposed on the X-ray image of Abell 2199.

4.4.2 Response Matrices

Observed Spectra are not identical to the real spectra from the object because it contains the instrumental responses which convert the incident X-ray energy E into the event pulse height P. Therefore, it is necessary to know the response matrix of the instrument own when we perform spectral fittings. Designating the incident

spectrum as $S(E)$, the observed spectrum $D(P)$ is represented as

$$D(P) = \int K(P;E)S(E)dE, \tag{4.1}$$

where $K(P;E)$ is a response matrix. If the instrument has an ideal energy response (i.e. $P = E$), the off diagonal elements would be zero. The pulse height P is expressed in terms of the pulse invariant (PI) which is appropriately corrected for the detector gains, depending on time, position on the detector, temperature, and so on. In X-ray spectral analysis, the detector response is usually decomposed into two components as

$$K(P;E) = R(P;E)A(E). \tag{4.2}$$

Here, $A(E)$ is an ancillary response file (ARF) which is the factor keeping the X-ray energy E in $K(P;E)$ unchanged. $R(P;E)$ is an energy redistribution matrix file (RMF), and is normalized as

$$\int R(P;E)dE = 1. \tag{4.3}$$

The merit to divide response into the two components is that the ARF must be calculated according to each spectral region because of its position dependent properties, while the RMF is calculated only once for an observation because of little position dependence.

To derive the real incident spectrum $S(E)$ from the observed spectra $D(P)$, "deconvolution" approach is a way, that is to correct $D(P)$ for the effects introduced by the response. However, the deconvolution method amplifies errors associated with $D(P)$ and makes it difficult to quantitatively estimate uncertainties in $S(E)$. Then, instead of that, an obtained spectra $D(P)$ is generally compared with the simulated data $\tilde{D}(P;a_i)$ in which detector response is convolved by the assumed model function $\tilde{S}(P;a_i)$ via equation 4.1. The model function contains both theoretical and empirical ones, and is described with a reasonable number of parameters $(a_i; i = 1, ..., N)$. The examination for agreement with $D(P)$ is performed thorough chi-square evaluation as

$$\chi^2 = \sum_{\mathrm{P}} \left[\frac{\tilde{D}(P;a_i) - D(P)}{\sigma(P)} \right]^2, \tag{4.4}$$

where $\sigma(P)$ is the statistical and systematic error associated with $D(P)$. By minimizing χ^2, best-fit parameters are determined. The 90 % confidence error for best-fit parameters is defined as the region of $\chi^2 < \chi^2_{min} + 2.71$, where χ^2_{min} is the minimum chi-square value. Thus, we can investigate the emission mechanism for incident X-ray spectrum.

4.4.3 Deprojection Method

The emission from the extended optically thin objects is always suffered by the projection effect. Then, we can measure only two-dimensional information integrated

along with line-of-sight. However, making some assumptions for three-dimensional ICM structures such as spherical symmetry, a three-dimensional emissivity profile is obtained without assuming any particular model. This technique is called deprojection analysis or the deconvolution method, and it has been applied to X-ray emission profiles of galaxy clusters. Since the recent new generation instruments enable us to get spectral and spatial information simultaneously, no additional assumption is necessary for obtaining the three-dimensional profiles of ICM temperature, density, and gravitational potential. We introduce the technique of Arabadjis, Bautz, and Garmire (2002) that we follow in this thesis.

We here formulate this deprojection method more quantitatively. When extracting spectra of N concentric shells from three-dimensional cluster, a detector image is correspondingly divided into N annuli as shown in figure 4.4. The contribution of i-th shell between the three-dimensional radii of r_{i-1} and r_i to an annular region on the detector between two-dimensional radii of b_{i-1} and b_i is calculated as a fraction M_{ij} of the shell volume shut by two cylinders. Then, by means of this matrix M_{ij} and the emitted photons D_j from each three-dimensional shell region, the photons received in a two-dimensional detector shell P_i is represented as

$$P_i = \sum_{j=1}^{N} M_{ij} D_j. \tag{4.5}$$

The projection matrix M_{ij} can be calculated as

$$M_{ij} = \begin{cases} 0 & (i > j) \\ \frac{(r_j^2 - r_{j-1}^2)^{\frac{3}{2}}}{r_j^3 - r_{j-1}^3} & (i = j) \\ \frac{(r_j^2 - r_{i-1}^2)^{\frac{3}{2}} + (r_{j-1}^2 - r_i^2)^{\frac{3}{2}} + (r_j^2 - r_i^2)^{\frac{3}{2}} + (r_{j-1}^2 - r_{i-1}^2)^{\frac{3}{2}}}{r_j^3 - r_{j-1}^3} & (i < j). \end{cases} \tag{4.6}$$

It is clear that the M_{ij} is an upper triangle matrix. Therefore, its inverse matrix M_{ij}^{-1} (i.e. deprojection matrix) is easily obtained. The deprojection matrix enable us to calculate D_i from P_j as

$$D_i = \sum_{j=1}^{N} M_{ij}^{-1} P_j. \tag{4.7}$$

When we simply apply this procedure to each energy bin, the deprojected spectra can be obtained. In fact, we must correct the annular spectra for the vignetting effect by exposure maps (§4.5) since the P_j is two-dimensional source before reaching at the detector. Another reminder in deprojection is the treatment of the emission coming outside the FOV. The deprojection analysis is applied to only Chandra data in this thesis. Since the FOV of Chandra is not wide enough to cover the whole emission from nearby clusters, significant contributions of foreground and background emission remain even beyond the outermost shell. We then assume in the region outside the FOV, that the spectral shape is the same as that in the outermost shell and that the spectral normalization changes according to the surface brightness described with the β model.

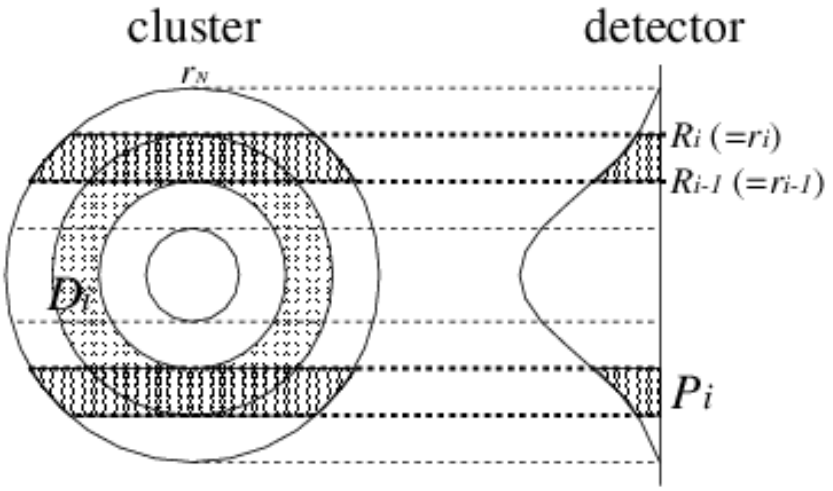

Figure 4.4: The schematic view of a cluster and its image on a detector. D_i and P_i are the number of photons from a three-dimensional shell region between r_i and r_{i-1}, and those from a two-dimensional annular region between b_i and b_{i-1}, respectively.

4.4.4 Spectral Model

After both on-source and background spectra, and adequate response are ready, we can get around to the spectral fitting in order to derive the ICM temperature and metal abundances. As described in §2.2.1, the ICM emission is composed of the thermal bremsstrahlung continuum and atomic lines from highly ionized ions in collisionally ionization equilibrium. There are two major ICM plasma emission models; MEKAL model (Kaastra & Mewe 1993) and APEC model (Smith et al. 2001). The difference between them lies in the treatment of ionizations and excitations of various ions in the collisionally ionized equilibrium. However, when they are applied to the ICM spectra with the energy resolution of X-ray CCD, there is little difference in determination of the temperature and metal abundances (e.g Matsushita et al. 2003). Although APEC better reproduces Fe-L lines around 1keV, clusters of galaxies usually have higher temperature, and then we use MEKAL model in this thesis. Abundance ratios are taken from the solar photospheric values in Anders and Grevesse (1989) as shown in table 4.5. For example, the number ratio of Fe/H is fixed to 4.68×10^{-5}.

The X-ray spectra are usually subject to the photoelectric absorption in the lower energy, especially <1 keV. This is caused by the cold matter along the line-of-sight, and is taken account by multiplying the initial emission model by an absorption factor of $\exp(-\sigma(E) \cdot N_H)$, where $\sigma(E)$ is the cross section for the photoelectric absorption. N_H is an equivalent hydrogen column density which is the quantity expressed with the product of hydrogen density and absorber thickness in the unit of cm^{-2}. In general, since N_H associated with the clusters themselves is small enough, it takes the value around $10^{20}\mathrm{cm}^{-2}$ according to the Galactic value, i.e., the absorption by the interstellar medium in our Galaxy toward the direction of the object. Then, there are finally four free parameters for the ICM emission; the ICM

temperature, metal abundance, hydrogen column density, and the overall spectrum normalization.

Table 4.5: Solar abundance ratios referring to the solar photospheric values by Anders & Grevesse (1989).

number ratio			
H	1.00	Si	3.55×10^{-5}
He	9.77×10^{-2}	S	1.62×10^{-5}
C	3.63×10^{-4}	Cl	1.88×10^{-7}
N	1.12×10^{-4}	Ar	3.63×10^{-6}
O	8.51×10^{-4}	Ca	2.29×10^{-6}
Ne	1.23×10^{-4}	Cr	4.84×10^{-7}
Na	2.14×10^{-6}	Fe	4.68×10^{-5}
Mg	3.80×10^{-5}	Ni	1.78×10^{-6}
Al	2.95×10^{-6}	Co	8.60×10^{-8}

On the other hand, non-thermal emission is represented by the empirical powerlaw model as described in §2.3. This model is defined by only two free parameters of the photon index and normalization. In the previous observations, the photon index of the non-thermal emission from clusters of galaxies ranges 1.5−2, reflecting the energy distribution of high energy electrons. The accuracy of the normalization as well as that of the photon index is very important in determining the non-thermal flux.

CXB model also has to be applied in spectral fittings for Suzaku instruments because the background model contain only NXB component (§4.3 and §5.5). Typical CXB spectrum is well represented by the cut-off powerlaw, which is in the form of the powerlaw-like shape with the sudden drop above a certain energy. There are three free parameters in this model; the photon index, cut-off energy, and normalization. Based on the HEAO-1 observations, the CXB spectrum is reported as follows (Boldt 1987);

$$9.0\times10^{-9}\left(\frac{E}{3\mathrm{keV}}\right)^{-0.29}\exp\left(\frac{-E}{40\mathrm{keV}}\right)\qquad[\ \mathrm{erg\ s^{-1}\ cm^{-2}\ keV^{-1}\ str^{-1}}].$$

Then, we fixed the photon index $\mu = 1.29$, and cut-off energy $E_{\mathrm{cut}} = 40keV$ for the CXB component. The normalization should be adjusted corresponding to the region size of the extracted spectra.

All the spectral fittings with these models are performed using the XSPEC package version 11.2.0, which is published by the NASA Goddard Space Flight Center (GSFC) and is commonly used in X-ray astrophysics community.

4.5 Spatial Analysis

As described in §2.2.2, we can measure the density or mass of the ICM, and the gravitational mass against the radius by fitting the surface brightness profiles with

the empirical β model and getting the parameter of β and $R_{\rm c}$ (core radius). However, before doing it, we have to perform some corrections to the radial surface profiles because the raw profiles includes the effect of the vignetting, dead pixel, and so on. We can correct these effects with the exposure map, which are generated by using the CIAO software package. In this software, not only the monoenergetic spectra but also the energy distribution of the spectra obtained in the observation can be considered into the exposure map. Figure 4.5 shows an example of the exposure map against the flat diffuse emission of 3 keV.

Another remaining correction is the background subtraction from the surface brightness profiles after correcting with the exposure map. The background level is usually low against the surface brightness, but its effect is not negligible in the outer region of clusters where the ICM emission is weaken. We create the background profiles from its image through the same procedure, and subtracted it from the surface brightness in each radius.

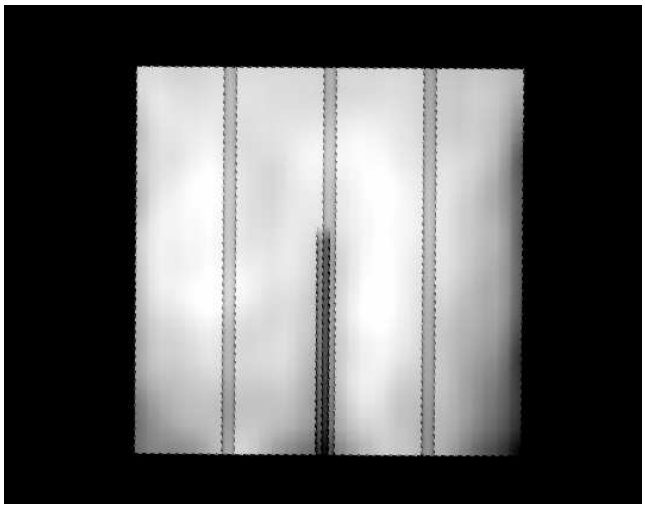

Figure 4.5: An exposure map of Chandra ACIS-S3 chip when the 3 keV monoenergetic uniform image is incident.

After all the correction described above are performed, we are ready to fit the surface brightness profiles. We extract the profiles from each cluster image in the energy band of 0.5−9.0 keV. Figure 4.6 left is an example of the surface brightness profile extracted from the image of Abell 2199, which is fitted with a single-β model. As seen in it, single-β models often fail to represent the surface brightness and the excess emission remains in the central region. In such a case, a double-β model which is a sum of two single-β profiles is usually utilized. Although it is not known whether the profiles really consist of two components, the fittings are extremely improved by applying the double-β model as shown in figure 4.6.

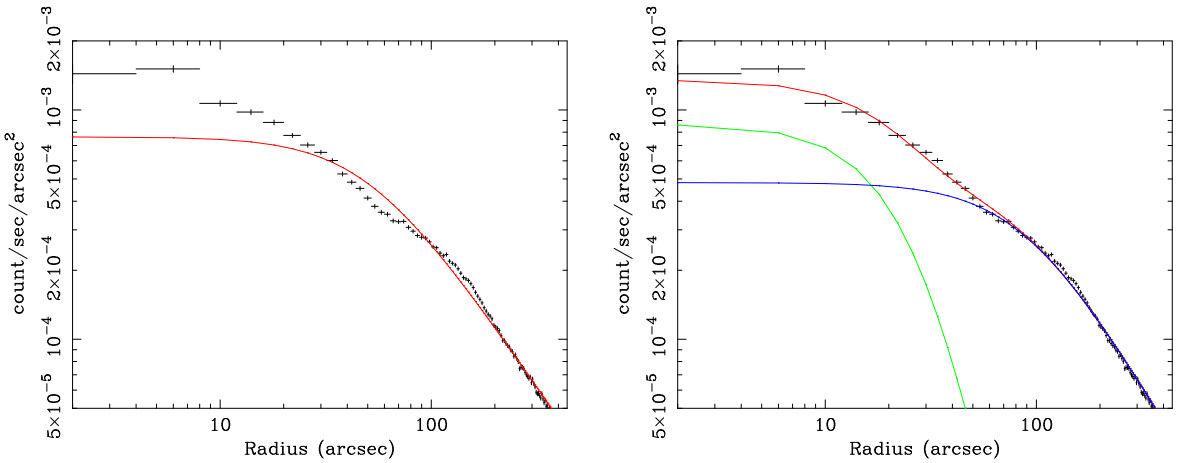

Figure 4.6: The ACIS-S3 surface brightness profile of Abell 2199, fitted by a single-β model (left) and by a double-β model (right). The black cross shows the data points. The red lines represent the fitted single or double-β model, which consists of an inner component (blue) and an outer component (green).

Chapter 5

RESULTS

5.1 Spectral Analysis

Here, we perform spectral fitting of the annular spectra in order to obtain the spatial distribution of the thermal parameter such as the ICM temperature, metal abundance, and absorption column density. This is essential to know physical condition of the central cool plasma in the clusters of galaxies.

5.1.1 Projected Spectral Fitting

In order to investigate the overall profiles of the ICM temperature, metal abundance, and column density, we extract the annular spectra as described in §4.4.1. The spectra of 2A 0335+096 in the radius of 0-10″, 30-40″, 60-90″, and 150-180″ are shown in figure 5.1 left. We can recognize some atomic lines of Fe-L, Si, and Fe-K around 1, 2, 6.4 keV, respectively. Fe-L line shifts toward the higher energy as it gets away from the cluster center, implying the temperature becomes higher to the cluster periphery. The drop of the count rate in the lower energy indicates that 2A 0335+096 places in the higher absorption direction than that of the typical Galactic absorption ($10^{20}\mathrm{cm}^{-2}$). We fitted the spectra with the absorbed thin plasma model, i.e., the MEKAL model with wabs (§4.4.4). The energy bands used in the fitting are 0.5−9.0 keV for clusters of galaxies, and 0.5−4.0 keV for groups of galaxies. All the radial profiles of the ICM temperature, absorption column density, and metal abundance are shown in figure 5.2, 5.3, Appendix B, and C.

Figure 5.1 is the temperature profile of 2A 0335+096. In the outer region, the temperature stays constant at $\sim$ 3 keV, while it is reduced by a factor of $\sim$2 and down to $\sim$ 1.6 keV in the central region. The radial profiles of the ICM temperature show similar trends among all the clusters of galaxies as seen in the figure; the temperatures decline toward the cluster centers. The temperature in the outer region is almost consistent with the observations performed by other instruments, XMM-Newton EPIC or ASCA, although Ophiuchus cluster, Abell 3112, Abell 3558, and MKW 4 have somewhat higher temperature due to worse photon statistics and high background rate. The central temperatures scatter in a wide temperature range of 0.61−4.02 keV, and become 1/3−1/2 of the outer temperature. Furthermore, the

ICM temperature becomes constant again in the very center within 30 kpc of 2A 0335+096. Such feature can be seen also in the central region of Perseus cluster, Abell 2052, HCG 62, NGC 5044, and NGC 533. Thus, the radial structure of the ICM temperature is largely inconsistent with the picture of cooling flow, in which the temperature shows a rapid decline toward the center and is predicted to be below 1 keV.

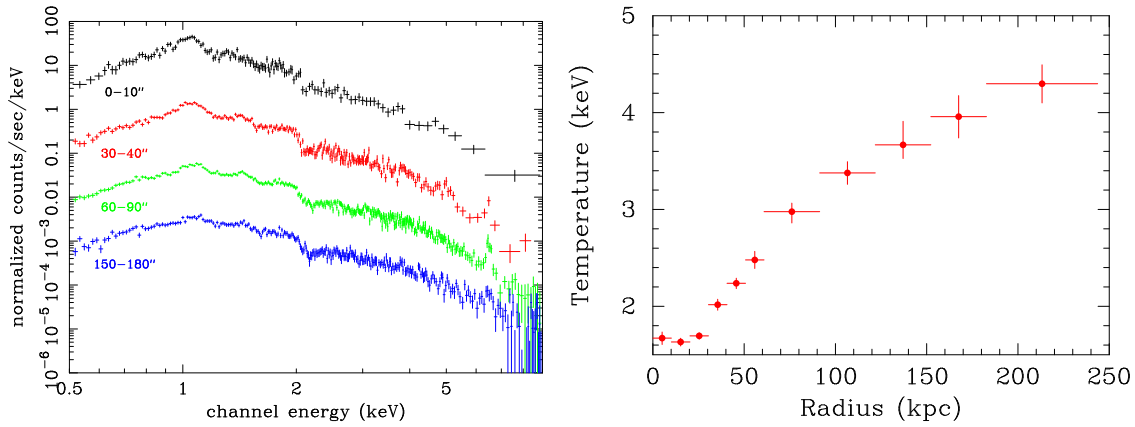

Figure 5.1: The annular spectra (left) and the radial temperature profile (right) of 2A 0335+096.

The column density can not be determined well and becomes almost zero in many cases. This is caused by the over-correction with *acisabs* against arf files, which compensate for the efficiency degradation of the Chandra ACIS chips suffered by the radiation damage (§3.3.1). We hence tried to fit with the fixed absorption column density with the Galactic value about such clusters. After applying this procedure, the ICM temperature or metal abundance is changed slightly but they are consistent within the errors for the previous values. Then, there is no remarkable effect due to the poor determination of the absorption. Many clusters that the absorption column density is determined in the fitting show the monotonous distributions against the radius as shown in figure 5.4 left. However, some clusters exhibit the central enhancement of the column density within $50-100''$ (see Appendix C), which may indicate the excess absorption by the central cool plasma in addition to the Galactic absorption. The Centaurus cluster (figure 5.4 right) has the largest central enhancement of absorption $\Delta N_H \sim 1.2 \times 10^{21} cm^{-2}$, which is roughly consistent with the value reported by Sanders & Fabian (2002). The column density of Perseus cluster and Abell 478 similarly increase but are smaller by $5 \times 10^{22} cm^{-2}$ overall cluster (Churazov et al. 2003; de Plaa et al. 2004). HCG62 and NGC 507 also show the larger excess, as well as the result by Paolillo et al. (2003). For NGC 5044, the absorption profile is similar to that observed with ASCA although the sharp enhancement can not be seen (Fukazawa et al. 1996). We discuss the amount of the cool gas estimated from the absorption enhancement later (§5.2.2).

Figure 5.5 is the radial profile of the metal abundance obtained from Abell 2052. Metal abundances increase in the central region of more than half clusters as well as Abell 2052. In some clusters such as Centaurus cluster, Abell 496, and MKW 4, the metal abundance at the cluster center reach >1 solar which is higher than

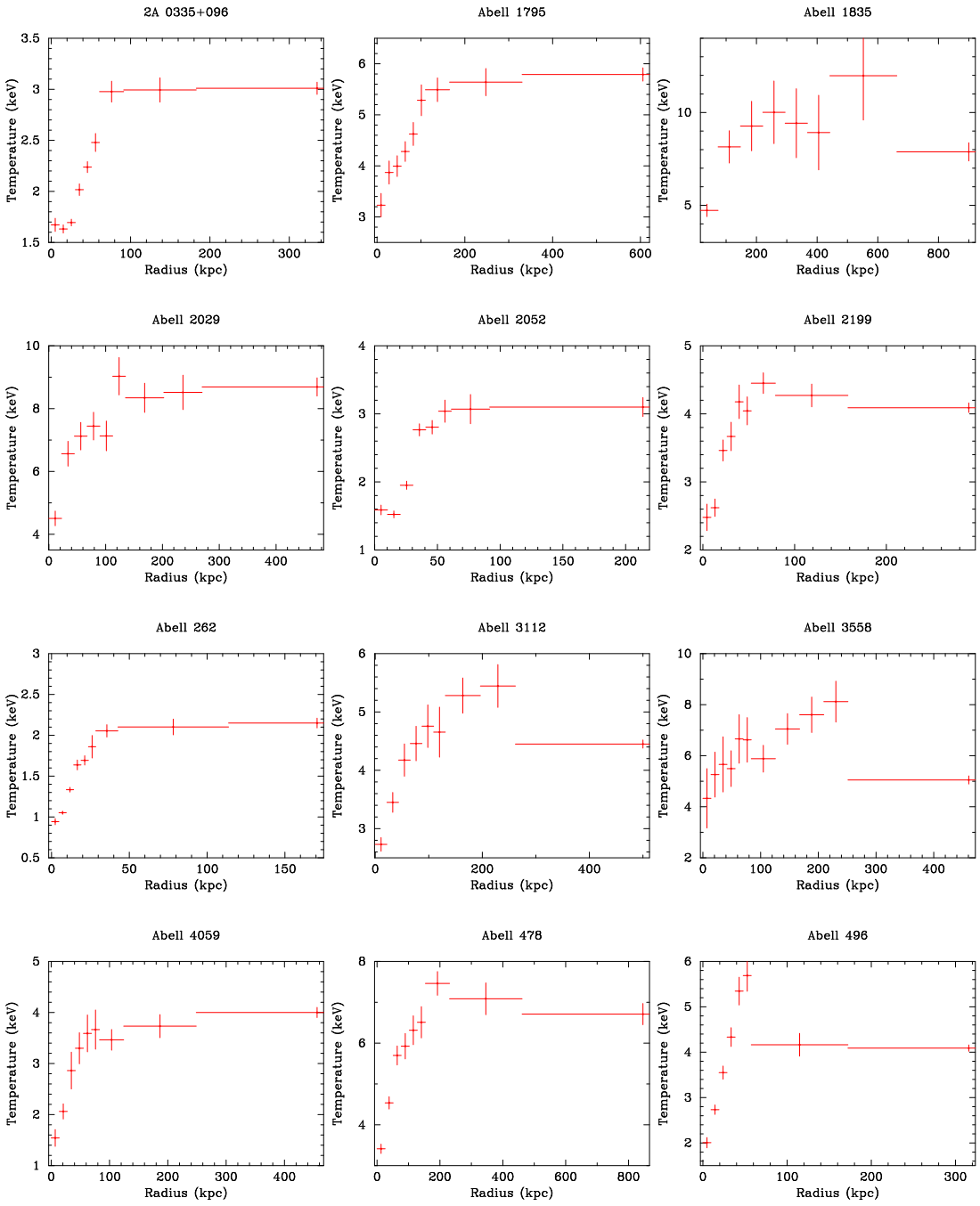

Figure 5.2: The radial profiles of the ICM temperature.

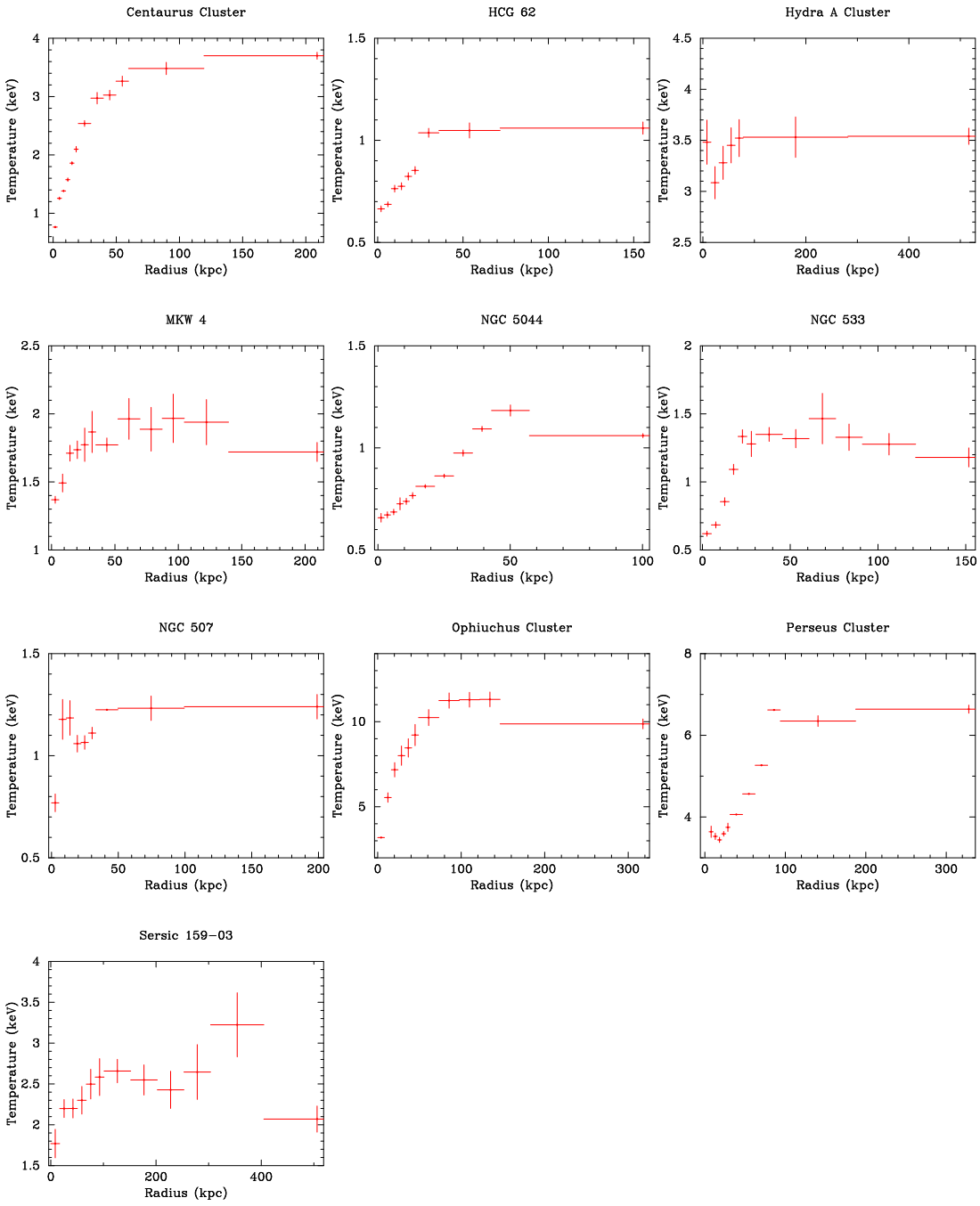

Figure 5.3: The radial profiles of the ICM temperature.

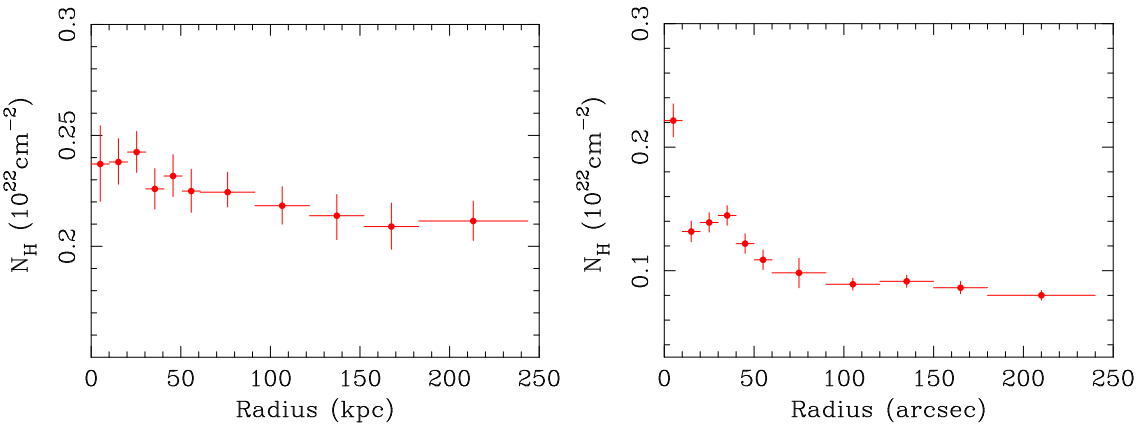

Figure 5.4: The absorption column density of 2A0335+096 (left) and Centaurus cluster (right) when fitted with single temperature MEKAL model.

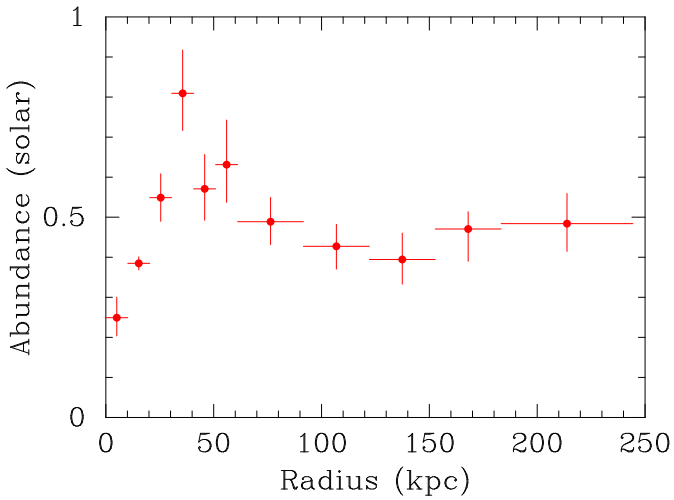

Figure 5.5: The radial abundance profile of Abell 2052 when fitted with single temperature MEKAL model.

cluster's typical abundance of 0.3 solar. When focused on the very central region, we can find the abundance drop within ∼30 kpc of Abell 2052. This feature is also remarkable in the Centaurus cluster, Abell 262, Abell 4059, Abell 496, and NGC 5044. The elliptical galaxies also show similar declination of the metal abundance. This is thought to by caused by the resonance scattering in the high density region, or the multi-temperature effect of the ICM (Matsushita et al. 2002).

In the above fitting model, the metal composition ratios are fixed to the values of the solar system. This may affect the determination of the ICM temperature and the absorption column density if the abundance ratio in the ICM is fairly different from the solar system. To examine such effect, we also utilized the variable abundance model vMEKAL as the thin plasma model, in which we can treat with the abundance of 14 elements independently. Here, the elemental abundances in the vMEKAL component are divided into some groups; C−N−O, Ne−Na−Al−Si, Mg, and S−Ar−Ca−Fe−Ni, and elemental abundances in each group are linked to the same value. The last element He is fixed to unity. The comparison of ICM

temperature and the absorption column density fitted with MEKAL and vMEKAL is shown in the figure 5.6. As seen in the figure, the profiles are little different between the MEKAL and vMEKAL. Therefore, we concluded that the effect of the metal abundance composition fixed with the value of solar system can be negligible in discussing the temperature or absorption. Hereafter, we apply not vMEKAL but MEKAL model in the spectral fittings.

We also tried to fit the spectra with two component plasma models, i.e., two temperature model. In this model, we fixed the ICM temperature of the first component to the value of the cluster outer region. The temperature of the second component, which accounts for the cool component, is left free. Figure 5.7 shows the resulting radial profiles of the metal abundance and absorption column density. Both profiles are very similar to those fitted with single temperature component model. The ICM temperatures of cool component also become roughly same values as the central temperature in single component fittings. The χ^2 of the clusters which have a higher temperature (> 4 keV), dose not largely improve in this procedure, while, in the cooler clusters, the χ^2 tend to become small significantly, especially in the central $\sim$50 kpc. This may reflect the projection effect in the spectra of cluster center.

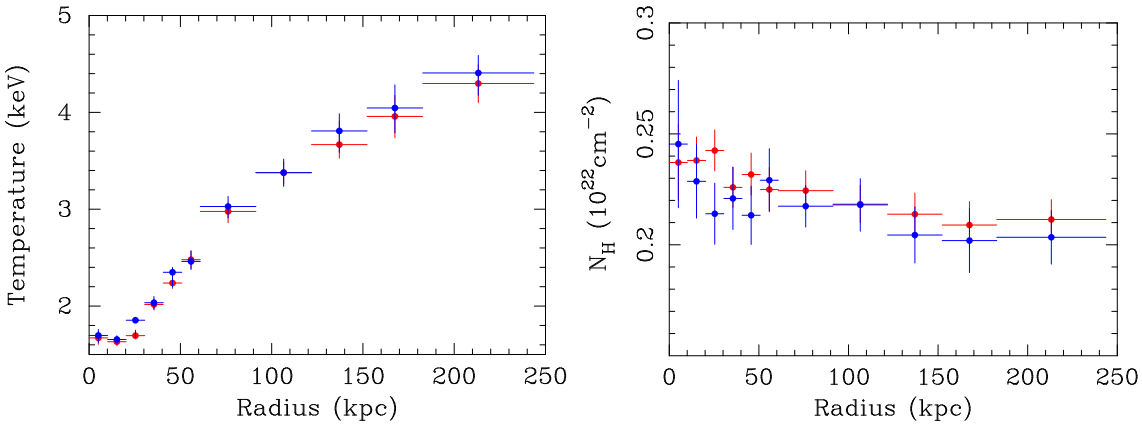

Figure 5.6: The ICM temperature (left) and absorption column density (right) of 2A 0335+096 when fitted with single temperature vMEKAL model.

5.1.2 Deprojected Spectra Fitting

As described in §5.1.1, the analysis of the projected spectra may affect the determination of the ICM parameters. Therefore, we extracted the deprojected spectra in the method explained in §4.4. Figure 5.8 left shows the deprojected spectra of 2A 0335+096 in the radii of $0-15''$, $30-45''$, $60-90''$, and $150-180''$. The resulting parameters of metal abundances and the absorption column density have larger errors because the spectra extracted through the deprojection method have larger statistical errors. Then, the remarkable differences on the resulting parameters without temperature are not found when compared with the fitting results of the projected spectra. On the other hand, the ICM temperature in the cluster center

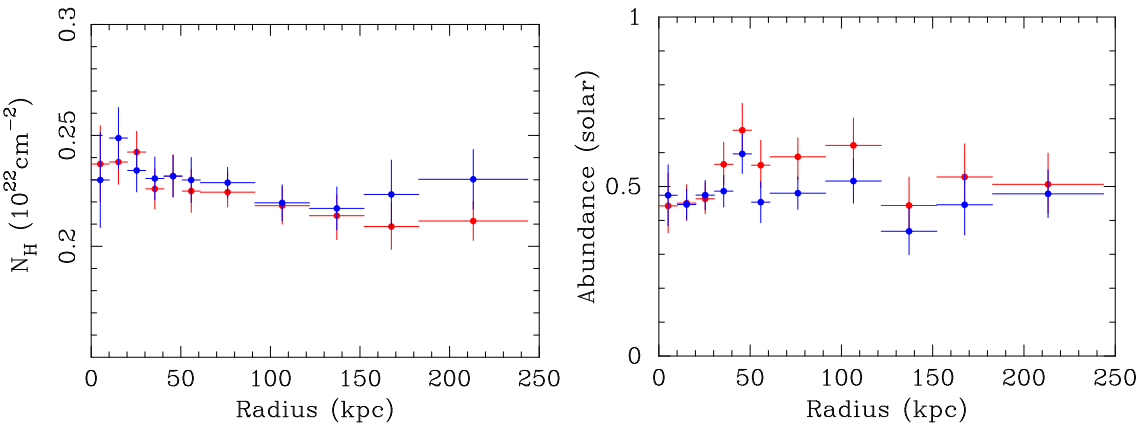

Figure 5.7: The absorption column density (left) and metal abundance (right) of 2A 0335+096 when fitted with two temperature MEKAL model.

tends to be significantly low. The radial temperature profiles obtained by fitting the projected and deprojected spectra are shown in figure 5.8 right. Within ∼50 kpc, the deprojected temperature is obviously low, indicating that the the ICM temperature is suffered by the projection effect. Then, we use the deprojected results only for the ICM temperature.

Since the Chandra cannot observe the outer region of the galaxy clusters because of its narrower FOV, we combined the ASCA results for the outer region, in order to investigate the temperature distribution up to the outside of the core region. All the temperature profiles obtained in this way are shown in figure 5.9. The temperature is normalized with the temperature in the outer region (hereafter $T_{\rm cluster}$). The radius on the x-axis is scaled by the virial radius R_{500}, within which the mass density is 500 times of the critical density. R_{500} is empirically represented by only the temperature as a function of $R_{500} = 2.78(T/10keV)(1+z)^{3/2}$ Mpc (Evrard et al. 1996). The $T_{\rm cluster}$ and R_{500} are listed in table 5.1. As well as the projected analysis above, the profiles are similar among the sample clusters. The temperature is almost constant in the outer region, and start to decline toward the cluster center at the vicinity of 0.05 R_{500}. This indicates that the temperature profiles follow a scaling law. Our results are consistent with the temperature profiles from XMM-Newton observations (Kaastra et al. 2004). The central temperature widely scatters in the range of ∼0.6−4.0 keV and the only a few galaxy clusters have a cool gas of < 1 keV, although the ratios of the central temperature $T_{\rm center}$ against the $T_{\rm cluster}$ mainly concentrate around ∼0.3−0.6. Even after removing the projection effect, the ICM temperature at the cluster center is obviously inconsistent with the cooling flow picture. The plasma heating exactly take place. The cooling time of the ICM via radiative cooling is in proportion with the second root of the ICM temperature, i.e. $t_{cool} \propto (kT)^{0.5}$. This indicates that the low temperature clusters are subject to cool earlier than the high temperature clusters. However, $T_{\rm center}/T_{\rm cluster}$ show similar values between them. Therefore, the low temperature clusters may be affected by a certain plasma heating more strongly.

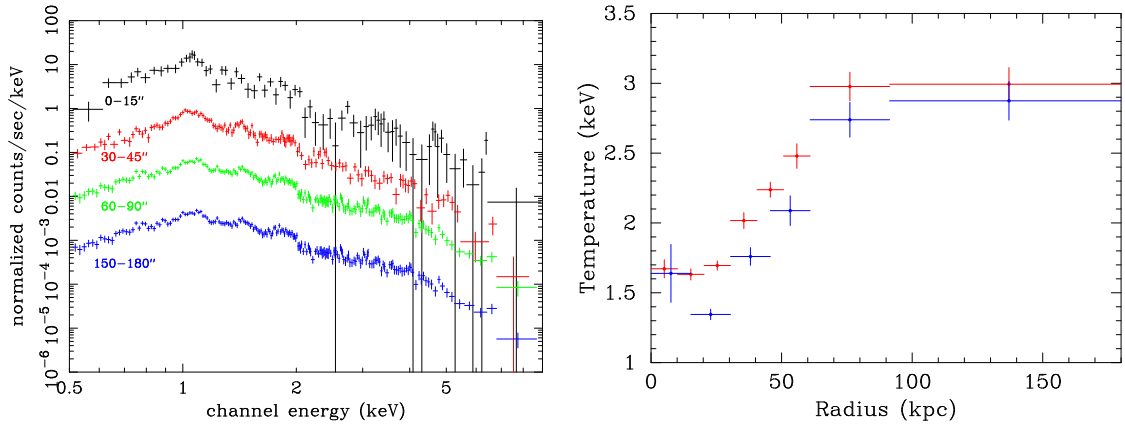

Figure 5.8: The deprojected annular spectra (left) and the radial temperature profile (right) of 2A 0335+096. In the right panel, red cross shows the projected profile while blue is the deprojected one.

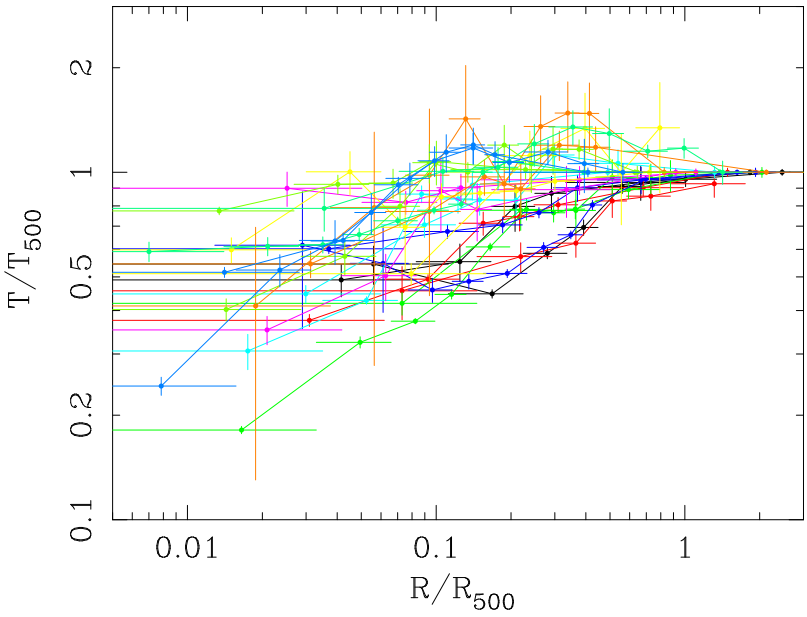

Figure 5.9: The radial temperature profiles of all the cluster samples. The temperature is normalized with the cluster-wide temperature $T_{\rm cluster}$, while the radius is scaled by the virial radius R_{500}.

Table 5.1: The cluster-wide temperature $T_{\rm cluster}$ and virial radius R_{500}.

	$T_{\rm cluster}$ (keV)	R_{500} (kpc)
2A 0335+096	3.01±0.06	136.06±19.21
Abell 2199	4.09±0.07	158.60±20.75
Abell 1795	5.79±0.13	188.71±28.28
Abell 2052	3.10±0.14	138.08±29.34
Abell 262	2.15±0.06	114.99±19.21
Abell 2029	8.69±0.29	231.19±42.23
Abel 478	6.71±0.26	203.15±39.99
Abell 4059	4.00±0.10	156.85±24.80
Centaurus	3.70±0.06	150.85±19.21
Hydra A	3.54±0.08	147.56±22.18
HCG 62	1.06±0.03	80.74±13.58
NGC 507	1.24±0.06	87.33±19.21
Abell 1835	7.88±0.49	220.15±54.90
Abell 3112	4.45±0.07	165.44±20.75
Abell 3558	5.05±0.16	176.24±31.37
Abell 496	4.09±0.07	158.60±20.75
MKW 4	1.72±0.07	102.85±20.75
Sérsic 159-03	2.41±0.16	121.75±31.37
NGC 5044	1.06±0.01	80.74±7.84
NGC 533	1.26±0.07	88.03±20.75
Ophiuchus	9.87±0.29	246.38±42.23
Perseus	6.64±0.10	202.09±24.80

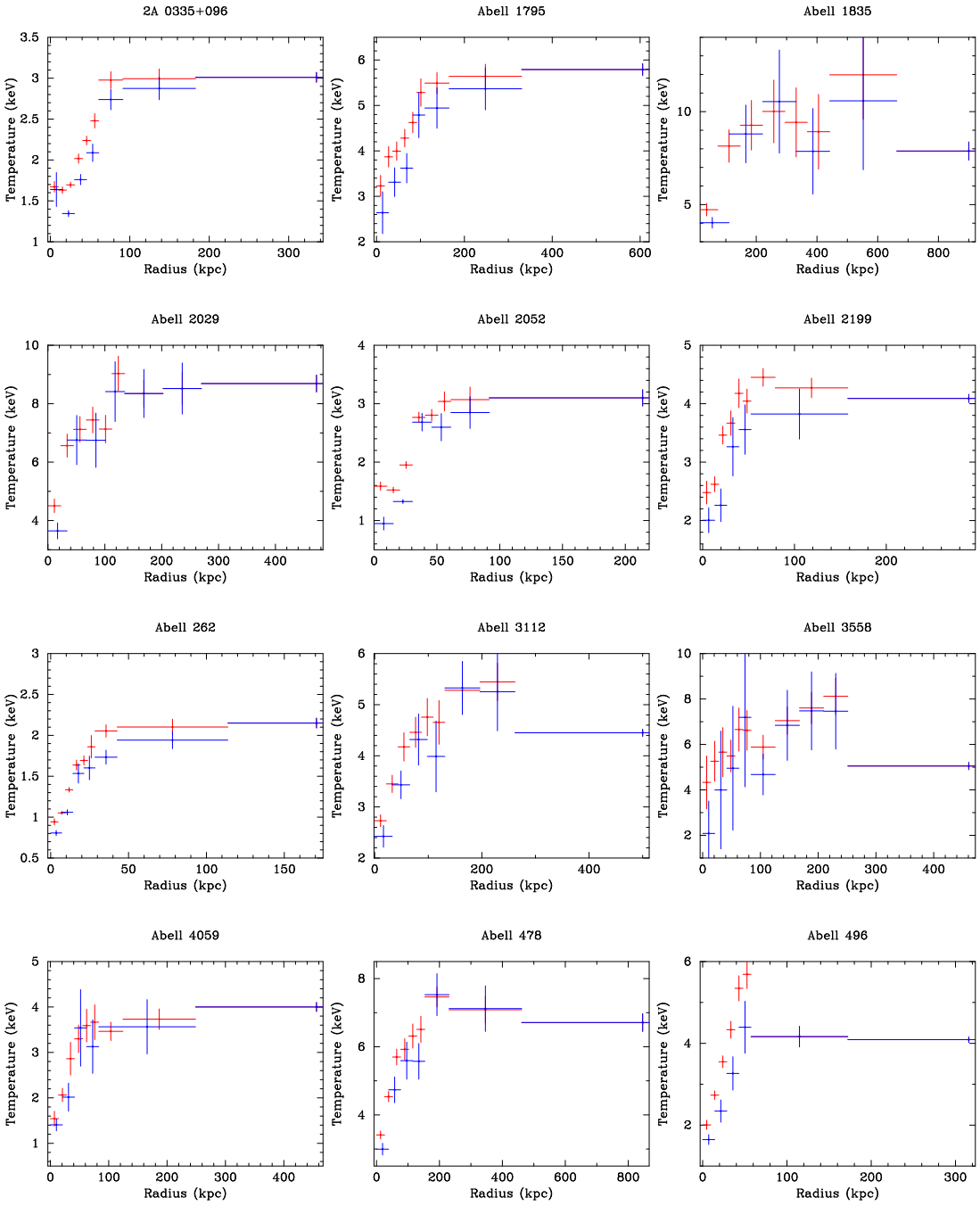

Figure 5.10: The radial profiles of the ICM temperature. The red and blue lines in each panel represent the projected and deprojected profiles.

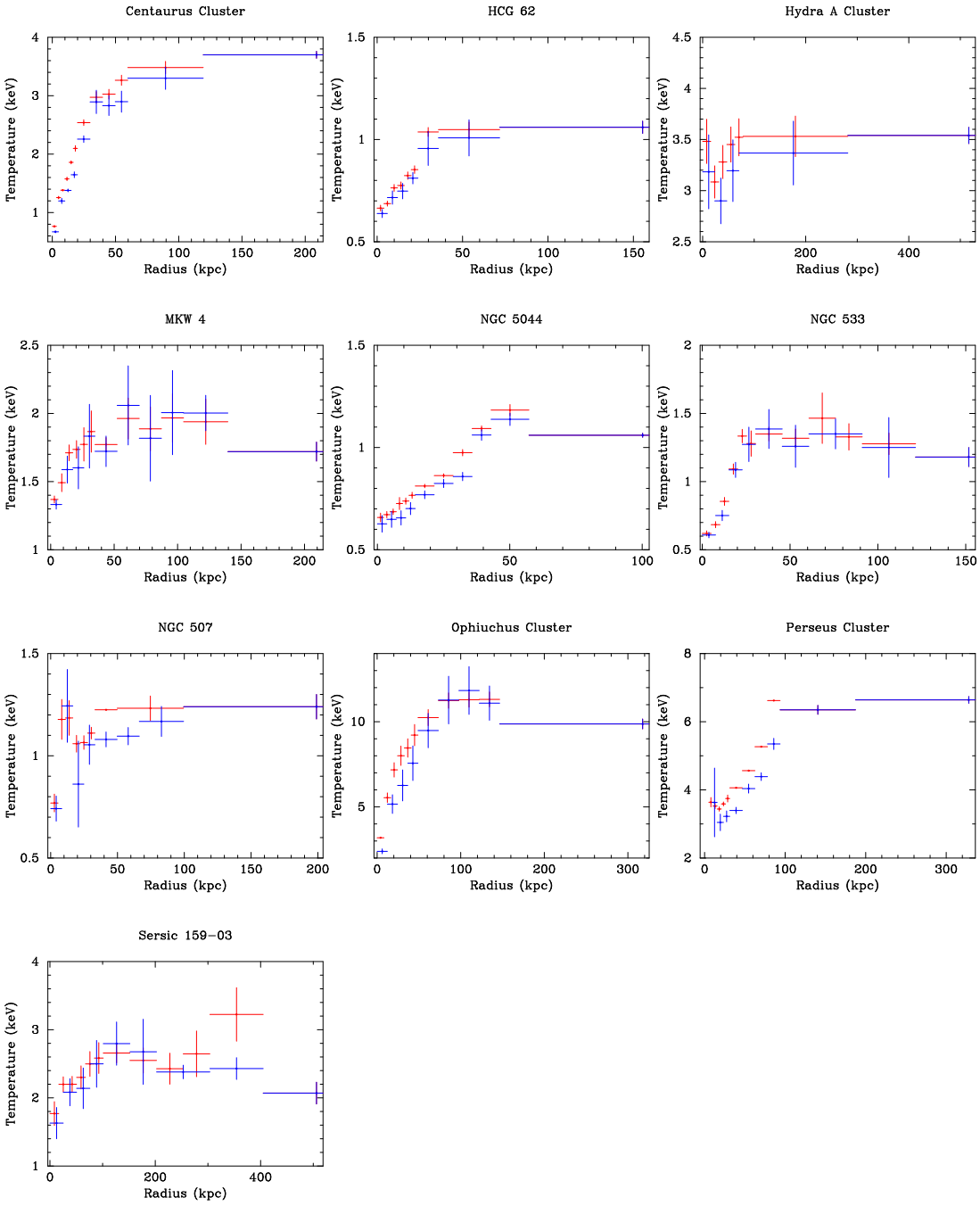

Figure 5.11: The radial profiles of the ICM temperature. The red and blue lines in each panel represent the projected and deprojected profiles.

5.2 Spatial Distribution of Mass Profiles

The mass of the central cool plasma is also important quantity as well as the spectral parameters derived in the previous section. Therefore, we perform the surface brightness fitting to obtain the density profile and investigate the mass distribution of the ICM.

5.2.1 X-ray Surface Brightness

In the previous observations, the X-ray images of galaxy clusters have the spherical symmetry distributions, as represented by a β model. A surface brightness profile extracted from a X-ray image shows the brightest emission at the cluster center and gets dark toward the peripheral regions of the clusters (i.e. outside of the core radius $R_{\rm c}$). Recently, thanks to Chandra's high spatial resolution, the X-ray distribution have found to be different from that considered before; it is more complex, especially in the central region of clusters. Figure 5.12 shows the X-ray image of Abell 2052 superposed on the radio contour (Blanton et al. 2003). Above and below of the cluster center, there are X-ray faint circular region which are called as "X-ray holes" or "cavities". Perseus cluster is also famous cluster which have the same structure. Such cavities are filled with the radio emission as seen in the image in many cases, implying that the ICM interacts with the radio lobes emitted from the AGN and is heavily disturbed. In the region somewhat apart from the very center of some clusters, there are the cavities which are not associated with any radio emission. These are considered to be a fossil of radio cavities, and then called "ghost cavities". Thus, the lack in uniformity of the X-ray distribution is rather common in the central region of galaxy clusters. The cavities are very interesting on the view that the strong interactions may cause the ICM heating to restrain the cooling flow. All the X-ray images of sample clusters obtained with Chandra are shown in Appendix A.

However, such phenomena positionally limited to the central region of the clusters, and therefore we can consider that the X-ray distribution is almost spherically symmetry in the overall cluster. Then, we extracted the X-ray surface brightness by subtracting the background and correcting with the exposure map (§4.5), and fitted with the ordinary β model in order to estimate the density distribution of the ICM pursuant to the equation 2.27. The X-ray surface brightness profile of 2A 0335+096 and Abell 2199 are shown in figure 5.13. The profile of 2A 0335+096 is well fitted by the single-β model, while in Abell 2199, it shows the excess from the β model in the central region. The central excess of the surface brightness is found in relatively many samples such as Abell 1795, Abell 2029, Abell 3112, Abell 3558, and so on (see Appendix D). These clusters tend to have a dimple in their surface brightness profiles and hence the central excess will be produced. We summarized the fitting parameter of the core radius $R_{\rm c}$, β, and the central density n_0 in table 5.2. The core radius $R_{\rm c}$ is typically several tens kpc, although some of the near clusters ($z \sim 0.01$) show small $R_{\rm c}$ of $<$10 kpc. The most of β except Centaurus cluster and Ophiuchus cluster takes the range of 0.3$-$0.6, which is somewhat smaller than the previous

observations ($\beta \sim 0.6$). Centaurus cluster has the smallest β of 0.17. It is because the surface brightness of Centaurus cluster which have dimple around $40''$ from the cluster center, is forcedly fitted with single-β model. The R_c of Ophiuchus cluster is reported to become $3.2-3.3'$ with ASCA (Watanabe et al. 2001; Fukazawa et al. 2004). Compared with them, our result gives a extremely small core radius of $<1''$ because of the limited image of Chandra within $\sim 4'$. The β of Ophiuchus cluster is probably reduced by the same reason. The central density n_0 apparently have fallen into the small value in the clusters whose surface brightness can not be represented well by a single-β model due to the strong dimple. For example, in NGC 507, the central density is reduced by an order of magnitude than the other clusters.

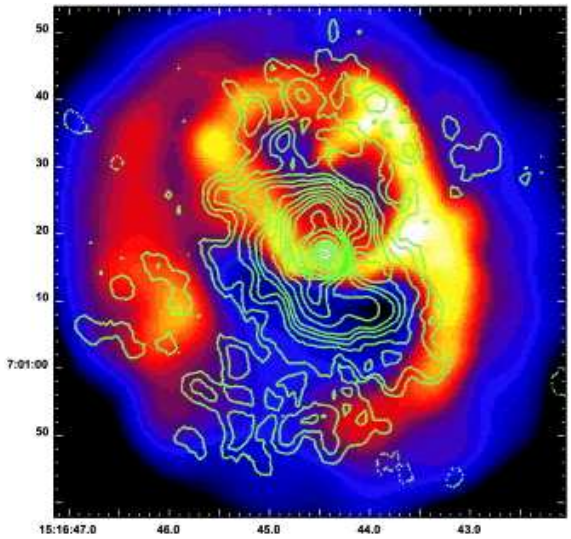

Figure 5.12: X-ray image and radio contour of Abell 2052 in the central $\sim 75'' \times 75''$ region (Blanton et al. 2003).

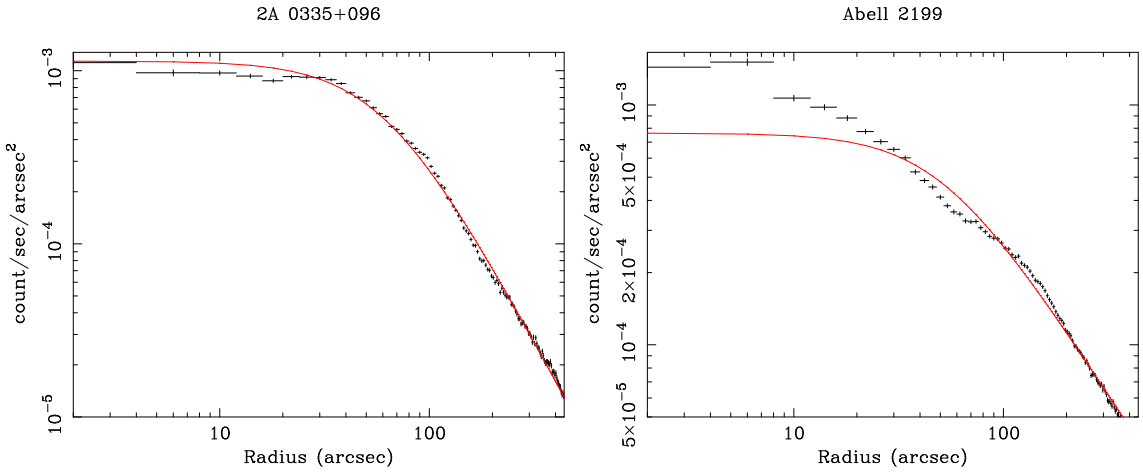

Figure 5.13: X-ray surface brightness of 2A 0335+096 (left) and Abell 2199 (right) when fitted with single-β model.

Table 5.2: The best fit parameters of a single-β model.

	n_0 (10^{-3} cm^{-3})	R_c (kpc)	β
2A 0335+096	53.21±0.37	30.87±0.23	0.54±0.0014
Abell 2199	31.43±0.43	25.10±0.48	0.39±0.0013
Abell 1795	30.95±0.24	28.41±0.26	0.50±0.0013
Abell 2052	34.51±0.26	21.88±0.20	0.44±0.00094
Abell 262	72.66±1.80	6.888±0.20	0.35±0.00087
Abell 2029	34.51±0.32	23.76±0.24	0.50±0.0011
Abell 478	38.78±0.32	23.72±0.21	0.51±0.0010
Hydra A	52.89±0.63	13.14±0.16	0.44±0.00092
Centaurus	167.27±2.44	10.13±0.17	0.38±0.00061
HCG 62	39.14±0.86	14.24±0.32	0.51±0.0025
NGC 507	9.98±0.23	41.89±2.06	0.36±0.0041
Abell 1835	55.40±0.79	8.76 ±0.10	0.54±0.0013
Ophiuchus	420.44±41.26	0.62 ±0.10	0.27±0.00024
Perseus	43.01±0.10	91.02±0.44	0.56±0.0016
Abell 3112	51.14±1.09	11.32±0.22	0.47±0.0012
Abell 3558	10.16±0.24	28.32±1.27	0.33±0.0023
Abell 496	61.44±0.94	9.91 ±0.19	0.35±0.00064
Abell 4059	13.81±0.23	33.02±0.86	0.40±0.0023
Sérsic 159-03	33.50±0.52	25.67±0.40	0.57±0.0029
MKW 4	76.15±2.46	4.73 ±0.14	0.41±0.0011
NGC 5044	38.32±0.40	41.62±0.61	0.50±0.0025
NGC 533	150.21±6.83	3.09 ±0.12	0.45±0.0017

As the next step to improve the fittings, we fitted the surface brightness profiles with a double-β model. In the fitting, the β is limited to be below 1 for both the inner and outer component, and the β of the inner component (β_1) is adjusted to take larger value than the outer one (β_2) since $\beta_1 < \beta_2$ is not realistic. Figure 5.14 shows again the surface brightness of 2A 0335+096 and Abell 2199 fitted with a double-β model. We can easily seen that the fitting is really improved in Abell 2199. In the most of cluster showing the central excess, the same improvements are found although such excess still remain in the very central region of Abell 1795, Hydra A, NGC 533. The χ^2 decreases even in Abell 262, Abell 496, Abell 1835, MKW 4, and Sérsic 190-03, whose surface brightness could be fitted with a single-β model as well as 2A 0335+096. The surface brightness profiles fitted with a double-β model are shown in Appendix D. The resulting parameters of all the clusters are shown in table 5.3. The R_c of both inner and outer component scatter in the wide range cluster by cluster. The β also takes various values of 0.27−1.0. Thus, there are no remarkable trends in common among the sample clusters for the R_c and β. The central densities have become much higher, especially in NGC 507 and Centaurus cluster, due to much better fittings with a double-β model. As a whole,

the densities exhibit higher values by a factor of 2−3 than that observed with the previous observation. Thus, Chandra observations enable us to obtain more proper profiles of the ICM density in the central region.

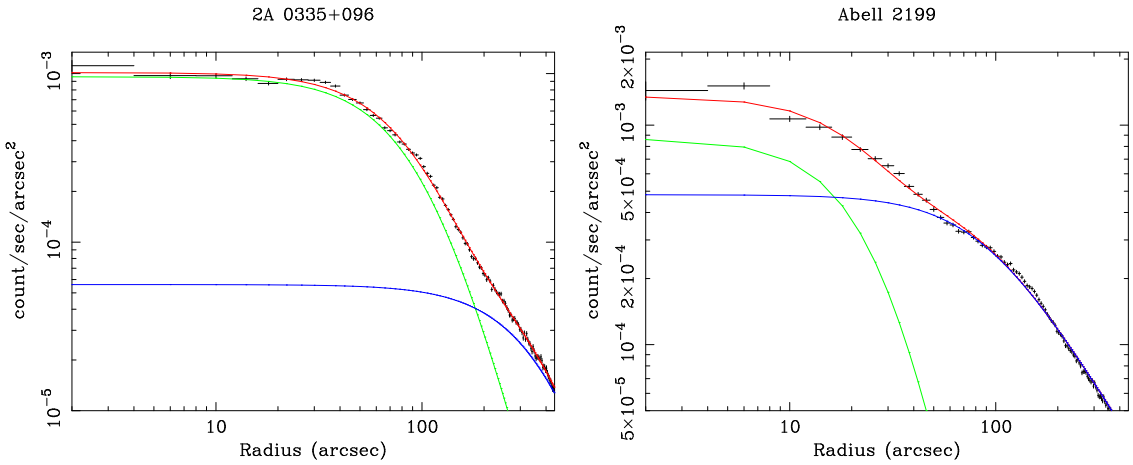

Figure 5.14: X-ray surface brightness of 2A 0335+096 (left) and Abell 2199 (right) when fitted with double-β model.

Table 5.3: The best fit parameters of a double-β model.

	n_1 (10^{-3} cm^{-3})	R_{c1} (kpc)	β_1	n_2 (10^{-3} cm^{-3})	R_{c2} (kpc)	β_2
2A0335+096	45.31±0.27	55.65± 0.20	0.98± fixed	5.28±0.03	240.00± 0.70	0.98± fixed
Abell 2199	62.31±2.06	15.76± 0.46	1.00± 0.021	1.96±0.32	44.58± 0.95	0.42± 0.0022
Abell 1795	28.87±0.20	34.01± 0.18	0.56± fixed	1.33±0.03	240.00±23.08	0.56± fixed
Abell 2052	28.22±0.19	52.04± 0.33	1.00± 0.0020	3.95±0.11	183.47±15.41	0.60± 0.040
Abell 262	54.22±0.85	13.21± 0.22	0.46± 0.0032	4.35±0.31	44.02± 4.08	0.25± 0.0037
Abell 2029	149.73±6.82	3.37± 0.14	0.51± fixed	25.04±0.31	31.81± 0.20	0.51± fixed
Abell 478	77.32±1.12	10.65± 0.16	0.60± fixed	16.42±0.22	54.36± 0.31	0.60± fixed
Hydra A	37.66±0.34	29.56± 0.19	0.73± fixed	2.76±0.05	227.27± 2.95	0.73± fixed
Centaurus	263.24±8.48	8.19± 0.20	1.00± 0.0068	103.91±1.89	16.69± 0.31	0.39± 0.00073
HCG 62	93.08±8.66	3.25± 0.35	0.53± fixed	29.23±1.18	18.33± 0.32	0.53± fixed
NGC 507	431.55±44.93	1.83± 0.19	0.62± 0.028	8.14±0.20	57.56± 2.62	0.38± 0.0051
Abell 1835	52.91±0.76	13.66± 0.18	1.00± 0.0088	9.36±0.50	34.09± 1.26	0.63± 0.0063
Ophiuchus	196.41±17.06	4.75± 0.82	0.91± 0.20	59.63±8.36	7.11± 1.71	0.27± 0.00055
Perseus	42.02±0.24	92.25± 0.30	0.59± fixed	8.50±0.61	168.85± 4.43	0.59± fixed
Abell 3112	108.24±4.01	5.11± 0.19	0.52± fixed	14.59±0.60	32.56± 0.58	0.52± fixed
Abell 3558	90.79±11.31	4.46± 0.33	1.00± 0.62	9.17±0.20	32.65± 1.38	0.33± 0.0025
Abell 496	46.81±0.61	17.87± 0.25	0.44± fixed	2.31±0.07	293.16±14.03	0.44± fixed
Abell 4059	35.15±1.93	14.08± 0.64	1.00± 0.056	10.20±0.19	49.07± 1.35	0.43± 0.0033
Sérsic159-03	32.66±7.90	18.27±3.38	0.60± fixed	19.01±7.99	36.14± 3.52	0.60± fixed
MKW 4	60.73±1.69	6.83± 0.15	0.45± fixed	0.68±0.07	214.65±25.30	0.45± fixed
NGC 5044	151.79±14.43	4.53± 0.38	0.52± fixed	32.68±0.42	49.63± 0.36	0.52± fixed
NGC 533	79.05±2.47	7.39± 0.14	0.57± fixed	0.66±0.04	297.05±63.90	0.57± fixed

5.2.2 Mass Profiles

Since the temperature and ICM density profile is obtained in §5.1.2 and 5.2.1, we can calculate the mass distribution of the ICM and the gravitational matter by substituting them into the equation 2.26 and 2.2. We use here the result of the

deprojected values for the ICM temperature and the double-β fittings for the density profiles. The ICM density profiles have already been represented as a function against the radius, which can be directly substitute into the equation of mass profile. On the other hand, the ICM temperature is not formularized yet. Then, we fit the ICM temperature profiles with the formula of

$$T(r) = t_0 + (t_1 - t_0)\frac{r}{\sqrt{(1 + ar^2)}}. \tag{5.1}$$

There are three parameters of t_0, t_1, and a, and the former two are corresponding to the central temperature and the outer (cluster-averaged) temperature. Figure 5.15 left shows the result of the ICM temperature fitting with this formula. Utilizing the temperature function, we estimate the mass profile of the ICM and the gravitational matter for each cluster as shown in figure 5.15 right. The point to notice is the dimple around 30 kpc in the gravitational mass profile. Such structure is found in many other clusters. The typical radii that the dimples locate on is as several times larger as the crossing radius of the inner and outer component in the β model fitting, where the surface brightness profiles become the flat form against the radius. Meanwhile, in the ICM temperature, the detail radial structure on a few arcsec order is not known and it is formularized with the monotonously increasing function against the radius. Therefore, the thermal equilibrium can not be represented well, around the dimple of mass profiles. This is a reason why a dimple appears. The other reason to arise the dimple is considered to be the flat core profile of the outer component. When the density distribute monotonous against the radius, the mass within the core radius is decreased toward the inner region.

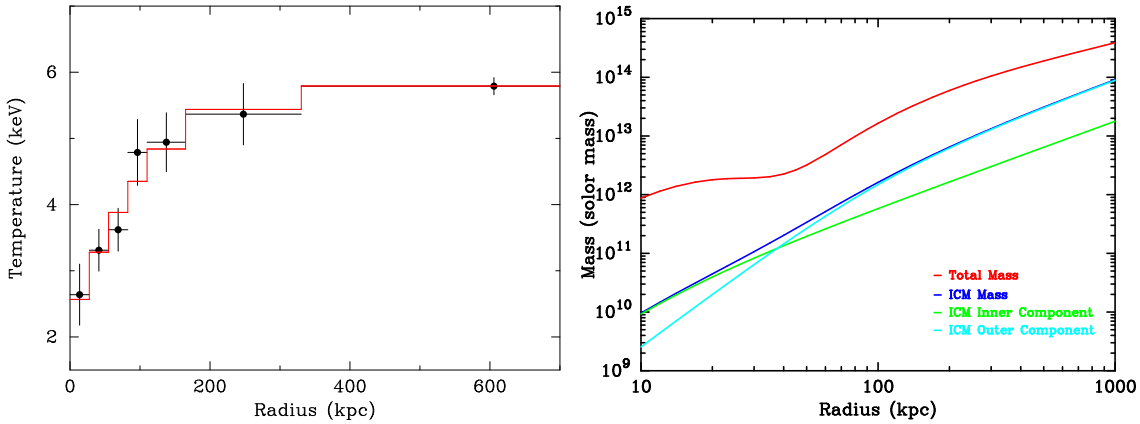

Figure 5.15: The temperature profile of Abell 1795 fitted with a function of equation 5.1 (left) and the mass profiles of Abell 2029 (right). The lines in mass profile present the total gravitational mass (red), the ICM mass (blue). and the mass of the inner component (green) and outer component (right blue) in double-β model fitting.

In order to break off these effects in estimating the mass profiles, we utilized another method by means of the normalizations in two temperature spectral fitting. The normalization is represented as

$$K = \frac{10^{-14}}{4\pi[D_{\rm A}(1+z)]^2}\int n_{\rm gas}^2 dV, \tag{5.2}$$

where D_A is the angular distance. As seen in this equation, we can estimate the emission measure from the deprojected normalization per unit area, and then obtain the density profile of the ICM. More concretely, introducing the filling factor f, the total gas density is represented as $n_{gas}(r) = f n_c(r) + (1-f) n_h(r)$. The subscripts c and h indicate the cool and hot component. Then, the normalization for each component become $K_c(r) = f n_c^2(r)$ and $K_c(r) = (1-f) n_h^2(r)$, respectively. The thermal equilibrium gives $n_c(R) k T_c = n_h(R) k T_h$. When T_c and T_h is defined as the central and outermost temperature in the deprojection analysis (§5.1.2), we can obtain the density distribution. The filling factor of the cool component against the hot component, and the ICM density profile of both component are shown in figure 5.16. The cool component is dominant as much as the hot component in the central region while the hot component become puissant toward the peripheral region.

By applying the ICM density obtained in this way to the equation 2.26 and 2.2, we estimate the mass profiles of the ICM and the total gravitating matter again. The mass profiles are summarized in Appendix E. Figure 5.17 shows the mass profiles of Abell 2029, together with the mass estimated with the density obtained in the double-β model fitting. It is obvious that the dimple have been eliminated in the total gravitational mass profile. Such improvement is common among all the clusters which exhibit the dimple. The mass fraction of the ICM to the total mass generally takes a few tens percent in the overall cluster while it is decreased in the cluster center where the mass of the galaxies (hence stars) concentrate.

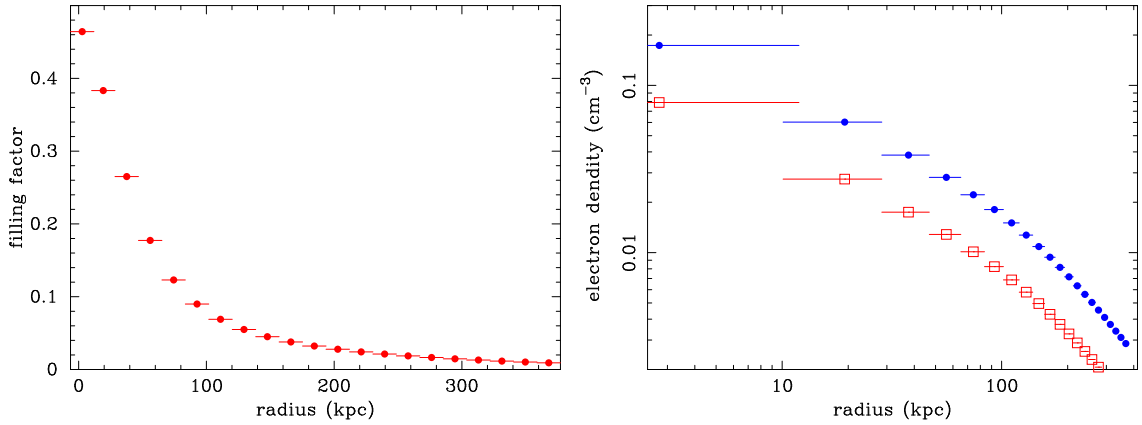

Figure 5.16: The filling factor (left) and the electron density profiles (right) of Abell 1795. The filled circle (red) and open square (blue) in the electrons density profile present the low and high temperature component in the two temperature fitting.

5.3 Properties of the Central Cool ICM

5.3.1 Temperature Structure

For the quantitative discussion of the ICM temperature structure, we here defined four parameters; T_{center}, $T_{cluster}$, R_{start}, and R_{cool}. T_{center} and $T_{cluster}$ are the central temperature and the cluster-wide temperature obtained by the deprojection analysis.

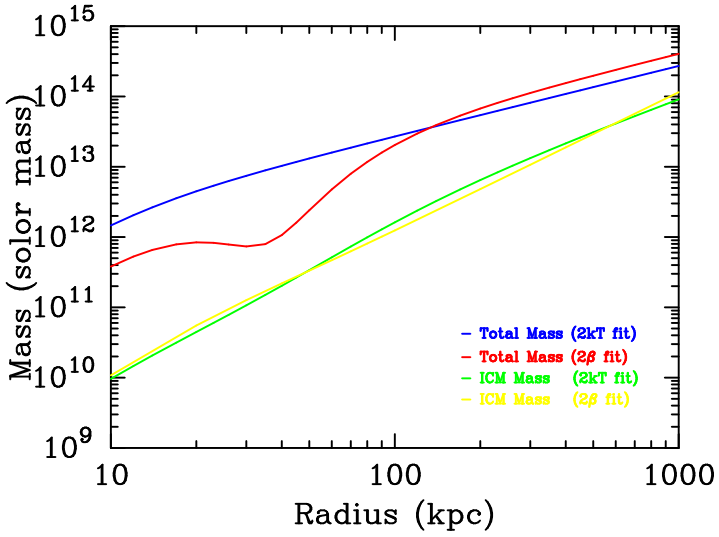

Figure 5.17: The mass distribution of the ICM and the total gravitational matter for Abell 2029. The red and yellow lines present the mass calculated by using double-β model parameters while the blue and green lines show that using two temperature model.

$R_{\rm start}$ is the radius where the ICM temperature starts to decline as shown in figure 5.18 left. Outside $R_{\rm start}$, the temperature gradient flattens. $R_{\rm cool}$ is the cooling radius where the cooling time is equal to the Hubble time (figure 5.18 right). We calculate $R_{\rm cool}$ from the equation 2.10 by means of the radial profile of the ICM temperature and density. It is suspected that the radiative cooling acts efficiently within $R_{\rm cool}$. The radiative cooling time at the cluster center is also calculated by substituting $T_{\rm center}$ and the central electron density ($n_1 + n_2$ in table 5.3) into the equation 2.10. All the parameters are listed in the table 5.4.

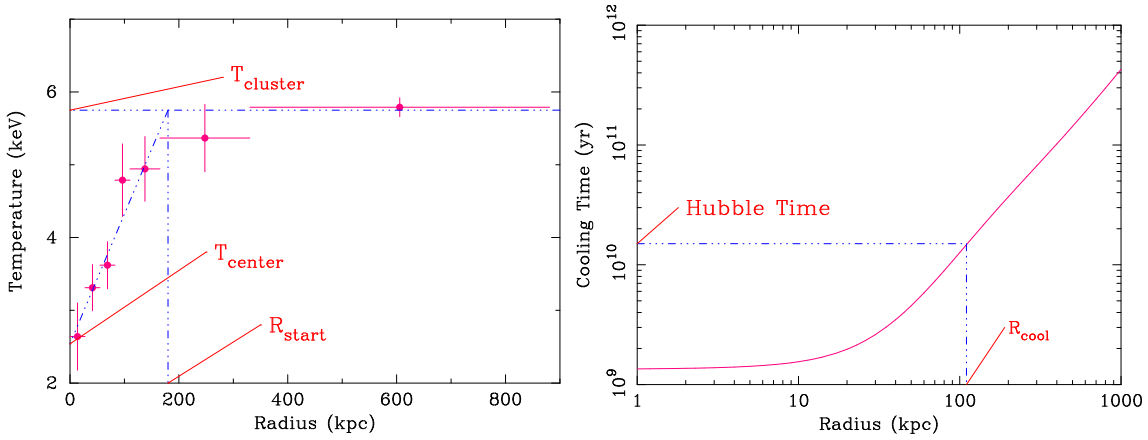

Figure 5.18: The parameter definition of $T_{\rm cluster}$, $T_{\rm cluster}$, and $R_{\rm start}$ (left), and $R_{\rm cool}$ (right).

The correlations between these parameters are presented in figure 5.19. We have found that the cooling radius $R_{\rm cool}$ is roughly close to the radius $R_{\rm start}$. This indicates

Table 5.4: The parameters characterizing the temperature profile.

	$T_{\rm center}$ (keV)	$T_{\rm cluster}$ (keV)	$R_{\rm start}$ (kpc)	$R_{\rm cool}$ (kpc)	$T_{\rm cool}$ (yr)
2A 0335+096	$1.64^{+0.17}_{-0.24}$	3.01±0.06	140±42	135.23±27.0	1.02×10^9
Abell 2199	$2.01^{+0.21}_{-0.21}$	4.09±0.07	100±30	100.67±20.1	8.32×10^8
Abell 1795	$2.64^{+0.50}_{-0.42}$	5.79±0.13	184±55	158.04±31.6	2.24×10^9
Abell 2052	$0.95^{+0.10}_{-0.12}$	3.10±0.14	50±15	95.40±19.1	1.66×10^9
Abell 262	$0.81^{+0.03}_{-0.03}$	2.15±0.06	60±18	48.03± 9.6	7.25×10^8
Abell 2029	$3.65^{+0.30}_{-0.25}$	8.69±0.29	100±30	148.86±29.8	5.22×10^8
Abell 478	$3.00^{+0.16}_{-0.18}$	6.71±0.26	179±54	203.99±40.8	8.81×10^8
Abell 4059	$1.41^{+0.17}_{-0.09}$	4.00±0.10	83±25	101.97±20.4	1.47×10^9
Centaurus	$0.67^{+0.02}_{-0.02}$	3.70±0.06	85±25	70.63±14.1	1.83×10^8
Hydra A	$3.18^{+0.36}_{-0.37}$	3.54±0.08	80±25	117.69±23.5	1.34×10^9
HCG 62	$0.64^{+0.02}_{-0.02}$	1.06±0.03	50±15	32.12± 6.4	2.84×10^8
NGC 507	$0.74^{+0.05}_{-0.07}$	1.24±0.06	50±15	70.58±14.1	6.93×10^7
Abell 1835	$4.02^{+0.29}_{-0.28}$	7.88±0.49	663±133	202.54±40.5	1.40×10^9
Abell 3112	$2.42^{+0.15}_{-0.27}$	4.45±0.07	196±39	120.86±24.2	5.19×10^8
Abell 3558	$2.08^{+1.72}_{-1.13}$	5.05±0.16	126±25	51.94±10.4	6.62×10^8
Abell 496	$1.65^{+0.11}_{-0.14}$	4.09±0.07	115±23	95.70±19.1	1.16×10^9
MKW 4	$1.33^{+0.03}_{-0.04}$	1.72±0.07	52±10	32.87± 6.6	5.80×10^8
Sérsic 159-03	$1.63^{+0.22}_{-0.24}$	2.41±0.16	177±35	140.20±28.0	1.10×10^9
NGC 5044	$0.63^{+0.04}_{-0.04}$	1.06±0.01	57±11	56.65±11.3	1.78×10^8
NGC 533	$0.61^{+0.02}_{-0.02}$	1.26±0.07	61±12	25.34± 5.0	3.82×10^8
Ophiuchus	$5.17^{+0.55}_{-0.55}$	9.87±0.29	147±29	64.59±12.9	4.11×10^8
Perseus	$3.63^{+1.22}_{-0.79}$	6.64±0.10	187±37	130.17±26.0	1.62×10^9

that the radiative cooling is surely taking place and producing the cool gas in the central regions of galaxy clusters. Such suggestion could be supported from the fact that the radiative cooling time of typically 10^{8-9} yr is shorter than the Hubble time at the cluster center. The size of cool cores, that is $R_{\rm start}$ or $R_{\rm cool}$, is a few 100 kpc in general. The $T_{\rm center}$ distribute along the line of $T_{\rm center}/T_{\rm cluster} = 0.5$ although the temperature itself takes various values. The ratios of $T_{\rm center}/T_{\rm cluster}$ somewhat scatter in the range of 0.3−0.6 in fact. Centaurus cluster, MKW 4, and Hydra A cluster have exceptional ratios of 0.18, 0.77, and 0.90, respectively. These reflect their peculiar temperature profiles; Centaurus cluster shows the steep temperature gradient while Hydra A cluster and MKW 4 have milder temperature gradient than other clusters even in the central region. We also found out a weak correlation between $T_{\rm center}$ and $R_{\rm start}$, which is similar to the relation between the cluster-wide temperature and the overall cluster size. The systematic temperature structure understood here is much different from the cooling flow picture, although it is consistent on the point that the radiative cooling takes place.

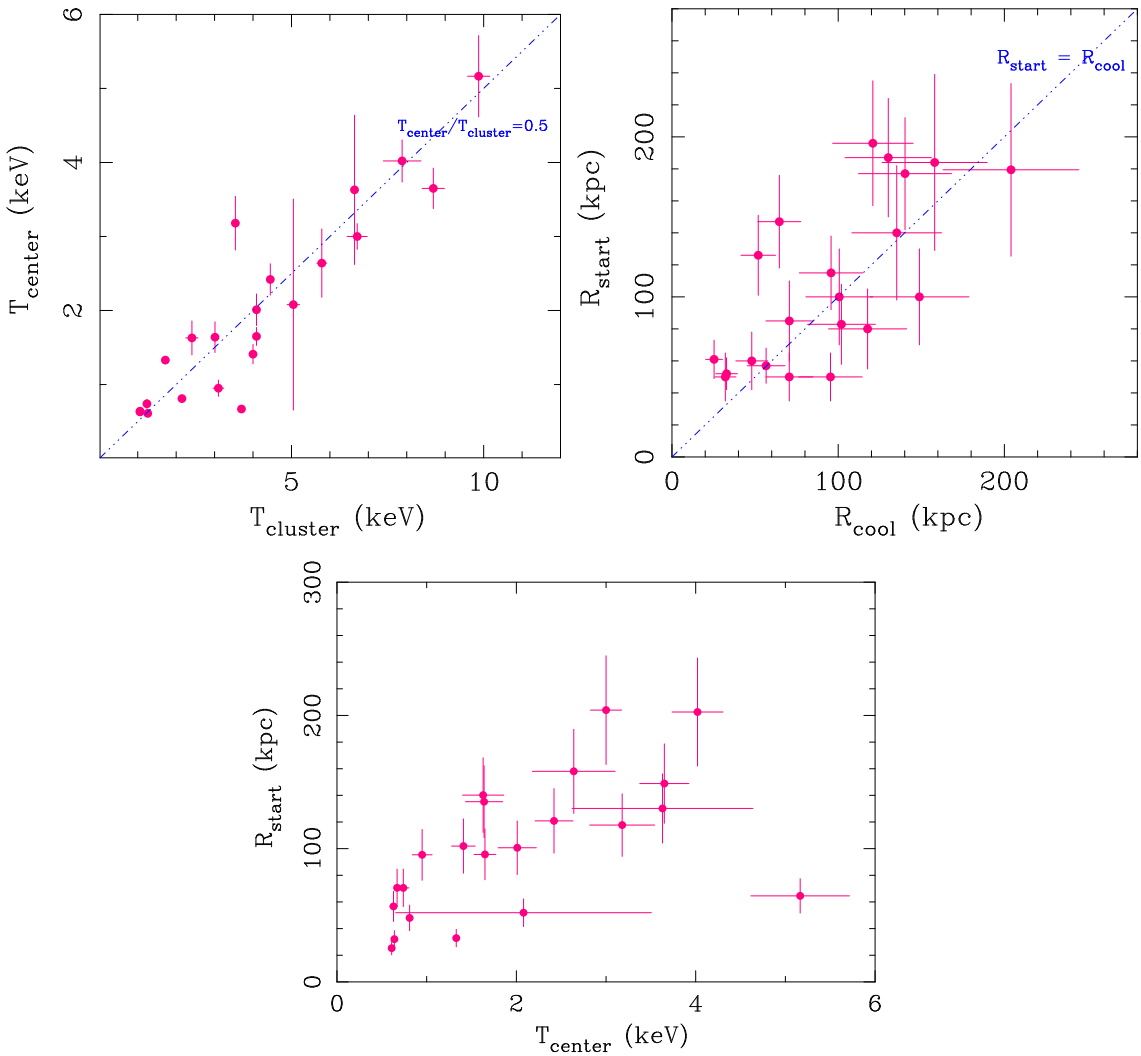

Figure 5.19: The relations of $R_{\rm start} - R_{\rm cool}$ (top left), $T_{\rm center} - T_{\rm cluster}$ (top right), and $R_{\rm start} - T_{\rm center}$ (bottom).

5.3.2 Mass of the Central Cool ICM

The cooling flow rate is an important quantity in order to know the amount of the central cool gas. We calculated the cooling rate $\dot{M}$ by following the equation of $\Delta L = \frac{5}{2}\frac{\dot{M}}{\mu m_{\rm H}} kT$ (equation 2.34). ΔL is the luminosity of the central cool gas, which is estimated from the emission measure obtained by two component fitting in §5.2.2. The temperature has been taken from $T_{\rm center}$ presented in table 5.4. The comparison of the cooling rate between our analysis and the previous observations is shown in figure 5.20 left. Our cooling flow rate is an order of magnitude smaller than the previous one at most as is the case with ASCA (Makishima et al. 2001). Since the cooling flow rate in the former observations are estimated from X-ray surface brightness profile which is limited in only the lower energy band of $\sim$0.2$-$3 keV, they are considered to be overestimated and the amount of cool gas accumulated by cooling flow is not so large in fact.

Additionally, the central excess of the absorption column density (§5.1.1) could

be one of the indicator for the amount of the cold gas, which is a result of the radiative cooling. In order to examine this, we firstly estimate the the central excess absorption $\Delta N_{\rm H}$, and then calculate the amount of the cold material by integrating $N_{\rm H}$ with the volume of the excess region. Here we deal with the galaxy clusters whose absorption profiles are well determined up to the outer region and show the central excess; 2A 0335+096, Abell 262, Abell 478, Centaurus cluster, Ophiuchus cluster, Perseus cluster, HCG 62, NGC 5044, NGC 533, and NGC507. When it is compared with the predicted mass by the cooling rate ($10^{11-13} M_{\odot}$) in the previous observations, the mass of the absorbing matter is again much smaller ($10^{9-11} M_{\odot}$) as shown in table 5.5. Therefore, we can conclude that there is no huge cold gas in the cluster center as the prediction of the cooling flow.

In the same way as the ICM mass estimation, the mass of the central cool gas can be calculated from the cool component emission measure obtained by the spectral fitting. Figure 5.20 right shows the mass of the cool gas against the cluster-wide ICM temperature. It is distributed typically in the range of $10^{10-12} M_{\odot}$, which is fairly higher than the amount of the interstellar medium (ISM). Since it is impossible to explain the central cool gas with only the ISM, such a cool gas is really associated with the galaxy clusters. This picture suggests the fact that the extent of the cool gas is larger by a factor of $\sim$3$-$5 than the size of the elliptical galaxies at the cluster centers. Some clusters such as Abell 262, MKW 4, and NGC533 show less mass of the central cool gas. This is because the region filled with the cool gas ($<15''$) is very small. Sérsic 159-03 also has a smaller mass of the cool gas due to low filling factor and somewhat narrower cool region.

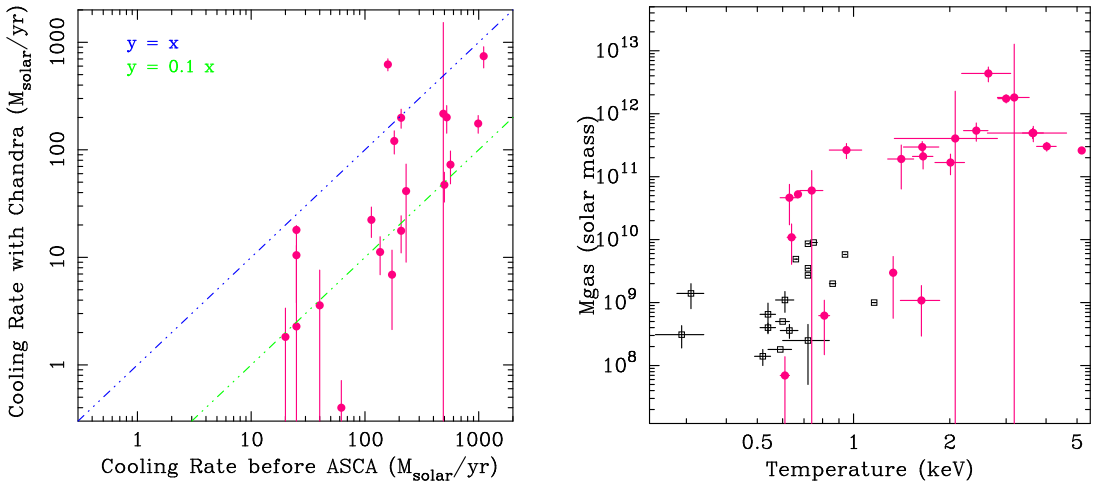

Figure 5.20: The comparison of our cooling flow rate with that obtained in the previous observations (left), and the mass of the central cool gas against the ICM temperature (right).

5.3.3 Correlation with Radio Properties

Radio emission is thought to be a indicator of the strong interaction between the radio lobes and the ICM at the cluster center (§5.2.1). Furthermore, some cooling

Table 5.5: The mass of central cool gas.

	$N_{\rm H}^a$ ($10^{22}{\rm cm}^{-2}$)	$\Delta N_{\rm H}^b$ ($10^{22}{\rm cm}^{-2}$)	radius^c (kpc)	$M_{N_{\rm H}}^d$ ($10^9\ M_\odot$)	$\dot{M}^e$ ($10^{11}\ M_\odot$)
2A 0335+096	23.7±1.7	2.6±2.6	91.3	33.6±2.69	27.2
Abell 262	10.9±1.6	5.9±2.6	28.4	5.85±2.46	9.3
Abell 478	30.2±1.0	4.0±1.9	154	151±9.08	149
Centaurus	22.2±1.3	12.4±1.7	19.9	2.98±0.298	3.8
HCG 62	13.3±1.8	7.5±3.6	35.9	11.5±5.51	–
NGC 507	16.0±4.6	13.2±6.0	66.3	88.7±74.5	6.0
NGC 5044	17.2±2.3	8.7±3.4	28.6	11.7±3.15	3.8
NGC 533	16.7±3.7	9.8±4.8	20.2	7.81±3.36	–
Ophiuchus	33.4±1.2	4.4±1.6	48.9	19.3±0.773	23.9
Perseus	13.5±0.6	3.0±0.8	31.2	2.01±0.101	31.2

a : the absorption column density at the cluster center.
b : the central excess of absorption column density.
c : the radius where the absorption column density is enhanced.
d : the mass of cool gas calculated with the central excess absorption.
e : the mass of cool gas calculated with the cooling flow rate

flow clusters are associated with the radio mini-halo, which implies the existence of the non-thermal electrons. It is interesting how our sample which have no mini-halo are connected to such clusters since it may give us the information about the origin of the mini-halos. Therefore, we investigate the radio parameters, such as radio flux, luminosity, and rotation measure, from the literature (i.e. Taylor et al. 2002). These quantities are summarized in table 5.6.

Following Gitti et al. (2004), we calculated the cooling flow power $\dot{M}kT/\mu m_{\rm p}$, by using the temperature and cooling flow rate obtained in our analysis (§5.3.2). We also estimate the radio power at 1.4 GHz from that at 5 GHz in table 5.6, and compare it with the cooling flow power. Figure 6.4.3 shows the results, together with the data of clusters which is associated with the radio mini-halo. Significant difference is not found between the clusters having the mini-halo or not. Gitti et al. conclude that the cooling flow power plays an leading role in powering the radio mini-halo because it is more than 2 orders of magnitude larger than the emitted radio power. Such consideration may be adopted to the clusters without mini-halo.

Taylor et al. (2002) have revealed a correlation between the cooling flow rate and rotation measure in the cooling flow clusters. This correlation implies the rotation measure reflects not the radio source but the properties of the clusters. We also plotted the rotation measure as function of cooling flow rate in the figure 6.4.3 right. However, remarkable correlation can not be found due to the large statistical errors. Since the errors are not presented in the results reported by Taylor et al. (2002), we can not understand whether it is reliable. If such correlation is really confirmed, it actually shift to right by factor of $\sim$0.5$-$1 because they use the larger

cooling rate obtained in previous observations.

Table 5.6: The radio properties of cooling flow clusters.

	Radio Source	S_{5000} (Jy)	$RM(1+z)^2$ (rad m^{-2})	P_{5000} (erg s^{-1})	$P_{\rm radio}$ (erg s^{-1})	$P_{\rm CF}$ (erg s^{-1})
Perseus	3C 84	50	–	7.9×10^{25}	8.7×10^{40}	$6.6\pm1.3\times10^{43}$
Hydra A	3C 218	14	-12000	2.0×10^{26}	2.2×10^{41}	$3.8\pm23\times10^{43}$
Centaurus	1246-410	1.4	1500	6.3×10^{25}	6.9×10^{40}	$3.3\pm0.32\times10^{42}$
Abell 2052	3C 317	1.0	-800	5.0×10^{24}	5.5×10^{39}	$3.5\pm1.1\times10^{42}$
Abell 2199	3C 338	0.48	2000	2.0×10^{24}	2.1×10^{30}	$3.6\pm1.4\times10^{42}$
Abell 1795	4C 26.42	0.26	3000	4.0×10^{24}	4.4×10^{39}	$5.8\pm1.7\times10^{43}$
Abell 4059	2354-350	0.11	-1500	1.0×10^{24}	1.1×10^{39}	$1.4\pm0.96\times10^{42}$
Abell 2029	1508+059	0.10	-8000	2.5×10^{24}	2.8×10^{39}	$2.1\pm0.63\times10^{43}$

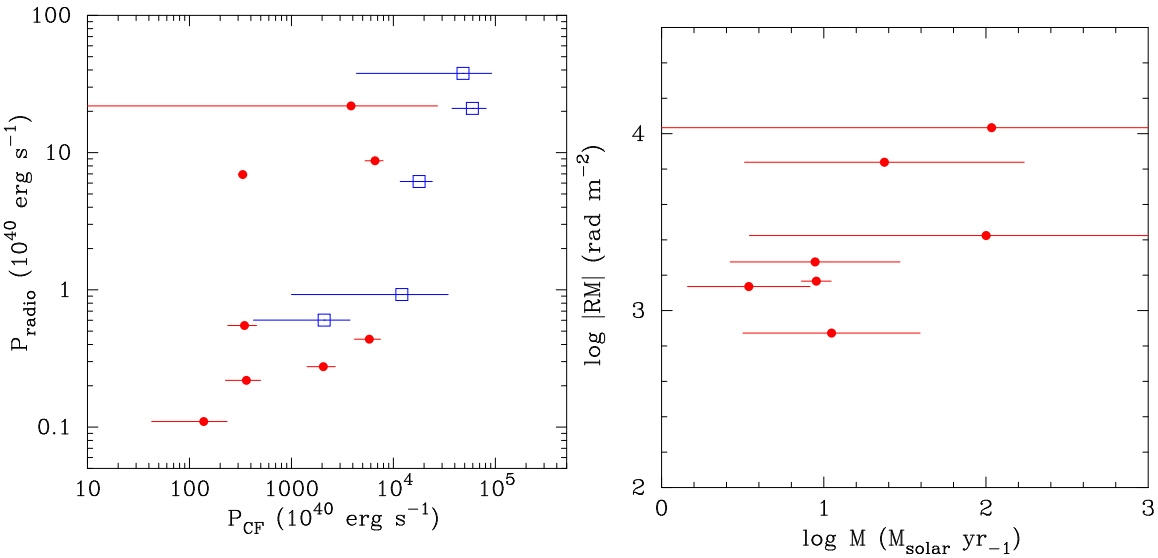

Figure 5.21: The correlations of $R_{\rm radio} - P_{\rm CF}$ (left) and $\dot{M}-$RM (right). The filled circle (red) in both panel is our results while the open square (blue) is the results quoted from Gitti et al. (2004).

5.4 Possibility of Excess Hard X-ray

Among our samples, Abell 2199 is the only target exhibiting the sign of the non-thermal hard X-ray in the observation of BeppoSAX. Although Chandra's field of view is smaller than the other instruments and then thermal flux is intense, we here tried to explore the excess hard X-ray emission from Abell 2199. To do this, we fit the spectrum with three component model; thermal emission (MEKAL), point source (powerlaw), and non-thermal emission (powerlaw). The photon indices of the powerlaws are assumed to be 1.5 and 2.0, for the point source and the non-thermal component, respectively. These assumptions are rather crucial one for the detection of the excess hard X-ray in order not to over-estimate it. Since the thermal emission become dominant as close as the cluster center, the spectrum is integrated up to 3 arcmin from the cluster center. Furthermore, we exclude the central 0.5 arcmin region due to avoiding the contribution of the powerful radio source at the center of Abell 2199. The point sources are detected with the script, *wavedetect* as shown in figure 5.22 left. Their total emission is so faint as $(7.1 \pm 1.6) \times 10^{-14}$ erg s^{-1} cm^{-2} with the photon index of $\Gamma = 1.5$. Thus, there are 5 free parameters, one of which is the non-thermal normalization, and the others are the ICM temperature, metal abundance, absorption column density, and the normalization of the thermal component.

When the spectrum is fitted with this model, the ICM temperature has become high contrary to our expectation (around 5.5 keV). The metal abundance also show higher values of $\sim$0.5 solar. Therefore, we fixed them with the value of 4.98 keV and 0.41 solar which are suspected from the radial profiles of the ICM temperature and metal abundance (figure 5.10, 5.11 and Appendix C). We re-fit the spectra with the revised model. Then, it is found that the flux of the non-thermal emission is comparable to that of the thermal one. This is inconsistent with the past results that the non-thermal component possess only 10$-$20 % flux of the thermal one, implying that the non-thermal emission is over-estimated here. In order to overcome this problem, we eliminate the non-thermal powerlaw from the fitting model and tried to estimate the non-thermal photon counts as the residual counts remaining after the thermal and the point source photons are subtracted from the total number counts. When the spectrum is fitted with two component model without the non-thermal emission, the thermal normalization has been increased by a factor of 2$-$3 than that above. Figure 5.22 right shows the spectrum with the model of each component. The enhancement of the fitting residual cen be seen above $\sim$5 keV, which would be considered to be originated from the excess hard X-ray. We hence use the energy band of 4$-$8 keV to examine the excess hard emission. The total source count in the 4$-$8 keV is 10990 counts while the total background count (CXB+NXB) is 1440. By the fitting results, the thermal emission count is 8337. The contribution of the point sources corresponds to 98 photon counts from the estimation with the *wavedetect*. As a result, their resulting number count becomes 1115 counts ($10990 - 1440 - 8337 - 98 = 1115$), which is equal to the flux of 5.1×10^{-12} erg s^{-1} cm^{-2} in the 2$-$10 keV. The photon index $\Gamma = 2.0$ is assumed here.

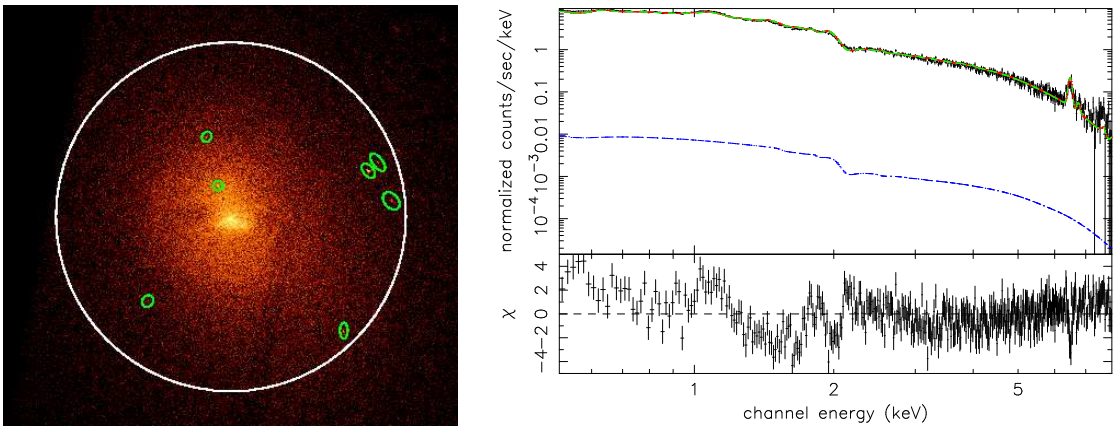

Figure 5.22: The X-ray image (left) and the spectra (right) of Abell 2199. The white circle in the left panel shows the central 3 arcmin region. The green circles represent the point sources contained in this region. In the right panel, the black cross are the data point, and the red line indicates the best fit model, which is the sum of the thermal emission (green) and the point sources (blue).

Here, let us discuss the statistical and systematic fluctuation of the residual hard X-rays. The statistical errors is calculated as the sum of statistical fluctuation caused by the source and background counts. The source fluctuation simply become $\sqrt{10990} = 105$ counts. For the background, it should be corrected by the exposure time of the background observation; $\sqrt{1440/t_{\rm SRC} \times t_{\rm BGD} \times t_{\rm SRC}/t_{\rm BGD}} = 15$ counts, where $t_{\rm SRC}$ and $t_{\rm BGD}$ represent the exposure time of the source and the background (18922 sec and 114890 sec). The total statistical error then become 120 counts. Next, we consider the systematic errors. The contribution of emission form galaxy clusters is negligible in the spectrum of the outer region, and then the source count rate in higher energy would correspond to that of background. We estimate the systematic fluctuation of the background (CXB+NXB) by comparing the source and background count rate with the spectra, which is extracted from the region between 3−4 arcmin in 8−10 keV. The systematic error has been known as ∼15 % of the background rate, i.e. 216 counts.

For the point source, the fluctuation is already known as 22 % of the its source count number, and then results in 98×0.22 = 15 counts. The thermal fluctuation is caused by the determination accuracy of the normalization in the MEKAL component and it becomes 35 counts. Moreover, we consider the fluctuation due to the fitting model, which is presented as the difference of the thermal counts when another model is utilized. We here treat APEC and Raymond-Smith model other than MEKAL model. This contribution is rather large as 297 counts. Taking these statistical and systematic fluctuation account, the resulting flux of the non-thermal emission is described as $5.1 \pm 0.55 \pm 4.0 \times 10^{-12}$ erg s^{-1} cm^{-2}. The total fluctuation results in fairly large, indicating that we can not find a strong sign of the non-thermal emission. Moreover, it is not revealed whether the excess emission extends up to the outside of the Chandra's field of view. Therefore, we aspire to detect the non-thermal emission from galaxy clusters by means of Suzaku data in the later (§5.6.3).

The PIN detector onboard Suzaku has achieved the lowest background than the previous instrument in a few tens keV band, where the effective measurement of the non-thermal emission is possible without the thermal contribution.

Table 5.7: The summary of the excess hard X-ray from Abell 2199.

item	number counts	statistical errors	systematic errors
Source total	10990	±105	–
Background	-1440	±15	±216
Thermal plasma	-8337	–	±35
Model dependence	–	–	±611
Point source	-98	–	±15
sum	1115	±120	±877

5.5 HXD PIN Background

5.5.1 Basic Properties of HXD PIN Background

In the satellite orbit, the background mainly consists of CXB and NXB (3.3.3). The CXB, which distributes almost uniform over the whole sky, is extensively investigated by the previous satellite, such as HEAO-1, Ginga, and ASCA. Therefore, its flux and spectrum shape are well known. On the other hand, The NXB originating from the charged particles is different from detector to detector according to its design or materials constituting it. We then have to develop the NXB estimation method suitable for each detector. In this section, we introduce the basic properties of the NXB for HXD PIN detector. Hereafter, we call the NXB of PIN simply as background.

There are two kinds of key components affecting the background count rate for the satellites launched from Japan which take low earth orbit (LEO) and typically have the inclination of 30° against the earth. The first item is the cutoff rigidity (COR). The background rate becomes higher at the position on the earth where the COR is low as mentioned in §4.3. The positional difference of the COR is caused by the slight misalignenemt between earth center and that of the magnetic dipole. Figure 5.23 shows the COR distribution in the typical orbital region of the Japanese satellite superposed on the earth map. On the sky of America southward or zonal area between the Africa southward and Australia, the COR is the lowest (then the highest background), while it becomes the highest on the sky of the Southeast Asia or Atlantic Ocean. Thus, the background of PIN detector has positional variation according to the satellite moving on the earth. The strong correlation between the background rate and COR (or PINUD which is charged particle monitor equipped with HXD) indicates that the COR component dominates the variation of PIN background (§5.30).

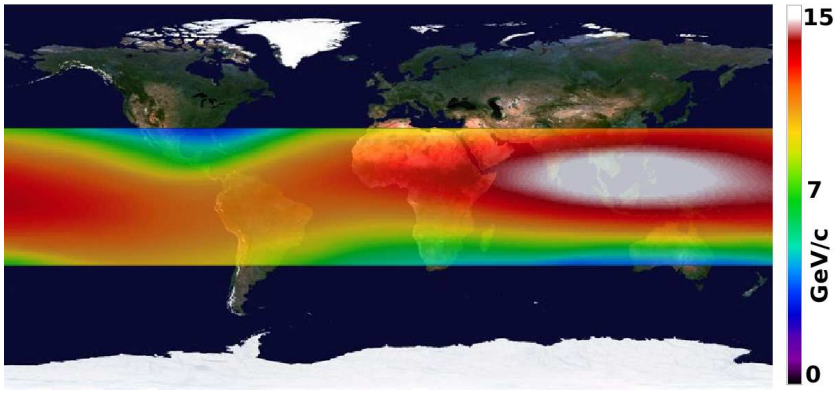

Figure 5.23: The COR distribution superposed on the photograph of the earth obtained from Japan Aerospace Exploration Agency (JAXA).

On the sky of Brazil, the earth's magnetic field becomes aberrant, where the radiation belt above the earth's magnetic field comes down to the satellite orbit due to the same reason as the COR distribution. This region is called South Atlantic

Anormaly (SAA). As shown in figure 5.24, the detector receive about 1000 times large amount of protons there. When a large amount of protons penetrate a detector through the SAA passage of satellite, the atomic nuclei of detector materials are excited and changed to the radioactive isotopes, which create irrelievable background. Such activation effect is the second item contributing to the PIN background. In the case of HXD, although PIN is almost free against the activation, GSO is significantly activated because the amount of activation depends on the stopping power and volume of each sensor. The X-rays by the GSO activation come into the PIN and become background. Furthermore, the activation creates various radioactive isotopes which have different half-life periods. This means that the spectrum of activation background exhibit complex variations as time goes by. We can roughly divide it into three components; the short, middle, and long-term component. The short-term variation within a day is made by the radioactive isotopes which decay rapidly with the time scale of <10000 sec after the passage of SAA. Then, this component becomes intense just after the SAA. The middle-term variation is caused by the Suzaku's orbital shift of $\sim 7^{\circ}$ against the earth longitude per one day, and hence it has 50 days period. Since the orbital shift bring the different path across the SAA, the number of incoming protons varies with 50 days period, and then background from radioactive isotopes with a decay time of several days also changes in the same manner. In fact, this phenomenon is clearly recognized with the PINUD count history as well as that of WAM (figure 5.25). The last component, long-term variation, is originated from the long-lived radioactive isotope with a decay time of several tens to hundred days. Long-lived radioactive isotopes begin to decay after the launch, and the background is gradually accumulated with time. The accumulation continues until the generation rate of the long-lived radioactive isotopes come to be equilibrium with the decay rate, which is called radiation equilibrium, is realized. Since the increase of the long-term background saturates after the radiation equilibrium, it is considered to exhibit the time evolution such as the exponential function. The enhancement of the baseline in WAM background light curve (figure 5.25) reflects the long-term transition. In this manner, the PIN background is ever-changing, depending on these four factors.

Figure 5.26 is the right curves obtained from the observation of North Polar Spur during $\sim$1.5 day which is regarded as the background for HXD PIN. Because of the COR variation, the light curve shows the sustained fluctuation over the observation in all the energy band. We also see the rate enhancement around 70000 sec after the beginning of the observation due to the shot-term variation of PIN activation background. The shot-term effect seems to become strong in the lower energy although it is hard to see from their ratio with this photon statistics. Meanwhile, figure 5.27 left is the background spectra obtained from the North Ecliptic Polar (NEP) observation on two epochs of September 2, 2005 and February 10, 2006. In the bottom panel of the figure, we can easily see that the flux of these spectra is different as much as $\sim$10 % in spite of the same target. Such difference is considered to be caused by the variation of PIN background. This is extremely serious to the faint non-thermal emission from clusters of galaxies. Furthermore, we divided the spectrum of the second observation into two periods within 6000 sec after SAA

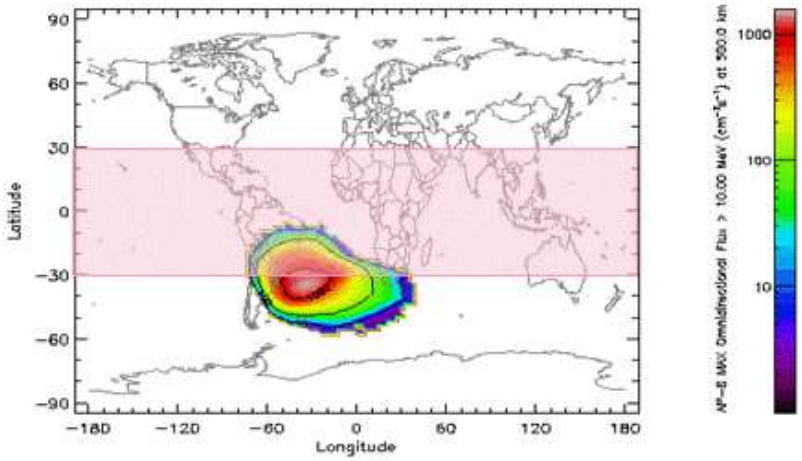

Figure 5.24: The distribution of the atomic protons trapped by the magnetic field of the earth at an latitude of 500 km.

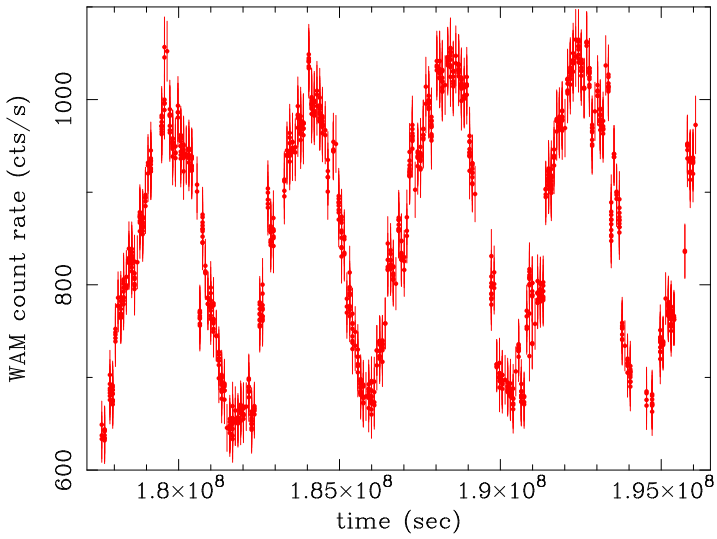

Figure 5.25: The light curve of WAM background during 7 months after launch. The remarkable period about 50 days and the baseline enhancement of count rate are seen.

passage and others, as shown in figure 5.27 right. The spectral shape in the lower energy is slightly different by the activation effect through the SAA.

Furthermore, we should take care the background behavior by the temperature change of the sensors. Although the heat pipes to control the temperature of the sensors are equipped with the satellite, one of two systems has been dysfunctional. Therefore, when a observation is performed in the large Sun angle, which is defined as the angle from the line-of-sight direction of the satellite (z-axis) to the direction of the Sun, the HXD sensors are warmed by the Sun. This gives rise to the enhancement of the thermal noise in the lower energy. Such effect appears in the spectra above -12°C in some degree. Though the events below a certain energy, which is set for

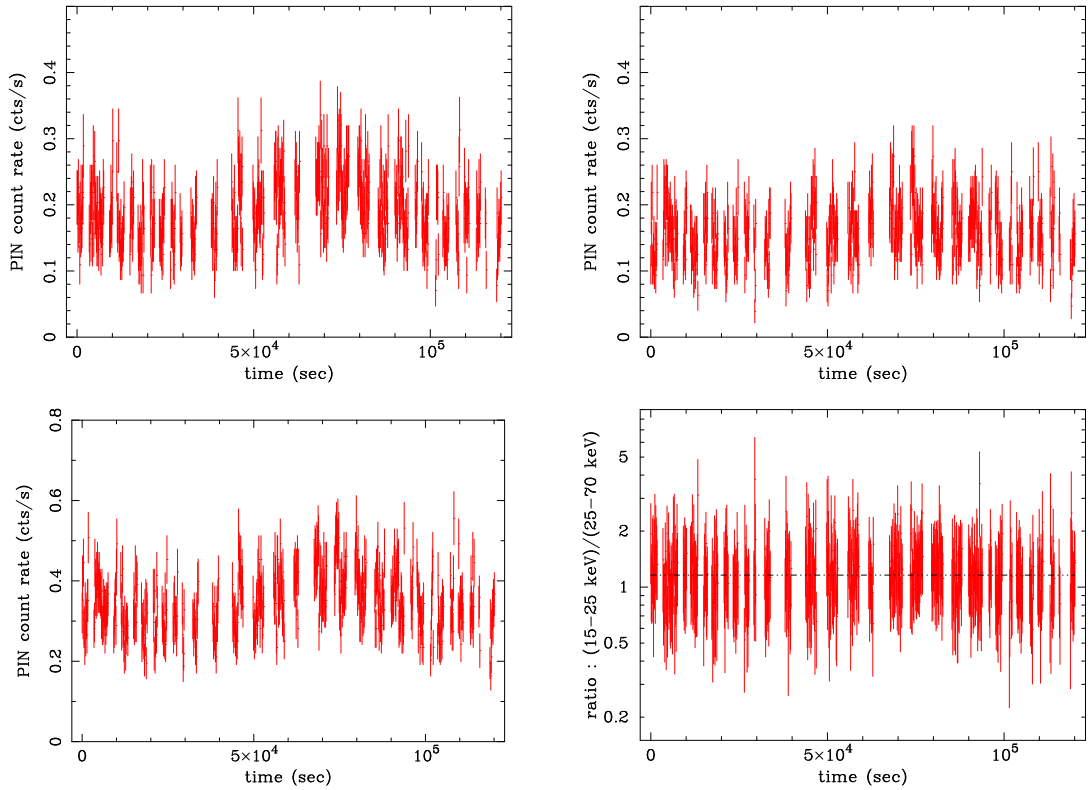

Figure 5.26: The light curve of North Polar Spur in the energy band of 15-25 (top left), 25-70 (top right), and 15-70 (bottom left) keV. The panel of bottom right is the softness ratio curve of (15-70 keV)/(25-70 keV).

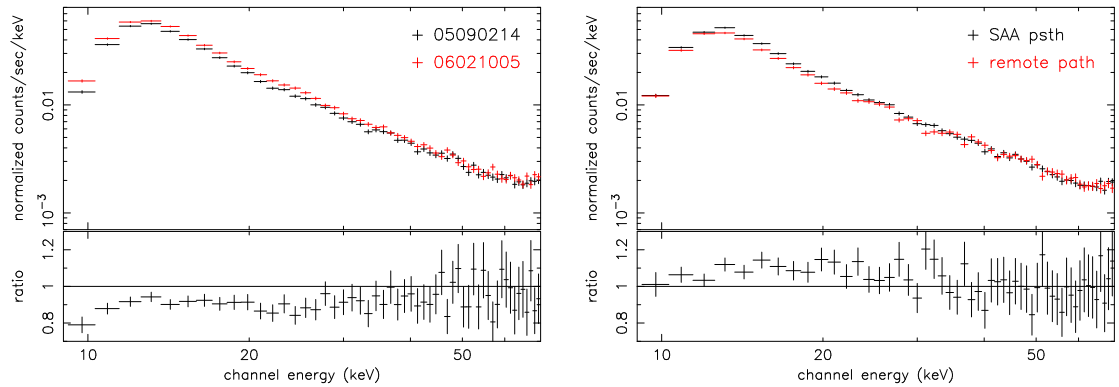

Figure 5.27: The spectra comparisons between two observations of the North Ecliptic Polar (left), and with or without the SAA passage of the second observation (right).

each PIN sensor, are rejected by the analogue and digital electronics in the orbit and the ground software, we discard the data obtained in the high temperature period to keep good data quality.

5.5.2 Background Template Map

The PIN background is mainly determined by COR dependency and the short-term component, and the contribution of the middle and long-term background

is relatively small. Therefore, we first estimate the background variation due to the COR and short-term activation. For this purpose, we extract the background template map which is sorted with the longitude and latitude on the earth. To do this, we used the earth occultation data (i.e. elevation < -5) from September 2, 2005 to March 11, 2006. The events selection with anti-coincidence by means of the hit pattern around 8 sensors is already performed. In addition to that, the events for the background map are carefully selected from the data through four procedure; the rejection of the events during the SAA period, the noise cut in the lower energy with the channel of Anode-LD + 5 where Anode-LD is the lower cutoff channel of the events, the rejection in the period of the temperature above -13°C. As a result, the total exposure becomes $\sim$ 2 Msec.

The background map is supposed to exhibit the different appearance according to whether the satellite undergoes the SAA passage or not (moving upward or downward). Therefore, we extract two kinds of maps with or without the SAA passage which are defined whether the satellite moves upward or downward. Furthermore, we should divide the background map into some energy band in order to look at the energy dependence and obtain the energy spectra of the PIN background. Since the observation of the non-thermal emission from galaxy clusters is under the statistically restricted condition, we prepared only the eight energy bins. The energy range for each bin is set as 0$-$11, 11$-$15, 15$-$20, 20$-$25, 25$-$32.5, 32.5$-$45, 45$-$70, and 70$-$90 keV, taking account that all the energy bins have the similar photon counts. The count rate of the PIN background between 15-70 is $\sim$0.4 cts/s. Then, the background count contained in the 1$\times$1 degree pixel become $\sim$35 counts. Considering to divide these into 8 energy band for each map with or without the SAA passage, the counts in 1 pixel reduced to only a few counts or less. In order to break up the lack of photon statistics, the background map is binned by 3$\times$3 degree which is the maximum size not to loss the positional dependences of PIN background and corresponds to 100 sec when converted to the time that the satellite pass through. Finally, the photon counts in 1 pixel become $\sim$20 counts with statistical error of $\sim$20 %.

The background template maps are shown in figure 5.28. Compared with the COR map (figure 5.23), the inverse correlation between the background rate and COR can be plainly found in each map. The difference with or without SAA passage also seen; on the upper right of SAA region around the longitude of 0$-$50° and latitude of 0$-$30°, the count rate of the PIN background is enhanced in the figures with SAA passage. In order to study the energy dependence of the background map, the softness ratio is also extracted. The softness ratio is defined as the ratio of the count rate in the 15$-$20 keV to that in the 32.5$-$45 keV. There are no remarkable trend in the softness map although it may become somewhat softer than the surroundings in the region just after the SAA .

Here, we examine the properties of the background generated from the template maps, by using the observational data of the background region or the source as faint as background for the PIN. The background is extracted on the condition that the COR $>$ 6, and at least 500 sec after the SAA passage in order to make the data quality high. We calculate the residuals of $(R_{source}\text{-}R_{background})/R_{background}$ in

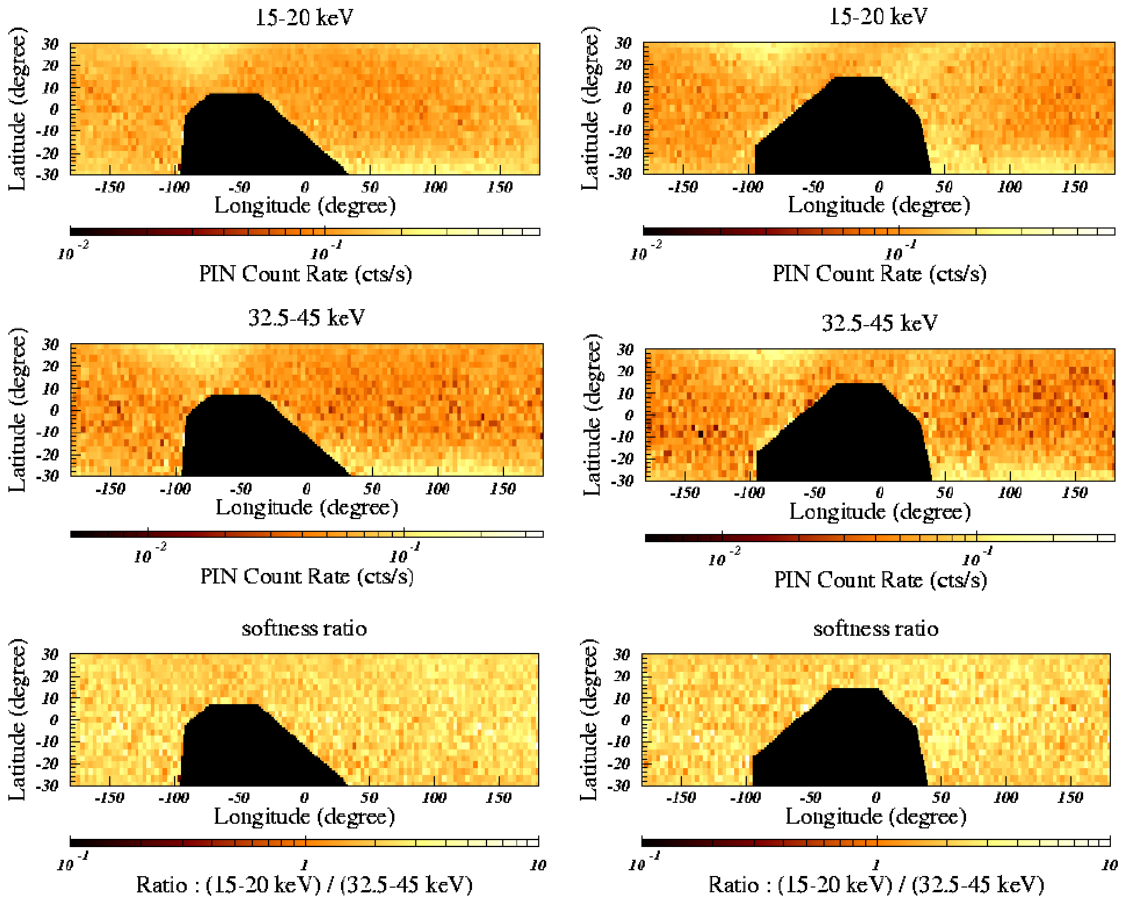

Figure 5.28: The background template maps in the energy band of 15−20 keV (top) and 32.5−45 keV (middle), and their ratio (bottom). The maps without SAA passage are shown in left hand while that with SAA are in right hand.

each observation, where R_{source} and $R_{background}$ are the averaged count rate of the observed source and the background estimated from the background map. The R_{source} contains not only the NXB but also CXB. Then, the residuals distribute around 1.05 because the count rate of the CXB is ∼5 % of the NXB rate. Figure 5.29 plots the residuals against the observation time. All the data show positive values around the CXB count rate as expected. However, a monotone increase by ∼10 % is clearly seen during half year. This is thought to indicate that the background template map can not represent the time variation of the middle and long-term component due to the activation. In other words, the effect of these component have been averaged in the background template map. We hence take account the time variation of the middle and long-term into the background map by fitting the light curve of the background data in the next section.

5.5.3 Time Variability of Background

In order to estimate the middle and long-term variation due to activation on the background map, we fit the light curve and obtain the parameters of the time variation factors. The light curve is extracted on the same data selection and conditions

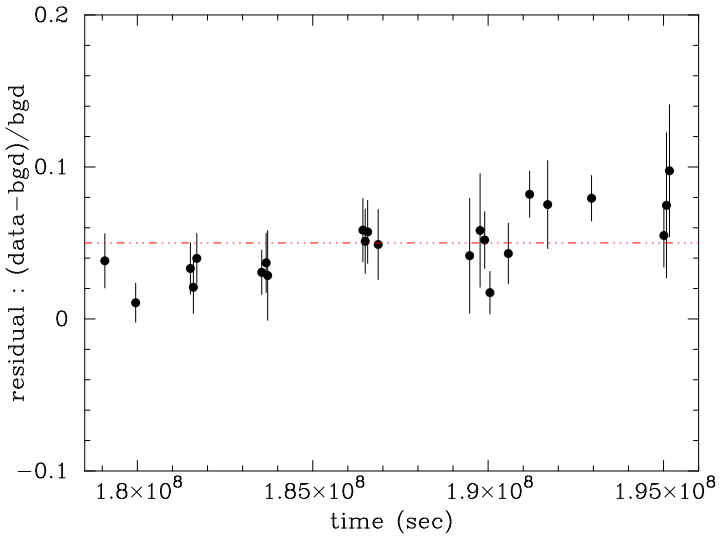

Figure 5.29: The residuals of the count rate between the observation data and estimated background (R_{source}-$R_{background}$)/$R_{background}$of against time.

as the background map, and is integrated in each 800 sec. The energy band is restricted to 15−70 keV. The fitting model consists of four components according to the background component. The middle-term activation component is represented as the sine curve in which the period is fixed to 50 days and the phase of the sine wave is a free parameter to be fitted. For the long-term variation, we applied the exponential function, which saturates with a certain decay time constant as mentioned above. We also have to model the remaining two components, i.e. the COR dependence and the shortterm variation of activation, as accurate as possible because they are main component of the PIN background.

On the COR dependence of the PIN background, the PINUD counter would reflect the number of charged particles incoming into the PIN as well as the COR values. The PINUD is the upper discriminator equipped with the PIN which counts the signals above 100 keV. Since the high voltage is applied to the PIN even during the SAA passage and the PINUD is always counted up, it can monitor the charged particles. We investigate the correlation of COR and PINUD with the background count rate to investigate which parameter should be utilized. The results are shown in figure 5.30. The PINUD counts seems to exhibit the tighter correlation with the background rate than the COR, and the correlation is almost linear. In fact, the dispersion of PINUD plot is ∼0.03 counts in root-mean-square (RMS) which is smaller than that of COR plot (∼0.06) when they are fitted with the linear function. The PINUD is considered to reflect the actual amount of the protons more directly.The COR map utilized for the Suzaku operation was made about 20 years ago for the Ginga satellite. This suggests a possibility that actual COR distribution is slightly changed by the secular variation of the earth's magnetic field. Therefore, we use the PINUD count as the COR-dependent component of PIN background. When the correlation between the PIN background and PINUD is fitted with a linear function, the residuals exhibit a concave trend as shown in figure 5.31 left. This indicates that they do not follow the proportionality relation exactly. Then,

we tried to fit by other functions such as quadratic function and power function. The fitting is obviously improved by using these functions. The reduced χ^2 are 1.29, 1.04, and 1.05 for linear, quadratic, and power function, respectively. We hence decide to utilize quadratic function for the relation between PIN background rate and PINUD count although its fitting accuracy is almost the same as that for power function. The fitting result with the quadratic function is shown in figure 5.31 right.

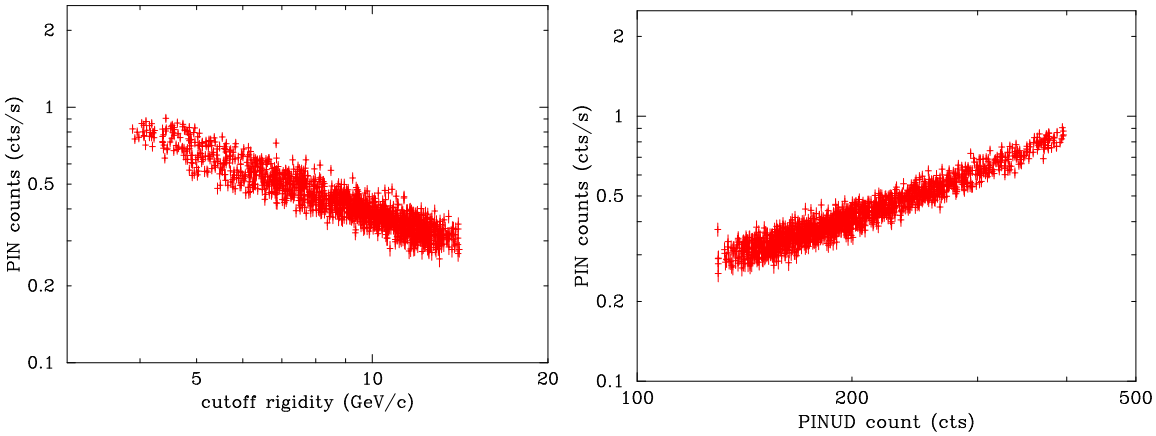

Figure 5.30: The PIN background distribution against the COR (left) and the PINUD count (right).

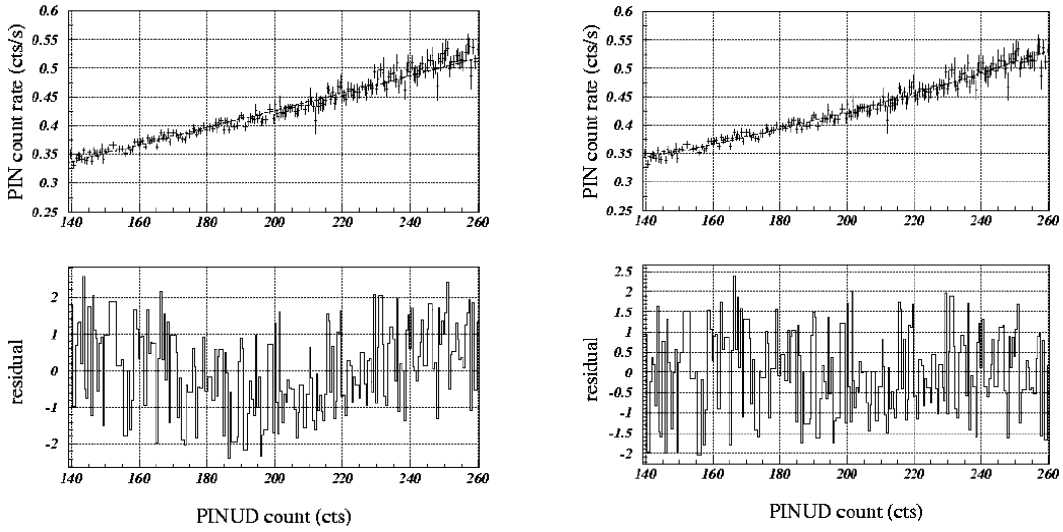

Figure 5.31: The fitting results of the relation between the PIN background rate and PINUD count by means of a linear (left) and quadratic (right) functions.

The last is the short-term component due to the activation. The light curve after the SAA passage is found to be represented well by the integrated PINUD count with a certain decay time constant, i.e. the function such as $\int (PINUD \times \exp(-t/\tau))\ dt$, by the study of HXD team. Figure 5.32 left is the light curve of the PINUD count during $\sim$ 2 days. When the decay constant of 12500 sec is assumed, the shape of integrated PINUD becomes as shown in the figure 5.32 right. The

decay time constant should be determined from some representative half-life periods of the radioactive isotopes which emit the intense X-ray. However, it is difficult to understand the line composition and their intensity due to the activation on the orbit because they changes rapidly and intricately depending on how the satellite pass the SAA region, and the background study of GSO have not been progressed well. Therefor, we prepare the integrated PINUD count with 10 different decay time constant of 5000, 7000, 8000, 9000, 10000, 11500, 12500, 13500, 15000, and 50000 sec. Among them, we select the decay time constant which minimizes the χ^2 in the light curve fitting. The χ^2 against the decay time is shown in the figure 5.33. As a result, we determine the decay time constant to be 12500 sec, which leads the smallest $/chi^2$.

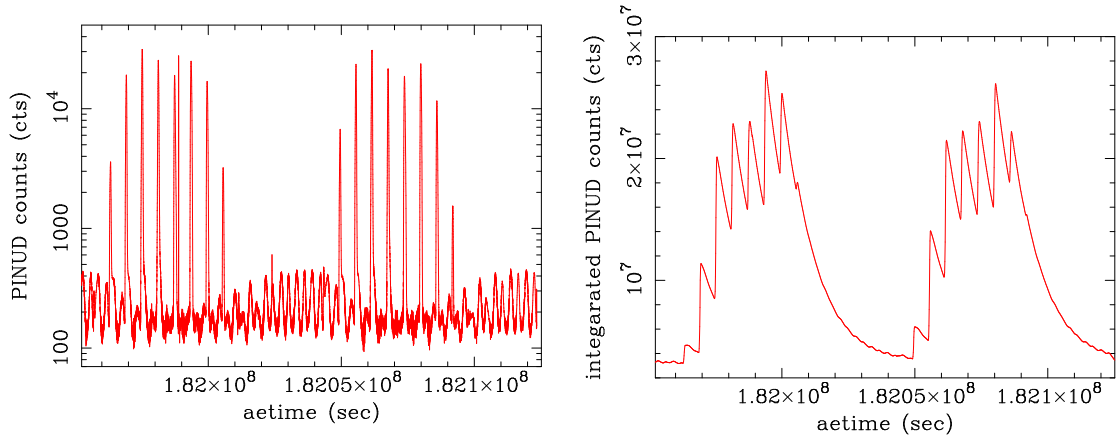

Figure 5.32: The light curves of PINUD count (left) and integrated PINUD count with the decay time of 12500 sec.

Now, the final form of the fitting model is represented as

$$\begin{aligned} BGD(t) &= A \times PINUD^2 + B \times PINUD + C \\ &+ D \times \left(\int PINUD \right)^E \\ &+ F \times (1 + \sin(2\pi \times 2.3 \times 10^{-7} \times (t - G))) \\ &+ H \times (1 - I \times \exp(-t/J)) \\ &+ K \quad (constant). \end{aligned} \tag{5.3}$$

There are 11 free parameters in this model (A to K). The constant 2.3×10^{-7} is the inverse number of the 50 days in unit of second. When the background light curves with or without SAA passage are fitted with this model, the decay time parameters (J) of the long term component different by an orders of magnitude among them. This parameter is considered not to be largely different between them. Then, we fixed the parameter J by the value obtained with the fitting of the summed light curve (i.e . the sum of the data with and without SAA). The phase parameters

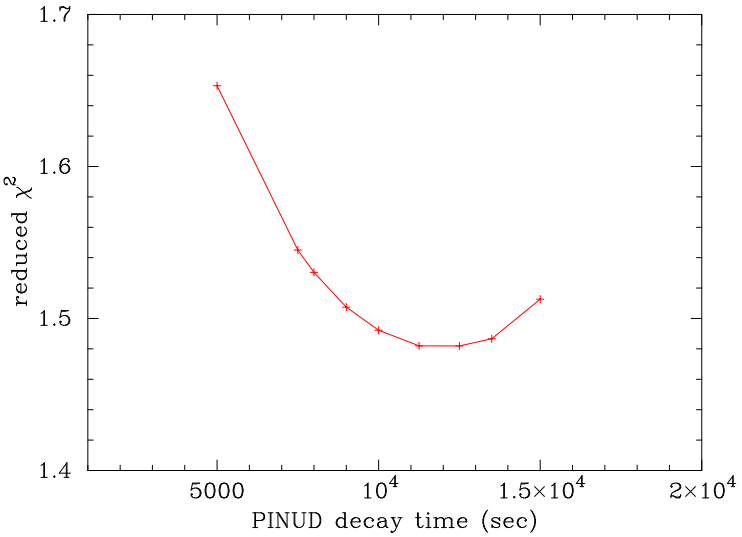

Figure 5.33: The χ^2 against the PINUD decay time in the light curve fitting of the PIN background.

(G) of middle-term component are also fixed the values in this manner by the same reason. Since the constant parameter C and K can be treated with one parameter, the free parameters in the model function are reduced into 8, and we tried to fit again the light curves with or without the SAA passage, respectively.

Figure 5.34 shows their light curves and the residual in the 15−70 keV band. The reduced χ^2 are 1.7 and 1.3 for the light curve with or without the SAA passage. Then, we can consider that the fittings are performed well. The best-fit parameters are summarized in table 5.8. The timing parameters such as G and J are shown in unit of second. The COR depending component predictably occupies the largest fraction, ∼70 % of total background rate. The parameters of the middle and long-term component are consistent between the light curve with and without SAA. The background variation of the long-term component is about 3 % while that of middle-term component is quite small (∼1 % or less). We also fit the right curves divided into two energy bands of 15−25 and 25−70. The fitting parameters are listed in table 5.9. Although the parameters between the COR and short-term component varies according to the energy band as shown in figure 5.26, they change only within the fitting errors except for the normalization of the long-term component. However, the difference corresponds to < 1 % of the background time variation, implying that the energy dependence is negligible. Then, we use the results for the total energy band (table 5.8) as the time variation factor to correct the background map. More specifically, we treat the ratio of the count rate at the moment to that averaged overall period as the time variation factor, and multiplied it by the positional count rate obtained from the temperature map.

After the correction of the background map with time variation factor, we again

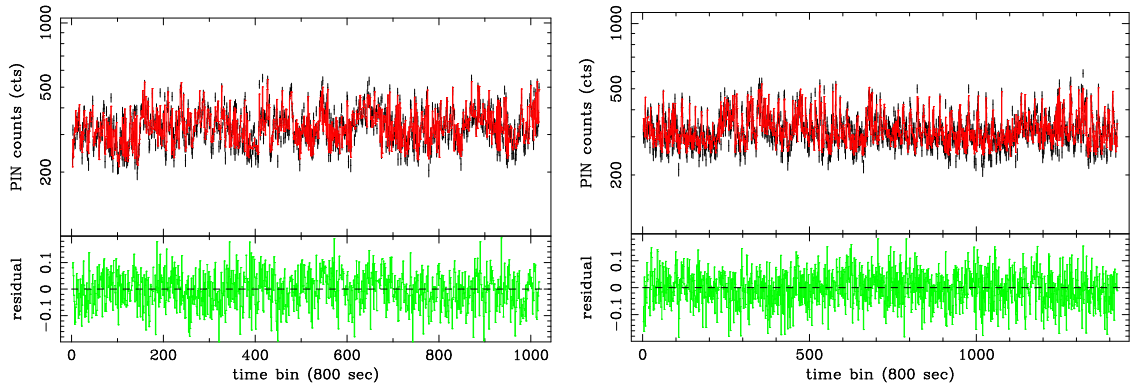

Figure 5.34: The light curves with (left) and without (right) the SAA passage fitted with the model function of the PIN background.

Table 5.8: Best fit parameters of the total band light curves.

parameters†		upward path	downward path
COR	norm (A)	$(2.38\pm0.039)\times10^{-6}$	$(1.94\pm0.030)\times10^{-6}$
	norm (B)	$(11.33\pm0.28)\times10^{-4}$	$(8.83\pm0.29)\times10^{-4}$
short-term	norm (D)	$(13.81\pm2.19)\times10^{-14}$	$(6.87\pm0.91)\times10^{-14}$
	index (E)	1.59 ± 0.0093	1.64 ± 0.0077
middle-term	norm (F)	$(1.45\pm0.96)\times10^{-3}$	$(2.96\pm0.95)\times10^{-3}$
	phase (G)*	5.06×10^{6} (fixed)	5.06×10^{6} (fixed)
long-term	norm (H)	0.093 ± 0.0048	0.098 ± 0.0063
	norm (I)	0.84 ± 0.13	0.97 ± 0.13
	tau (J)*	3.34×10^{6} (fixed)	3.34×10^{6} (fixed)
constant	(C+K)	0.042 ± 0.0048	0.0015 ± 0.0080

† : The alphabets in the parenthetic correspond to parameters denoted in the formula of the model function.
∗ : presented in the unit of sec.

estimate the residuals for the background or faint source observations. Figure 5.35 shows the result. Compared with that before the correction, the deviation of the residuals obviously reduced by a factor of ~ 2 and reaches at $\sim$5 %, which is within the statistical fluctuation. The background estimated in our procedure is considered to have enough accuracy.

5.5.4 Properties of the Estimated Background

The background generated from the background template maps after the time variation correction have reached at good reproductive accuracy. We here investigate the systematic error and some features of the estimated background. At first, the estimated backgrounds are compared with with the actual earth occultation data. We select the data which have the exposure of the observation longer than 3000 sec ($\sim$1000 counts). The comparison of the count rates between the background

Table 5.9: Best fit parameters of the total band light curves.

parameters†		upward path		downward path		
		15-20 keV	20-70 keV	15-20 keV	20-70 keV	
COR	norm (A)	1.21±0.030	1.17±0.013	1.03±0.029	0.94±0.021	$\times 10^{-6}$
	norm (B)	4.14±0.21	4.67±0.09	5.08±0.25	6.13±0.21	$\times 10^{-4}$
short-term	norm (D)	16.8±2.74	0.70±0.09	2.70±0.50	9.04±3.09	$\times 10^{-14}$
	index (E)	1.56±0.0096	1.69±0.0074	1.67±0.011	1.56±0.020	
middle-term	norm (F)	5.57±6.92	9.23±6.12	3.97±6.96	25.6±6.42	$\times 10^{-4}$
	phase (G)*	5.06 (fixed)	5.06 (fixed)	5.06 (fixed)	5.06 (fixed)	$\times 10^{6}$
long-term	norm (H)	0.037±0.0035	0.057±0.0024	0.068±0.0027	0.028±0.0036	
	norm (I)	0.94±0.71	0.76±0.13	0.99±0.99	0.99±0.95	
	tau (J)*	3.34 (fixed)	3.34 (fixed)	3.34 (fixed)	3.34 (fixed)	$\times 10^{6}$
constant	(C+K)	0.041±0.004	0.00±0.044	0.00±0.050	0.005±0.004	

† : The alphabets in the parenthetic correspond to parameters denoted in the formula of the model function.
∗ : presented in the unit of sec.

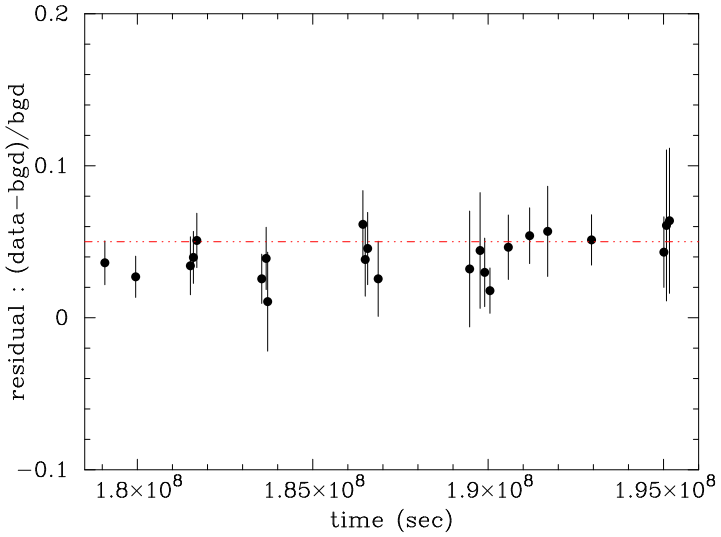

Figure 5.35: The residuals of the count rate between the observation data and estimated background (R_{source}-$R_{background}$)/$R_{background}$of against time. The time variation factors have been corrected.

and earth occultation data is shown in the figure 5.36 for the energy range of 15−70, 15−30, and 30−70 keV, respectively. The estimated background correlates closely with the earth occultation data in each energy band. Furthermore, the majority of the plotted data without largely scattered data are consistent within 5 %. The energy dependence of the distributions are not found. When the ratio of $R_{\rm occultation}/R_{\rm background}$ plotted against the time (the bottom right panel of the figure 5.36), it is suspected that they are stable against the time. We make the distribution of the ratios and fit it with a Gaussian curve in order to estimate their systematic error. Figure 5.37 shows the fitting result. The value at the Gaussian peak is 1.008, which indicates the estimated background and the earth occultation data is consistent within 0.8 % in average. Therefore, we consider the sigma of the Gaussian curve as the systematic error. The systematic error of the estimated background

become about 3.5 % at 1 σ.

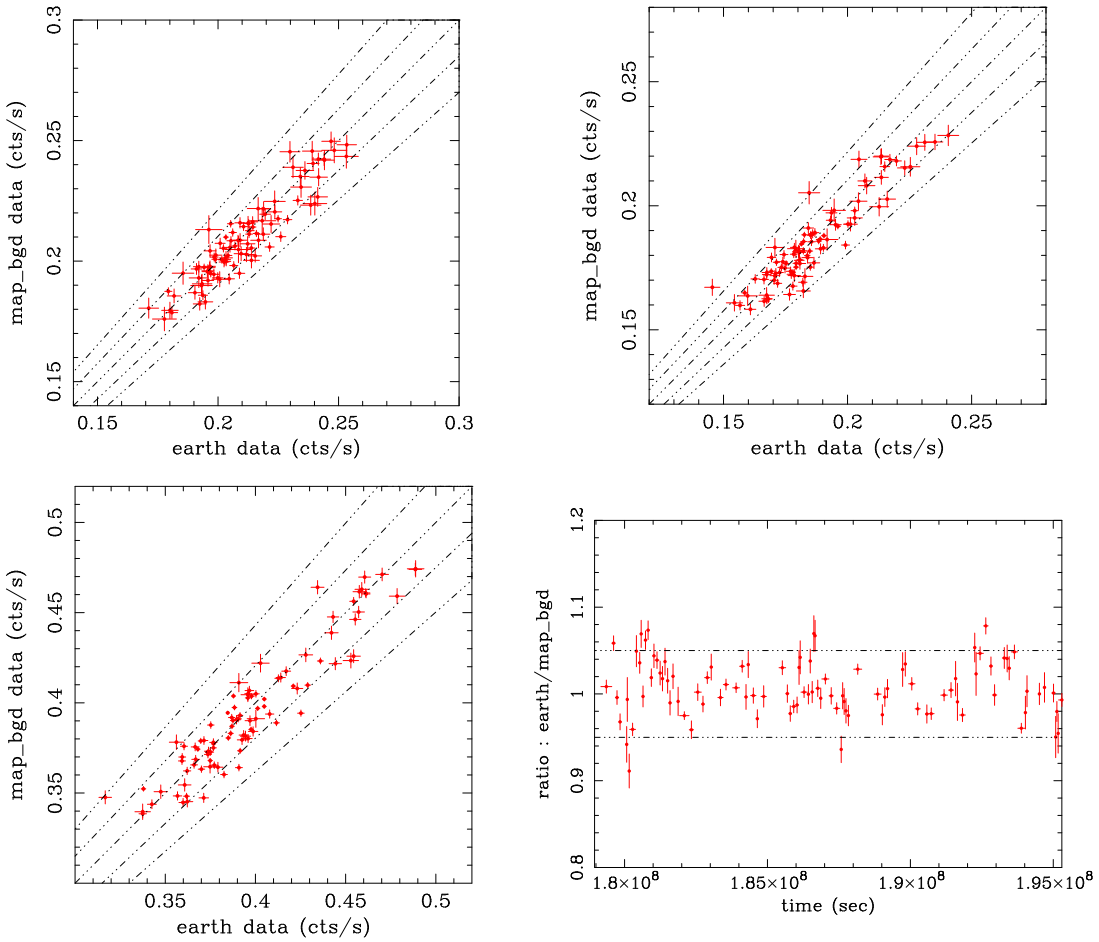

Figure 5.36: The correlation of the count rate between the estimated background and the earth occultation data in the energy band of 15−25 (top left), 25−70 (top right), and 15−70 (bottom left) keV. The panel at the bottom left shows their ratio against the time in 15−70 keV.

We also investigate the behaviour of the light curves and spectra extracted from the estimated background. Figure 5.38 shows the light curves of the source (RXJ 1713.7-3946, a shell-like SNR), estimated background, and background-subtracted data for the three energy band of 15−25, 25−70, and 15−70 keV. The background-subtracted light curves are constant against time within the statistical errors. This is desirable because the RXJ 1713.7-3946 is the target which exhibits no time variation. Next, we extract the background-subtracted spectra in three different periods and compare them as shown at the bottom right of figure 5.38. The flux of this target is ∼25 % of the background. Since the exposure time of each spectrum is ∼45 ks, the statistical error become >10 %. While, the systematic error is about 3.5 % at 1 σ. This indicated that the flux difference in each energy bin among three spectra is explained by the statistical errors. Thus, the estimated background is found to be sufficiently accurate in both the light curves and the spectra.

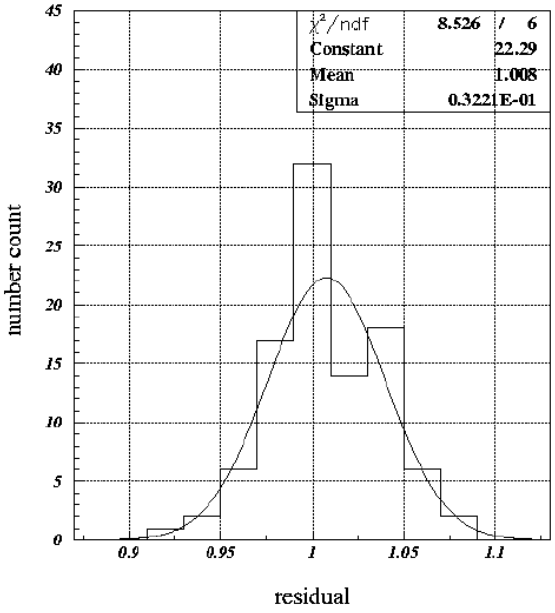

Figure 5.37: The distribution of the count rate ratio between the estimated background and the earth occultation data fitted with a Gaussian curve.

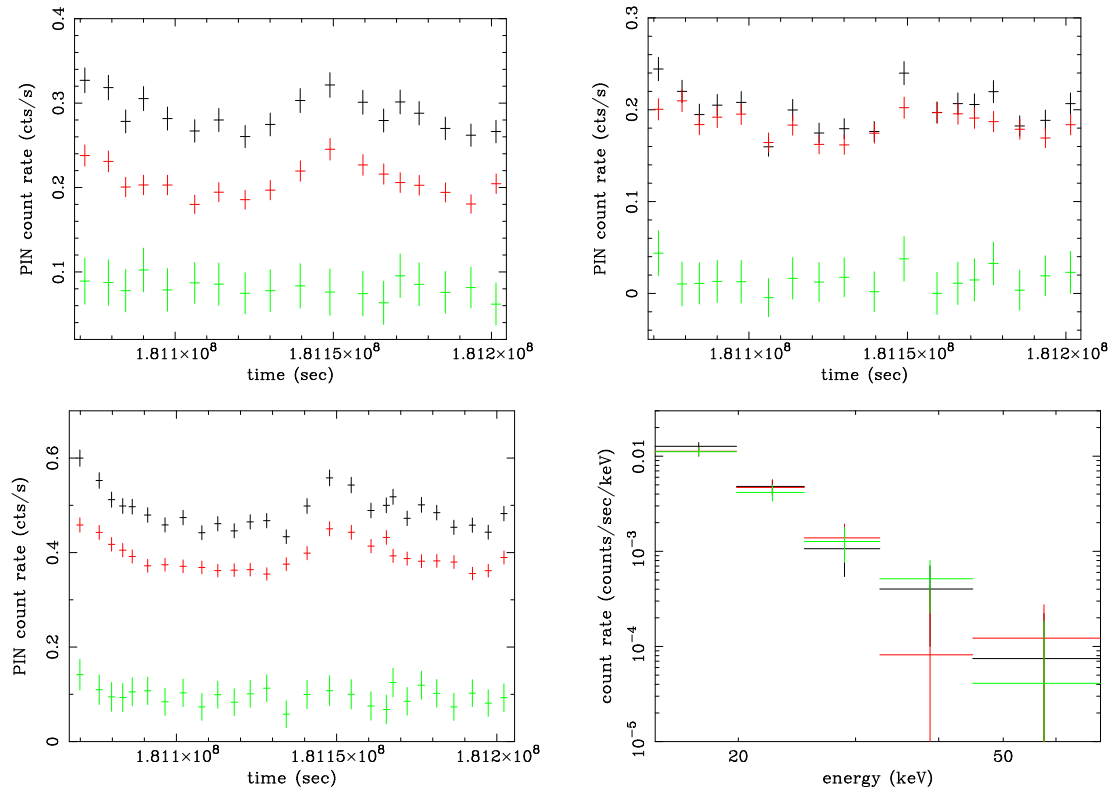

Figure 5.38: The light curves of RXJ 1713.7-3946 in the 15−25 (top left), 25−70 (top right), and 15−70 keV. In each panel, the source (black), estimated background (red), and background-subtracted data are shown. The panel at bottom right is the comparison of its spectra divided into three periods.

5.6 Non-thermal X-ray Emission

5.6.1 Estimation of the Point Source Flux

The X-ray spectra of the PIN is considered to consists of four components; the CXB, thermal emission, emission of the point sources, and possible non-thermal emission. Therefore, we have to find out the contribution of the point sources as well as that from the thermal emission before examining the hard X-ray spectra of the PIN, which is extracted by means of the estimated background. In this section, we investigate the point source flux and model the spectrum of the point sources according to its integration region of each target.

Firstly, we pick up the point sources from the PSPC point source catalog (2RXP catalog). The number of point sources is rather few (less than 5 point sources). The flux of each source is not intense such as $(1-3)\times10^{-13}$erg s^{-1} cm^{-2} in 2−10 keV band when the photon index of $\Gamma = 1.5$ is assumed. However, the angular resolution of PSPC is inferior to the recent instruments such as Chandra ACIS, XMM-Newton MOS. We hence tried to detect the point sources from their images since no point source catalog is available for those instruments. For this purpose, the software, *wavedetect* and *edetect_chain* are employed for the ACIS and MOS, respectively. These tasks employ the Mexican Hat wavelet function represented as

$$W(\sigma, x, y) = \frac{1}{2\pi\sigma^2}\left[2 - \frac{x^2+y^2}{\sigma^2}\right]\exp\left(-\frac{x^2+y^2}{2\sigma^2}\right).$$

The sources are detected by convolving the image with the Mexican Hat function for several values of σ. A local maximum with its significance higher than a certain threshold was recognized as a point source. Here, we set the detection threshold at 7 σ. We used the image of MOS for Abell 1060 and Centaurus cluster because it has larger field of view than that of ACIS while the ACIS data are utilized for Abell 3376 because the archival data obtained with the MOS has not been available yet.

When we list up the point sources contained in each spectral region after these task, some point sources are detected by more than one instrument. For such sources, the MOS or Chandra data are selected since the point source flux of the PSPC catalog are measured in the limited energy band of 0.2−2.35 keV. The resulting number of the point sources has increased by a factor of 3−5 although the flux is not significant again (typically 1×10^{-13} erg s^{-1} cm^{-2}). Figure 5.39 shows the detected point sources in Abell 1060.

From the final source list, we calculate the source flux in the energy band of the 2−10 keV and 15−50 for XIS and HXD, respectively. The extracted region of the spectra is the central 7′ circle for XIS while the field of view overall for HXD. The photon index is assumed as $\Gamma = 1.5$ which belongs to the harder category and then becomes the maximum contribution to be expected. The total estimated flux for each target is listed in table 5.10.

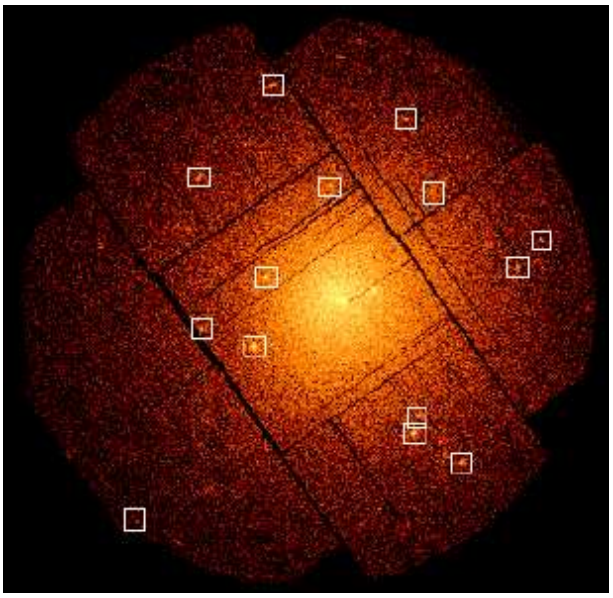

Figure 5.39: The detected point sources in the Abell 1060. The positions of the point sources are superposed on the MOS image as the white squares.

Table 5.10: The flux of the point sources.

target	position	$F^a_{\rm XIS}$	$N^c_{\rm XIS}$	$F^c_{\rm HXD}$	$N^a_{\rm HXD}$
Abell 3376	Center/East-Relic	2.04±0.20	5	7.32±0.59	27
	West-Relic	3.14±0.33	2	7.77±0.63	4
Abell 1060	Center	11.01±1.58	7	14.02±2.32	14
	Offset	—	0	6.74±1.03	6
Centaurus	Center	16.10±2.48	9	19.87±3.27	17
	Offset1	6.58±1.00	4	18.07±2.88	15
	Offset2	3.91±0.82	4	17.66±2.91	14

a: the flux in the XIS energy range of 2−10 keV in the unit of 10^{-13} erg s^{-1} cm^{-2},
b: the flux in the HXD energy range of 15−50 keV in the unit of 10^{-13} erg s^{-1} cm^{-2},
c: the number of the detected point sources in the spectral region of XIS (circular region within central $7'$) and HXD ($34' \times 34'$).

5.6.2 Estimation of the Thermal Emission

In order to investigate the contribution of the thermal component for the PIN spectra, we here confirm the the thermal emission by means of the XIS spectra. Since the parameters such as the temperature, metal abundance, and column density is necessary to characterize the thermal emission of each target, the spectral fitting is performed for the XIS spectra. The spectra are extracted from the central $7'$ region for all the observations. The energy range is limited to 0.3−8 keV for XIS1, and 0.5−8.0 for the other instruments. The FI chips of XIS are sensitive up to more than 10 keV. However, the spectral humps in 8−10 keV range is reported for some another targets and the factor for this structures is under investigation now. This

phenomenon is considered to have an adverse affect on examining the non-thermal emission. Then, the energy range in the fitting is limited below 8 keV here. The background spectra are extracted from the background data created with the script, *xisntebgdgen* (§4.3), in the same region as the source spectra. The efficiency degradation in the lower energy, which is described in §3.2.1, is taken account into the ARF file which is made with $xissimarfgen$. For the RMF file, we used the newest ones which is published on 13 February, 2006.

In the case of Chandra (§5.4), the non-thermal component is excluded from the fitting model in order not to over-estimate it. We here treat the three component model of the thermal, the point sources, and the CXB according to this method. We utilized the MEKAL model for the thermal emission. The point sources are represented with a powerlaw model with the photon index of $\Gamma = 1.5$. The CXB is also intended by a powerlaw with $\Gamma = 1.29$ but it has cutoff in 40 keV, whose flux is adjusted to 7.4×10^{-13} in the $2-10$ keV band according to the spectral integrated area of the XIS. Figure 5.40 right shows the spectra of Abell 1060 center obtained with XIS0, in which three components of the fitting model are plotted individually. The residuals above 5 keV seems to be enhanced slightly. Without Abell 3376 West-Relic, the spectral model fit the spectra well. When all the parameters in MEKAL are left free, Abell 3376 West-Relic shows the extremely high ICM temperature of $\sim$6.5 keV while the temperature in the central region is $\sim$4.3 keV as well as the previous observations. The remarkably higher temperature may be caused by the lack of the photon statistics in the offset region where the thermal emission is fainter by an order of magnitude than that of the central region. The temperature distribution is reported to be rather monotonous by XMM-Newton (Bagchi et al. 2005). We then fixed the ICM temperature with that obtained from the spectra of Abell 3376 Center and re-fit it. However, the normalization of the thermal emission becomes larger by a factor of 3 than that in the cluster center. This is not realistic result since the thermal emission becomes fainter toward the cluster periphery obeying the β model. Therefore, we add the non-thermal powerlaw to the fitting model in stead of the fixed temperature. All the parameters (without the normalization) in MEKAL model becomes consistent with the results of the central spectrum. The fitting parameters are summarized in table 5.11.

The temperature of Abell 3376 observations is consistent with the results of XMM-Newton (Bagchi et al. 2005) or ASCA (Fukazawa 2004). For Abell 1060 Center, the central spectra is represented well with the ICM temperature of $\sim$3 keV, which is consistent with ASCA results (e.g. Fukazawa et al. 2004). Although Abell 1060 Offset region exhibits somewhat lower temperature, this is consistent with the temperature map observed with ASCA (Furusho et al. 2001). The Centaurus cluster is known to have complex temperature structure in the previous study. Takahashi (2004) has investigated its structure hard and conclude that the spectra is well represented with the two temperature component of $\sim$3.7 and $\sim$1.8, and additional component of $\sim$0.7 keV appears within the central $1'$. We hence employ three temperature model for the spectral fittings of the Centaurus cluster. This brings the significant improvement of the spectral fitting, especially around the Fe-L line, and the χ^2 is reduced to 1.57 compared with the fitting using one component model

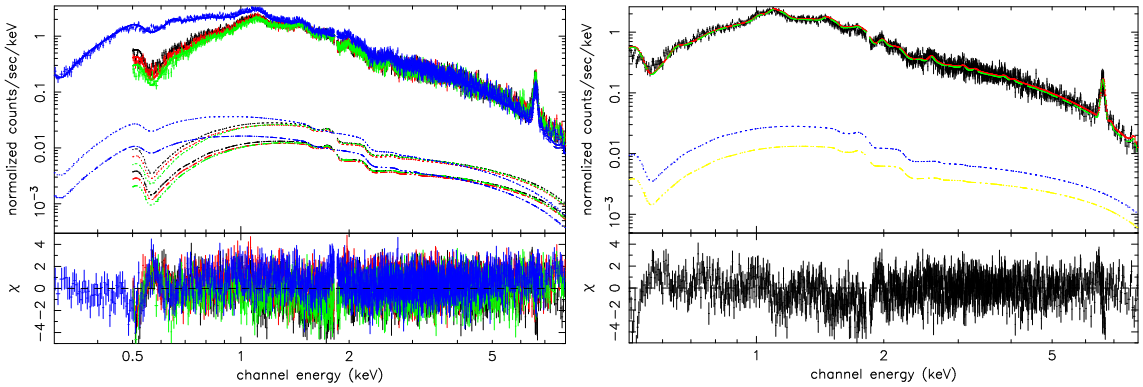

Figure 5.40: The XIS spectra of Abell 1060 center. The left panel contains all the spectra of XIS chips and the lines of black, blue, red, and green correspond to the XIS0, 1, 2, and 3, respectively. The right panel shows only the XIS0 spectrum. The black and red lines is the data and total model. The other lines represent the thermal emission (green), the point sources (blue), and the CXB (yellow).

($\chi^2 = 1.89$).

The metal abundance of Abell 3376 is consistent with the previous results even for the offset spectra. Abell 1060 Offset shows low metal abundance although it is comparable to the results obtained with the other instruments in Abell 1060 Center. Centaurus cluster is found to show the violent change of the metal abundance. In the outer region, the metal abundance is $\sim$0.4 solar while it is extremely increased within a few arcmin and reached at $\sim$1.3 solar as described in §5.1.1. The difference between the metal abundance obtained the central and offset spectra reflects abundance variation against the radius from the cluster center. The absorption column densities roughly agree with the Galactic values in both of Abell 3376 observations and Abell 1060 Center. For Abell 1060 Offset, the absorption column density can not be determined well. Centaurus cluster exhibits slightly higher value than Galactic absorption. This is considered to be derived from the central excess of the column density observed with Chandra (§5.3.2). The flux of the thermal emission is consistent with ASCA results. The fitting of Abell 3376 West-Relic contains the non-thermal powerlaw component. Its photon index results in 1.8, which is resemble to that obtained with the synchrotron emission from the radio halo ($\Gamma \sim 2.0$).

5.6.3 Hard X-ray Spectra Observed with HXD PIN

Now, being geared up to examine the non-thermal emission from galaxy clusters, we extract the background-subtracted spectra of the PIN for a start. Figure 5.41 shows the PIN spectra of Abell 3376 West-Relic. There are the remaining X-ray emission comparable to $\sim$10 % level of the background below 30 keV, which roughly corresponds $\sim 1 \times 10^{-11}$erg s^{-1} cm^{-2}. This emission should be made up of the thermal emission, the point source, the CXB, and possible non-thermal emission. Therefore, we extrapolate these component without the non-thermal emission for the background-subtracted PIN spectra, in order to see whether the excess hard X-ray appears or not. Before performing this procedure, the flux of the thermal

Table 5.11: Best fit parameters of XIS spectra.

		kT^a (keV)	$A^b_{\rm Fe}$ (solar)	$N^c_{\rm H}$ (10^{20} cm^{-2})	$F^d_{\rm th}$ (erg s^{-1} cm^{-2})
Abell 3376	Center/East-Relic	$4.34^{+0.05}_{-0.05}$	$0.27^{+0.01}_{-0.01}$	$3.87^{+0.15}_{-0.15}$	1.01×10^{-11}
	West-Relic	$4.29^{+1.13}_{-0.83}$	$0.31^{+0.21}_{-0.11}$	$1.80^{+0.95}_{-0.89}$	1.06×10^{-12}
Abell 1060	Center	$3.25^{+0.02}_{-0.02}$	$0.39^{+0.01}_{-0.01}$	$5.33^{+0.15}_{-0.15}$	3.33×10^{-11}
	Offset	$2.80^{+0.07}_{-0.07}$	$0.23^{+0.03}_{-0.03}$	$0.31^{+0.36}_{-0.31}$	3.70×10^{-12}
Centaurus	Center	– (fixed)†	$0.77^{+0.01}_{-0.01}$	$11.19^{+0.16}_{-0.15}$	6.31×10^{-11}
	Offset1	– (fixed)†	$0.48^{+0.01}_{-0.01}$	$8.82^{+0.22}_{-0.19}$	4.46×10^{-11}
	Offset2	– (fixed)†	$0.56^{+0.01}_{-0.01}$	$10.21^{+0.22}_{-0.20}$	4.83

a: the ICM temperature, b: the metal abundance, c: the column density,
d: the flux of the thermal emission in the 2−10 keV,
† : the temperature is fixed to 0.7, 1.8, 3.7 keV against three temperature component.

emission and the CXB must be adjusted to the field of view of the PIN spectra. On the other hand, we can use the parameters in table 5.10 directly for the point source emission.

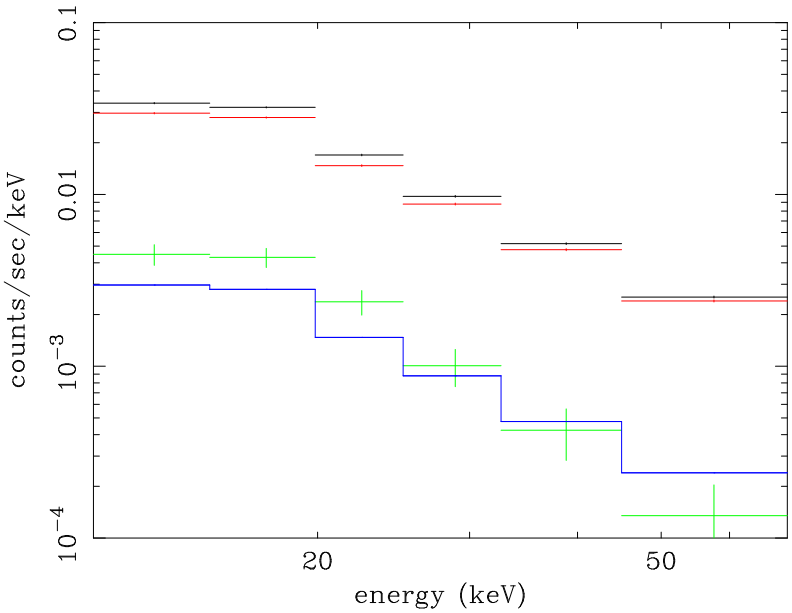

Figure 5.41: The PIN spectra of Abell 3376 West-Relic. The four lines present the source (black), the estimated background (red), the background-subtracted (green), and 10 % level of background spectra (blue).

The surface brightness profiles of the thermal emission empirically obey the β model. When a certain β profile is assumed, we can calculate the fraction of the X-ray contained in a desired region. Therefore, it is enable to scale the thermal flux in the XIS spectral region into that of the HXD region by means of the ratio between the X-ray fraction of XIS and HXD. We here utilize the β model profile observed

with ASCA GIS (Fukazawa et al. 2004), because it gives us the surface brightness profiles over the wider region than that obtained with any other instruments. The β model parameters and the resulting fraction in the HXD field of view are listed in table 5.12.

In this manner, the emission component without the non-thermal emission are compared with the background-subtracted spectra obtained with the PIN. Figure 5.42 shows the PIN spectra for each observation. To our regret, the background-subtracted spectra of Abell 1060 and Centaurus cluster are well represented with the emission except for the non-thermal one. There is no necessity to the non-thermal emission. The same result is found for Abell 3376. However, the spectra of Abell 3376 West-Relic exhibits the excess hard X-ray even after the contribution of three other component is eliminated. Thus, the sign of the non-thermal emission has been obtained from Abell 3376 West-Relic. We discuss both the statistic and systematic errors in the next section, in order to examine the superiority of this hard excess emission.

Table 5.12: The thermal emission parameters.

target	β^a	$R_{\rm c}^b$ (kpc)	n_0^c (10^{-3} cm^{-3})	$f_{\rm thermal}^d$
Abell 3376	$0.59^{+0.28}_{-0.00}$	$297.3^{+141.1}_{-0.00}$	$1.28^{+0.00}_{-0.28}$	3.98 / 5.74†
Abell 1060	$0.52^{+0.00}_{-0.10}$	$67.3^{+0.00}_{-14.7}$	$5.15^{+2.05}_{-0.52}$	4.05 / 6.81†
Centaurus	$0.38^{+0.04}_{-0.00}$	$11.5^{+1.2}_{-0.00}$	$27.71^{+3.84}_{-9.54}$	5.13 / 5.59†

a, b & c: the β, the core radius, and the central electron density in the β model obtained with ASCA (Fukazawa et al. 2004).
d: the fraction of the thermal emission in the HXD field of view against the XIS spectral region, when the surface brightness profile is represented with single β model.
† : the former is the thermal emission fraction for the central observation while the latter is for the offset observation.

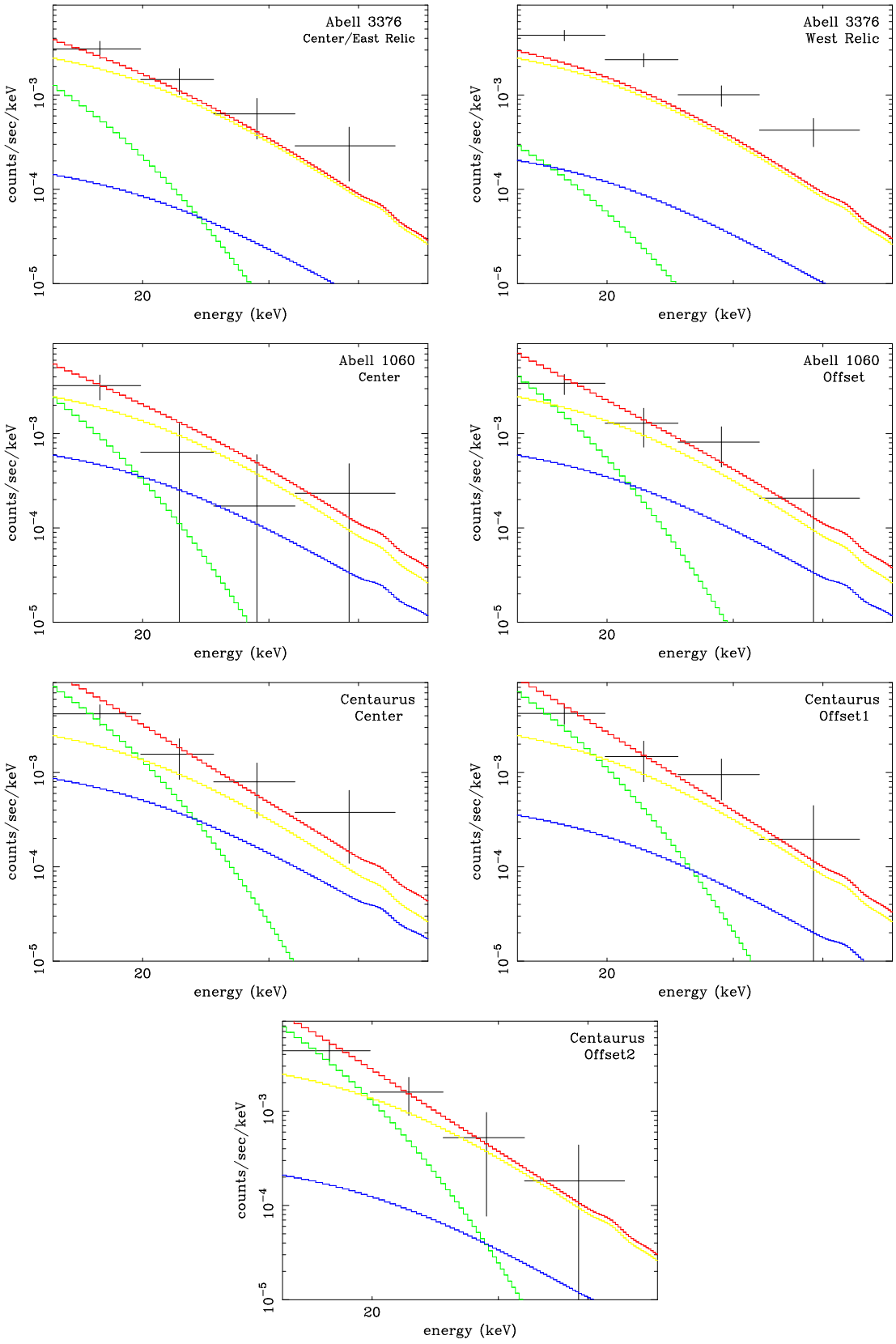

Figure 5.42: The PIN spectra of each observation in the 15−50 keV. The black cross is the observational data. The red line presents the summed spectral model of the thermal emission (green), the CXB (yellow), and the point sources (blue).

5.6.4 Superiority of the Hard X-ray Emission

We estimate the statistical and systematic error for the excess hard X-ray from Abell 3376 West-Relic. Here, we use the data in the 15−50 keV where the PIN efficiency is the highest so that more accurate examination can be performed. The total source count is 36041 while the background count is 33058 for this observation. The remaining count is 2983 in this stage. The statistical error becomes 190 and 182 counts for the source and background count, respectively.

Next is the systematic error, which is associated to each modeled component; the background, the CXB, the point sources, and the thermal emission. The systematic error of the estimated background is already discussed in the previous section (§5.5.4). It has found to be 3.5 %, and then the systematic error becomes $33058 \times 0.0035 = 1157$ counts. For the CXB, the statistical fluctuation of the source number count in the detector field of view bring the the CXB brightness fluctuation. Such fluctuation is described as

$$\sigma_{\rm CXB}/I_{\rm CXB} \propto \Omega_{\rm e}^{-0.5} S_{\rm c}^{0.25},$$

where $\Omega_{\rm c}$ represents the effective solid angle of the observation, and $S_{\rm c}$ is the upper cut-off flux of the detectable discrete sources in the detector field of view (see Appendix F for the details). Since the CXB fluctuation has been measured with HEAO-1, Ginga, and ASCA as listed in table 5.13, we can speculate on the CXB fluctuation for the PIN by means of this relation. Among three results, the HEAO-1 observations is most useful because it has the advantage of a large number of data samples and wide energy range. The spectral integrated region, i.e. the HXD's field of view, is $34' \times 34'$ square, which yields $\Omega_{\rm c} = 0.321$ deg^2. We assume here the upper cut-off flux of HXD as its detection limit $\sim 1 \times 10^{-12}$erg s^{-1} cm^{-2} in the 15−50 keV ($\sim$1% of background). Then, it becomes $\sim 5 \times 10^{-13}$erg s^{-1} cm^{-2} in the 2−10 keV. By using these quantities, the fractional CXB fluctuation is calculated as $2.8 \times (15.8/0.321)^{0.5} \times (8 \times 10^{-11}/5 \times 10^{-13})^{-0.25} = 5.5$ %. Since the CXB number count is 1644 counts, the CXB fluctuation results in 90 counts. Here, the number counts of the excess hard X-ray is reduced to $2983 - 1644 = 1339$ counts.

The point sources also have their own statistical fluctuation. It is already known from the PSPC catalog or in the point source detection procedure with *wavedetect* and *edetect_chain*, and listed in table 5.10. We just use these values in estimating the statistical errors for modeling of the point source emission. The number counts of point source contribution is 197 counts, and then the systematic fluctuation becomes $197 \times (0.63/7.77) = 16$ counts. Lastly, we consider the error of the thermal emission. It can be found from the of the normalization of MEKAL model. The fitting error of the normalization at 90 % confidence level is 12 % for the thermal emission from Abell 3376 West-Relic. Then, the systematic error is calculated as $75 \times 0.12 = 9$ counts. We also take account the fluctuation caused by using the different plasma code. There are two major plasma emission models other than MEKAL, such as APEC and Raymond-Smith model. When the APEC or Raymond-Smith model are utilized, the number count of the thermal emission 78 and 76 counts, respectively. Considering the number count of 75 obtained with MEKAL model, the systematic

Table 5.13: CXB fluctuation in the 2−10 keV band.

Instrument	HEAO-1 A2[a]	Ginga LAC[b]	ASCA GIS[c]
Data	698 samples	151 samples	10 samples
Effective Area	530 cm^2	4000 cm^2	200 cm^2
Energy Range	2.5−46 keV	2−10 keV	0.6−10.0 keV
Field Of View	3°×3°	1°×2°	20′ circle
			(with 3′ resolution)
$\Omega_e^\dagger$	15.8 deg^2	1.3 deg^2	∼0.5 deg^2 / sample
			(0.14 deg^2 / pointing)
$S_c^\ddagger$	8×10^{-11}	6×10^{-12}	2×10^{-12}
σ_{CXB}/I^*_{CXB}	2.8 %	∼6 %	≤3.4 %

a: from Shafer (1998), b: from Hayashida (1990), c: from Ishisaki (1996).
†: the effective solid angle of the observations (see Appendix F).
‡ : the upper cutoff of the 2−10 keV flux from discrete sources in the field of view.
∗: the fractional CXB fluctuation in RMS, which corresponds to the excess variance after subtracting statistical errors and NXB estimation errors.

fluctuation due to the plasma model is 3 counts.

We summarized all the number count and the statistical or systematic error count in table 5.14. The remaining number count is $1339 - 197 - 75 = 1067$ counts after subtracting the counts of the point sources and thermal emission. The total statistic error due to source and background of 372 counts is small enough against the hard X-ray number count. On the other hand, the systematic errors finally has reached at 1275 counts. The hard X-ray is buried in the systematic fluctuation. Thus, it is hard to claim the significant detection of the excess hard X-ray. However, our result has a profitable implication when the observed hard X-ray count is considered to present the maximum limit of the non-thermal emission. Being assumed the photon index of the non-thermal emission as $\Gamma = 2.0$, its flux in the 15−50 keV becomes $(5.1 \pm 1.8 \pm 6.1) \times 10^{-12}$erg s^{-1} cm^{-2}. BeppoSAX also has observed Abell 3376 and obtained the non-thermal flux of $(11.0 \pm 7.7) \times 10^{-12}$erg s^{-1} cm^{-2} when scaled into the 15−50 keV flux by a powerlaw with $\Gamma = 2.0$ (Nevalainen et al. 2004). Our flux is smaller by a factor of 2/3 roughly even when the systematic fluctuation is taken account, bringing the restricted maximum flux of the non-thermal emission than that observed with BeppoSAX.

5.6.5 Comparison with the XIS results

Most remarkable feature of the XIS is the lower NXB than the other CCDs. This gives us the higher sensitivity than that of PIN in the high energy band of XIS. Therefore, it may be possible to detect the non-thermal emission from clusters of galaxies with XIS although the thermal contribution is more enhanced than that in the case of the PIN. In the same procedure as PIN, we estimated the non-thermal

Table 5.14: Summary of the excess hard X-ray observed with PIN.

	component	error estimation	number counts	error counts
Statistical	source	$\sqrt{36041}$	36041	±190
errors	NXB	$\sqrt{33058}$	-33058	±182
sum		excess counts =	2983	±372
Systematic	NXB estimation error	33058×0.035	–	±1157
errors	CXB fluctuation	1644×0.055	-1644	±90
	point source contribution	197×0.08	-197	±16
	thermal contribution	75×0.12	-75	±9
	thermal modeling error		–	±3
sum		excess counts =	1067	±1275
total errors		excess counts =	1067	±372 ±1275

flux by using the CXB spectrum (§4.4.4), the thermal parameters (table 5.11), and the point source flux (table 5.10). The energy range is restricted in the 4−8 keV band here. The systematic error of the NXB is estimated to be 5 % as described in §4.3. Moreover, the fractional CXB fluctuation is calculated as 8.5 %, considering the spectra integrated region of $\Omega_c = 0.043$ deg^2 (7′ circle) and the upper cutoff flux of $S_c \sim 5\times10^{-14}$erg s^{-1} cm^{-2}. As a result, there are four targets exhibiting the sign of the excess hard X-ray above the systematic errors; Abell 3376 Center, Abell 3376 West-Relic, Abell 1060 Center, and Centaurus cluster Offset1. The flux or the errors both the statistical and systematic are listed in table 5.15. The photon index of the non-thermal excess is again assumed as $\Gamma = 2.0$.

Table 5.15: Summary of the excess hard X-ray observed with XIS.

target	position	$F^a_{\rm HXR}$	statistical errors[b]	systematic errors[c]
Abell 3376	Center/East-Relic	0.37 (0.86)	±0.037 (0.087)	±0.19 (0.44)
Abell 3376	East-Relic	0.59 (1.4)	±0.025 (0.059)	±0.12 (0.27)
Abell 1060	Center	1.2 (2.8)	±0.10 (0.24)	±0.50 (1.2)
Centaurus	Offset1	1.2 (2.8)	±0.089 (0.21)	±0.65 (1.5)

a: the 4−8 keV flux of the excess hard X-ray in the unit of 10^{-12} erg s^{-1} cm^{-2}.
b & c: the statistical and systematic errors in the unit of 10^{-12} erg s^{-1} cm^{-2}.
The values in parentheses represent the 2−10 keV flux.

The non-thermal flux observed with XIS would depend on the photon index. Then, we have analyzed the relation between the flux and the photon index for the targets showing the sign of the non-thermal emission, as shown in figure 5.43. The relations for HXD, which are scaled into the XIS energy range, are also represented. Except for Abell 3376 West-Relic, the sign of the non-thermal emission could not be detected. Therefore, we treat the detection limit of the PIN as the the upper

limit of the non-thermal emission for them, i.e. $\sim$3.5 % of the background flux ($\sim 3.5 \times 10^{-12}$erg s^{-1} cm^{-2} in 15$-$50 keV).

From the crossing area with PIN and XIS relations, the non-thermal emission of Abell 3376 West-Relic has a photon index around 1.7. However, the flux for the PIN is not corrected with the difference of the field of view between XIS and PIN. In other words, the red lines in figure 5.43 assumes the observed flux with PIN come from only the limited region corresponding to the integration area of XIS spectra. If the non-thermal emission extend over the HXD field of view or more, the flux is reduced at the level of blue line. It predicts the photon index of $\sim$2.2. Thus, the non-thermal emission form Abell 3376 West-Relic is considered to be represented as a powerlaw with $\Gamma = 1.7 - 2.2$. This is liberally consistent with the typical photon index ($\sim$2.0-2.5) of synchrotron radio emission such as radio halo or radio relic. Furthermore, it is possible that the non-thermal emission extends up to the the region comparable to the HXD's field of view, i.e. 15$-$60$'$. This indicates that the area emitting the non-thermal emission seems to be somewhat broader than the size of the West Relic (cf. §4.1.2 figure 4.3). For Abell 1060 and Centaurus Offset1, the crossing points lie at the photon index of $\sim$1.9. They also consistent with that observed from the radio halos. However, the difference of the field of view has not taken account yet. If the field of view is corrected, their photon indices are increased up to > 2.5, which is larger than the empirical indices from the radio observations. Then, the non-thermal emission is seems to be limited to be the same size as the XIS spectral region. With the same reason, the extent of the non-thermal emission from Abell 3376 Center is also comparable to the spectral integrated area of the XIS (within 7$'$).

5.6.6 Spatial Distribution

The sign of the non-thermal emission is obtained from Abell 3376 West-Relic with HXD PIN. From the observation of XIS, Abell 3376 Center, Abell 1060, and Centaurus cluster Offset1 show the possibility of the non-thermal emission. Combining the PIN and XIS observation, the non-thermal emission from Abell 3376 West-Relic is supposed to extend over the larger area than that of the radio emission. However, the other target is lacking of the information on the distribution of the non-thermal emission. In order to obtain information about the non-thermal emission extent, we utilized the data obtained with Chandra ACIS, XMM-Newton MOS1, and ASCA GIS. Since these instruments have different field of view, we can obtain the spatial information for the non-thermal emission when the spectra is accumulated according to their own field of view. The spectra integrated region is the central 3$'$, 10$'$, and 15$'$ for ACIS, MOS1, and GIS, respectively. Although Abell 3376 West-Relic has been observed with GIS, it is insufficient because the data is available from only the restricted region which is almost same size as XIS spectra. Instead, we extracted the XIS spectra within the central 3 arcmin.

Figure 5.44 shows the integrated non-thermal and thermal flux against the radius for each target. If the non-thermal emission extends over the wide area, the integrated flux should be increased in proportion to the square of the radius. However,

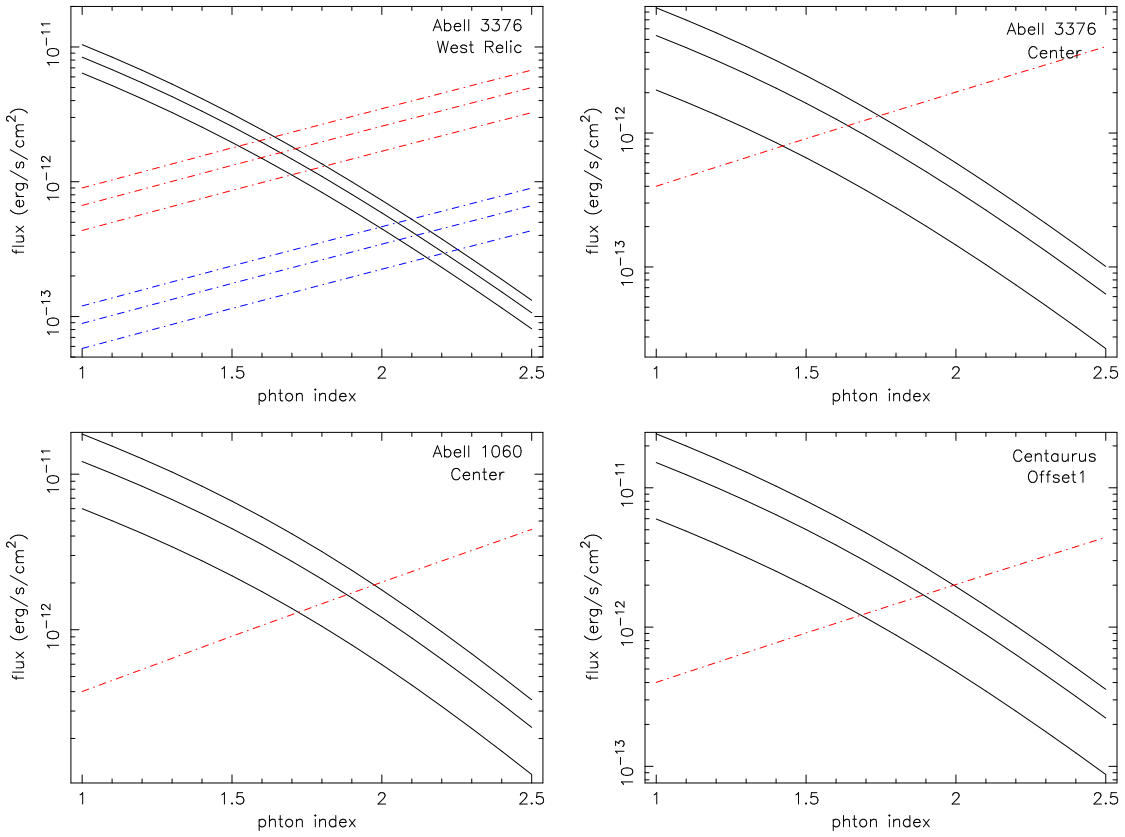

Figure 5.43: The relation between the non-thermal flux and the photon index of Abell 3376 West-Relic (top left), Abell 3376 Center (top right), Abell 1060 Center (bottom left), and Centaurus Offset1 (bottom right). The black lines present the relations for XIS and upper and lower errors (statistical + systematic). The red and blue lines are for PIN, which contain only the statistical errors. The former are not corrected the difference of the field of view while it has taken account for the latter.

the flux of the non-thermal emission has large systematic errors, and then remarkable trend can not be understood. We just make a rough comment on the distribution of the non-thermal emission from Abell 3376 West-Relic. The non-thermal emission increase along the line showing the square of radius, which is roughly consistent with the result shown in §5.6.5. Compared it with the thermal distribution, the non-thermal emission may have more diffuse distribution.

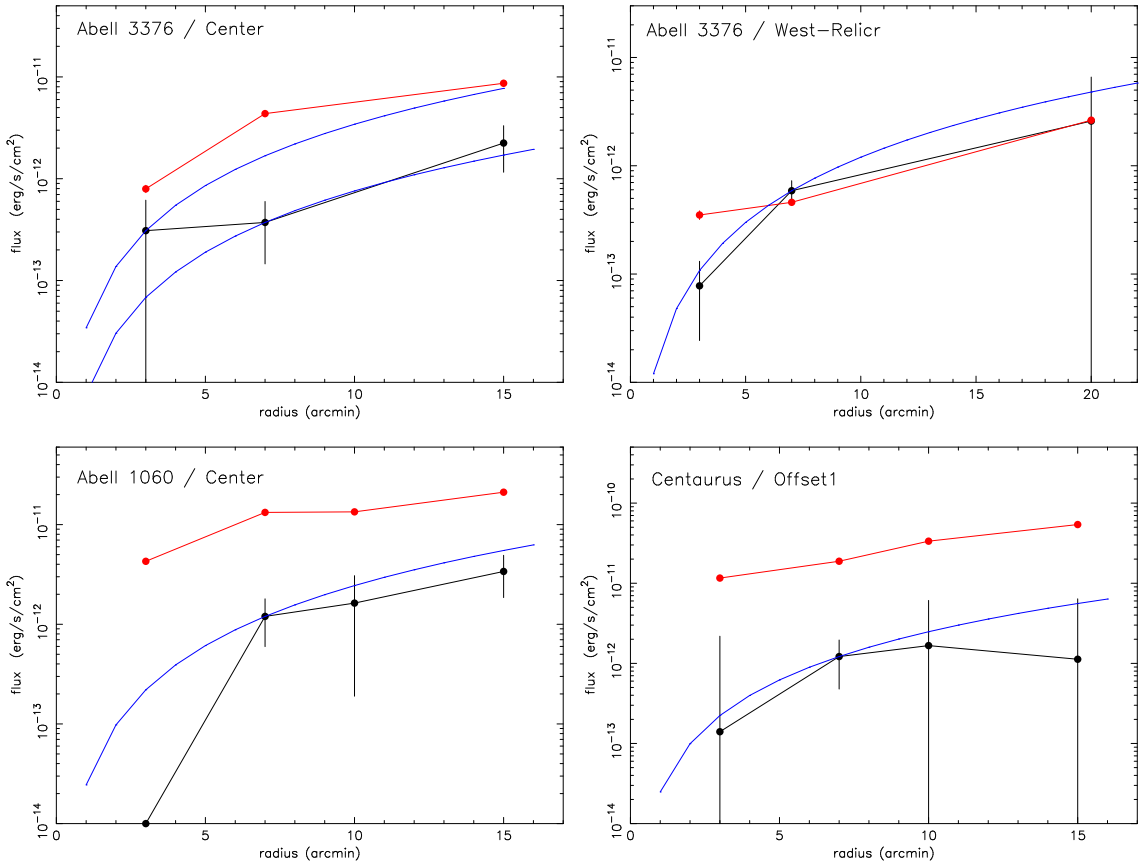

Figure 5.44: The integrated flux against the radius from the cluster center. The black circles present the non-thermal emission and the red circles are the thermal emission. The blue lines is in proportion to the square of the radius.

Chapter 6

Discussion

6.1 Summary of Results

We investigate the ICM temperature structure of 18 galaxy clusters and 4 galaxy groups in detail. Our results give the different picture from the simple cooling flow. Although the radiative cooling is surely taking place in the central 100−200 kpc region of the galaxy clusters ($R_{\rm cool} - R_{\rm cluster}$ relation), the temperature gradient toward the cluster center is rather milder ($T_{\rm cool}/T_{\rm center} \sim 0.3 - 0.6$). The ICM temperature is typically higher than 1 keV even at the very cluster center. Furthermore, the cooling rate or the central excess absorption as well as the mass of the central cool gas implies that the cooled gas is far less than the prediction of the cooling flow by an order of magnitude. Thus, the radiative cooling is restricted by the some heating mechanism. In comparison with the radio observation, the remarkable correlation between X-ray and radio power, which is seen in the mini-halo clusters, can not be found.

On the other hand, the sign of the non-thermal emission is detected from Abell 3376 West-Relic observed with HXD PIN. This is considered to arise by the high energy electron interacting with the CMB photons as well as emitting the diffuse radio radiation. The flux of the non-thermal emission is $(5.1 \pm 1.8 \pm 6.1) \times 10^{-12}$erg s^{-1} cm^{-2}. This results in more restricted maximum flux of the non-thermal emission than that observed with BeppoSAX although it has large systematic error. Combined with the XIS observation, the photon index is suspected to be 1.7−2.2 and is consistent with that from the typical radio emission. The obtained photon index implies that the non-thermal emission seems to extend over a region which is almost same size of the HXD's field of view.

In the §6.2 & 6.3, we discuss three major heating mechanism which restricts the radiative cooling in the cluster center, as well as the possibility of the plasma heating associated with the supernova by the central excess of the heavy elements. We also examine the properties of the non-thermal emission from the galaxy clusters; the acceleration model, the comparison with the radio parameters, and energetics in the §6.4. Additionally, the origin of the plasma heating and particle acceleration is discussed in the §6.5.

6.2 Plasma Heating Mechanism in the Cluster Center

6.2.1 AGN in the Cluster Center

The AGN jet associated with the cD galaxy is the most preferred heating mechanism because AGN exists in the central region of almost all the cD clusters. Since the cD clusters exhibit stronger cooling than the other type clusters, the AGN jet is thought to be a prevalent candidate of the plasma heating. Moreover, it is possible to maintain heat input for a long time due to their self-regulating feedback facility. We measure the ICM temperature distribution in the central $1' \times 1'$ region of Abell 2199 in order to investigate the plasma heating effect by the AGN radio jet. Abell 2199 has a radio jet of $\sim$ 3 kpc in its center, and also the diffuse radio lobes extending over $\sim$50 kpc scale which disturb the X-ray distribution (figure 6.1 left). The temperature map shows a weak correlation with the distribution of the radio lobe, around which the ICM temperature varies by $\sim$1 keV. Since the scale of the temperature patches is $\sim$10 kpc, the energy input by the radio lobe in to the ICM corresponds to $\sim 10^{57}$ erg from the $nk\Delta T \times \Delta V$. Here, n, ΔT, ΔV represent the ICM density, temperature variation of $\sim$1 keV, and the volume of the temperature fluctuation when the spherical symmetry is assumed. The thermal conduction flux which eliminates such temperature fluctuation become 10^{42} erg s^{-1} (Spitzer 1956). This indicates that the temperature fluctuation are vanished on the time scale of 10^7 years. Meanwhile, the ICM energy radiated during the past 10^7 years reaches at 10^{59} erg because the radiation rate (i.e. the luminosity) is $\sim 10^{44}$ erg s^{-1} in the cluster center. The ICM energy loss then becomes larger by a factor of 100 than the energy input from the radio lobes, implying that the plasma heating by the AGN jet has not worked effectively at least during this 10^7 years.

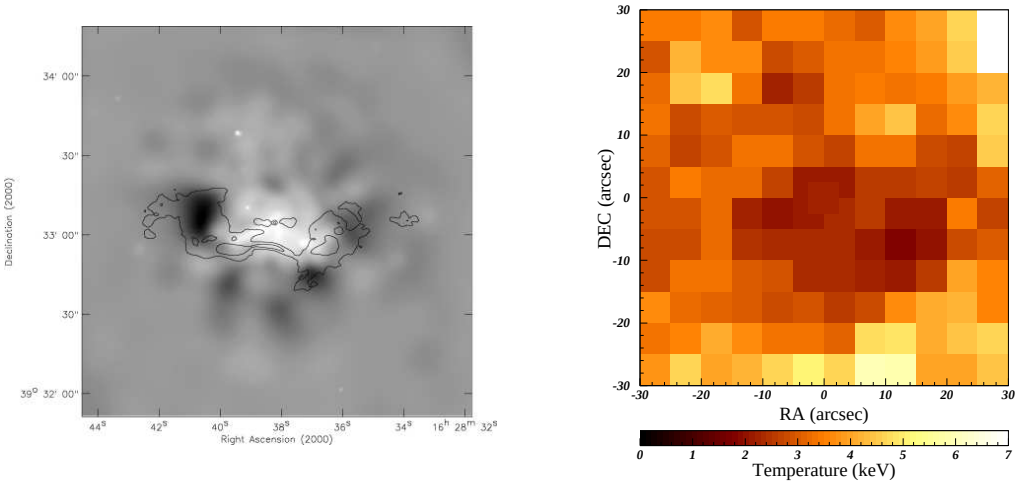

Figure 6.1: The X-ray image superposed on the radio contour (left) and the temperature map in the central $60'' \times 60''$ region of Abell 2199 (right).

As shown by the X-ray image of Abell 2052 (§5.2.1), it is found that many radio cavities yielded by the AGN jet exist in the central region of galaxy clusters. Birzan

et al (2004) have calculated the instantaneous mechanical luminosities of the radio cavities, which is defined as $L_{\rm mech} = W_{\rm cavity}/t_{\rm cavity}$. The quantities $W_{\rm cavity}$ and $t_{\rm cavity}$ are the work done in forming the radio cavities by the AGN jet and the age of the cavities. They revealed that the derived luminosities are large enough to balance the radiative cooling in a half of their sample. However, the energy of the work is not sufficient to affect the radiative cooling in the rest of the galaxy clusters, that is, at least an energy input 4−16 times as large as the observed work is necessary. It could be settled by considering that the central black hole is temporary in down (inactive) state at the moment although the correlation between the degree of quenching the radiative cooling and the time variability of the black hole activity has not been understood well. In addition, even if the AGN jet heats the central cool plasma up, its efficacious area is limited in the vicinity of the cluster center ($\sim$ a few tens kpc).

6.2.2 Thermal Conduction

Thermal conduction caused by the surrounding hotter ICM is one of the major heating mechanism to restrict the radiative cooling. The heat source in this case is the thermal energy of the ICM which implements overall clusters of galaxies, and then, the vast energy injection into the ICM is expected. The conductivity of the hydrogen plasma completely free from the magnetic fields was derived by Spitzer (1962) as

$$k_{\rm S} = \frac{1.84 \times 10^{-5} T^{5/2}}{\ln\Lambda} \qquad [\ {\rm erg\ cm^{-1}\ K^{-1}}], \tag{6.1}$$

where ln Λ represents the Coulomb logarithm,

$$\ln\Lambda = 37.8 + \ln\left[\left(\frac{T}{10^8\ {\rm K}}\right)\left(\frac{n_{\rm e}}{1 -^{-3}\ {\rm cm^{-3}}}\right)^{-1/2}\right]. \tag{6.2}$$

This is known as the classical Spitzer conductivity. In this way, the thermal conductivity can be estimated from the ICM temperature and density. The Spitzer value is considered to be the thermal conductivity in the direction parallel to the magnetic field lines in the magnetized plasma such as the ICM. While, it become 0 in the direction perpendicular to the field lines. Thus, the thermal conductivity has a strong anisotropy for the magnetized plasma.

Voigt and Fabian (2004) calculated the effective conductivity by using the temperature gradient and the emission measure obtained with Chandra, assuming that the radiative cooling is in balance with the heating by the thermal conduction. When the effective conductivities are compared with the classical Spitzer value, it is found that the effective conduction larger than the Spitzer one is needed in order to balance with the radiative cooling for the cooler galaxy clusters (T <5 keV). On the other hand, the higher temperature clusters show the thermal conductivity comparable to the Spitzer one. This indicates that the thermal conductivity must be adjusted in the region to region of a cluster according to the ICM temperature gradient. Thus, the fine-tuned conductivity is necessary to balancing with the radiating cooling along with maintaining the observed temperature gradient. Thus, it hardly provides a

general solution to the heating problem in the central cool plasma. Moreover, their thermal conductivities was derived by only the temperature and density gradient, and the information of the magnetic field are not contained. Actual conductivity should distribute more intricately according to the positional magnetic field, and it becomes an anisotropic quantity. Hence, it is difficult to discuss the heating by the thermal conduction by referring to the averaged conductivity.

6.2.3 Hierarchical Evolution

In addition to the AGN jet and thermal conduction, the gravitational heating through the hierarchical evolution is a possible candidate. Recently, N-body simulations of the cluster evolution (i.e. the large scale structure) have been developed according to the progress of the super computer. Motl et al. (2004) carried out the N-body dynamical simulation of galaxy clusters by the merging. The remarkable point of their study is that the radiative cooling is taken account in the simulation. The resulting X-ray image and the temperature distribution are shown in figure 6.2. They found that the cluster growth involving the radiative cooling can produce a cool core of a few hundred kpc scale although such structure does not appear when only the adiabatic evolution is taken account. The central temperature is maintained more than 1 keV thorough the evolution by the gravitational heating. These features resemble the temperature structure derived in our analysis, suggesting that this model can reproduce the scaled temperature profile (§5.1.2). The X-ray surface brightness image shows the spiry distribution toward the cluster center, and the subclusters which is believed to arise from recent merger activity.

In addition to the temperature structure and the X-ray distribution, the cooling flow rates are also consistent with the recent observations. The velocity map of the central cool plasma shows a random flow and there is no sign of cooling flow. Moreover, the observed X-ray morphology, such as the filament structure as seen in Abell 1795 (Fabian et al. 2001) or Centaurus cluster (Sanders and Fabian 2002), and the cold front found in Abell 2141 (Markevitch et al. 2000), are also identified. This model thus provides better consistency with the observational features. Therefore, the hierarchical evolution with mergers and radiative cooling is expected to play an important role for the ICM heating in the central region of galaxy clusters.

6.3 Amount of the Iron in the Cluster Center

In the elliptical galaxies, Type Ia supernovae (SNe) is dominant while Type II is rare phenomenon. Since a larger amount of Fe is ejected by Type Ia SNe than Type II SNe, Fe-rich metal composition can be the evidence for the metal transfer from the elliptical galaxies through the Type Ia SNe. In fact, Fe abundance increases toward the central region in many galaxy clusters as shown in §5.1.1. Then the central excess Fe is considered to originate from the metals ejected by the giant elliptical galaxy, i.e. the cD galaxy, at the cluster center through Type Ia SNe. This implies that the energy released in Type Ia SNe may heat the ICM up. Since Type

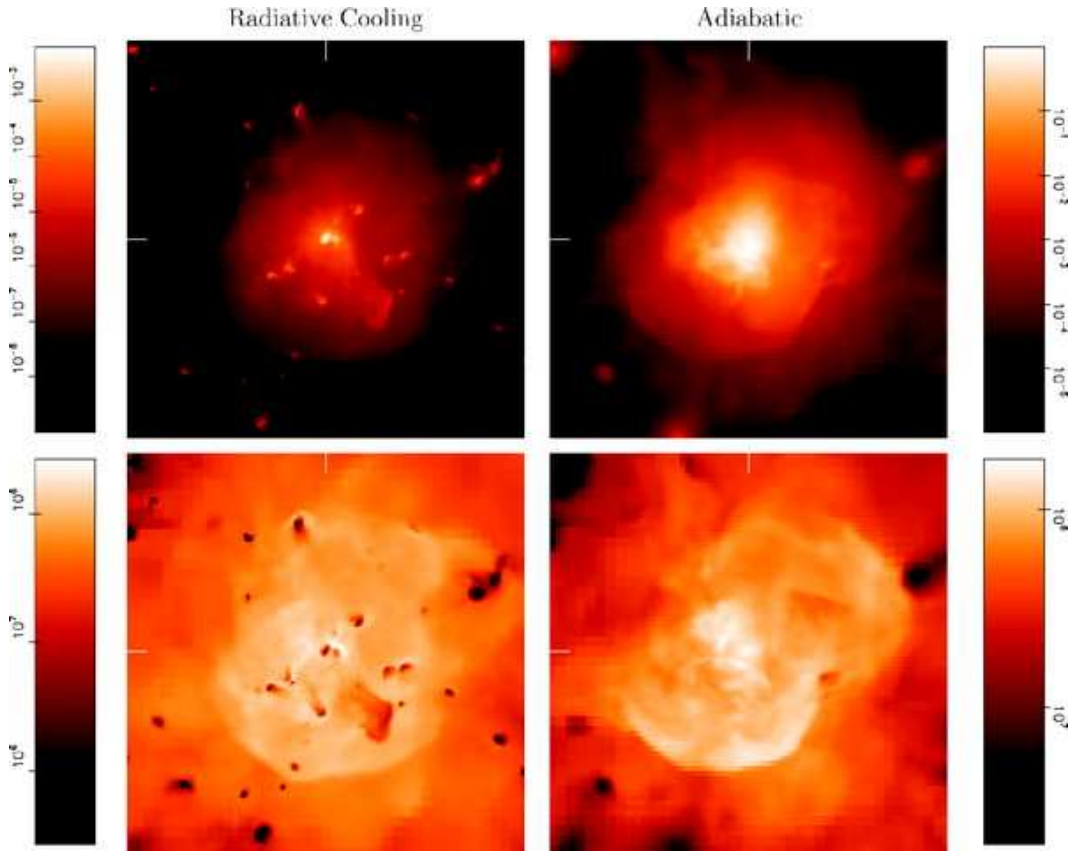

Figure 6.2: The simulated X-ray surface brightness image in the 1−10 keV band (top) and the projected temperature map (bottom). The panels on the left hand shows the evolution associated with the radiative cooling while the adiabatic one on the right hand. The size of each image is the central 5 Mpc.

Ia SNe are intermissive events over the Hubble Time, the continuous energy input is possible. Then, we investigate here the heating energy due to Type Ia SNe in the cluster center.

We estimated the mass of the excess Fe from the radial profile of the Fe abundance and the electron density from the equation of

$$M_{\rm Fe}(r) = \int_0^R n_{\rm H}(r) A_{\rm Fe}(r) m_{\rm Fe} \left(\frac{N_{\rm Fe}}{N_{\rm H}}\right) \cdot 4\pi r^2 dr. \tag{6.3}$$

Here, $n_{\rm H}(r)$ is a radial distribution of the hydrogen number density which is regarded as that of the electron density, $A_{\rm Fe}(r)$ is a Fe abundance profile, $m_{\rm Fe}$ is a Fe mass, and $N_{\rm Fe}/N_{\rm H}$ is the 1 solar Fe abundance (4.68×10^{-5}). As a result, the mass of the excess Fe distributes in the range of $\sim10^{8-10}$ $M_\odot$. If it is assumed that all the central excess Fe is yielded by Type Ia SNe which have occurred in cD galaxy, we can calculate the total number of SNe by using the Fe mass yield per a Type Ia SN of 0.7 $M_\odot$ to be 1.4×10^9. Since the energy released from each Type Ia SNe is know to be $\sim10^{51}$ erg, the total energy released during the Hubble time is estimated as $\sim10^{60}$ erg. This gives us the energy input rate of $\sim10^{42}$ erg s^{-1}. On the other hand, the energy loss rate of the ICM by the radiation is typically $\sim10^{44}$ erg s^{-1}. Thus, the

plasma heating by the energy injection from Type Ia SNe would not be relativistic although it may produce minute effect in the X-ray faint clusters or groups.

6.4 Non-Thermal X-ray Emission

6.4.1 Non-Thermal Bremsstrahlung

For the non-thermal emission from the clusters of galaxies, there are two major candidates of its emission mechanism. One possible interpretation of the non-thermal emission is that the relativistic electrons scatter the CMB photons via IC process and boost them into hard X-rays. The other is the non-thermal bremsstrahlung (NTB) from the superthermal electrons. We here discuss whether the NTB scenario is valid or not.

Introducing the powerlaw momentum distribution for the superthermal electrons, the electron number with the range of momentum, P to $P + dP$ is defined as,

$$N(p) = N_0 p^{-\mu}, \tag{6.4}$$

where $p \equiv P/m_{\rm e}c$ is the normalized momentum and μ is the powerlaw index. The μ is related with the energy index α as $\mu/2 = \alpha$. Taking a typical value of $\alpha = 1$ for cluster non-thermal emission, μ is derived to be $\mu = 2$. When the Bethe-Heitler bremsstrahlung cross section (equation 2.46) is assumed, the non-thermal bremsstrahlung spectrum is represented as

$$\frac{dL_\epsilon}{d\epsilon} = \frac{32\pi^{\frac{3}{2}}}{3}\frac{e^6}{m_{\rm e}c^4 h}\left[\frac{\Gamma(\frac{\mu}{2})}{\mu\Gamma\left(\frac{\mu+1}{2}\right)}\right] \times (\Sigma n_{\rm Z} Z^2) N_0 \left(\frac{m_{\rm e}c}{2\epsilon}\right)^{\frac{\mu}{2}}, \tag{6.5}$$

where the $\Sigma n_{\rm Z}$ is the total number of the ICM ion whose atomic number is Z. Since the ICM number density of Abell 3376 West-Relic is calculated to be 2.0×10^{-4} cm^{-3} by assuming β profile, the equation 6.5 is re-written as

$$\frac{dL_\epsilon}{d\epsilon} = 7.5 \times 10^{-27} N_0 \left(\frac{1}{\epsilon}\right) \qquad [\text{erg s}^{-1}\ \text{cm}^{-2}\ \text{erg}^{-1}]. \tag{6.6}$$

Utilizing observed non-thermal luminosity, this gives the total number of the superthermal electrons $N_0 < 4.3 \times 10^{70}$ within the HXD's field of view. Here we just used the upper limit luminosity because the detection is indefinite. Following Sarazin and Kempner (2000), we define the lower cut-off energy of the superthermal electron to be $3kT = 3$ keV, from which the normalized electron momentum becomes $p = \sqrt{(1 + (3kT)/(m_{\rm e}c^2))^2 - 1} = 0.11$. When we integrate the energy of these electrons up to 100 keV, i.e. $p = 0.65$, the total kinetic energy of the non-thermal emission is represented to be

$$E_{\rm tot}^{\rm NTB} = \int_{0.11}^{0.65} N_0 m_{\rm e}c^2 \frac{\sqrt{p^2+1}-1}{p^2} dp < 5.5 \times 10^{63} \qquad [\text{erg}]. \tag{6.7}$$

On the other hand, the total energy of the thermal emission is written as

$$E_{\rm total}^{\rm th} \sim \frac{3}{2}\left(2 \times N_{\rm tot}^{\rm th} \times kT\right) = 1.5 \times 10^{63} \qquad [\text{erg}]. \tag{6.8}$$

This is comparable to that of the non-thermal energy predicted with the NTB scenario, implying that the non-thermal emission can affect the thermal component. However, such effect on the ICM temperature has not been found because the temperature in Abell 3376 West-Relic region are consistent with that from the central region.

Another difficulty of the NTB interpretation is a great amount of Coulomb loss due to electron-electron encounter in the thermal plasma. The Coulomb loss rate is $\sim 10^4$ times higher than the bremsstrahlung loss rate for a 100 keV electron, by which the cooling time of electrons is shortened to $\sim 1 \times 10^8$ year. This indicates that the non-thermal electrons dissipate the kinetic energy of $\sim 10^{65}$ erg during the Hubble time ($\sim 10^{10}$ year). As a result, the ICM should be heated up to extremely high temperature. However, such sign is not found in the temperature profile (§5.1), and therefore, the NTB scenario is thought to be implausible.

6.4.2 Inverse Compton Scattering

In the last section, the NTB scenario is found to be unrealistic. Then, we here discuss the inverse Compton (IC) interpretation for the non-thermal emission.

As shown in §5.6.5, the observed non-thermal flux with HXD PIN and XIS suggests that the non-thermal emission would have the photon index of $\Gamma \sim 2$. This is consistent with the radio halo spectra of $\sim 2.0-2.5$ obtained from the previous observations. When the relativistic electrons have powerlaw-like energy distribution ($N_{\rm e}(\gamma) = N_0 \gamma^{-\mu}$), the electron number index are represented as $\mu = 2\alpha + 1 = 2(\Gamma - 1) + 1 = 3$. This is comparable to the cosmic ray electron spectrum at the top of the earth atmosphere. Then, we adopt this index to discuss IC emission.

The spectrum of the IC emission is written as

$$\begin{aligned} \frac{dL_{\rm IC}}{d\nu} &= \frac{3\pi\sigma_{\rm T}}{h^2c^2} b(\mu) N_0 (kT_{\rm CMB})^3 \left(\frac{kT_{\rm CMB}}{h\nu_{\rm IC}}\right)^{\alpha} \\ &= 5.55 \times 10^{-27} \frac{N_0}{\nu}, \qquad [\rm erg\ s^{-1}\ Hz^{-1}] \qquad (6.9) \\ b(\mu) &= \frac{2^{\mu+3}(\mu^2+4\mu+11)\ \Gamma\left(\frac{\mu+5}{1}\right)\ \zeta\left(\frac{\mu+5}{1}\right)}{(\mu+3)^2(\mu+1)(\mu+5)}. \qquad (6.10) \\ & \qquad (6.11) \end{aligned}$$

This equation allows us to introduce IC scattering parameters by means of the observed luminosity of the non-thermal emission. Here, we use upper limits of non-thermal luminosity again since the detection is indefinite for all observations with the HXD and XIS. The luminosity of the non-thermal emission from Abell 3376 West-Relic, $<1.2\times10^{44}$ erg s^{-1}, in 15−50 keV, is converted to $<1.6\times10^{44}$ erg s^{-1} in 2−10 keV by assuming the photon index of 2. Then we obtain $N_0 < 5.3 \times 10^{70}$. The total energy of the non-thermal electrons is derived by integrating the powerlaw-like spectrum described above multiplied by $\gamma m_{\rm e} c^2$ as

$$E^{\rm CR}_{\rm total} = \int_{\gamma \rm min}^{\infty} N_0 \gamma m_{\rm e} c^2 N_{\rm e}(\gamma) d\gamma = \int_{\gamma \rm min}^{\infty} N_0 \frac{\gamma m_{\rm e} c^2}{\gamma^3} d\gamma \qquad [erg]. \qquad (6.12)$$

Then, the total energy of the non-thermal electrons can be calculated to be $<4.7\times10^{61}$ erg. Assuming that the volume emitting the non-thermal emission is comparable to the HXD's field of view, the energy density becomes $<1.1\times10^{-13}\left(\frac{1000}{\gamma_{\rm min}}\right)$ erg cm^{-3}.

In the same manner, we calculate the parameters of the IC scattering for the other targets, assuming that the non-thermal flux obtained with XIS is the its upper limit. The flux is estimated in the 2−10 keV, and the volume of the non-thermal emission is defined as a sphere with the radius of $7'$. The energy densities are roughly consistent among these targets. Compared with the thermal energy density, which is estimated in 6.4.4 with reference to the equation 6.8, that of the non-thermal electron is smaller by two orders of magnitude typically. The IC parameters derived here are summarized in table 6.1.

Table 6.1: The IC scattering parameters.

target	position	$L^a_{\rm HXR}$ (erg s^{-1})	N^b_0	$E^c_{\rm CR}$ $\left(\frac{1000}{\gamma_{\rm min}}\right)$ (erg)	$U^d_{\rm CR}$ $\left(\frac{1000}{\gamma_{\rm min}}\right)$ (erg cm^{-3})
Abell 3376	Center/East-Relic	$<1.9\times10^{43}$	$<2.4\times10^{69}$	$<2.0\times10^{60}$	$<9.0\times10^{-14}$
	West-Relic	$<1.6\times10^{44}$	$<5.3\times10^{70}$	$<4.6\times10^{61}$	$<1.1\times10^{-13}$
Abell 1060	Center	$<1.6\times10^{42}$	$<2.0\times10^{68}$	$<1.6\times10^{59}$	$<4.9\times10^{-13}$
Centaurus	Offset1	$<3.7\times10^{42}$	$<4.6\times10^{68}$	$<3.8\times10^{59}$	$<1.1\times10^{-12}$

a: the non-thermal emission in the 2−10 keV.
b: the electron number in the HXD field of view for Abell 3376 West-Relic, and in the central $7'$ circle for other targets.
c & d: the total energy and energy density of the non-thermal electrons.

6.4.3 Comparison with Radio Observation

The relativistic electrons produce the synchrotron emission at the same time by interacting with magnetic field. The spectrum of the synchrotron emission also becomes powerlaw form represented as

$$\frac{dL_{\rm sync}}{d\nu} = \frac{\sqrt{3}e^3BN_0}{m_{\rm e}c^2}\frac{\Gamma(\frac{3\mu+19}{12})\Gamma(\frac{3\mu+1}{12})}{(\mu+1)}\left(\frac{3eB}{2\pi m_{\rm e}c\nu_{\rm sync}}\right)^{\alpha}, \tag{6.13}$$

where $e = 4.8\times10^{-10}$ is the electron charge in cgs unit, Γ is the gamma function (Rybicki & Lightman 1979), and $\alpha = (\mu-1)/2 = \Gamma-1$ is the energy index. Combined with the IC spectrum of equation 6.9, the luminosity ratio of the synchrotron and IC emission is simply given as

$$\frac{L_{\rm IC}}{L_{\rm sync}} = \frac{U_{\rm CMB}}{U_{\rm B}}. \tag{6.14}$$

Here, $U_{\rm CMB}$ is the energy density of the CMB, and have been known by the observations as well as $L_{\rm IC}$ and $L_{\rm sync}$. Then, the rest parameter $U_{\rm B}$ can be obtained,

which is precious way to measure the averaged cluster magnetic field. We estimate the magnetic field for each target below.

When the non-thermal emission from Abell 3376 West-Relic is diffuse, the non-thermal photons are considered to be created by the same electrons which generate the radio emission of West-Relic if non-thermal photons are generated via IC scattering. From the radio observation with VLA, the integrated flux of the West-Relic is 82±5 mJy at 1.4 GHz (Bagchi 2002). Using the photon index of $\Gamma = 2$, the synchrotron luminosity becomes $1.9{\times}10^{40}h_{50}^{-2}$ erg s^{-1} over 1−5 GHz. The energy density of the CMB photons is represented as $U_{\rm CMB} = 4.2 \times 10^{-13}(1+z)^4$ erg cm^{-3}. Moreover, the non-thermal luminosity in the 2−10 keV is $L_{\rm HXR} < 1.6 \times 10^{44}$ erg s^{-1} as shown in the previous section. Then the averaged magnetic field at the West-Relic is calculated as $B > 0.04$ μG from the relation of equation 6.14.

In the case of Abell 3376 Center, Abell 1060, and Centaurus cluster, most of the radio emission is associated with a member galaxy. This suggests that only small portion of the radio emission is appendant with the ICM. We here introduce the fractional factor f, which represents the fraction of the radio emission contained in the ICM against the total emission. The factor f would take small value of $\ll 1$.

For the Abell 3376 Center, the East-Relic is located outside of the spectral integrated area ($r < 7'$). Then, if exist, the non-thermal emission is considered to be coincident with the radio galaxy (MRC 0600-399) at the cluster center as shown in figure 6.3. We obtained the radio flux, 136 mJy, of the radio galaxy from a catalog published by NRAO VLA Sky Survey (NVSS) (Condon et al. 1998). Hence, the integrated luminosity is estimated as $2.7f{\times}10^{40}$ erg s^{-1}. When the non-thermal luminosity of $L_{\rm HXR} < 1.9 \times 10^{43}$ erg s^{-1} obtained with XIS is assumed to be a upper limit of the non-thermal emission, it provides the lower limit of magnetics field $B > 0.13\sqrt{f}$ μG. In the case of Abell 1060, there are two radio source associated with two dominant galaxies at the cluster center (figure 6.3). Since the summed flux become 112 (63+49) mJy, the radio luminosity is calculated as $2.5f{\times}10^{39}$ erg s^{-1}. The upper limit of the non-thermal luminosity $L_{\rm HXR} < 1.6 \times 10^{42}$ gives us the averaged magnetic field of $B > 0.13\sqrt{f}$ μG. Centaurus cluster has the radio source (1246-410) in its center. The synchrotron flux is reported to be 1.4 Jy at 5 GHz (Taylar et al. 2002). This corresponds the radio luminosity $3.9f{\times}10^{40}$ erg s^{-1}. By using the upper limit of the non-thermal luminosity $L_{\rm HXR} < 3.6{\times}10^{42}$, the magnetic field is found to be $>0.33\sqrt{f}$ μG. The synchrotron luminosity and magnetic field are summarized in table 6.2.

In this way, the IC scattering interpretation requires the low magnetic field, especially for Abell 3376 West-Relic (0.04 μG), since the recent radio observations indicate that the clusters of galaxies typically have the magnetic field of a few μG. One ides to resolve this discrepancy is the inhomogeneous distribution of the magnetic field. It is suspected that the magnetic field forms a number of compressed flux tubes where the field strength reaches up to μG. Meanwhile, the magnetic field is relatively weak outside the flux tubes. If the relativistic electrons are kept outside the flux tubes, they would not show strong synchrotron emission while they produce significant IC emission. Thus, the IC scattering may be able to explain the lower magnetic field.

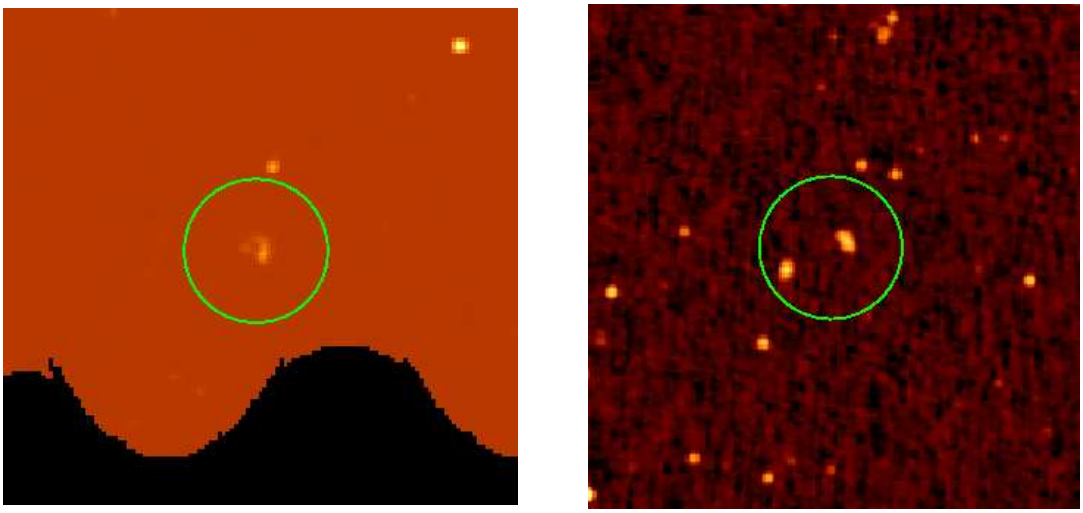

Figure 6.3: The radio image of Abell 3376 (left) and Abell 1060 (right) obtained from NVSS. The green circles show the central 7′ region.

Table 6.2: The synchrotron parameters.

target	position	$L^a_{\rm HXR}$ (erg s^{-1})	$L^b_{\rm sync}$ (erg s^{-1})	$U^c_{\rm CMB}$ (erg cm^{-3})	B^d (μG)	$\tau^e_{\rm cool}$ (year)
Abell 3376	Center/East-Relic	$<1.9\times10^{43}$	$2.7f\times10^{40}$	5.0×10^{-13}	$>0.13\sqrt{f}$	$1.1\times10^{8}\left(\frac{B}{\mu G}\right)^{1/2}$
	West-Relic	$<1.2\times10^{43}$	1.9×10^{40}	5.0×10^{-13}	>0.04	$1.1\times10^{8}\left(\frac{B}{\mu G}\right)^{1/2}$
Abell 1060	Center	$<1.6\times10^{42}$	$2.5f\times10^{39}$	4.3×10^{-13}	$>0.13\sqrt{f}$	$1.3\times10^{8}\left(\frac{B}{\mu G}\right)^{1/2}$
Centaurus	Offset1	$<3.7\times10^{42}$	$3.9f\times10^{42}$	4.3×10^{-13}	$>0.33\sqrt{f}$	$1.3\times10^{8}\left(\frac{B}{\mu G}\right)^{1/2}$

a: the 2−10 keV luminosity of the non-thermal emission.
b: the luminosity of the synchrotron emission obtained from radio observations.
c: the energy density of the CMB.
d: the magnetic field of the ICM.
e: the cooling time of the non-thermal electrons.

Meanwhile, the Lorentz factor gives us the cooling time of the relativistic electrons. The relation between the frequency and the Lorentz factor is presented as

$$\nu_{\rm sync} = 4.2\left(\frac{B}{\mu G}\right)\gamma^2. \tag{6.15}$$

Then, the Lorentz factor of the electron is $\gamma = 1.8\times10^4\left(\frac{B}{\mu G}\right)^{-1/2}$ at 1.4 GHz. The cooling time of the relativistic electron ($\tau_{\rm cool} = \gamma/b_{\rm IC}$) is calculated from the Lorentz factor γ, and the energy loss function of $b_{\rm IC}$ which is represented as

$$b_{\rm IC} = \frac{4}{3}\frac{\sigma_{\rm T}}{m_{\rm e}c}\gamma^2 U_{\rm CMB}. \tag{6.16}$$

Using the Lorentz factor derived above, the cooling time of the relativistic electrons in Abell 3376 West-Relic is found to be $\tau_{\rm cool} \sim 1 \times 10^8 \left(\frac{B}{\mu G}\right)^{1/2}$ year. The cooling time resembles each other among sample clusters. During the Hubble time, the total energy of the non-thermal emission by IC scattering is calculated to be $\sim 10^{63}$ erg at most. Since this is comparable to the thermal energy (equation 6.8), the IC scattering is free from heating up effect of the ICM mentioned in the NTB process.

6.4.4 Total Energy and Energy Densities

Since the total energy and energy density of the relativistic electrons as well as the averaged magnetic field are derived in §6.4.2 and 6.4.3, we compare the energetics between the non-thermal and the thermal emission.

With the method as described in equation 6.8, the total energy of the thermal plasma can be estimated from the averaged number density and the temperature. In addition, the total energy of the magnetic field is represented as

$$E^{\rm B}_{\rm total} = U_{\rm B} \times \frac{4}{3}\pi R^3, \tag{6.17}$$

where $U_{\rm B}$ is the energy density of the magnetic field, and R is the integration radius. The total energy and energy density for each component is summarized in table 6.3. The energy density of the magnetic field is extremely low as compared with the non-thermal one in Abell 3376 West-Relic. This may implies that the energy equipartition between the non-thermal electrons and the magnetic field is not approved although the non-thermal emission must be surely detected to discuss more detail.

We also compare the energetics derived here with the previous analysis of Coma (Fusco-Femiano et al. 1999), Abell 2256 (Fusco-Femiano et al. 2000), Abell 2199 (Kempner & Sarazin 2000), and HCG 62 group (Nakazawa 2000). Figure 6.4 shows the comparison between the thermal and non-thermal energy. Our results have a similar distribution to that of the other observations. The ratio of the non-thermal to the thermal one roughly similar among these targets, and is $\sim 0.1-1 \left(\frac{1000}{\gamma_{\rm min}}\right)$ %.

When we mention the Lorentz factor of the relativistic electrons from the thermal plasma density and the magnetic field, their cooling time becomes longest at $\gamma \sim 100-300$ as shown in figure 2.3.5. The $\gamma_{\rm min}$ which is as low as a few hundred implies that the non-thermal energy may be an order of magnitude higher than that when the generally used value of $\gamma_{\rm min} = 1000$ (e.g. Fusco-Femiano et al. 2000) is assumed.

Table 6.3: The total energy and energy density.

target/item	total energy (erg)	energy density (erg cm^{-3})	N_0^a
Abell 3376 Center/East-Relic			
thermal emission	4.1×10^{62}	1.9×10^{-11}	2.3×10^{70}
relativistic electron	$<2.0\times10^{60}\left(\frac{1000}{\gamma_{\rm min}}\right)$	$<9.0\times10^{-14}\left(\frac{1000}{\gamma_{\rm min}}\right)$	$<2.4\times10^{69}$
magnetic field	$>2.7f\times10^{57}\left(\frac{B}{0.13\mu{\rm G}}\right)^2$	$>3.4f\times10^{-16}\left(\frac{B}{0.13\mu{\rm G}}\right)^2$	–
Abell 3376 West-Relic			
thermal emission	1.5×10^{63}	3.6×10^{-12}	8.7×10^{70}
relativistic electron	$<4.6\times10^{61}\left(\frac{1000}{\gamma_{\rm min}}\right)$	$<1.1\times10^{-13}\left(\frac{1000}{\gamma_{\rm min}}\right)$	$<1.6\times10^{70}$
magnetic field	$>4.0\times10^{55}\left(\frac{B}{0.04\mu{\rm G}}\right)^2$	$>9.5\times10^{-20}\left(\frac{B}{0.04\mu{\rm G}}\right)^2$	–
Abell 1060 Center			
thermal emission	1.6×10^{61}	4.8×10^{-11}	1.2×10^{69}
relativistic electron	$<1.6\times10^{59}\left(\frac{1000}{\gamma_{\rm min}}\right)$	$<4.9\times10^{-13}\left(\frac{1000}{\gamma_{\rm min}}\right)$	$<2.0\times10^{68}$
magnetic field	$>3.2f\times10^{56}\left(\frac{B}{0.13\mu{\rm G}}\right)^2$	$>9.4f\times10^{-16}\left(\frac{B}{0.13\mu{\rm G}}\right)^2$	–
Centaurus Offset1			
thermal emission	5.1×10^{61}	1.6×10^{-10}	3.3×10^{69}
relativistic electron	$<3.8\times10^{59}\left(\frac{1000}{\gamma_{\rm min}}\right)$	$<1.1\times10^{-12}\left(\frac{1000}{\gamma_{\rm min}}\right)$	$<4.6\times10^{68}$
magnetic field	$>2.1f\times10^{56}\left(\frac{B}{0.33\mu{\rm G}}\right)^2$	$>6.4f\times10^{-16}\left(\frac{B}{0.33\mu{\rm G}}\right)^2$	–

a: the total number of the thermal or relativistic electrons.

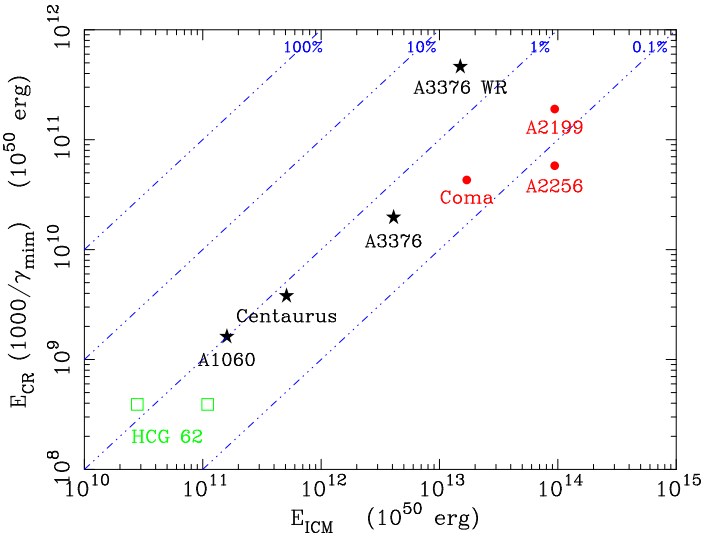

Figure 6.4: The total non-thermal energy against that of the thermal emission.

6.5 Acceleration and Heating Mechanism

Since the energetics of the non-thermal emission is obtained, we discuss the possible mechanism of particle acceleration and plasma heating in Cooling Flow clusters.

The heating energy of cool plasma in the cluster center is calculated by multiplying the volume of cool plasma with the equation 6.8. The ICM temperature at the center is $\sim$1$-$5 keV (§5.3.1), and the central electron density reaches at $\sim$0.05 cm^{-3} (§5.2.1). The heating effect restricting Cooling Flow is limited in the central a few tens kpc. Assuming the heating area as $\sim$30 kpc, we can derive the total thermal energy of the central cool plasma to be $\sim 10^{59-60}$ erg. By means of the cooling time of the ICM at the cluster center, $\sim 10^{8-9}$ years, the energy loss rate of the central cool plasma is calculated to be $\sim 10^{42-44}$ erg s^{-1}. On the other hand, the non-thermal energy within the central 30 kpc become roughly $<10^{58}$ erg from the table 6.4. Then the cooling time of the non-thermal electrons, $\sim 10^{8}$ years (table 6.2), gives the non-thermal energy loss rate of $<10^{41}$ erg s^{-1}. As compared with the cool plasma, it is found that the energy ratio of the non-thermal electrons to the thermal ones is $<$10 %.

The supernova remnant is noble target because it is observationally revealed that the acceleration and plasma heating take place at the same time. From the energetics in our Galaxy, the typical energy ratio of non-thermal to thermal emission is considered to be 1$-$10 %. The acceleration mechanism of supernova is shock acceleration (i.e. the first order Fermi acceleration). Therefore, the energy ratio should take lower value $<$1 % when the particle acceleration occurs thorough the second order Fermi acceleration by turbulent. Our ratio calculated above is applicable to both mechanism. Then, we can not draw a conclusion to which mechanism concerns to the plasma heating at the cluster center.

Although it is impossible to discuss acceleration mechanism (shock wave or turbulent), we argue about the energy injection of physical phenomena in the clusters of galaxies. As shown in §6.2, there are three proposed models to explain the plasma heating; AGN jet, thermal conduction, and hierarchical evolution with merger. The thermal conduction is excluded from discussion since it has no concern to particle acceleration. The AGN jet model is build up on the basis of the shock acceleration while the hierarchical evolution model contains both shock and turbulent acceleration. Besides these models, the galaxy motion give a possibility to cause the particle acceleration by magnetohydrodynamics turbulent when the member galaxies interact with the magnetized ICM (§2.2.6). Hence, we argue about the energy supply to ICM by the AGN jet, hierarchical evolution, and galaxy motion below.

First is the AGNs which hosts in the cD galaxy at the cluster center. When matter accretes on a massive black hole at the center of AGN, it is thought that $\sim$10 % of the rest mass energy of the accreting matter is converted into plasma heating or particle acceleration (Ensslin et al. 1998). Such energy is considered to be injected into the ICM by the jet or lobes of the AGN. Considering the typical mass of a black hole, 10^7 $M_\odot$, the total energy of the relativistic particles is to be $\sim 2\times 10^{60}$ erg over its typical epoch of $\sim 10^8$ year (e.g. Valagaes & Silk 1999). Then, the energy input rate from AGN during 10^{8-9} years is $\sim 10^{43-44}$ erg s^{-1}, which implies

that AGN could supply the enough thermal energy into the central cool plasma as well as the non-thermal electron. However, the restriction that the AGNs should repeat the jet explosion to order to inject huge energy to the ICM continuously is necessary because the epoch time of AGN explosion is shorter than the cooling time. Furthermore, the energy input by the AGNs is effective for only the limited region around them. The typical scale of radio lobe $\sim$100 kpc makes a possibility of the non-thermal emission from Abell 3376 West-Relic be unrealizable.

Next candidate is the merger event during hierarchically evolving which is caused between the groups or clusters of galaxies, It is known to be observationally common feature among the galaxy clusters. A galaxy group with a typical bulk velocity of 1000 km s^{-1} has a kinetic energy of 10^{62} erg when the mass of a galaxy is assumed to be 10^{13} $M_{\odot}$. If at least 1 % of the derived kinetic energy is released, the energy loss rate during 10^{8-9} years becomes $\sim 10^{43-44}$ erg s^{-1}. The energy input is considered to become much higher in the case of the cluster merger. Then, it is possible for the released energy from the cluster merger to explain not only the total energy of the non-thermal electron but also the central cool plasma. Since the merger shock is observed in a few tens % of galaxy clusters, the clusters of galaxies are considered to experience merger event at once per 10^9 years. On the other hand, the energy loss time scale of the cool plasma or the non-thermal electrons is 10^{8-9} years. This implies that clusters of galaxies must undergo recent merger in order to cause the plasma heating and particle acceleration via merger event.

The huge kinetic energy from the random motion of galaxies is also a candidate for the plasma heating and particle acceleration. Assuming the mass-to-light ratio of $M_{\rm star}/L_{\odot} = 8$, the total mass of the stellar component for a galaxy having a typical optical luminosity of $L_{\rm B} = 1 \times 10^{11} L_{\odot}$ is estimated to be $M_{\rm star} = 8 \times 10^{11} M_{\odot}$. When the galaxies are moving in the ICM with the velocity of $v \sim 700$ km s^{-1}, their kinetic energy becomes as much as $\frac{1}{2} M_{\rm star} \times (700 {\rm km\ s^{-1}})^2 = 4 \times 10^{60}$ erg. When there are a few tens galaxies in the cluster center, the total kinetic energy reaches at $\sim 10^{61}$ erg. If it is assumed that the galaxies release $\sim$10 % (i.e. $\sim 10^{60}$ erg) of their kinetic energy in 10^{8-9} years, the energy injection rate due to the galaxy motion is estimated as $\sim 10^{43-44}$ erg s^{-1}. Although the galaxy motion also be able to explain both the thermal and non-thermal energy, there are one matter for consideration. When the galaxies keep on losing their own energy with the energy release efficiency above, they should fall into the bottom of the cluster potential well during the Hubble time. Recent Chandra observation has found the indication of the ICM-galaxy interaction (ram stripping pressure) but the observational evidence is not enough yet. Thus, we can not understand the time scale of the galaxy infalling under the present situation.

In this way, each candidate discussed above could supply enough energy for the plasma heating and particle acceleration. Particularly the cluster merger is able to release huge energy. However, it is difficult for all the candidates to input the energy into thermal/non-thermal electrons constantly during the cooling time of 10^{8-9} years. They can not be simply adopted as the origin of the particle acceleration and plasma heating. The observational progress is essential to resolve the problem for each candidate. As well as it, we dearly hope to settle a controversy for the existence of the non-thermal emission or turbulent acceleration in the near future.

Chapter 7

Conclusion

From our study of the thermal and non-thermal emission from clusters of galaxies, we have arrived at following conclusions.

- Although the radiative cooling is considered to take place from the $R_{\rm start} - R_{\rm cool}$ relation, the ICM temperature gradient ($T_{\rm center}/T_{\rm cluster} = 0.3-0.6$) is milder than the prediction of Cooling Flow hypothesis. The ICM temperature at the cluster center of $T_{\rm center} = 0.6 - 5.1$ keV also conflicts with the Cooling Flow picture.

- The mass of the cooled plasma have found to be by an order of magnitude smaller than that predicted from the Cooling Flow. Such feature is confirmed by the cooling flow rate which is also smaller by an order of magnitude as well as ASCA results. Furthermore, the mass of cool plasma estimated from the central excess absorption brings the same result.

- As the heating mechanism preventing the ICM from radiatively cooling, the hierarchical evolution with merger and radiative cooling is found to be preferable. This model can reproduce not only the observed temperature structure of the ICM but also the morphological feature such as the X-ray filament or cold front.

- The sign of the non-thermal emission from Abell 3376 West-Relic is detected with HXD PIN. The flux in 15−50 keV is $(5.1 \pm 1.8 \pm 6.1) \times 10^{-12}$erg s^{-1} cm^{-2}, which gives more restricted upper limit $< 1.3 \times 10^{-11}$erg s^{-1} cm^{-2} than that from BeppoSAX of $< 2.0 \times 10^{-11}$erg s^{-1} cm^{-2}. From the combined analysis with XIS, the photon index and the extent of the non-thermal emission is estimated to be 1.7−2.2 and $\sim$15−60$'$. For the other targets from which the sign of non-thermal emission is found with XIS, we just obtain the upper limit flux of the non-thermal emission.

- The non-thermal luminosity from Abell 3376 West-Relic is $<1.6\times10^{44}$ erg s^{-1} in 2−10 keV, which is roughly <10 % of the thermal emission as well as the other targets. The total energy of the relativistic electron is $<5 \left(\frac{1000}{\gamma_{\rm min}}\right)$ % of the thermal energy.

- There are no mechanism which can be simply adopted to the particle acceleration and plasma heating in the cluster center among the possible candidates such as the AGN, merger event, and galaxy motion. The observational progress is essential to resolve the problem for each candidate as well as the existence of the non-thermal emission or turbulent acceleration in the near future.

Appendix A

X-ray images

2A 0335+096

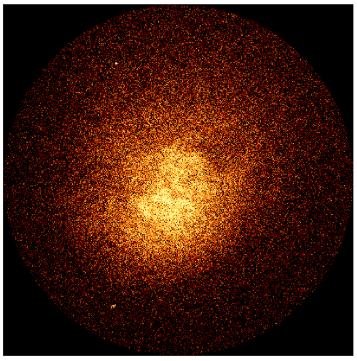

Abell 1795

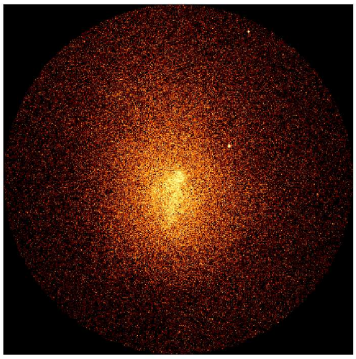

Abell 1835

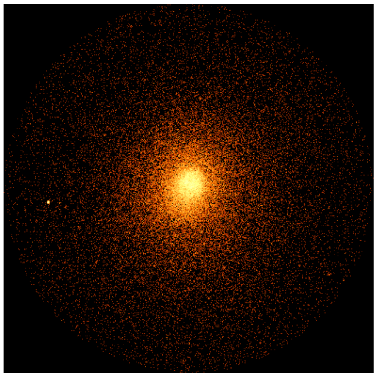

Abell 2029

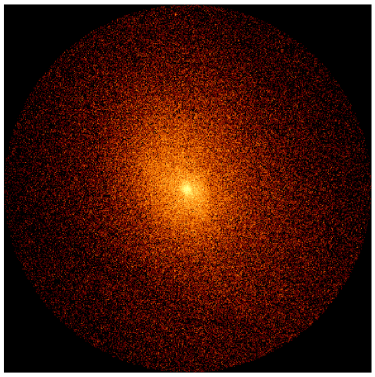

Abell 2052

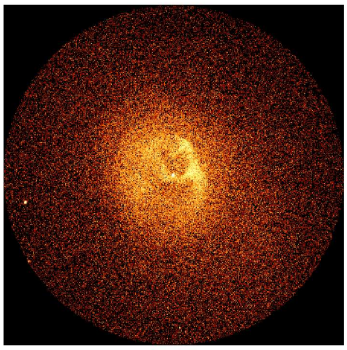

Abell 2199

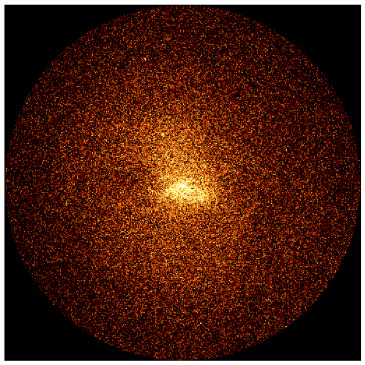

Abell 262

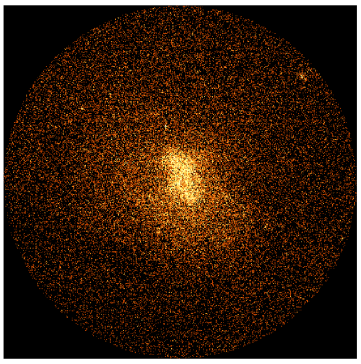

Abell 3112

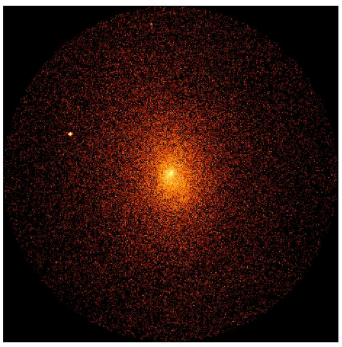

Abell 3558

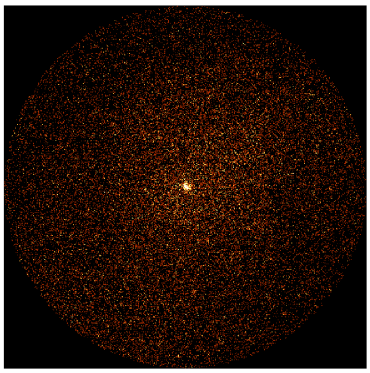

Abell 4059

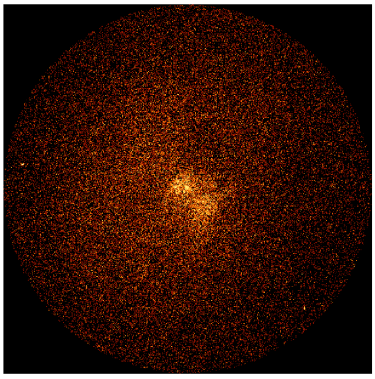

Abell 478

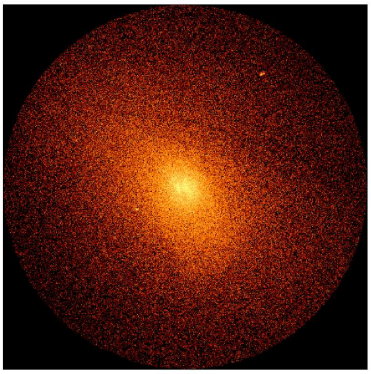

Abell 496

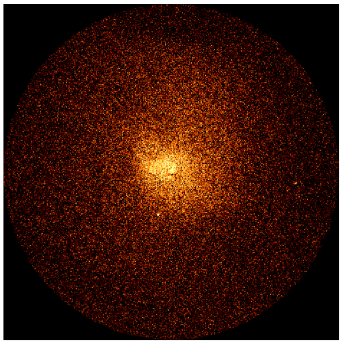

Centaurus

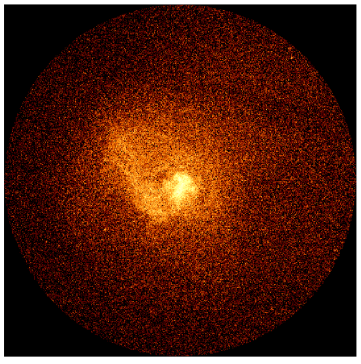

HCG 62

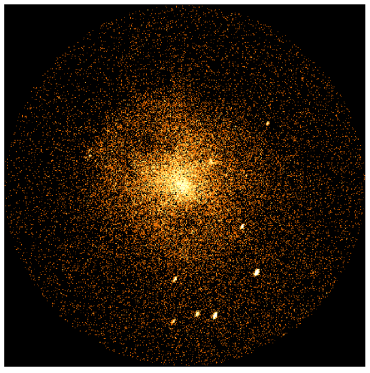

Hydra A

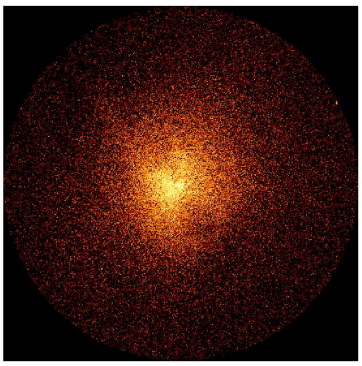

MKW 4

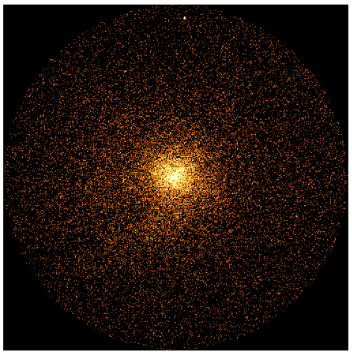

NGC 5044

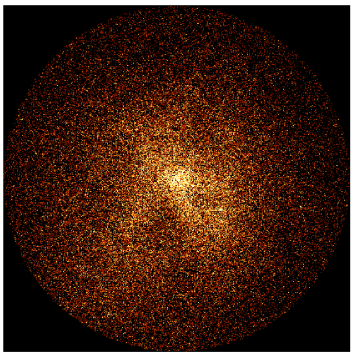

NGC 533

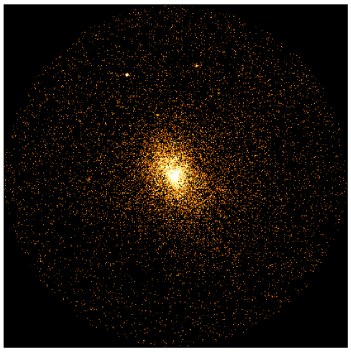

NGC 507

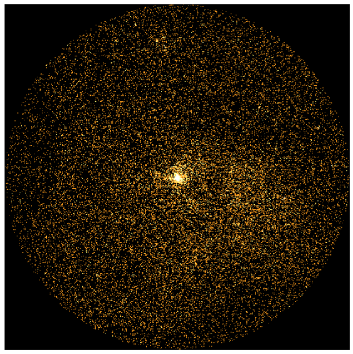

Ophiuchus

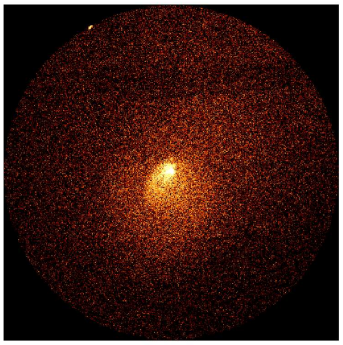

Perseus

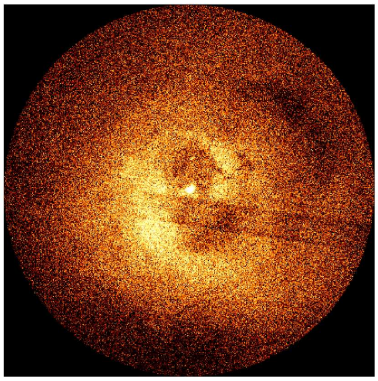

Sérsic 159-03

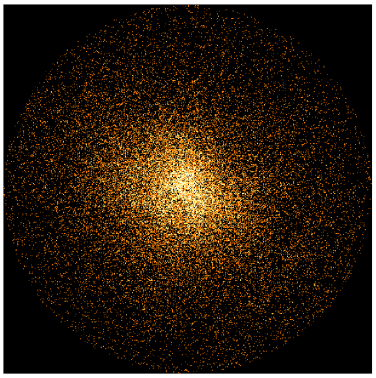

Appendix B

Radial Profiles of the Meral Abundance

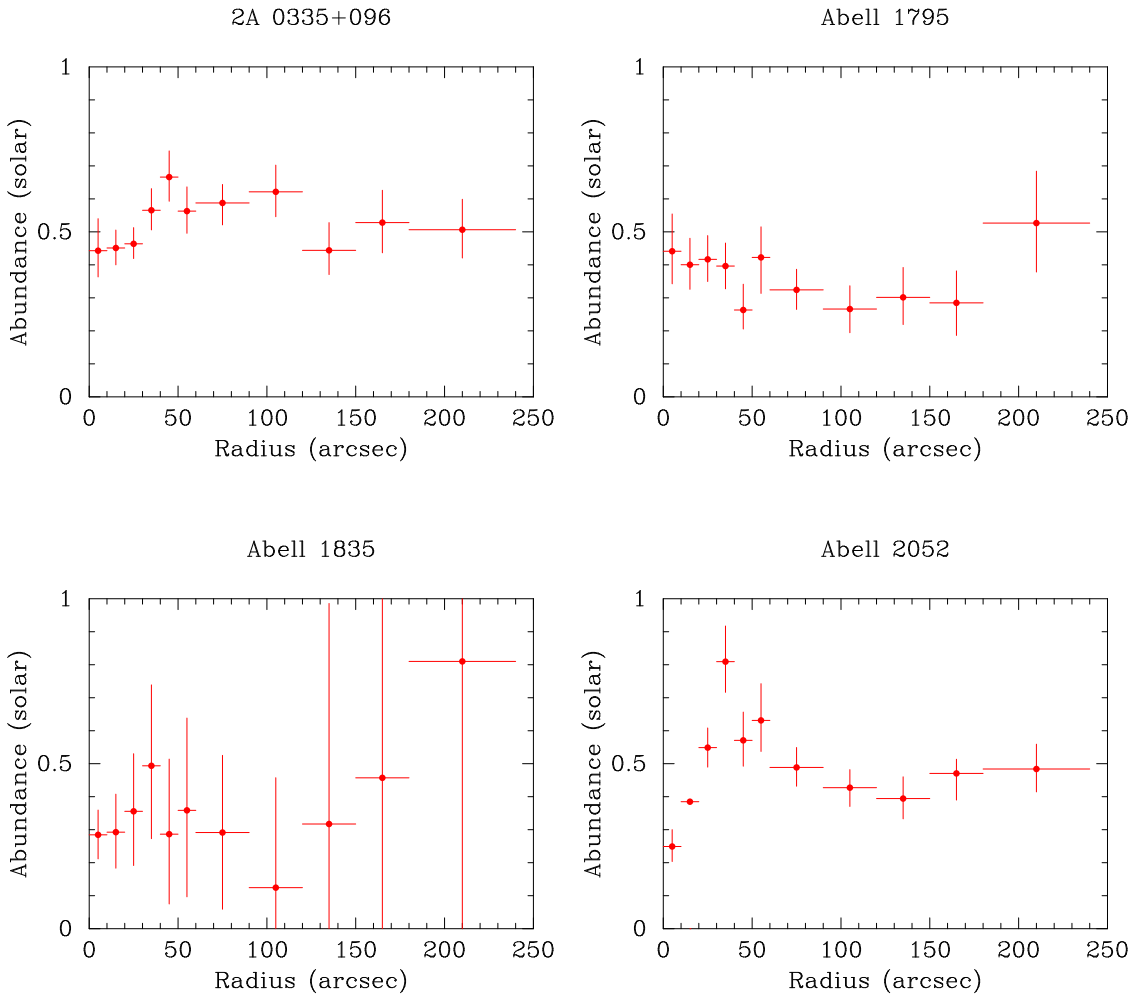

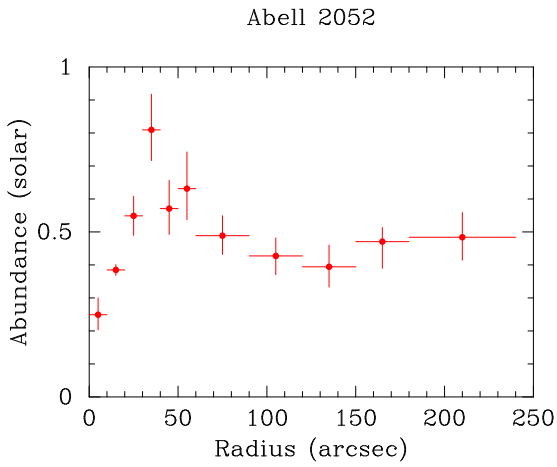
Abell 2052
Abundance (solar)
Radius (arcsec)
0
0.5
1
0
50
100
150
200
250

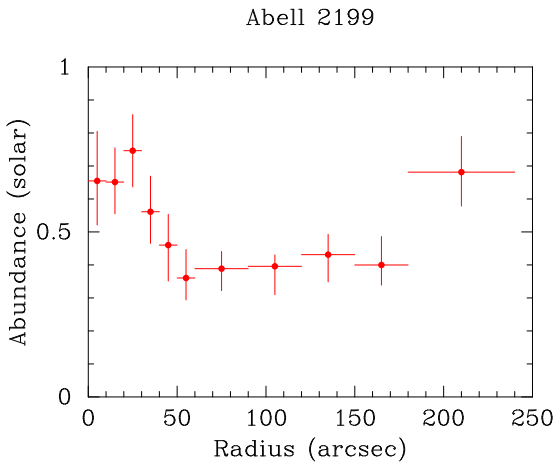
Abell 2199
Abundance (solar)
Radius (arcsec)
0
0.5
1
0
50
100
150
200
250

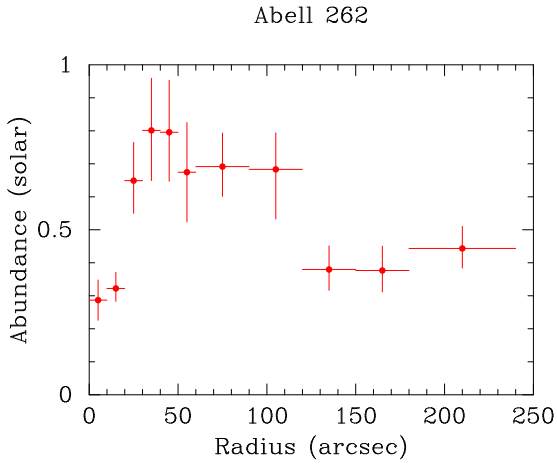
Abell 262
Abundance (solar)
Radius (arcsec)
0
0.5
1
0
50
100
150
200
250

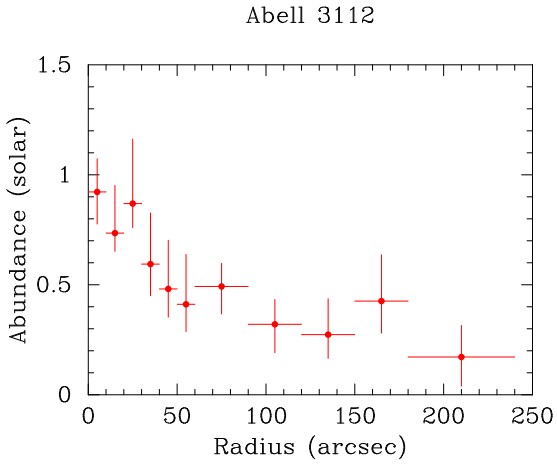
Abell 3112
Abundance (solar)
Radius (arcsec)
0
0.5
1
1.5
0
50
100
150
200
250

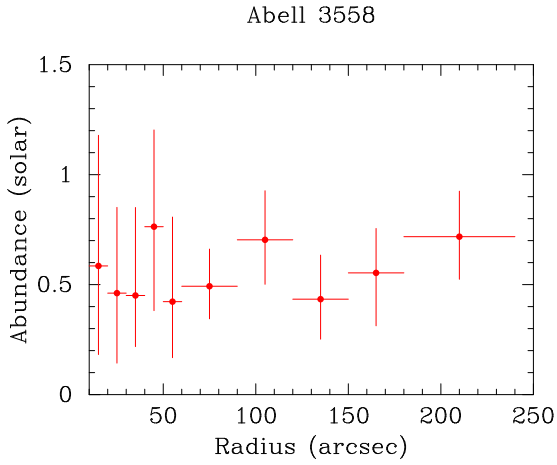
Abell 3558
Abundance (solar)
Radius (arcsec)
0
0.5
1
1.5
50
100
150
200
250

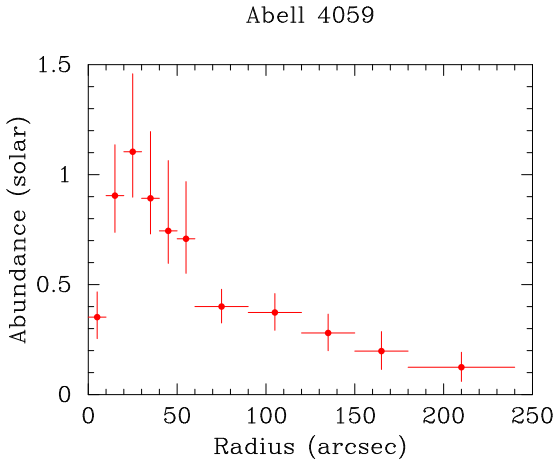
Abell 4059
Abundance (solar)
Radius (arcsec)
0
0.5
1
1.5
0
50
100
150
200
250

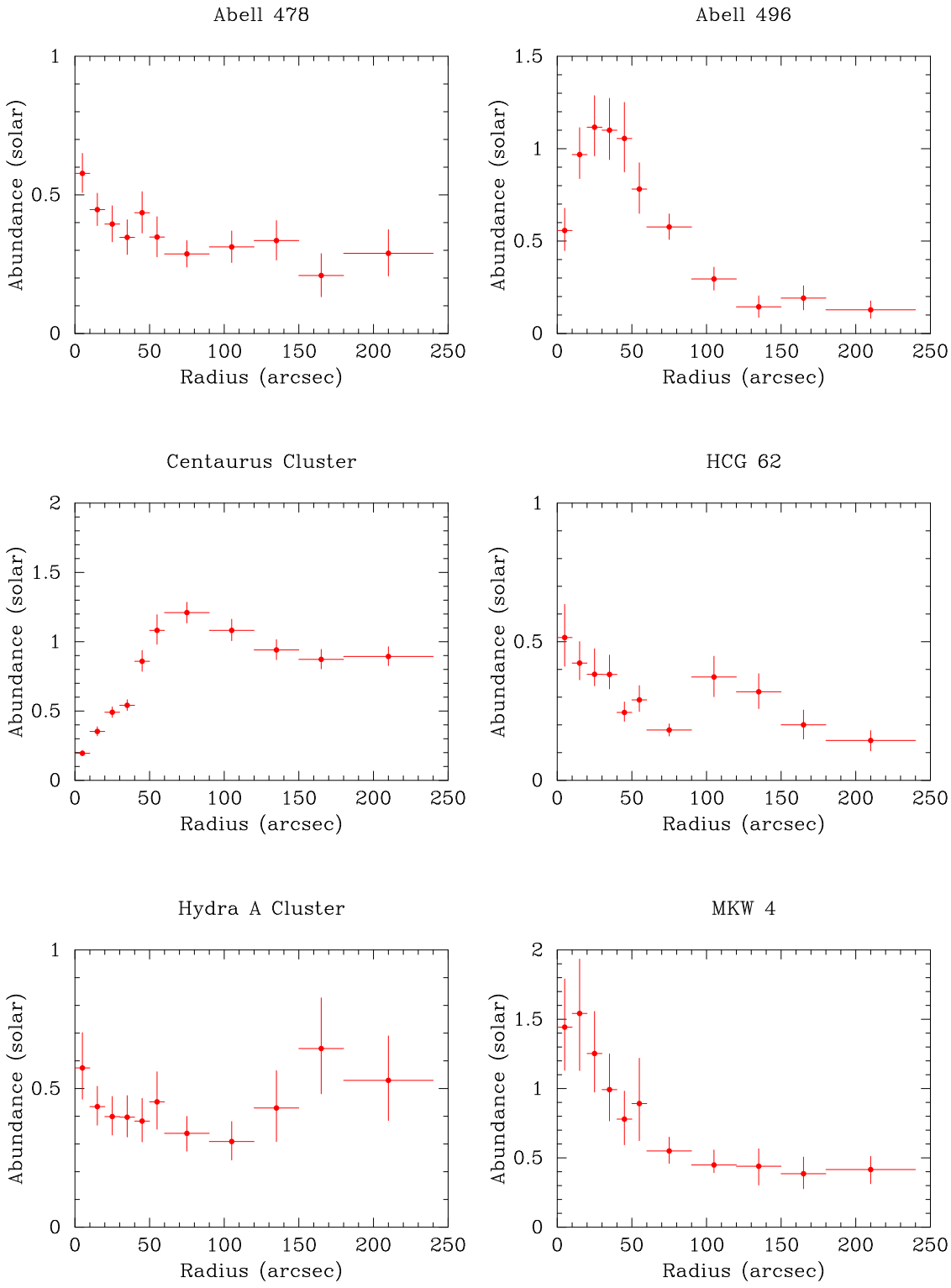
Abell 478
Abell 496
Centaurus Cluster
HCG 62
Hydra A Cluster
MKW 4
Abundance (solar)
Radius (arcsec)

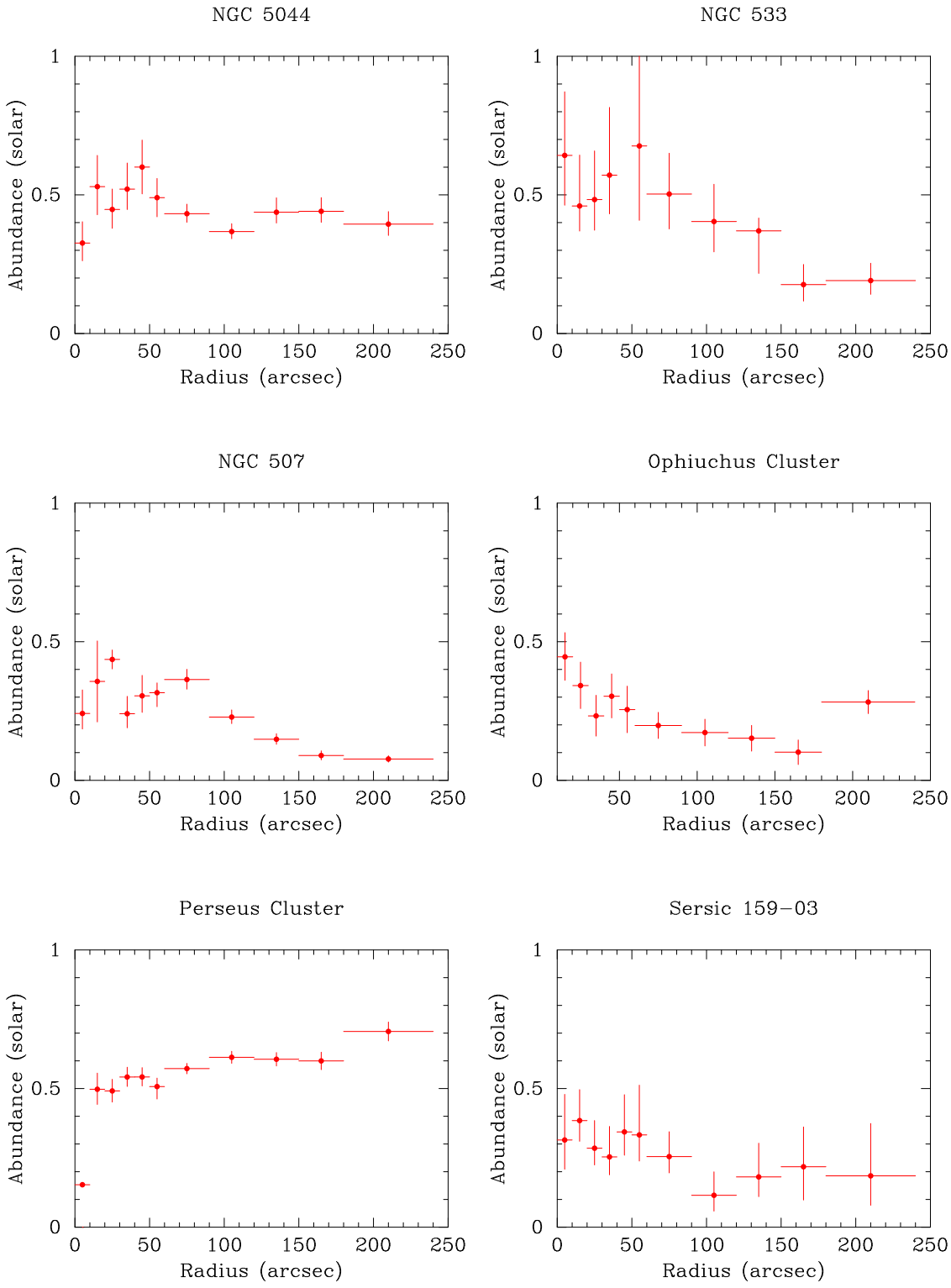
NGC 5044
NGC 533
NGC 507
Ophiuchus Cluster
Perseus Cluster
Sersic 159−03
Abundance (solar)
Radius (arcsec)
0
0.5
1
0
50
100
150
200
250

Appendix C

Radial Profiles of the Absorption Column Density

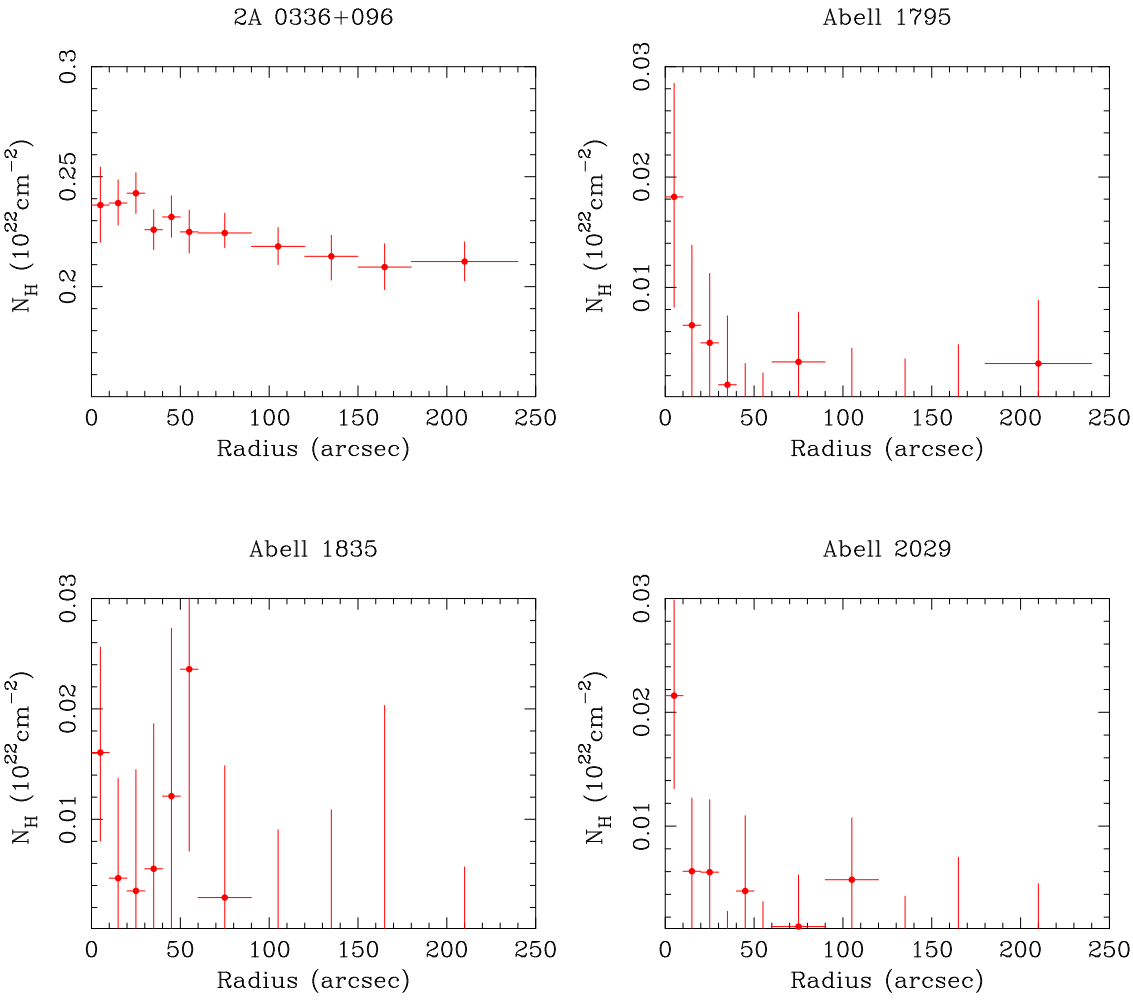

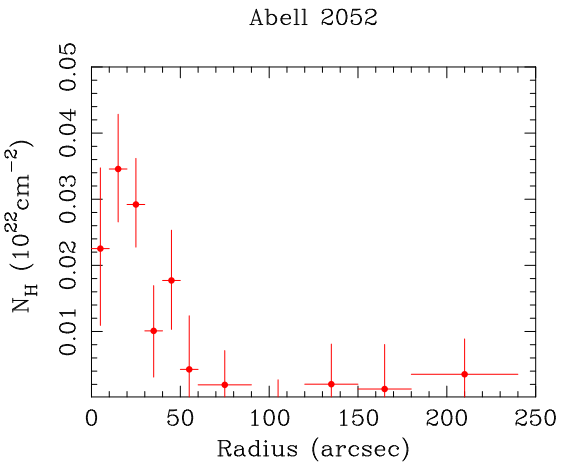
Abell 2052
N_H (10^{22}cm^{-2})
0.01 0.02 0.03 0.04 0.05
0 50 100 150 200 250
Radius (arcsec)

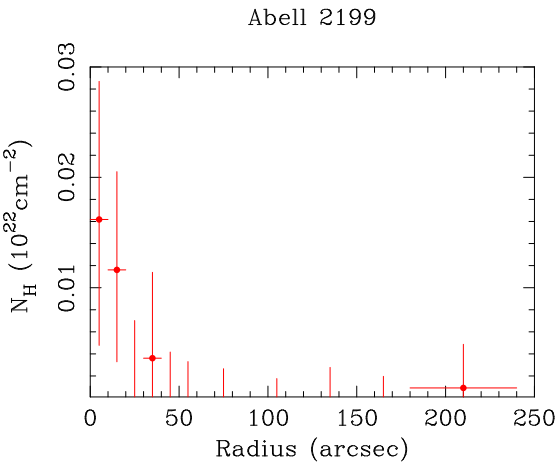
Abell 2199
N_H (10^{22}cm^{-2})
0.01 0.02 0.03
0 50 100 150 200 250
Radius (arcsec)

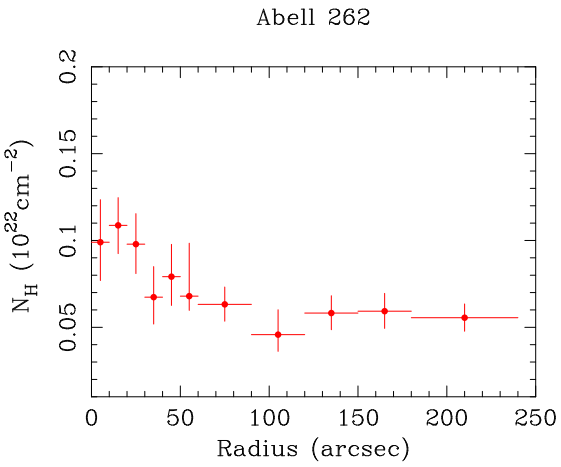
Abell 262
N_H (10^{22}cm^{-2})
0.05 0.1 0.15 0.2
0 50 100 150 200 250
Radius (arcsec)

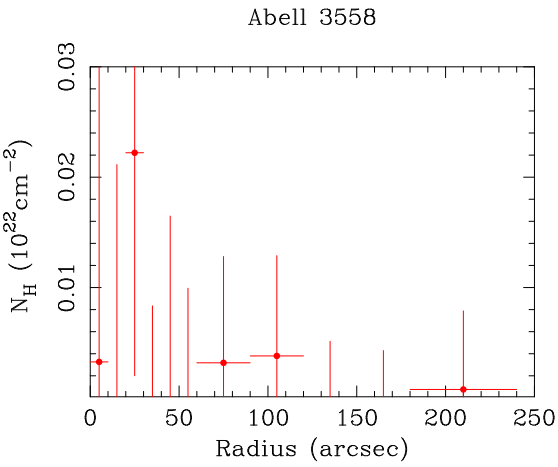
Abell 3558
N_H (10^{22}cm^{-2})
0.01 0.02 0.03
0 50 100 150 200 250
Radius (arcsec)

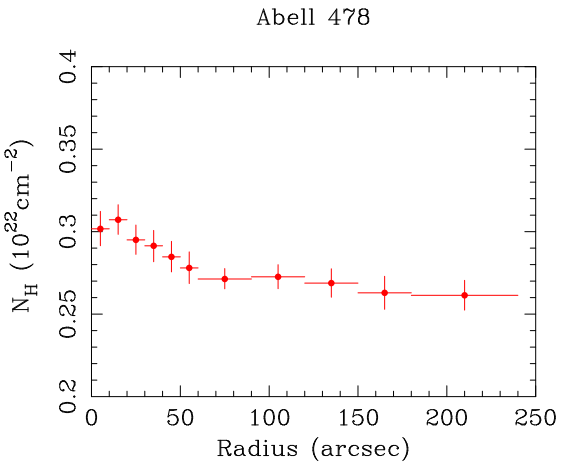
Abell 478
N_H (10^{22}cm^{-2})
0.2 0.25 0.3 0.35 0.4
0 50 100 150 200 250
Radius (arcsec)

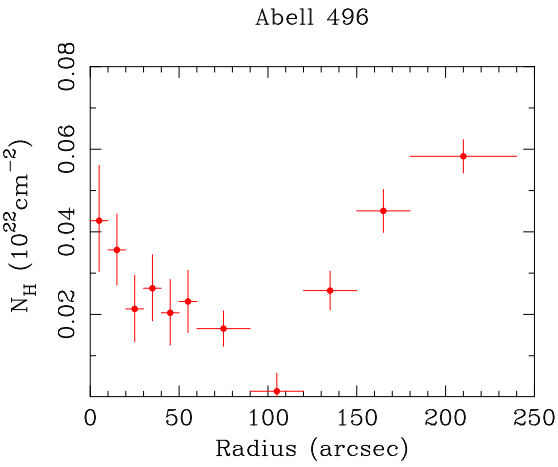
Abell 496
N_H (10^{22}cm^{-2})
0.02 0.04 0.06 0.08
0 50 100 150 200 250
Radius (arcsec)

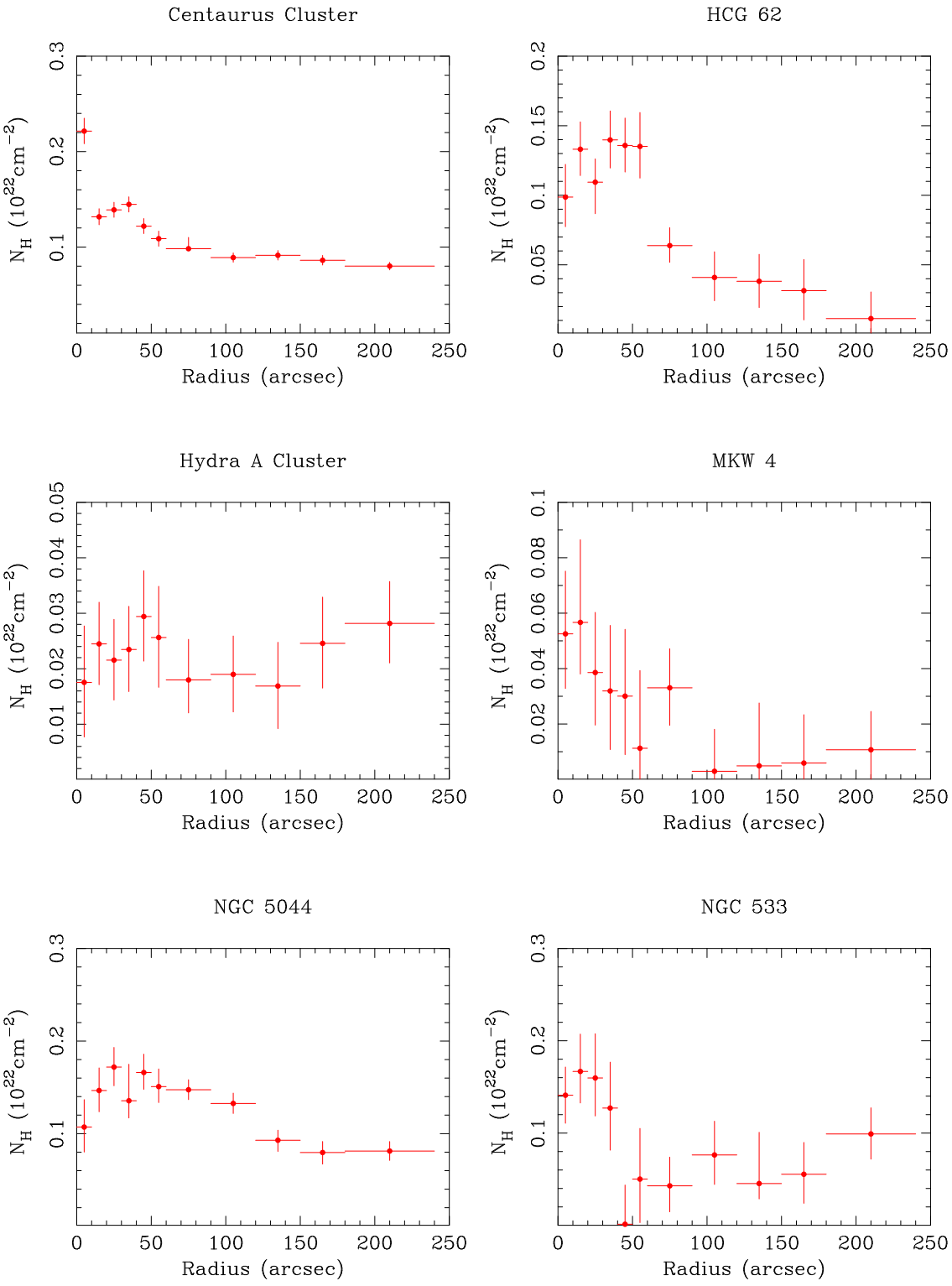
Centaurus Cluster
HCG 62
Hydra A Cluster
MKW 4
NGC 5044
NGC 533
N_H (10^{22}cm^{-2})
Radius (arcsec)

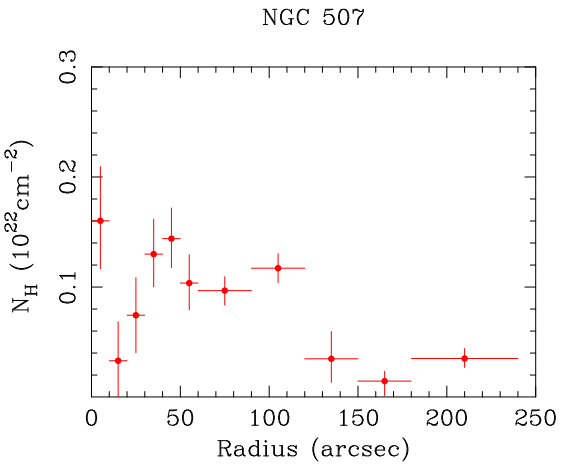
NGC 507
N_H (10^{22}cm^{-2})
0.1
0.2
0.3
0
50
100
150
200
250
Radius (arcsec)

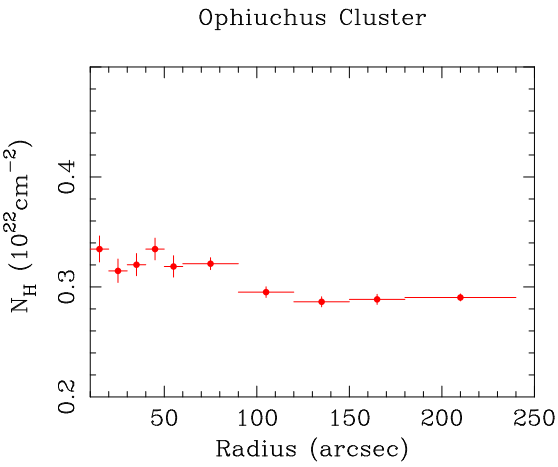
Ophiuchus Cluster
N_H (10^{22}cm^{-2})
0.2
0.3
0.4
50
100
150
200
250
Radius (arcsec)

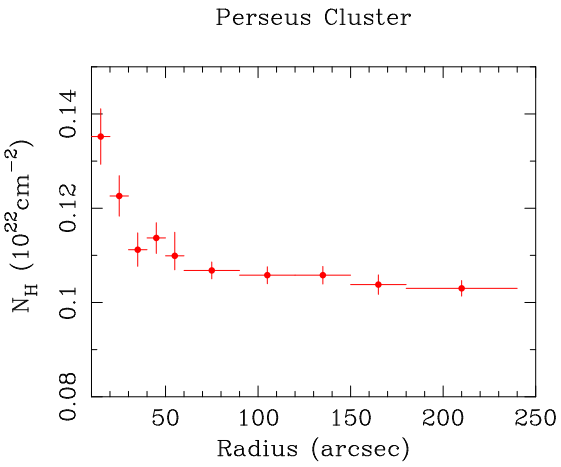
Perseus Cluster
N_H (10^{22}cm^{-2})
0.08
0.1
0.12
0.14
50
100
150
200
250
Radius (arcsec)

Appendix D

X-ray Surface Brightness Profiles

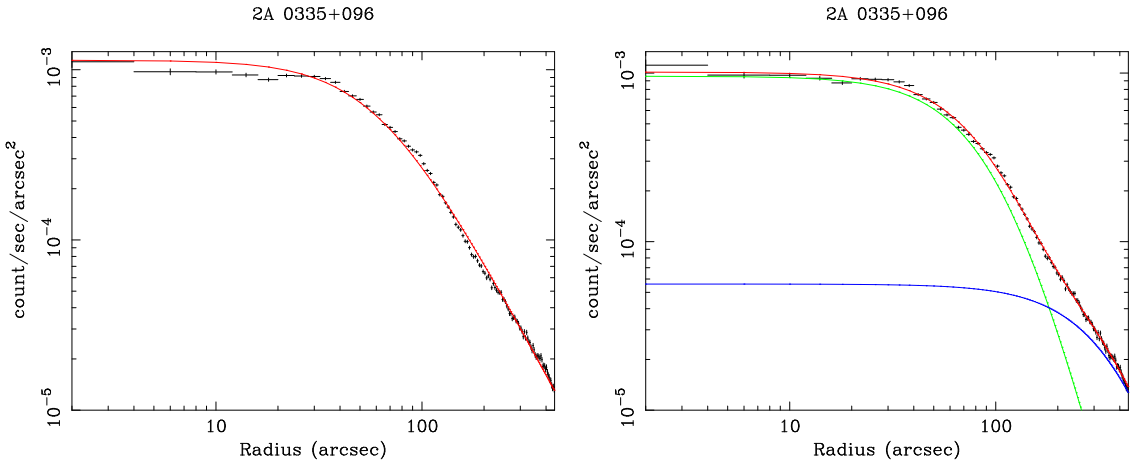

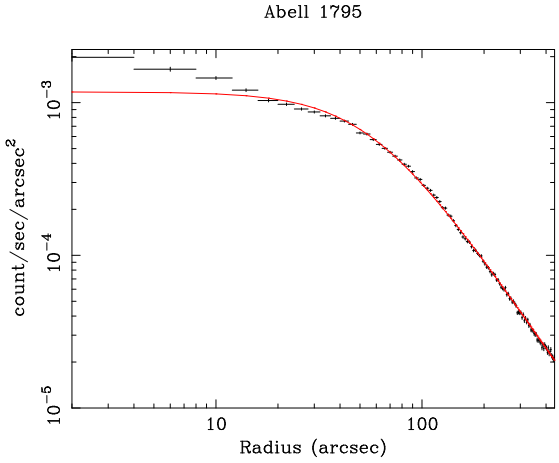

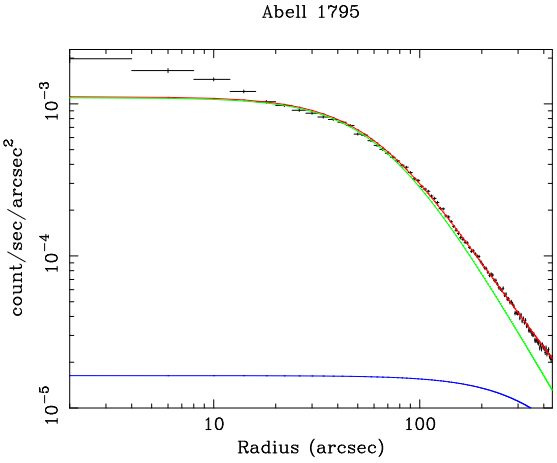

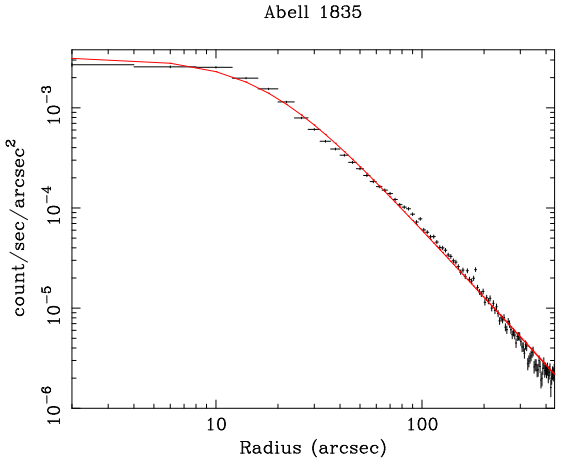
Abell 1835
count/sec/arcsec^2
10^{-3}
10^{-4}
10^{-5}
10^{-6}
10
100
Radius (arcsec)

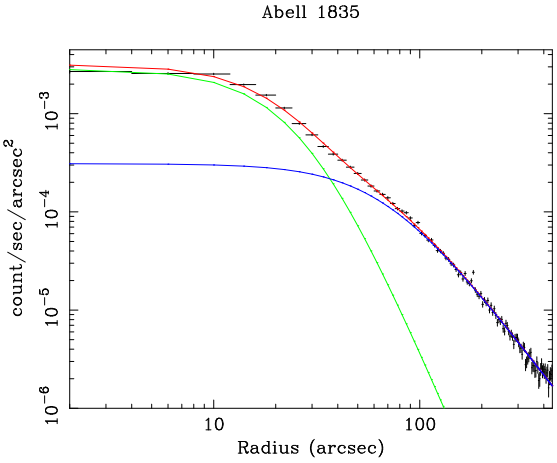
Abell 1835
count/sec/arcsec^2
10^{-3}
10^{-4}
10^{-5}
10^{-6}
10
100
Radius (arcsec)

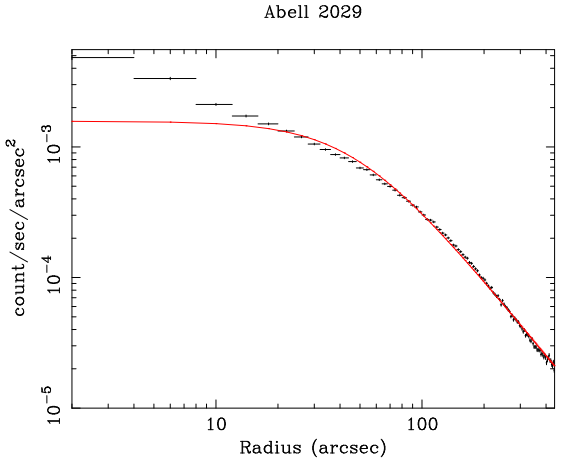
Abell 2029
count/sec/arcsec^2
10^{-3}
10^{-4}
10^{-5}
10
100
Radius (arcsec)

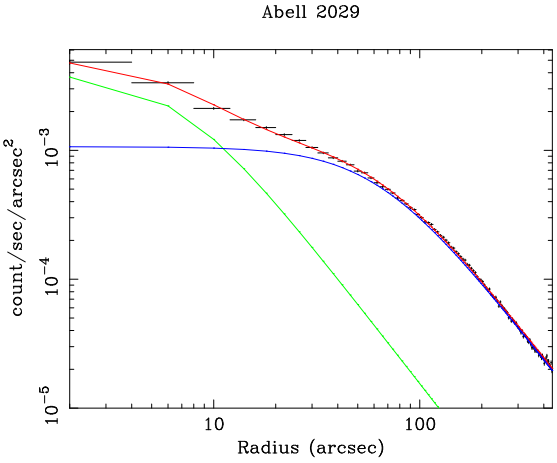
Abell 2029
count/sec/arcsec^2
10^{-3}
10^{-4}
10^{-5}
10
100
Radius (arcsec)

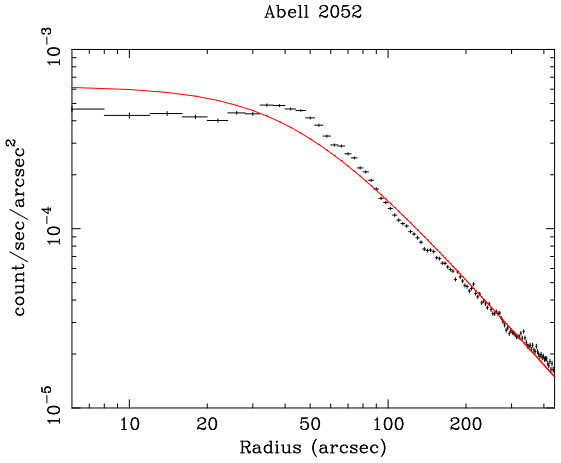
Abell 2052
count/sec/arcsec^2
10^{-3}
10^{-4}
10^{-5}
10
20
50
100
200
Radius (arcsec)

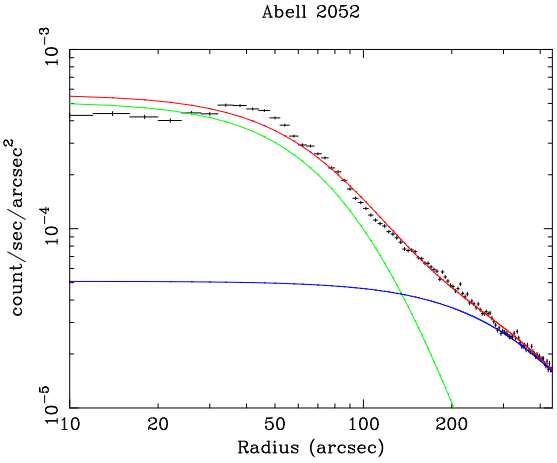
Abell 2052
count/sec/arcsec^2
10^{-3}
10^{-4}
10^{-5}
10
20
50
100
200
Radius (arcsec)

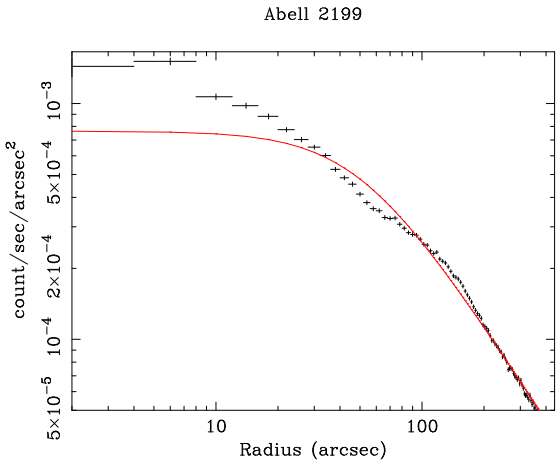
Abell 2199
count/sec/arcsec^2
Radius (arcsec)

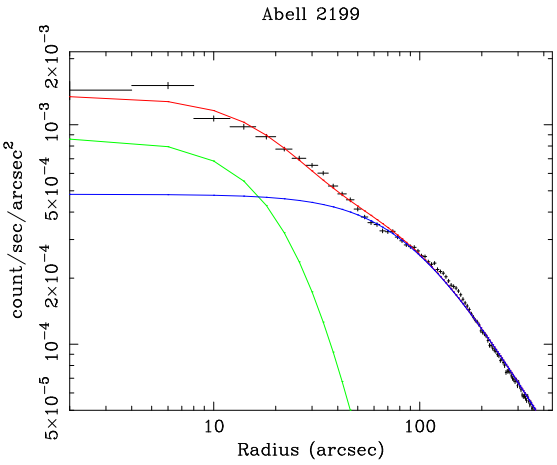
Abell 2199
count/sec/arcsec^2
Radius (arcsec)

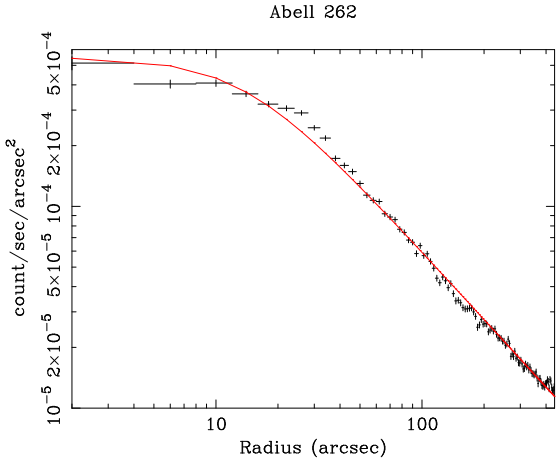
Abell 262
count/sec/arcsec^2
Radius (arcsec)

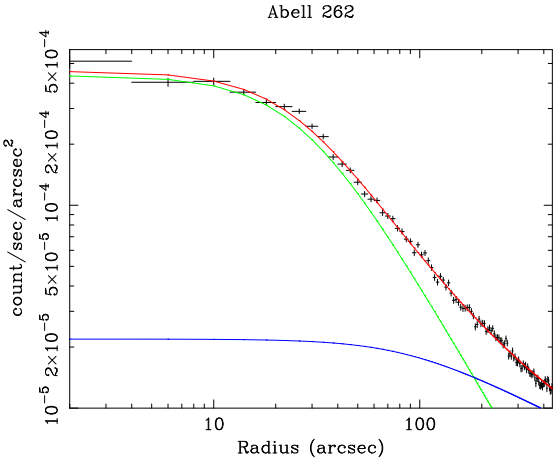
Abell 262
count/sec/arcsec^2
Radius (arcsec)

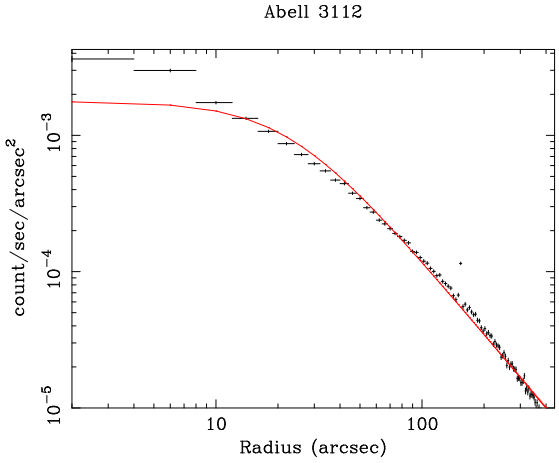
Abell 3112
count/sec/arcsec^2
Radius (arcsec)

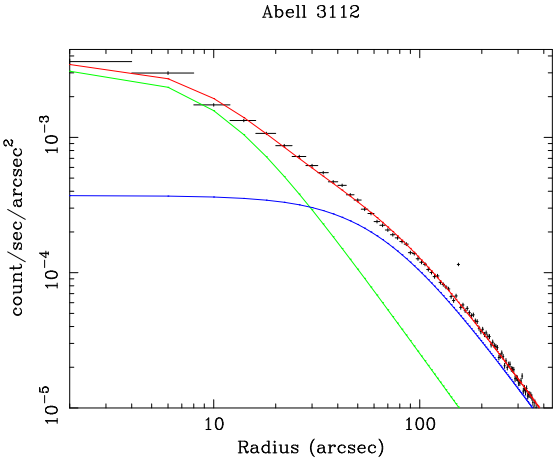
Abell 3112
count/sec/arcsec^2
Radius (arcsec)

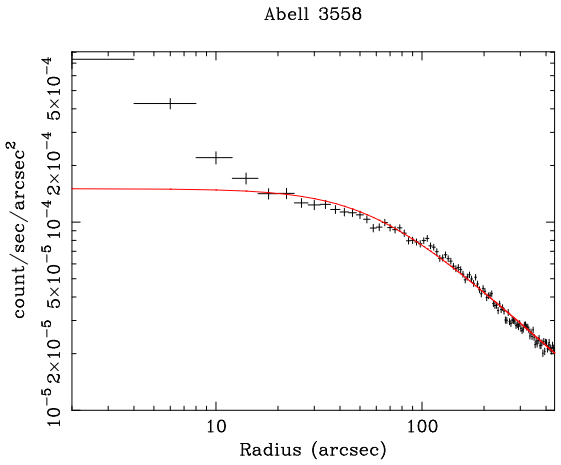
Abell 3558
count/sec/arcsec^2
10^{-5} 2×10^{-5} 5×10^{-5} 10^{-4} 2×10^{-4} 5×10^{-4}
10
100
Radius (arcsec)

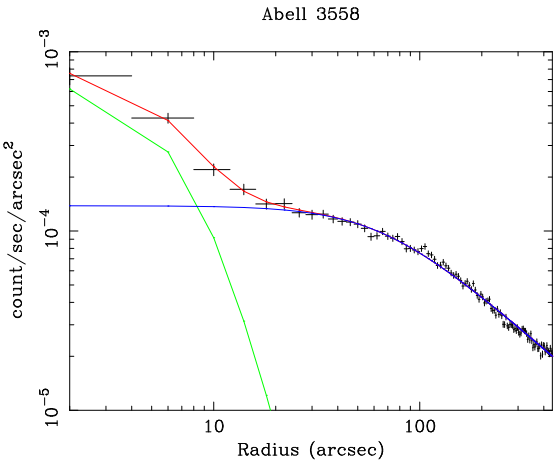
Abell 3558
count/sec/arcsec^2
10^{-3} 10^{-4} 10^{-5}
10
100
Radius (arcsec)

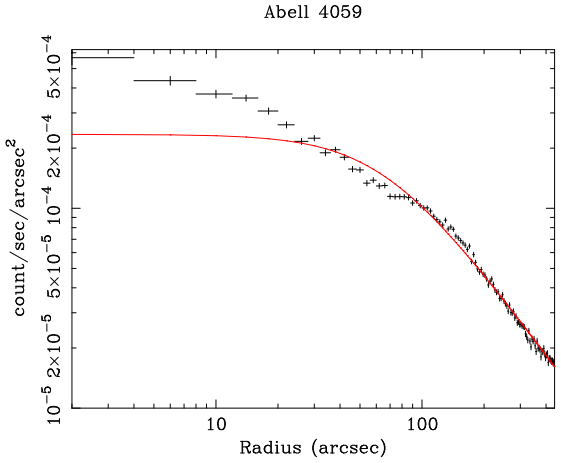
Abell 4059
count/sec/arcsec^2
10^{-5} 2×10^{-5} 5×10^{-5} 10^{-4} 2×10^{-4} 5×10^{-4}
10
100
Radius (arcsec)

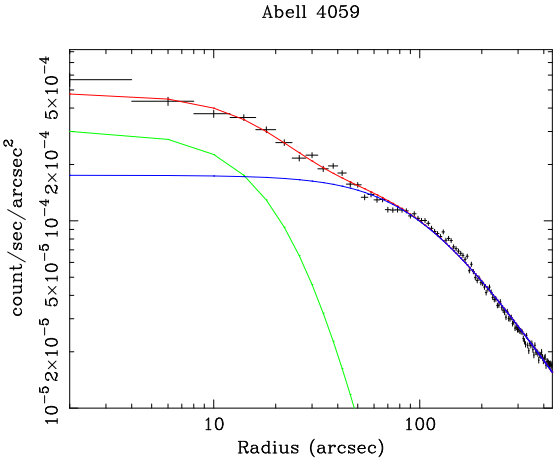
Abell 4059
count/sec/arcsec^2
10^{-5} 2×10^{-5} 5×10^{-5} 10^{-4} 2×10^{-4} 5×10^{-4}
10
100
Radius (arcsec)

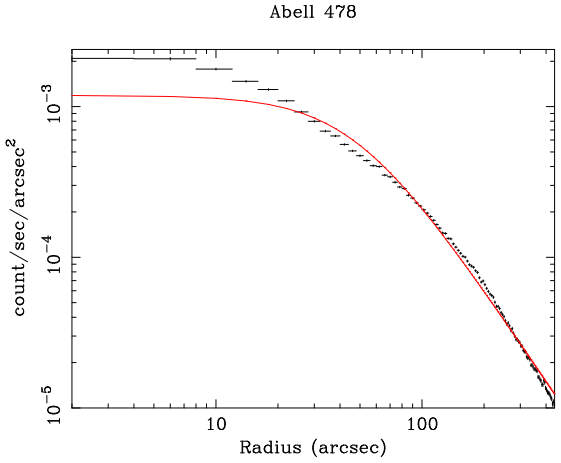
Abell 478
count/sec/arcsec^2
10^{-3} 10^{-4} 10^{-5}
10
100
Radius (arcsec)

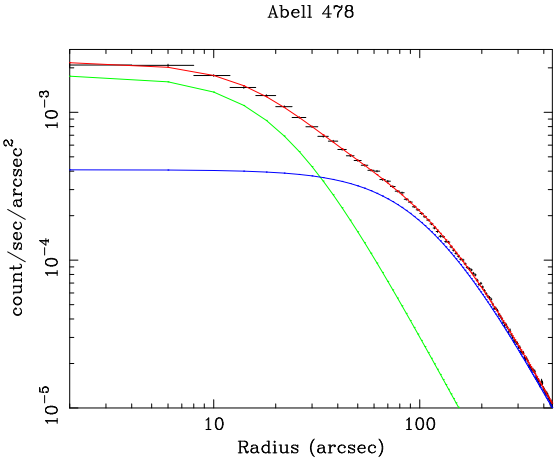
Abell 478
count/sec/arcsec^2
10^{-3} 10^{-4} 10^{-5}
10
100
Radius (arcsec)

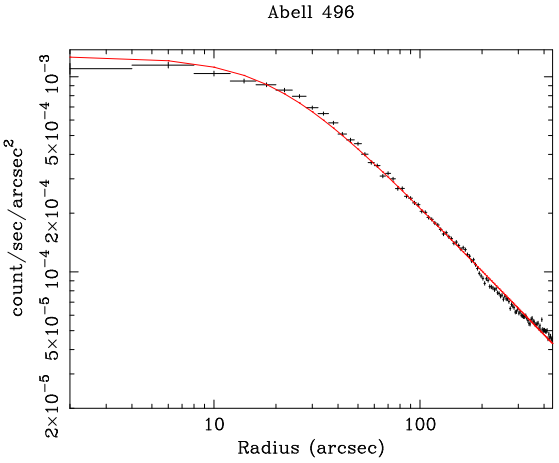
Abell 496
count/sec/arcsec^2
2×10^{-5} 5×10^{-5} 10^{-4} 2×10^{-4} 5×10^{-4} 10^{-3}
10
100
Radius (arcsec)

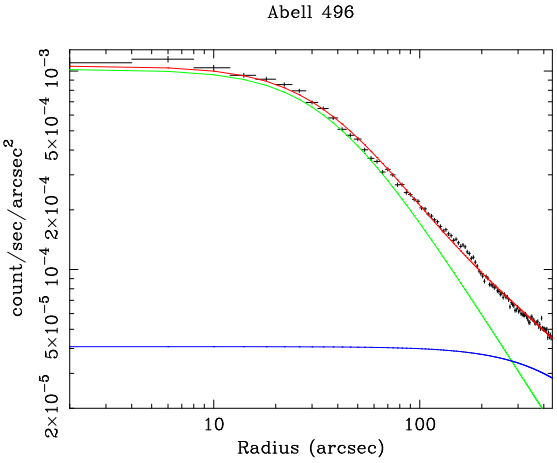
Abell 496
count/sec/arcsec^2
2×10^{-5} 5×10^{-5} 10^{-4} 2×10^{-4} 5×10^{-4} 10^{-3}
10
100
Radius (arcsec)

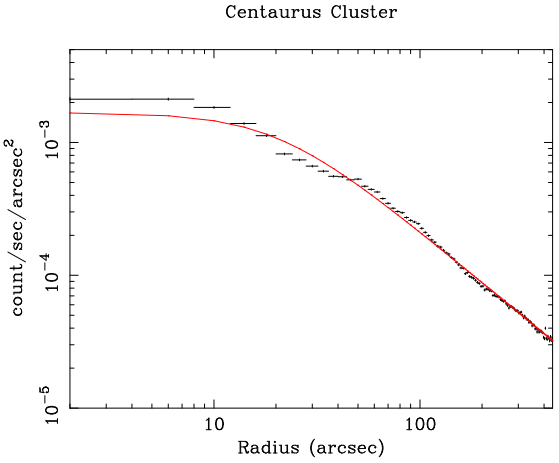
Centaurus Cluster
count/sec/arcsec^2
10^{-5} 10^{-4} 10^{-3}
10
100
Radius (arcsec)

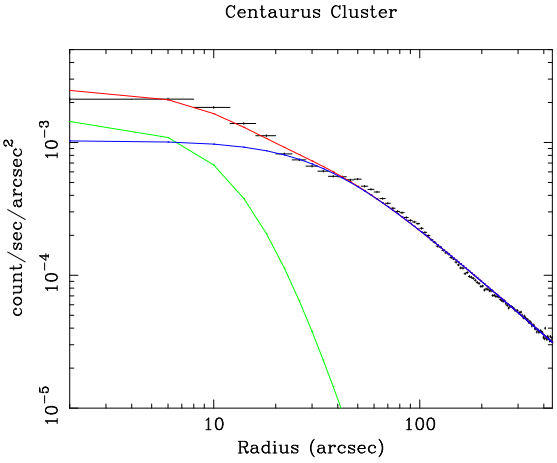
Centaurus Cluster
count/sec/arcsec^2
10^{-5} 10^{-4} 10^{-3}
10
100
Radius (arcsec)

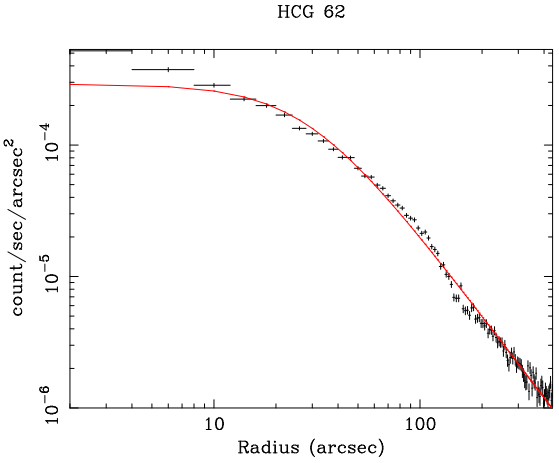
HCG 62
count/sec/arcsec^2
10^{-6} 10^{-5} 10^{-4}
10
100
Radius (arcsec)

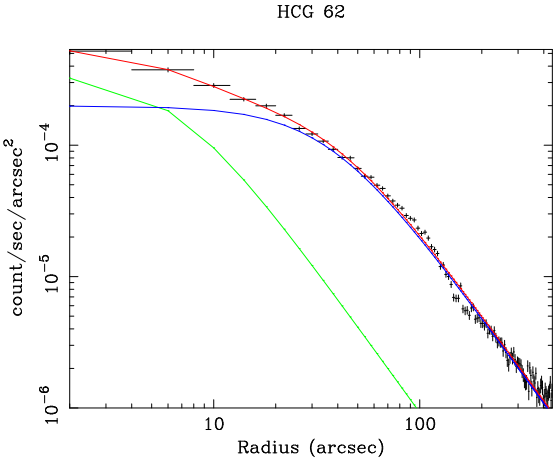
HCG 62
count/sec/arcsec^2
10^{-6} 10^{-5} 10^{-4}
10
100
Radius (arcsec)

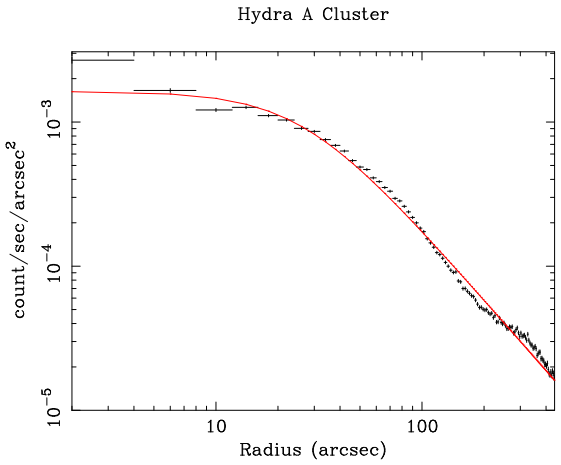
Hydra A Cluster
count/sec/arcsec^2
10^{-3}
10^{-4}
10^{-5}
10
100
Radius (arcsec)

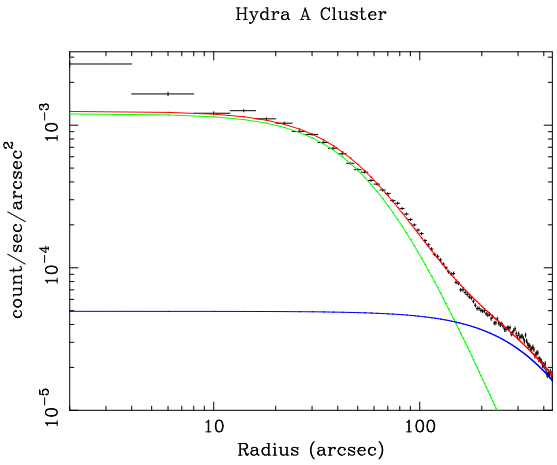
Hydra A Cluster
count/sec/arcsec^2
10^{-3}
10^{-4}
10^{-5}
10
100
Radius (arcsec)

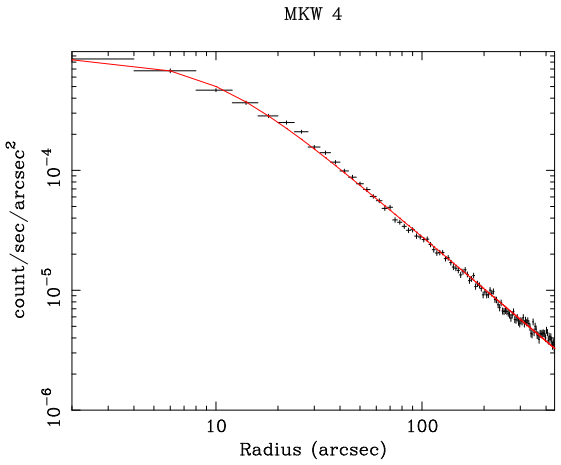
MKW 4
count/sec/arcsec^2
10^{-4}
10^{-5}
10^{-6}
10
100
Radius (arcsec)

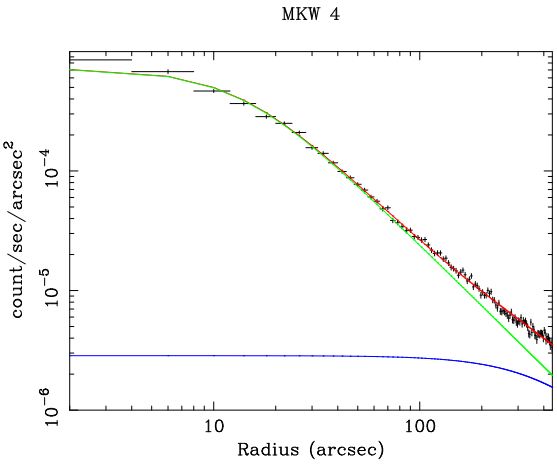
MKW 4
count/sec/arcsec^2
10^{-4}
10^{-5}
10^{-6}
10
100
Radius (arcsec)

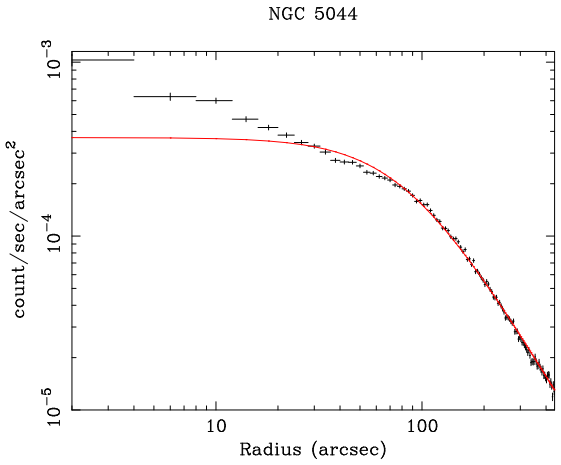
NGC 5044
count/sec/arcsec^2
10^{-3}
10^{-4}
10^{-5}
10
100
Radius (arcsec)

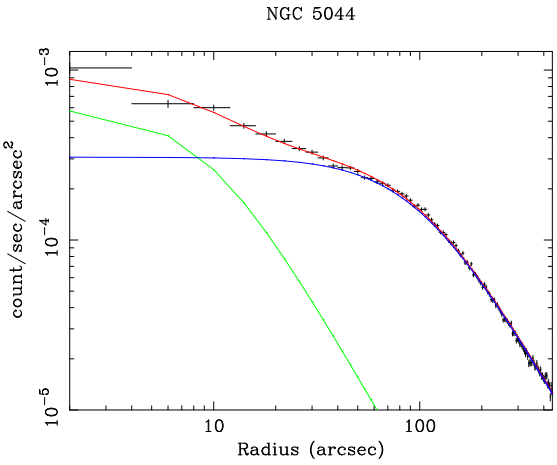
NGC 5044
count/sec/arcsec^2
10^{-3}
10^{-4}
10^{-5}
10
100
Radius (arcsec)

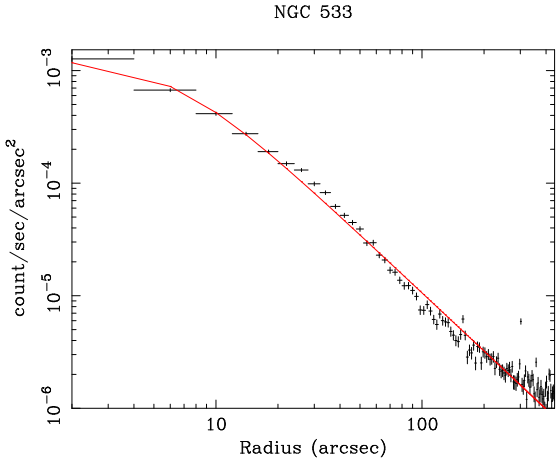
NGC 533
count/sec/arcsec^2
Radius (arcsec)

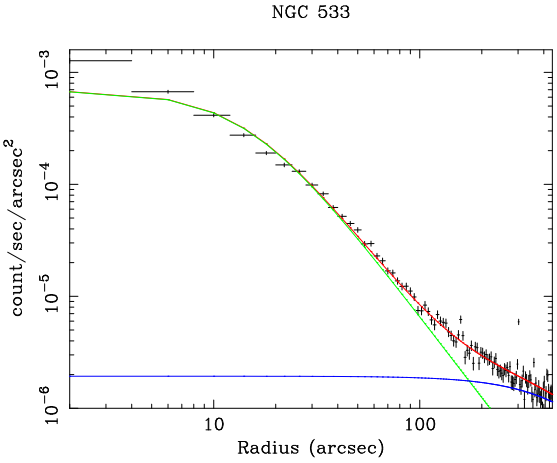
NGC 533
count/sec/arcsec^2
Radius (arcsec)

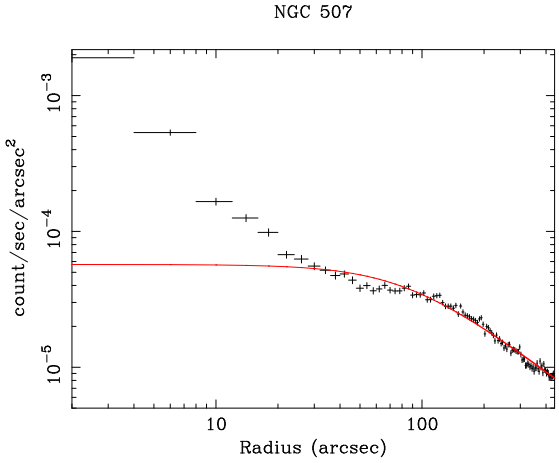
NGC 507
count/sec/arcsec^2
Radius (arcsec)

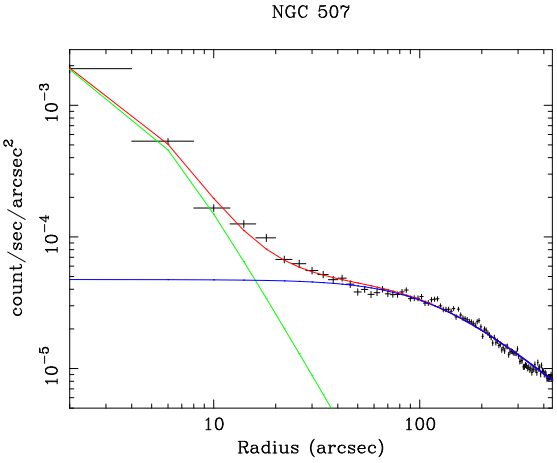
NGC 507
count/sec/arcsec^2
Radius (arcsec)

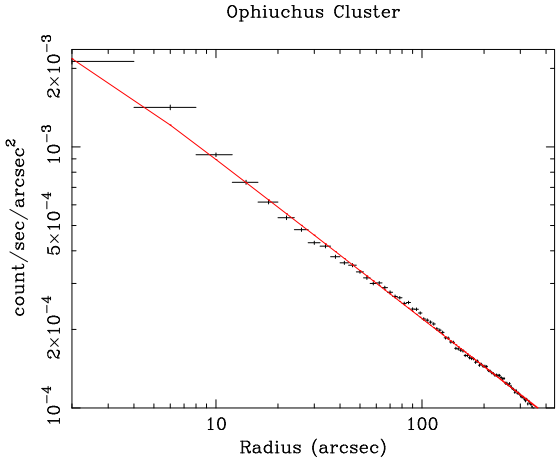
Ophiuchus Cluster
count/sec/arcsec^2
Radius (arcsec)

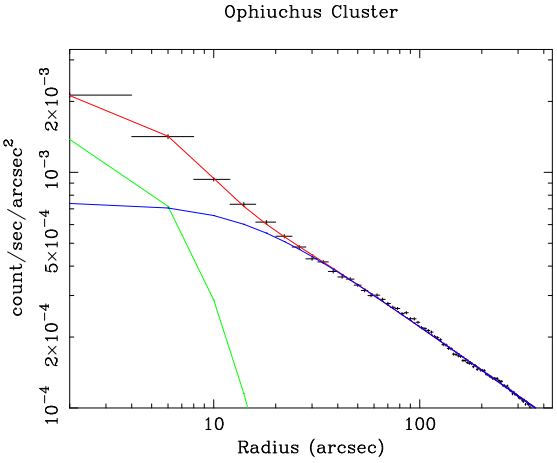
Ophiuchus Cluster
count/sec/arcsec^2
Radius (arcsec)

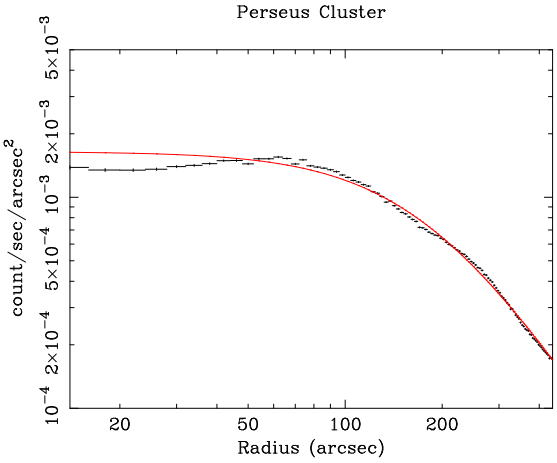
Perseus Cluster
count/sec/arcsec^2
10^{-4} 2×10^{-4} 5×10^{-4} 10^{-3} 2×10^{-3} 5×10^{-3}
20 50 100 200
Radius (arcsec)

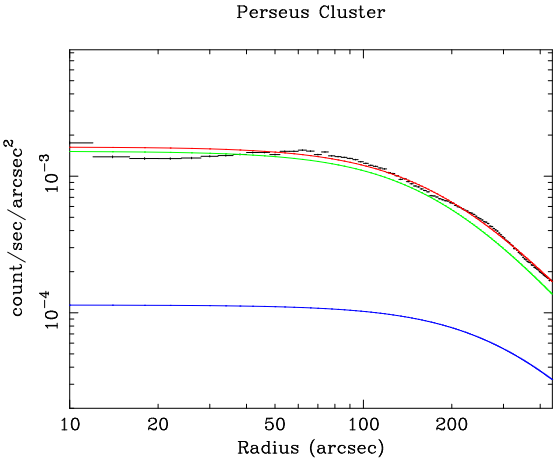
Perseus Cluster
count/sec/arcsec^2
10^{-3} 10^{-4}
10 20 50 100 200
Radius (arcsec)

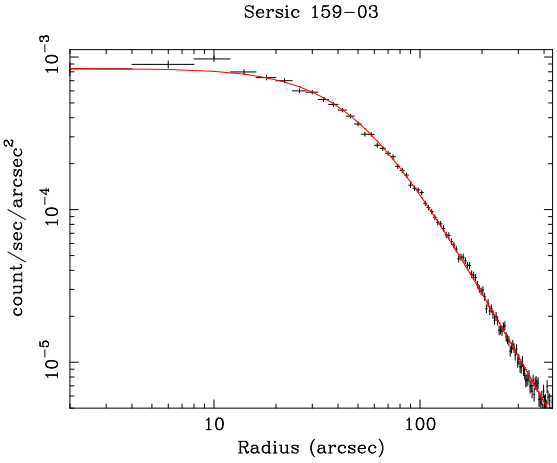
Sersic 159−03
count/sec/arcsec^2
10^{-3} 10^{-4} 10^{-5}
10 100
Radius (arcsec)

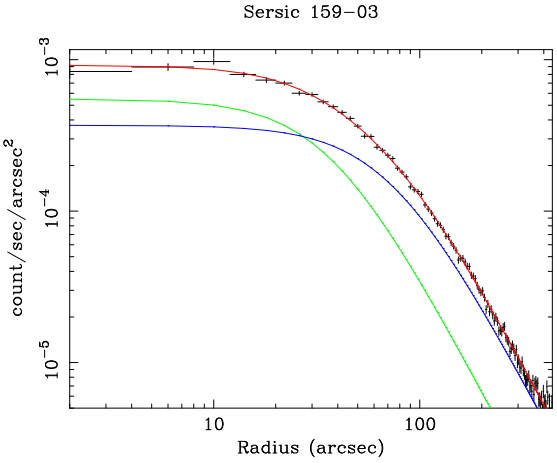
Sersic 159−03
count/sec/arcsec^2
10^{-3} 10^{-4} 10^{-5}
10 100
Radius (arcsec)

Appendix E

Radial Mass Profiles

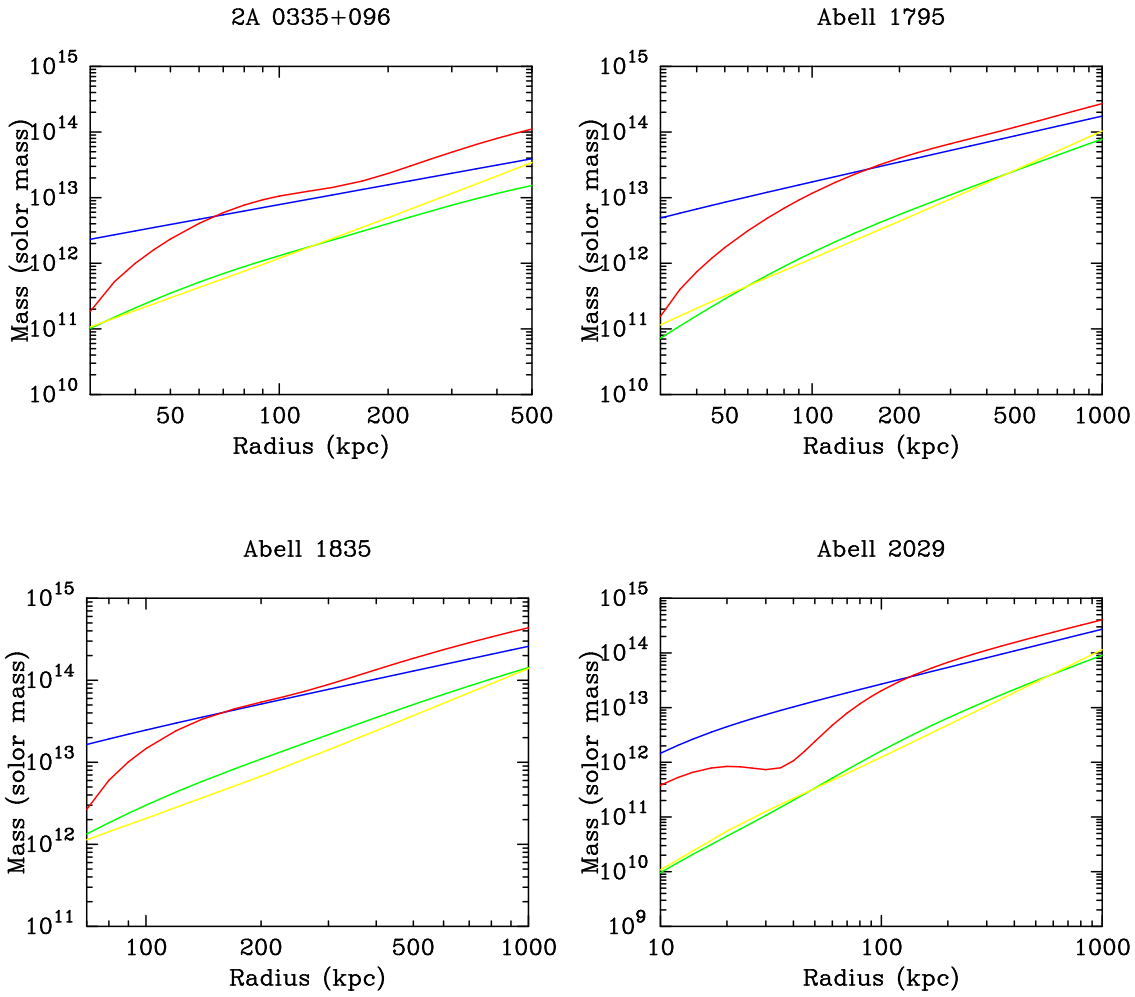

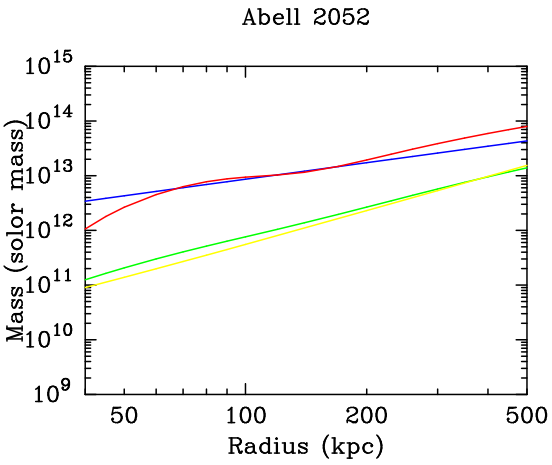
Abell 2052
Mass (solor mass)
Radius (kpc)

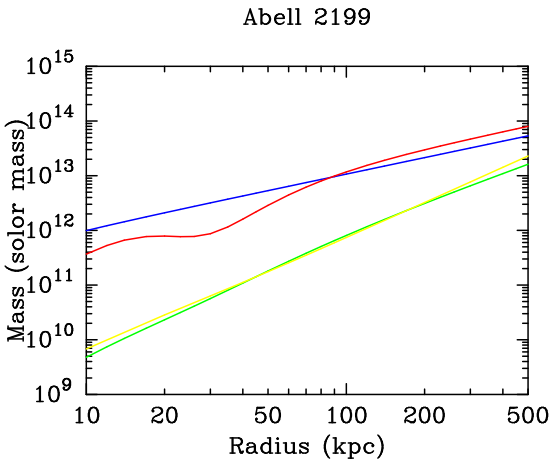
Abell 2199
Mass (solor mass)
Radius (kpc)

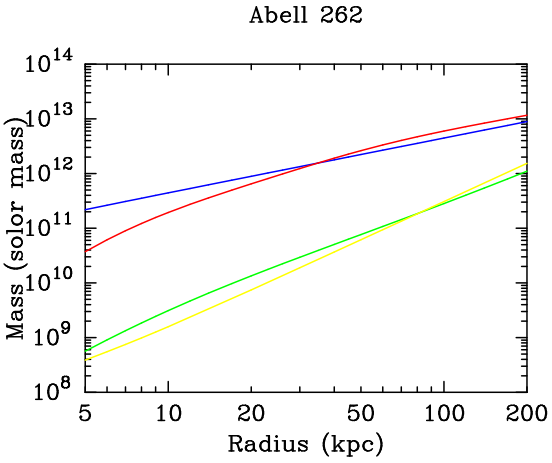
Abell 262
Mass (solor mass)
Radius (kpc)

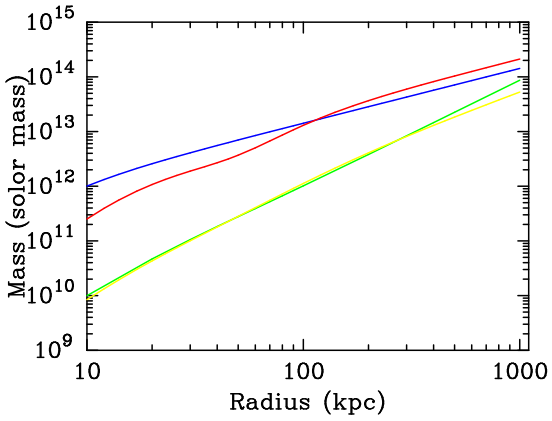
Abell 3112
Mass (solor mass)
Radius (kpc)

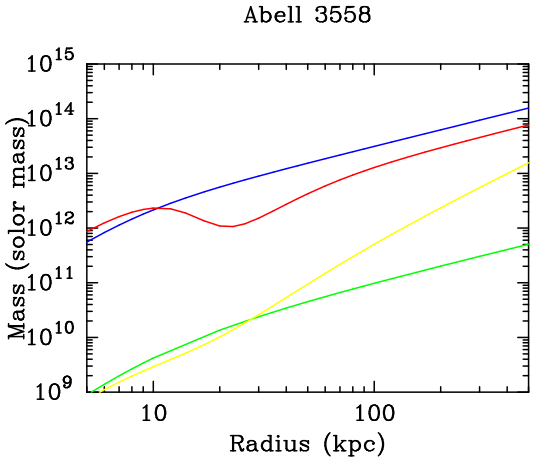
Abell 3558
Mass (solor mass)
Radius (kpc)

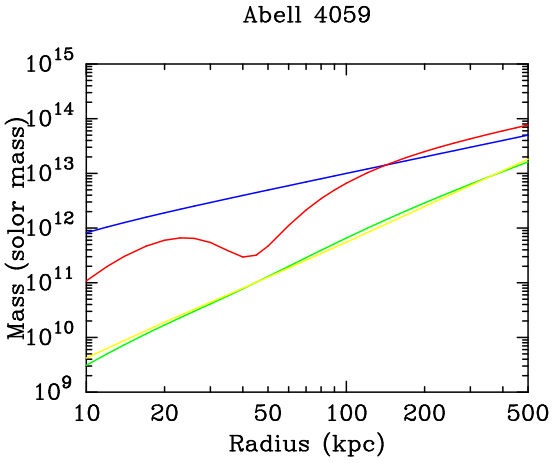
Abell 4059
Mass (solor mass)
Radius (kpc)

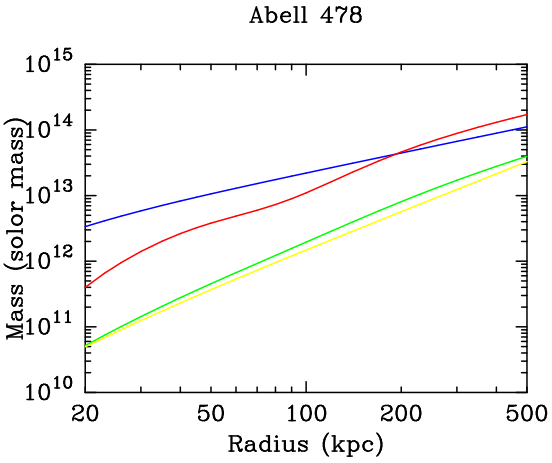
Abell 478
Mass (solor mass)
Radius (kpc)

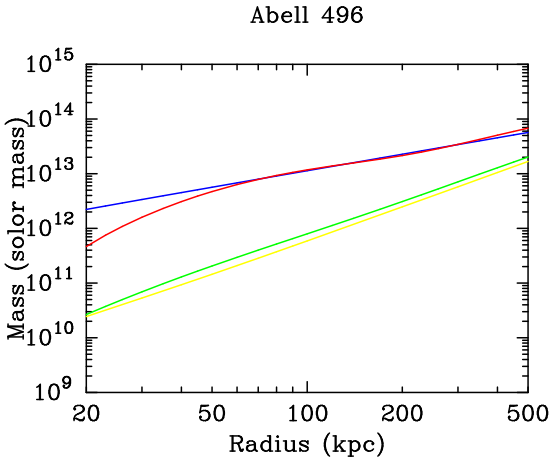
Abell 496
Mass (solor mass)
Radius (kpc)

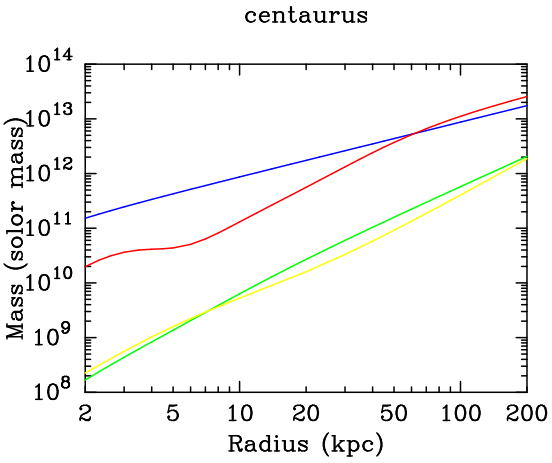
centaurus
Mass (solor mass)
Radius (kpc)

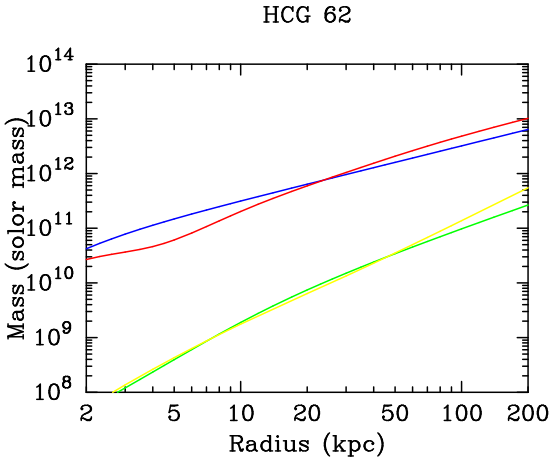
HCG 62
Mass (solor mass)
Radius (kpc)

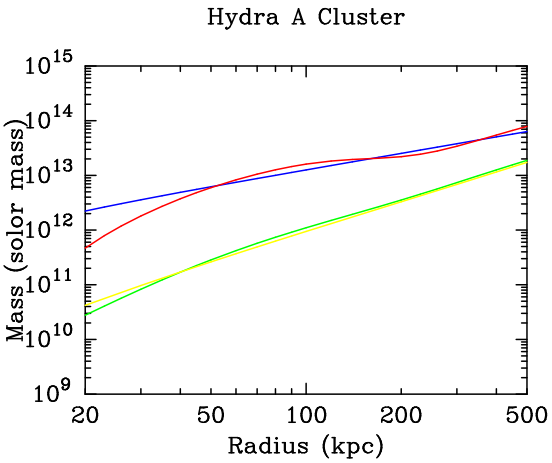
Hydra A Cluster
Mass (solor mass)
Radius (kpc)

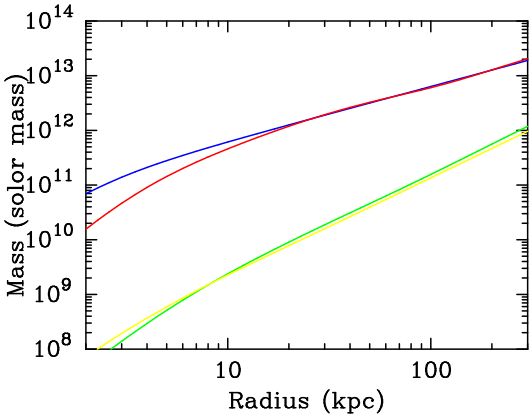
MKW 4
Mass (solor mass)
Radius (kpc)

NGC 5044

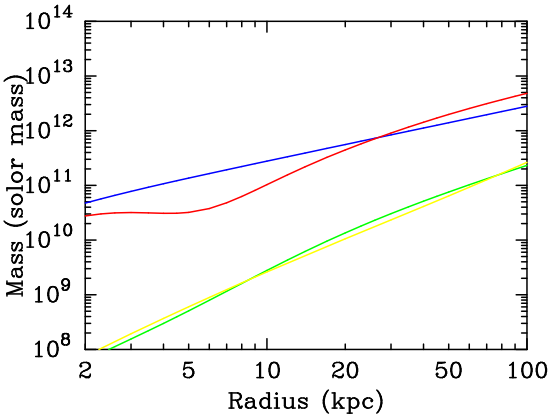

NGC 533

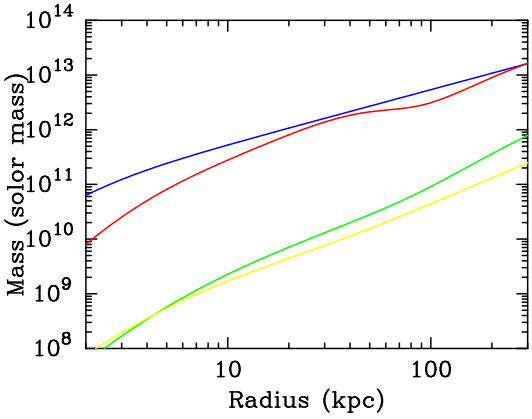

NGC 507

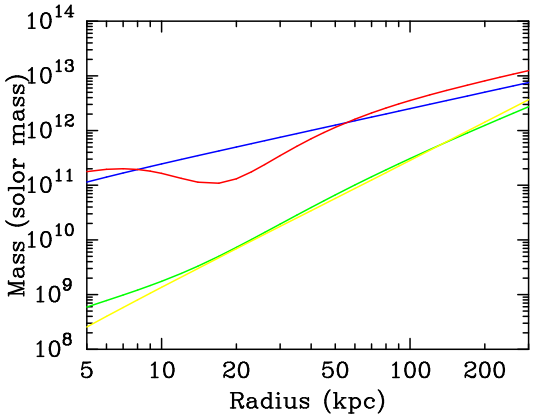

Ophiuchus Cluster

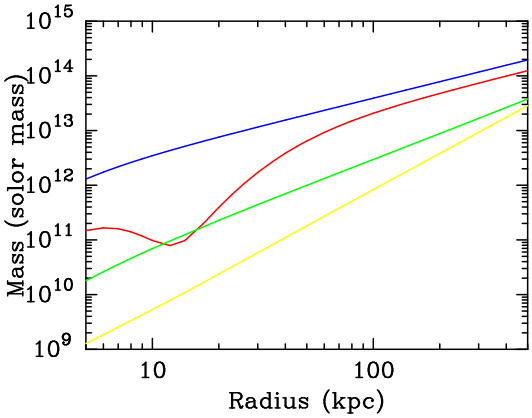

Perseus Cluster

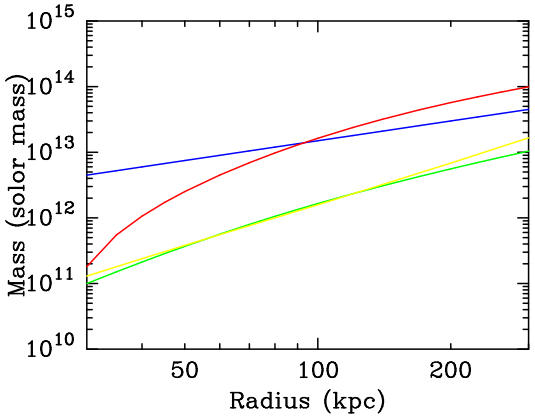

Sersic 159−03

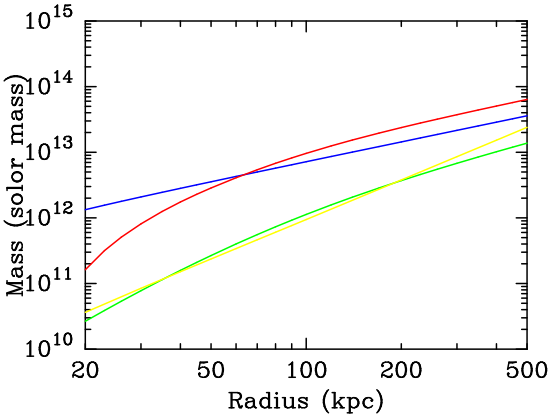

Appendix F

CXB Fluctuation

Defining a quantity $n(S)$ is the differential source number density with the flux S (erg s^{-1} cm^{-2}), $n(R)$ represents the log$N$-log$S$ relation, generally expressed by

$$n(S) = kS^{-\gamma}, \tag{F.1}$$

where the index $\gamma = 2.5$ for the Euclidian universe.

The transmission function $f(\theta, \phi)$, is represented with the observed counting rate c (c s^{-1} cm^{-2}) for the detector to the flux S from the source locating at $\Omega = (\theta, \phi)$ on the sky as

$$c = Af(\Omega)S, \tag{F.2}$$

where A is a constant which normalize $f(\theta, \phi)$ to be 1.0 at its peak (generally at the optical axis of each detector).

From these quantities, the expectation of the source number $d\bar{n}(c)$ with the count rate in the range of $c \sim c + dc$ is calculated as

$$d\bar{n}(c)d\Omega = n(S)\ dS\ d\Omega = n\left(\frac{c}{Af(\Omega)}\right)\frac{c}{Af(\Omega)}\ d\Omega. \tag{F.3}$$

Assuming that the log$N$-log$S$ relation in equation F.1

$$d\bar{n} \quad = \quad kA^{\gamma-1}c^{-\gamma}\Omega_{\rm e}\ dc, \tag{F.4}$$

where

$$\Omega_{\rm e} \equiv \int [f(\Omega)]^{\gamma-1} d\Omega. \tag{F.5}$$

The quantity $\Omega_{\rm e}$ is called "effective beam size" and represents the response of the detector to the source confution.

By using the equation F.4, the expectation of the observed counting rate C (c s^{-1} cm^{-2}) can be estimated as

$$\bar{C} = \int_{C_0}^{\infty} c\ d\bar{n} = kA^{\gamma-1}\Omega_{\rm e}\int_{C_0}^{\infty} c^{-\gamma+1}dc = \frac{kA^{\gamma-1}\Omega_{\rm e}}{2-\gamma}\ C_0^{2-\gamma}, \tag{F.6}$$

where C_0 is a lower cut-off of c, avoiding the divergence of the integral. Since dn should obey the Poisson distribution ($\delta(dn)-2 = d\bar{n}$), we can calculate the stantard deviation σC of the observed counting rate C as

$$\sigma_{\rm C}^2 = \int_0^{C_{\rm cut}} \frac{[c\delta(dn)]^2}{dc} = \int_0^{C_{\rm cut}} c^2 d\bar{n} = \frac{kA^{\gamma-1}\Omega_{\rm e}}{3-\gamma}\ C_{\rm cut}^{3-\gamma}, \tag{F.7}$$

where $C_{\rm cut}$ is an upper cut-off of c. Therefore, the fraction of the CXB fluctuation becomes

$$\sigma_{\rm C}/\bar{C} = \frac{(kA^{\gamma-1}\Omega_{\rm e})(2-\gamma)}{(3-\gamma)(kA^{\gamma-1}\Omega_{\rm e}}2-\gamma) = \frac{2-\gamma}{\sqrt{(3-\gamma)k\Omega_{\rm e}}}\left(\frac{C_{\rm cut}}{A}\right)^{(3-\gamma)/2}\left(\frac{C_0}{A}\right)^{\gamma-2}. \tag{F.8}$$

For the Euclidian universe (i.e. $\gamma = 2.5$), we can obtain

$$\sigma_{\rm C}/\bar{C} \propto \Omega_{\rm e}^{-0.5}\ S_{\rm cut}^{0.25} \quad (S_{\rm cut} \equiv C_{\rm cut}/A). \tag{F.9}$$

Bibliography

[1] Abell, G. O. 1958, ApJS, 3, 211

[2] Abell, G. O., Corwin, H. G. Jr., & Olowin, R. P. 1989, ApJS, 70, 1

[3] Albert, C. E., White, R. A., & Morgan, W. W. 1977, ApJ, 211, 309

[4] Allen, S. W. et al. 1996, MNRAS, 283, 263

[5] Allen, S. W., & Fabian, A. C. 1997, MNRAS, 286, 583

[6] Anders, E., & Grevesse, N. 1989, GeCoA, 53, 197

[7] Arabadjis, J. S., Bautz, M. W., & Garmire, G. P. 2002, ApJ, 572, 66

[8] B$\hat{i}$rzan, L. et al. 2004, ApJ, 607, 800

[9] Bacchi, M. et al. 2003, A&A, 400, 465

[10] Bagchi, J. astro-ph/0210553

[11] Bardelli, S. et al. 1996, A&A, 305, 435

[12] Bautz, L. P., & Morgan, W. W. 1970, ApJ, 162, 149

[13] Bird, C. M., Mushotzky, R. F., & Metzler, C. A. 1995, ApJ, 453, 40

[14] Blanton, E. L., Sarazin, C. L. & McNamara, B. R. 2003, ApJ, 585, 227

[15] Boella, G. et al. 1997, A&AS, 122, 299

[16] Boldt, E. 1987, IAUS, 124, 611

[17] Bradt, H. V., Rothschild, R. E., & Swank, J. H. 1993, A&AS, 97, 355

[18] Byram, E. T., Chubb, T. A., & Friedman, H. 1966, AJ, 71, 379

[19] Carnevali, P., Cavaliere, A., & Santangelo, P. 1981, ApJ, 249, 449

[20] Canizares, C. R., Stewart, G. C., & Fabian, A. C. 1983, ApJ, 272, 449

[21] Cavaliere, A., & Fusco-Femiano, R. 1976, A&A, 49, 137

[22] Churazov, E. et al. 2003, ApJ, 590, 225

[23] Condon, J. J. et al. 1998, AJ, 115, 1693

[24] David, L. P. et al. 1993, ApJ, 412, 479

[25] Deiss, B. M. et al. 1997, A&A, 321, 55

[26] de Plaa, J. et al. 2004, A&A, 423, 49

[27] Dreher, J. W., Carilli, C. L. & Perley, R. A. 1987, ApJ, 316, 611

[28] Edge, A. C., Stewart, G. C., & Fabian, A. C. 1992, MNRAS, 258, 177

[29] Ensslin, T. A. et al. 1998, A&A, 333, 47

[30] Evrard, A. E.; Metzler, C. A. & Navarro, J. F. 1996, ApJ, 469, 494

[31] Fabian, A. C. 1994, ARA&A, 32, 277

[32] Fabian, A. C. & Nulsen, P. E. J. 1977, MNRAS, 180 479

[33] Fabian, A. C. et al. 1994, ApJ, 436, 63

[34] Fabian, A. C. et al. 2001, MNRAS, 321, 33

[35] Feretti, L. & Giovannini, G. 1996, IAUS, 175, 333

[36] Feretti, L. et al. 1995, A&A, 302, 680

[37] Feretti, L. et al. 2004, A&A, 423, 111

[38] Fritz, G. et al. 1971, ApJ, 164, 81

[39] Fujita, Y., & Takahara, F. 1999, ApJ, 519, 51

[40] Fukazawa, Y. et al. 1996, PASJ, 48, 395

[41] Fukazawa, Y. et al. 2000, MNRAS, 313, 21

[42] Fukazawa, Y. et al. 2001, ApJ, 546, 87

[43] Fukazawa, Y. et al. 2004, PASJ, 56, 965

[44] Fukazawa, Y., Makishima, K., & Ohashi, T. 2004, PASJ, 56, 965

[45] Fukazawa. Y. 1997, Ph.D. thesis, The University of Tokyo

[46] Furusho et al. 2001, PASJ, 53, 421

[47] Fusco-Femiano, R. et al. 1999, ApJ, 513, 21

[48] Fusco-Femiano, R. et al. 2000, ApJ, 534, 7

[49] Fusco-Femiano, R. et al. 2001, ApJ, 552, 97

[50] Fusco-Femiano, R. et al. 2004, ApJ, 602, 73

[51] Gehrels, N., & Williams, E. D. 1993, ApJ, 418, 25

[52] Girardi, M. et al. 1996, ApJ, 457, 61

[53] Gitti, M. et al. 2004, A&A, 417, 1

[54] Gitti, M., Brunetti, G., & Setti, G. 2002, A&A, 386, 456

[55] Govoni, F. et al. 2004, ApJ, 605, 695

[56] Gursky, H. et al. 1971, ApJ, 167, 81

[57] Heitler, W. 1954, Teh Quantum Theory of Radiation (Oxford)

[58] Hickson, P., Kindl, E., & Auman, J. R. 1989, ApJS, 70, 687

[59] Ikebe, Y. et al. 1996, Nature, 379, 427

[60] Ikebe, Y. et al. 1997, ApJ, 481, 660

[61] Ikebe, Y. et al. 1999, ApJ, 525, 58

[62] Jones, C., & Forman, W. 1984, ApJ, 276, 38

[63] Kaastra, J. S. & Mewe, R. 1993, A&AS, 97, 443

[64] Kaastra, J. S. et al. 1999, ApJ, 519, 119

[65] Kaastra, J. S. et al. 2001, A&A, 365, 99

[66] Kaastra, J. S. et al. 2004, A&A, 413, 415

[67] Kaastra, J. S., & Mewe, R. 1993, A&AS, 97, 443

[68] Kim, D. W. & Fabbiano, G., 1995 ApJ, 441, 182

[69] King, I. 1962, AJ, 67, 471

[70] Koyama, K et al. 1984, PASJ, 36, 65

[71] Lubin, L. M., & Bahcall, N. A. 1993, ApJ, 415, 17

[72] Makishima, K. et al. 1996, PASJ 48, 171

[73] Makishima, K. et al. 1989. PASJ. 41. 531

[74] Makishima, K. et al. 2001, PASJ, 53, 401

[75] Markevitch, M. 1998, ApJ, 504, 27

[76] Markevitch, M. et al. 2000, ApJ, 541, 542

[77] Masai, K. 1984, Ap&SS, 98, 367

[78] Masai, K. 1997, A&A, 324, 410

[79] Matsumoto, R. Advanced Space Research, 25, 3/4, 499

[80] Matsumoto, Y. et al. 2001, PASJ, 53, 475

[81] Matsushita, K. et al. 1994, ApJ, 436, 41

[82] Matsushita, K., Finoguenov, A., & Böhringer, H. 2003, A&A, 401, 443

[83] Meekins, J. F. et al. 1971, Natur, 231 107

[84] Mitchell, R. J. et al. 1976, MNRAS, 175, 29

[85] Morgan, W. W., Kayser, S., & White, R. A. 1975, ApJ, 199, 545

[86] Motl, P. M. et al. 2004, ApJ, 606, 635

[87] Mulchaey, J. S., Davis, S. S., Mushozky, R. F., & Burstein, D. 1996, ApJ, 456, 80

[88] Mushotzky, R. F. Physs. Scripta, T7, 157

[89] Nakazawa. Y. 2000, Ph.D. thesis, The University of Tokyo

[90] Nevalainen, J. et al. 2004, ApJ, 608, 166

[91] Ohashi, T. et al. 1996, PASJ, 48, 157

[92] Paolillo, M. et al. 2003, ApJ, 586, 850

[93] Ponman, T. J., Cannon, D. B., & Navarro, J. F. 1999, Natur, 397, 135

[94] Raymond, J. C. & Smith, B. W. 1977, ApJS, 35, 419

[95] Rephaeli, Y. 1979, ApJ, 227, 364

[96] Rephaeli, Y., Gruber, D, & Blanco, P. 1999, ApJ, 511, 21

[97] Rephaeli, Y., Gruber, D. E., & Rothschild, R. E. 1987, ApJ, 320, 139

[98] Rephaeli, Y., Ulmer, M., & Gruber, D. 1994, ApJ, 429, 554

[99] Rood, H. J., & Sastry, G. N. 1971, PASP, 83, 313

[100] Rybicki, G. B., & Lightman, A. P. 1979, *RadiativeProcessesinAstrophysics*

[101] Sanders, J. S., & Fabian, A. C. 2002, MNRAS, 331, 273

[102] Sarazin, C. L. 1999, ApJ, 520, 529

[103] Sarazin, C. L. & Kempner, J. C. 2000, ApJ, 533, 73

[104] Smith, R. K. et al. 2001, ApJ, 556, 91

[105] Spergel, D. N. et al. 2003, ApJS, 148, 175

[106] Takahashi. I. 2004, Ph.D. thesis, The University of Tokyo

[107] Tanaka, Y. et al. 1984, PASJ, 36, 641

[108] Tanaka, Y., Inoue, H., & Holt, S. S. 1994, PASJ, 46, L37

[109] Taylor, G. B. & Perley, R. A. 1993, ApJ, 416, 554

[110] Taylor, G. B., Fabian, A. C., & Allen, S. W. 2002, MNRAS, 334, 769

[111] Thierbach, M.; Klein, U.; Wielebinski, R. 2003A&A...397...53T

[112] Valageas, P., & Silk, J. 1999, A&A, 350, 725

[113] Voigt, L. M. & Fabian, A. C. 2004, MNRAS, 347, 1130

[114] Watanabe, M. et al. 2001, PASJ, 53, 605

[115] Weisskopf, M. C. et al. 2000

[116] White, S. D. M. 1976, MNRAS, 177, 717

[117] Xu, H. et al. 1998, ApJ, 500, 738

[118] Xue, Y. J. & Wu, X. P. 2000, ApJ, 538, 65

[119] Zwicky, F. et al. 1961–1968, *Catalogue of Galaxies and Clusters of Galaxies*, Vol.1–6 Pasadena: Caltech

Acknowledgment

I would like to express my special gratitude to Prof. T. Ohsugi for his continuous guidance and advice throughout the five years of my graduate course, especially in finishing this thesis. I greatly appreciate Prof. Y. Fukazawa for his technical support in analysis, valuable discussions, and hearty encouragement as well as giving me a opportunity of studying Astrophysics.

I owe a great deal to all the scientists and engineers who worked or are working on the development and operation for the *ASTRO-E*, *ASTRO-E2*, and *Suzaku* project. *Suzaku* had been launched on 2005 July 10, with the great efforts of *Suzaku* team members. I greatly appreciate having the opportunity to be engage on this project and analyze the *Suzaku* data in this thesis.

I would greatly appreciate Dr. K. Nakazawa for his lucid advice on the analysis of galaxy clusters, and technical support in calibrating and analyzing the *HXD-II* data. I would like to thank to Prof. K. Makishima, Dr. M. Kokubun, Dr. I. Takahashi, and Dr. M. Murashima for their support and cooperation in manufacturing the *HXD-II* detector. I am deeply grateful to Mr. S. Uno, Mr. A. Ohto, Mr. S. Kawasoe, and Mr. K. Kawamoto, who shared my graduate course. Their words and faith encouraged me so much. I wish to thank to Mr. M. Ohno for his encouragement and valuable discussions for my study. I am also much obliged to all the past and present members of High Energy Particle & Astrophysics group in the Hiroshima University.

Finally, I would like to thank my family and friends. This work cannot be done without their understanding and hearty supporting.